frontiers | Research Topics

In celebration of women in science: Lipids, membranes, and membranous organelles

Edited by
Elena G. Govorunova and Isabel María López-Lara

Published in
Frontiers in Molecular Biosciences

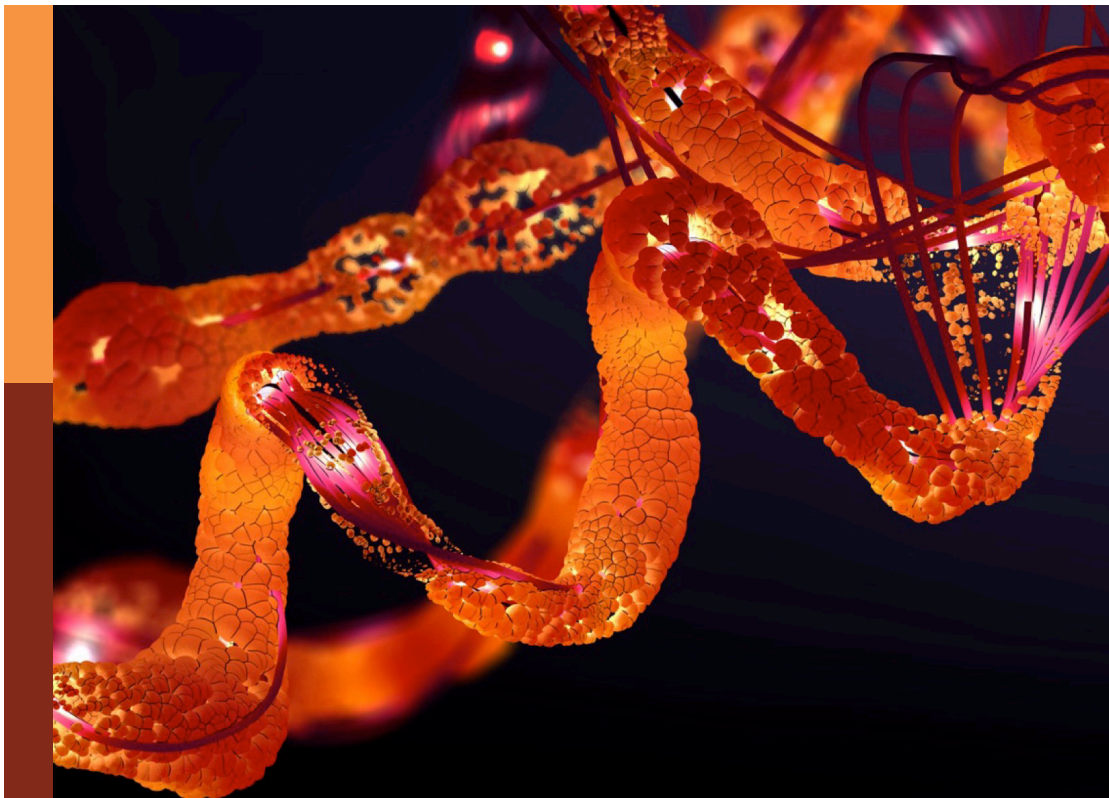

ISSN 1664-8714
ISBN 978-2-8325-2271-4
DOI 10.3389/978-2-8325-2271-4

About Frontiers

Frontiers is more than just an open access publisher of scholarly articles: it is a pioneering approach to the world of academia, radically improving the way scholarly research is managed. The grand vision of Frontiers is a world where all people have an equal opportunity to seek, share and generate knowledge. Frontiers provides immediate and permanent online open access to all its publications, but this alone is not enough to realize our grand goals.

Frontiers journal series

The Frontiers journal series is a multi-tier and interdisciplinary set of open-access, online journals, promising a paradigm shift from the current review, selection and dissemination processes in academic publishing. All Frontiers journals are driven by researchers for researchers; therefore, they constitute a service to the scholarly community. At the same time, the *Frontiers journal series* operates on a revolutionary invention, the tiered publishing system, initially addressing specific communities of scholars, and gradually climbing up to broader public understanding, thus serving the interests of the lay society, too.

Dedication to quality

Each Frontiers article is a landmark of the highest quality, thanks to genuinely collaborative interactions between authors and review editors, who include some of the world's best academicians. Research must be certified by peers before entering a stream of knowledge that may eventually reach the public - and shape society; therefore, Frontiers only applies the most rigorous and unbiased reviews. Frontiers revolutionizes research publishing by freely delivering the most outstanding research, evaluated with no bias from both the academic and social point of view. By applying the most advanced information technologies, Frontiers is catapulting scholarly publishing into a new generation.

What are Frontiers Research Topics?

Frontiers Research Topics are very popular trademarks of the *Frontiers journals series*: they are collections of at least ten articles, all centered on a particular subject. With their unique mix of varied contributions from Original Research to Review Articles, Frontiers Research Topics unify the most influential researchers, the latest key findings and historical advances in a hot research area.

Find out more on how to host your own Frontiers Research Topic or contribute to one as an author by contacting the Frontiers editorial office: frontiersin.org/about/contact

In celebration of women in science: Lipids, membranes, and membranous organelles

Topic editors

Elena G. Govorunova — University of Texas Health Science Center at Houston, United States

Isabel María López-Lara — National Autonomous University of Mexico, Mexico

Citation

Govorunova, E. G., López-Lara, I. M., eds. (2023). *In celebration of women in science: Lipids, membranes, and membranous organelles*.

Lausanne: Frontiers Media SA. doi: 10.3389/978-2-8325-2271-4

Table of contents

frontiers | Frontiers in Molecular Biosciences

TYPE Editorial
PUBLISHED 13 April 2023
DOI 10.3389/fmolb.2023.1187356

OPEN ACCESS

EDITED AND REVIEWED BY
B. J. Wilkinson,
Illinois State University, United States

*CORRESPONDENCE
Isabel M. López-Lara,
isabel@ccg.unam.mx
Elena G. Govorunova,
Elena.G.Govorunova@uth.tmc.edu

RECEIVED 16 March 2023
ACCEPTED 04 April 2023
PUBLISHED 13 April 2023

CITATION
López-Lara IM and Govorunova EG (2023), Editorial: In celebration of women in science: Lipids, membranes, and membranous organelles.
Front. Mol. Biosci. 10:1187356.
doi: 10.3389/fmolb.2023.1187356

Editorial: In celebration of women in science: Lipids, membranes, and membranous organelles

Isabel M. López-Lara[1]* and Elena G. Govorunova[2]*

[1]Centro de Ciencias Genómicas, Universidad Nacional Autónoma de México, Cuernavaca, Mexico, [2]Department of Biochemistry and Molecular Biology, Center for Membrane Biology, The University of Texas Health Science Center at Houston McGovern Medical School, Houston, TX, United States

KEYWORDS

women in science, membrane lipid, membrane transport protein, fatty acid, lipid bilayer, lipid remodeling

Editorial on the Research Topic
In Celebration of Women in Science: Lipids, Membranes, and Membranous Organelles

Integral membrane proteins have always been the focus of biomedical research because of their central role in transmembrane transport and signaling, energy transduction, maintaining of homeostasis, and numerous other cellular processes (Sachs and Engelman, 2006). In contrast, a lipid bilayer was initially considered as a relatively inert background for protein players. However, experimental evidence of functional modulation of membrane proteins by lipids challenged this view already ~30 years ago (Bogdanov and Dowhan, 1995). Since then, a bewildering complexity has been revealed. Protein function is controlled, on the one hand, by bulk biophysical properties of the bilayer, such as its thickness, fluidity and elastic stress (Baccouch et al., 2022), and, on the other hand, by specific lipid-protein interactions (Jodaitis et al., 2021).

This Research Topic on the Celebration of Women in Science features articles by women authors and principal investigators active in the fields of Lipids, Membranes, and Membraneous Organelles. Frontiers in Molecular Biosciences has launched the Specialty Section "Lipids, Membranes, and Membranous Organelles" to create a forum for the exchange of results and ideas on the structure and function of membrane lipids and proteins, and on the entire membrane as a dynamic system. A dynamic view of the membrane reveals previously unrecognized regulatory mechanisms and facilitates understanding of cellular pathologies resulting from disruption of the normal membrane structure and function. This Research Topic is an inaugural Research Topic for this new Specialty Section and provides a snapshot of research conducted by women in the field. Contributors to this Research Topic examine various aspects of lipid, protein and membrane complexity using a wide range of approaches, from classical biochemistry (Stępniak et al.) to electron paramagnetic resonance (EPR) spectroscopy (Bartucci and Aloi), molecular modeling (Hryc et al.), confocal microscopy (Bulatova et al.) and lipidomic analyses (Balbi et al.).

A research team led by Malgorzata Karbownik-Lewinska (Stępniak et al.) found that membrane lipids in the thyroid comparing to non-endocrine tissues are less sensitive to pro-oxidative effects of Fenton reaction substrates, whereas melatonin decreased lipid

peroxidation regardless of the oxidative stress associated with thyroid hormone production.

A mini-review by Bartucci and Aloi summarizes recent advances in probing librational (swaying) dynamics of lipids in model and natural membranes by electron spin echo (ESE) methods of time-resolved, pulsed EPR spectroscopy at cryogenic temperatures.

In plants, fatty acids (FAs) are synthesized in the chloroplast stroma and transferred to the endoplasmic reticulum (ER), where they are assembled into acyl lipids, including triacylglycerol stored in the oil bodies. In a collaborative paper by the groups of Katrin Philippar, Yonghua Li-Beisson and Michael Schroda (Peter et al.), the authors characterized FAX (fatty acid export) proteins in the unicellular green alga *Chlamydomonas reinhardtii* used for biofuel and biomaterial production.

P-glycoprotein (Pgp) is a multidrug transporter that binds a wide variety of hydrophobic compounds including anticancer drugs and uses the energy of ATP to pump the drugs out of the cells. The research group of Ina L. Urbatsch systematically investigated modulation of verapamil-stimulated ATPase activity of Pgp by artificial lipid mixtures that mimic the lipid composition of mammalian plasma membranes (Tran et al.).

Hyrc et al. carried out computational studies to identify the network of interactions of the lipid/water interfase of the thylakoid-forming lipids monogalactosyldiacylglycerol (MGDG) and digalactosyldiacylglycerol (DGDG). They concluded that the interaction network at the DGDG bilayer interface is more stable than in the MGDG bilayer.

The membrane protein NaPi2b is a sodium-dependent phosphate transporter that has been demonstrated to be overexpressed in ovarian and other cancers. A research team led by Ramziya Kiyamova and Mikhail Bogdanov (Bulatova et al.) show experimental evidence of the topology of untagged NaPi2b transporter in intact ovarian cancer cells. This precise information is of great importance for engineering therapeutic antibodies directed to fully accessible extramembrane domains.

A proper lipid composition of the membrane is essential for all forms of life. In humans, mutation of the *TAFAZZIN* gene leads to Barth syndrome, a mitochondrial lipid disorder causing severe cardiomyopathy. TAFAZZIN is a transacylase that is required for remodeling of cardiolipin acyl chains. Liang et al. present a perspective that focus on the link between TAFAZZIN dysfunction and an elevated level of reactive oxygen species (ROS). Authors propose that understanding the mechanism that leads to ROS formation in Barth syndrome can provide new tools for treatment.

Some microbial organisms are faced with harsh environmental conditions and to maintain membrane integrity they use different strategies. Tamby et al. review membrane lipid adaptations used by microbes living in the extreme conditions of the deep-see that is characterized by high hydrostatic pressure and low temperatures. To maintain fluidity of the membranes, bacteria increase unsaturation of fatty acyl chains while archaea show a rise in cyclisation of alkyl chains.

The lipid bilayer constitutes a semipermeable barrier for exogenous substances, and it is also the target for some molecules, among them membrane-acting antibiotics like daptomycin (Nguyen et al.) or the aegerolysin-based protein complexes derived from *Pleurotus* (Balbi et al.). Nguyen et al. review the mechanisms adopted by the bacterial cell membrane of Gram-positive pathogens acquiring resistance to the antibiotic daptomycin. Generally, changes in phospholipids are responsible for the acquired resistance to daptomycin.

Protein complexes of aegerolysins cause pores in insect gut cells by binding specifically to the sphingolipid ceramide phosphoethanolamine (CPE). Balbi et al. present evidence that also the sphingolipid ceramide aminoethylphosphonate (CAEP) can act as high-affinity receptor for aegerolysins protein complexes. CAEP is specifically found in plant pathogen oomycetes and in fouling marine invertebrates, and aegerolysin protein complexes could be used to eliminate them.

To conclude, we would like to note that the current view attributes underrepresentation of women in science, technology, engineering, and mathematics (STEM) to a complex interplay of social and cultural forces (Girelli, 2022). According to the United States Bureau of Labor Statistics, the gender gap is particularly large in some of the fastest-growing and highest-paid jobs such as computer programmers (only 19.5% of them were women in the year 2021). However, in biological sciences women were represented much better at 48.1% in the same year. This Research Topic is, no doubt, yet another demonstration of the success of female investigators in science.

Author contributions

IL-L and EG wrote the article and approved the submitted version.

Funding

IL-L was supported by UNAM-PAPIIT IN208222.

Acknowledgments

The editors would like to thank all the authors and expert reviewers who have participated in the preparation and evaluation of manuscripts presented in this Research Topic.

Conflict of interest

The authors declare that the research was conducted in the absence of any commercial or financial relationships that could be construed as a potential conflict of interest.

Publisher's note

References

Baccouch, R., Rascol, E., Stoklosa, K., and Alves, I. D. (2022). The role of the lipid environment in the activity of G protein coupled receptors. *Biophys. Chem.* 285, 106794. doi:10.1016/j.bpc.2022.106794

Bogdanov, M., and Dowhan, W. (1995). Phosphatidylethanolamine is required for *in vivo* function of the membrane-associated lactose permease of *Escherichia coli*. *J. Biol. Chem.* 270, 732–739. doi:10.1074/jbc.270.2.732

Girelli, L. (2022). What does gender has to do with math? Complex questions require complex answers. *J. Neurosci. Res.* 101 (5), 679–688. doi:10.1002/jnr.25056

Jodaitis, L., van Oene, T., and Martens, C. (2021). Assessing the role of lipids in the molecular mechanism of membrane proteins. *Int. J. Mol. Sci.* 22, 7267. doi:10.3390/ijms22147267

Sachs, J. N., and Engelman, D. M. (2006). Introduction to the membrane protein reviews: The interplay of structure, dynamics, and environment in membrane protein function. *Annu. Rev. Biochem.* 75, 707–712. doi:10.1146/annurev.biochem.75.110105.142336

frontiers | Frontiers in Molecular Biosciences

ORIGINAL RESEARCH
published: 25 May 2022
doi: 10.3389/fmolb.2022.902706

Ceramide Aminoethylphosphonate as a New Molecular Target for Pore-Forming Aegerolysin-Based Protein Complexes

Teresa Balbi[1†], Francesco Trenti[2†], Anastasija Panevska[3], Gregor Bajc[3], Graziano Guella[2], Caterina Ciacci[4], Barbara Canonico[4], Laura Canesi[1] and Kristina Sepčić[3]**

[1]Department of Earth, Environmental and Life Sciences, University of Genoa, Genoa, Italy, [2]Bioorganic Chemistry Laboratory, Department of Physics, University of Trento, Trento, Italy, [3]Department of Biology, Biotechnical Faculty, University of Ljubljana, Ljubljana, Slovenia, [4]Department of Biomolecular Sciences, University of Urbino Carlo Bo, Urbino, Italy

OPEN ACCESS

Edited by:
Isabel María López-Lara, National Autonomous University of Mexico, Mexico

Reviewed by:
Xabier Contreras, University of the Basque Country, Spain
Arun Radhakrishnan, University of Texas Southwestern Medical Center, United States

***Correspondence:**
Kristina Sepčić
kristina.sepcic@bf.uni-lj.si
Laura Canesi
laura.canesi@unige.it

†These authors have contributed equally to this work

Specialty section:
This article was submitted to Lipids, Membranes and Membranous Organelles, a section of the journal Frontiers in Molecular Biosciences

Received: 23 March 2022
Accepted: 20 April 2022
Published: 25 May 2022

Citation:
Balbi T, Trenti F, Panevska A, Bajc G, Guella G, Ciacci C, Canonico B, Canesi L and Sepčić K (2022) Ceramide Aminoethylphosphonate as a New Molecular Target for Pore-Forming Aegerolysin-Based Protein Complexes. Front. Mol. Biosci. 9:902706. doi: 10.3389/fmolb.2022.902706

Ostreolysin A6 (OlyA6) is a 15 kDa protein produced by the oyster mushroom (*Pleurotus ostreatus*). It belongs to the aegerolysin family of proteins and binds with high affinity to the insect-specific membrane sphingolipid, ceramide phosphoethanolamine (CPE). In concert with its partnering protein with the membrane-attack-complex/perforin domain, pleurotolysin B (PlyB), OlyA6 can form bicomponent 13-meric transmembrane pores in artificial and biological membranes containing the aegerolysin lipid receptor, CPE. This pore formation is the main underlying molecular mechanism of potent and selective insecticidal activity of OlyA6/PlyB complexes against two economically important coleopteran plant pests: the western corn rootworm and the Colorado potato beetle. In contrast to insects, the main sphingolipid in cell membranes of marine invertebrates (i.e., molluscs and cnidarians) is ceramide aminoethylphosphonate (CAEP), a CPE analogue built on a phosphono rather than the usual phosphate group in its polar head. Our targeted lipidomic analyses of the immune cells (hemocytes) of the marine bivalve, the mussel *Mytilus galloprovincialis,* confirmed the presence of 29.0 mol% CAEP followed by 36.4 mol% of phosphatidylcholine and 34.6 mol% of phosphatidylethanolamine. Further experiments showed the potent binding of OlyA6 to artificial lipid vesicles supplemented with mussel CAEP, and strong lysis of these vesicles by the OlyA6/PlyB mixture. In *Mytilus* haemocytes, short term exposure (max. 1 h) to the OlyA6/PlyB mixture induced lysosomal membrane destabilization, decreased phagocytic activity, increased Annexin V binding and oxyradical production, and decreased levels of reduced glutathione, indicating rapid damage of endo-lysosomal and plasma membranes and oxidative stress. Our data suggest CAEP as a novel high-affinity receptor for OlyA6 and a target for cytolytic OlyA6/PlyB complexes.

Keywords: aegerolysins, bioinsecticides, ceramide aminoethylphosphonate, hemocytes, marine bivalves, *Mytilus galloprovincialis*, *pleurotus*, toxicity

1 INTRODUCTION

Aegerolysins (Pfam 06355; InterPro IPR009413) are small (13–20 kDa) acidic proteins that have been identified in several eukaryotes and prokaryotes, and are especially abundant in bacteria and mushrooms (Novak et al., 2015; Butala et al., 2017). Several edible oyster mushrooms (e.g., *Pleurotus ostreatus, P. eryngii, P. pulmonarius*) harbour various highly identical (78%–98%) aegerolysin sequences in their genomes (Panevska et al., 2021). The most prominent feature of these *Pleurotus* aegerolysins is their ability to specifically interact with selected membrane lipids and lipid domains (Butala et al., 2017; Grundner et al., 2021; Panevska et al., 2021). Furthermore, *Pleurotus* aegerolysins can act in concert with pleurotolysin B (PlyB) or erylysin B, highly (>95%) identical 59-kDa protein partners that have a membrane-attack-complex/perforin (MACPF) domain and are produced by *P. ostreatus* and *P. eryngii,* respectively (Tomita et al., 2004; Ota et al., 2013; Lukoyanova et al., 2015; Milijaš Jotić et al., 2021). Upon binding to the membrane lipid receptor, aegerolysin recruits the MACPF-partnering protein that undergoes extensive conformational changes and penetrates the membrane. The final bi-component transmembrane pore is composed of 13 MACPF-protein molecules, each sitting atop of an aegerolysin dimer (Ota et al., 2013; Lukoyanova et al., 2015; Milijaš Jotić et al., 2021). This pore formation results in direct cell death, or in the creation of a passageway for other molecules that can kill the cell.

In particular, the aegerolysin ostreolysin A6 (OlyA6) from the edible oyster mushroom (*P. ostreatus*) can interact with moderate affinity (k_D~ 1 μM) with membrane nanodomains enriched in sphingomyelin and cholesterol (Chol) (Skočaj et al., 2014; Bhat et al., 2015), where it specifically senses the Chol-bound conformation of sphingomyelin (Endapally et al., 2019), and can therefore be applied as ideal non-toxic marker for visualization of the structure and dynamics of membrane rafts in living mammalian cells (Skočaj et al., 2014; Endapally et al., 2019). Furthermore, OlyA6 can interact with high affinity (k_D~ 1 nM) with artificial lipid vesicles and biological membranes that contain physiologically relevant concentrations (1–5 mol%) of ceramide phosphoethanolamine (CPE) (Bhat et al., 2015; Panevska et al., 2019a; Novak et al., 2020; Panevska et al., 2021), which is the major sphingolipid in invertebrate cell membranes and is not found in other taxa (Panevska et al., 2019b). Through this CPE-binding, the OlyA6/PlyB cytolytic complexes have been shown to act as potent and species-specific bioinsecticides, for use against selected coleopteran pests, such as western corn rootworm and Colorado potato beetle (Panevska et al., 2019a). We confirmed that the molecular mechanism of action of these insecticidal protein complexes arises from their specific interactions with their membrane lipid receptor, the CPE (Milijaš Jotić et al., 2021) at the acidic conditions that are characteristic for beetles' midgut.

In addition to arthropods (Crone and Bridges, 1963; Masood et al., 2010; Kraut, 2011; Panevska et al., 2019a), the presence of CPE was also found in deep-sea mussels (Kellermann et al., 2012) and some marine gastropods (sea snails) (Hori et al., 1967), protozoa (Broad and Dawson, 1973; Kaneshiro et al., 1997), oomycetes (Moreau et al., 1998), and Bacteroidetes (Batrakov et al., 2000). Moreover, marine invertebrates (bivalves, gastropods, cephalopods, oysters, sea anemones, hydrocorals) synthesize as the main membrane component an even more peculiar sphingophosphonolipid, ceramide-2-aminoethylphosphonate (CAEP), which contains a carbon-phosphorus bond and has a unique triene type of sphingoid base in its structure (Moschidis, 1984; Tomonaga et al., 2017; Imbs et al., 2019). Also, some marine protozoa, bacteria (*Bdellovibrio bacteriovous*), and plant pathogen oomycetes (*Pythium prolatrum*) can contain CAEP in their membranes (Moschidis, 1984), but in mammals this lipid is very rare, as it is the CPE. The CAEP lipid has 2-aminoethylphosphonate as its polar head group, with a phosphorus atom directly attached to a carbon atom (C-P bond) (Tomonaga et al., 2017), in contrast to the C-O-P bond found in phosphoethanolamine as the polar head group of CPE (**Figure 1**). The data on the physical properties and morphology of CAEP-containing membranes are still sparse in the literature and have not been studied in detail. Although there is a lack of information on the physical properties of this lipid, CAEP has a high structural similarity to CPE, and is considered as even more stable molecule than CPE (Vacaru et al., 2013). The biological role of CAEP has not been fully elucidated, but it is thought to have similar activity in marine invertebrates as the major mammalian sphingolipid, sphingomyelin (Wang et al., 2020).

Recent analysis of the lipidome of the marine bivalve, the Mediterranean mussel (*Mytilus galloprovincialis*) revealed the presence of CAEP species (Donato et al., 2018). During our evaluation of toxicity of insecticidal complexes based on *Pleurotus* aegerolysins on various target and non-target terrestrial and aquatic invertebrates, we explored the possibility that these protein complexes, in particular OlyA6/PlyB, might exert toxicity also against mussel cells. In this regard, mussel immune cells (hemocytes), a widespread experimental model to evaluate the effects and mechanisms of action of different chemicals in mussels (Katsumiti et al., 2019; Balbi et al., 2021), were utilized as a model to further explore the lipid composition of *Mytilus* cells, to identify the possible OlyA6 membrane lipid receptor, and to evaluate the toxicity of OlyA6/PlyB complexes.

2 RESULTS

2.1 Lipidome Analysis and CAEP Isolation From *M. galloprovincialis* Hemocytes

Our ^{31}P-NMR analyses of lipids extracted from *M. galloprovincialis* hemocytes showed three major phospholipids classes: phosphatidylcholine (PC); phosphatidylethanolamine (PE) and CAEP. The latter represented 29.0 mol% of all phospholipids, with a contribution of 4.4 mol% hydroxylated CAEP and 24.6 mol% miscellaneous CAEP counting different chain length and degree of unsaturation. PC and PE contributed to the phospholipid content by 36.4 mol% and 34.6 mol%, respectively (**Figure 2**). Phosphatidylcholines were found as a

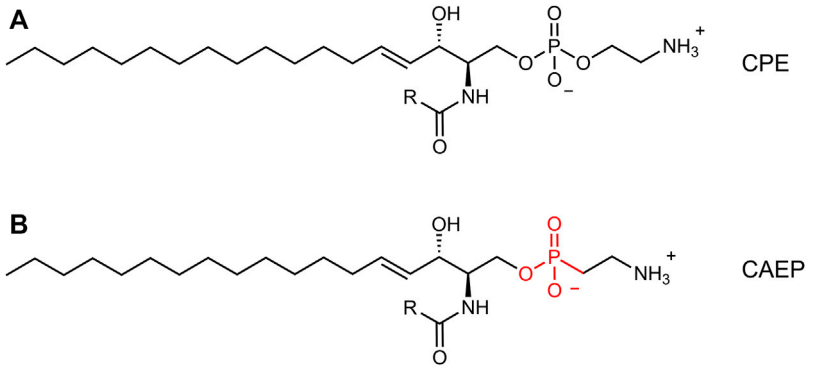

FIGURE 1 | Comparison between canonical ceramide phosphoethanolamine (CPE, **(A)** and ceramide aminoethylphosphonate (CAEP, **(B)**. The latter bears a phosphonate headgroup instead of a phosphate group.

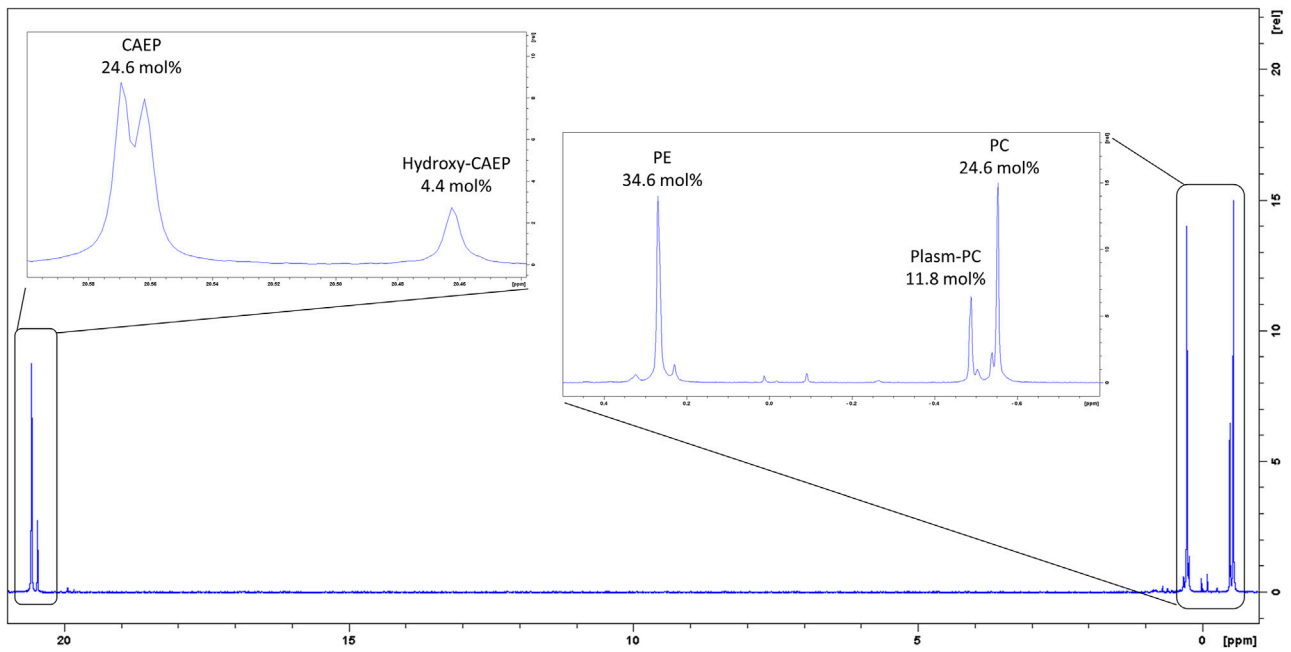

FIGURE 2 | ^{31}P-NMR spectrum of *M. galloprovincialis* hemocytes raw extract.

mixture of canonical PC and plasmenyl-PC, accounting for the 24.6 mol% and 11.8 mol%, respectively. ^{1}H-NMR spectrum allowed us to estimate the membrane fluidity by calculating the ratio between PC and total Chol. We found the value of PC/Chol ratio to be 1.6, indicating a presence of about 22 mol% of Chol in mussel hemocytes. A thorough analysis of the ^{1}H and ^{13}C-NMR spectra (including 2D measurements) of the raw extract allowed to establish the structural features of the isolated CAEP lipids as summarized in **Figure 3**.

In particular, the ethylamino moieties of PE and CAEP were clearly identified by the ^{1}H-NMR signal (**Supplementary Figure S1**). In fact, the methylene group–$\mathbf{CH_2}$-NH_2 in CAEP is characterized by geminal protons at δ_H 3.09 td (7.0, 13.9 Hz) coupled to δ_C 36.9 whilst the corresponding methylene group of PE shows signals at δ_H 3.13 brt (7.0 Hz) coupled to δ_C 41.9 (**Supplementary Figure S1**). The coupling pattern of the former resulting from the significant ^{3}J (P,H) value (13.9 Hz) is expected only in CAEP lipids. Differences were even more significant on the adjacent methylene group (–$\mathbf{CH_2}$-CH_2NH_2) whose resonances in CAEP are strongly shielded (δ_H 1.87 td (7.2, 15.9 Hz); δ_C 32.7) with respect to PE (δ_H 4.03 t (7.0); δ_C 67.3). As outlined below, the most abundant CAEP found in the extract showed a strong UV absorption at λ 232 nm, suggesting the presence of a conjugated diene moiety in the sphingosine backbone, beside the expected isolated C (4) = C (5) double bond. We

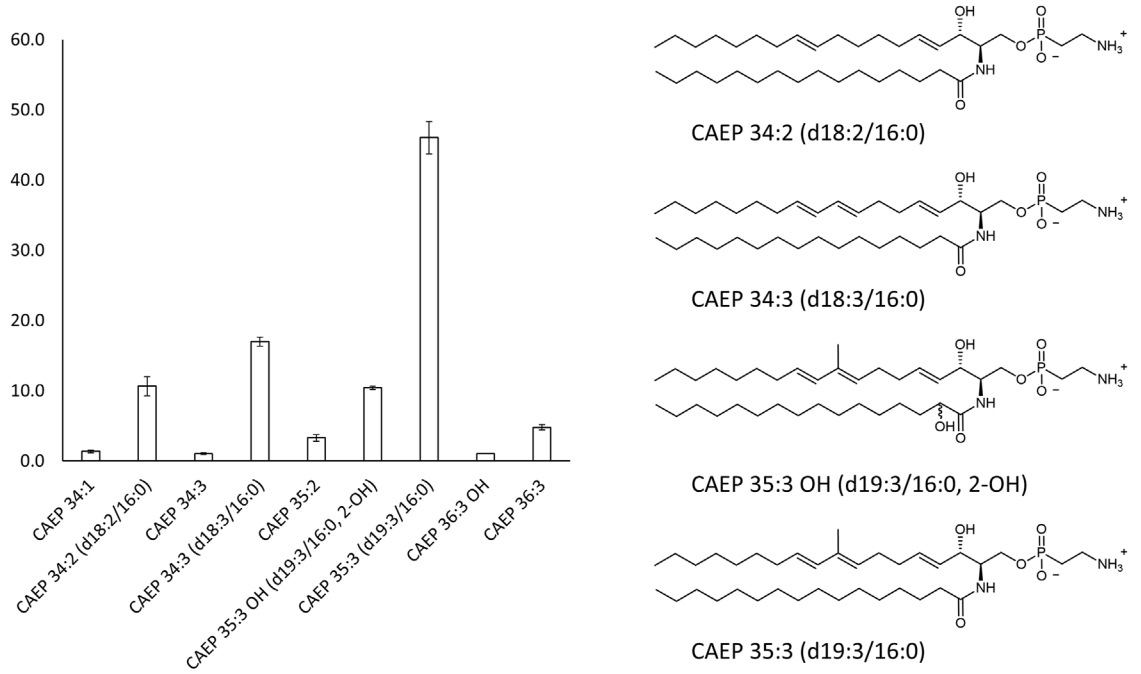

FIGURE 3 | Main CAEP relative components of the *M. galloprovincialis* hemocytes raw extract (>3 mol%) and their corresponding structures.

suggest here that in our CAEP we are dealing with a (8*E*,10*E*) diene system where the signals for the "inner" (H-9 and H-10) and the "outer" olefinic protons (H-8 and H-11) coalesced giving two signals at δ_H 6.02 d (15.3 Hz) and δ_H 5.53 dt (15.3, 7.2 Hz), respectively. The analysis of the coupling patterns, further supported by 2D-NMR spectra (HSQC, HMBC and COSY) allowed us to establish that the sphingosine moiety of these CAEP is built on a (4E, 8E, 10E) triene system. It is worth noting that several CAEP lipid species contain a sphingosine backbone with an odd number of carbon atoms (19); our NMR data strongly suggest that in these species the C (9) carbon atom of the conjugated diene system is methylated (δ_H 1.71 (s)). Concerning the CAEP bearing an extra–OH group, NMR analysis indicated that it resides on the C (2') of the fatty acyl chain (δ_H 3.99 m; δ_C 72.7).

The overall profile of CAEP in term of sphingosine/amide chain lengths and unsaturation was then established by liquid chromatography mass-spectrometry (LC-MS) and LC-MS-MS measurements. The most abundant CAEP species present in the raw extract were (**Figure 3**): CAEP 35:3 OH ((= CAEP d19:3/16:0, 2-OH), 10 mol%); CAEP 34:3 ((= CAEP d18:3/16:0), 18 mol%); CAEP 35:3 ((= CAEP d19:3/16:0), 47 mol%) and CAEP 34:2 ((= CAEP d18:2/16:0), 11 mol%). Minor CAEP lipids, including species bearing an N-methyl-amino, were also found, but their abundance did not exceed 3 mol%.

The components of the CAEP bearing the conjugated diene system on the sphingosine backbone were isolated from the raw extract by high pressure liquid chromatography (HPLC-UV (λ = 234 nm) chromatography) (**Supplementary Figure S2**) and they were then tested as a mixture in affinity bioassays.

2.2 OlyA6/PlyB Interaction With Artificial Lipid Membranes Containing Mussel CAEP

Surface plasmon resonance studies with large unilamellar vesicles (LUVs) immobilized on a chip revealed the interaction of the *Pleurotus* aegerolysin OlyA6 with artificial lipid membranes composed of an equimolar mixture of CAEP (isolated from mussel hemocytes), palmitoyl-oleoyl-phosphatidylcholine (POPC), and Chol. We applied a kinetic titration approach by injecting OlyA6 at five concentrations ranging from 0.03 to 0.5 μM over the LUVs immobilized on the chip, without dissociation time between protein injections. The resulting sensorgrams showed that OlyA6 interacted strongly and irreversibly with CAEP-enriched membranes (**Figure 4A**). The interaction of OlyA6 with CAEP-enriched LUVs was considerably stronger in the presence of PlyB (**Figure 4A**), indicating the formation of more stable proteolipid complexes. The binding kinetics of OlyA6 to CAEP-containing membranes was comparable with the interaction of OlyA6 with CPE-containing LUVs (**Figure 4B**), and in both cases the dissociation phase indicated an irreversible interaction with these lipid membranes, alone or in the presence of PlyB.

Monitoring of the fluorescence of calcein released from the small unilamellar equimolar lipid vesicles composed of CAEP/POPC/Chol confirmed the concentration-dependent membrane permeabilization by OlyA6 in combination with PlyB (**Figure 5**). As in the binding studies using surface plasmon resonance, the lytic activity of OlyA6/PlyB on equimolar CPE/POPC/Chol membranes was comparable to the lytic activity of OlyA6/PlyB on the newly studied CAEP-containing membranes. However, the OlyA6/PlyB protein complex showed slightly higher

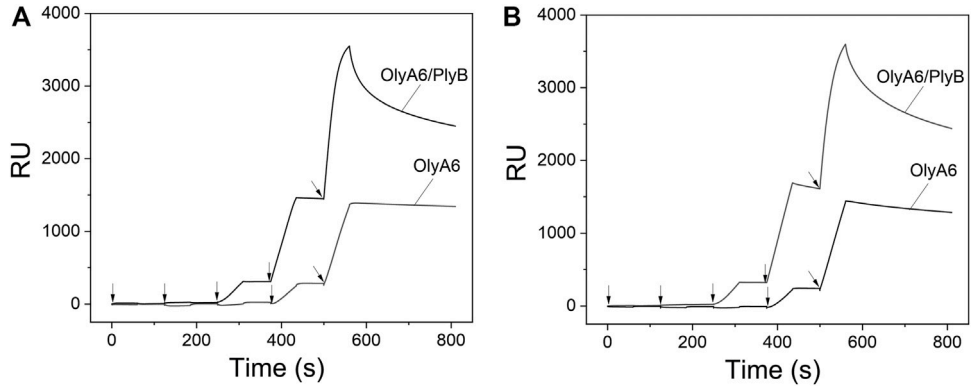

FIGURE 4 | Binding of OlyA6 and OlyA6/PlyB (12.5/1, molar ratio) to immobilized equimolar CAEP/POPC/Chol **(A)** and CPE/POPC/Chol **(B)** large unilamellar vesicles using the kinetic titration approach in a single cycle by successive injections of 0.03, 0.06, 0.12, 0,25, and 0.5 μM (from left to right) concentration. Vesicles were immobilized on the Biacore L1 chip to approximately 8,000 response units (RU). Representative sensorgrams from two independent experiments are shown. CPE-ceramide phosphoethanolamine, Chol-cholesterol, POPC-1-palmitoyl-2-oleoyl-*sn*-glycero-3-phosphocholine, CAEP-ceramide aminoethylphosphonate.

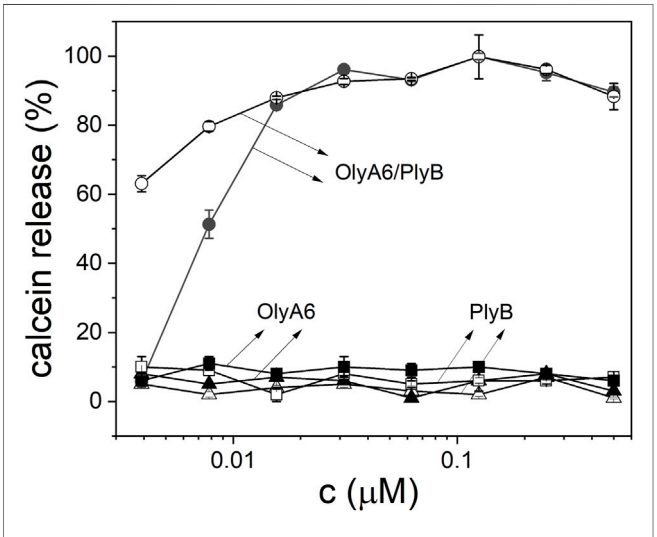

FIGURE 5 | Concentration dependence of permeabilization of equimolar CAEP/POPC/Chol (full symbols) and CPE/POPC/Chol (open symbols) small unilamellar vesicles by OlyA6/PlyB. OlyA6/PlyB molar ratio = 12.5/1. Individual proteins, OlyA6 and PlyB, were also tested as controls. CPE-ceramide phosphoethanolamine, Chol-cholesterol, POPC-1-palmitoyl-2-oleoyl-*sn*-glycero-3-phosphocholine, CAEP-ceramide aminoethylphosphonate.

permeabilization on CAEP-containing membranes compared with CPE-containing membranes when tested at lower (<15 nM) protein concentrations (**Figure 5**). OlyA6 and PlyB alone did not induce vesicle permeabilization (**Figure 5**).

2.3 Effect of Aegerolysin-Based Complexes on Haemocytes of *Mytilus galloprovincialis*

In *Mytilus* hemocytes exposed to the OlyA6/PlyB mixture for 30 min, lysosomal membrane stability was evaluated as a marker of cellular stress by the neutral red retention (NRR) time assay, and the results are shown in **Figure 6**. OlyA6/PlyB induced a dose-dependent decrease in hemocyte lysosomal membrane stability, with an EC_{50} of 6.5 μg/ml (95% CI: 2.305–18.2), whereas OlyA6 and PlyB alone were ineffective (**Figure 6A**). Optical microscopy observations for each concentration tested are also reported (**Figure 6B**). Lower concentrations of the protein mixture (5 and 10 μg/ml) did not affect hemocyte lysosomal membrane stability, whereas a significant decrease was observed at 25 μg/ml (−80%; $p < 0.01$). At this concentration, several cells with red cytosol, indicating neutral red leakage from lysosomes, and round shaped, due to detachment from the substrate, were observed (**Figure 6B**). At 50 μg/ml, lysosomal membranes were completely destabilized, and all the cells were rounded, indicating cell detachment and death (−98%; $p < 0.01$) (**Figure 6B**). Interestingly, the highest concentration tested (500 μg/ml) apparently caused complete loss of cytoplasm and organelles, and only cell membranes ("ghost" hemocytes) could be observed (**Figure 6B**). Exposure of mussel hemocytes to different concentrations of the OlyA6/PlyB mixture for 30 min also induced a significant decrease in the percentage of phagocytic cells with respect to controls at 5 and 10 μg/ml (about −30% for both concentrations; $p < 0.01$), while higher concentrations were ineffective (**Figure 7**).

The effects of hemocyte incubation with OlyA6/PlyB (10 and 25 μg/ml) on mitochondrial and oxidative stress parameters were evaluated by cell staining with TMRE, MitoSOX and C-DCF, for determination of mitochondrial membrane potential, mitochondrial superoxide ($O_2^{\cdot-}$) and intracellular hydrogen peroxide (H_2O_2) production, respectively. Representative confocal laser scanning microscopy images are reported in **Figure 8**. At the lowest concentration tested (10 μg/ml), OlyA6/PlyB exposure did not affect the TMRE signal and cell morphology, whereas at 25 μg/ml the cells were rounded and showed a clear increase in fluorescence with respect to controls, indicating decreased mitochondrial membrane potential (**Figure 8A**). The MitoSOX and C-DCF signals were barely detectable in control hemocytes, but a progressive increase was observed in cells exposed to both concentrations of the OlyA6/

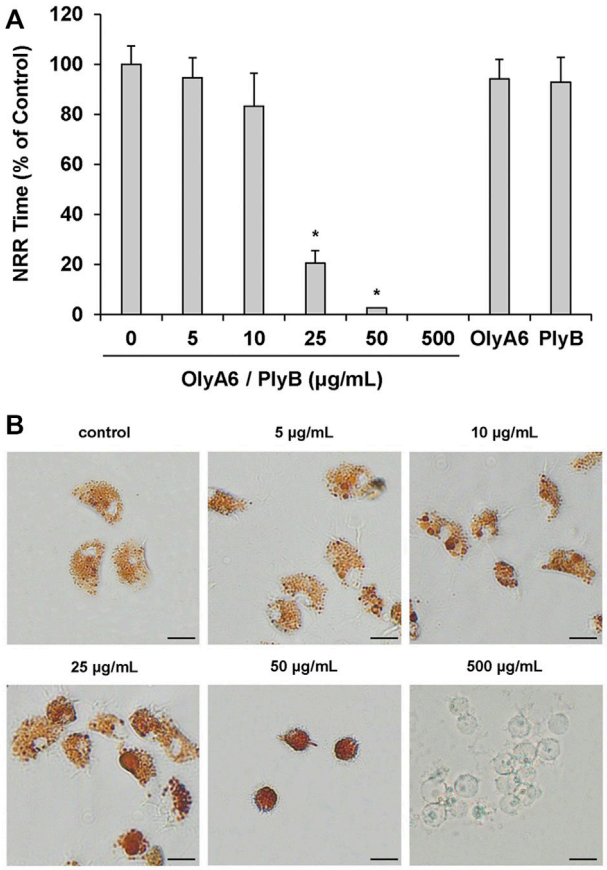

FIGURE 6 | Effects of the OlyA6/PlyB mixture on lysosomal membrane stability of *M. galloprovincialis* hemocytes. Hemocytes were exposed to different concentrations of the mixture (5, 10, 25, 50, 500 µg/ml; OlyA6/PlyB molar ratio 12.5/1) and to OlyA6 (25 µg/ml) or PlyB alone (2 µg/ml). **(A)** Data, reported as percent values of neutral red retention time with respect to controls, representing the mean ± SD of four experiments in triplicate, were analysed by the Mann Whitney *U* test. *$p < 0.01$. **(B)** Representative images of hemocytes treated with different concentrations of the protein mixture, as indicated. NRR–neutral red retention time. Scale bar = 10 µm.

PlyB mixture with respect to controls (**Figures 8B,C**), demonstrating the stimulation of reactive oxygen species production.

The effects of hemocyte incubation with OlyA6/PlyB (25 and 50 µg/ml) on apoptotic and oxidative stress markers were quantified by flow cytometry and the results are reported in **Figure 9**. With regards to apoptosis-related parameters, both concentrations of the mixture induced a significant increase in the ratio Annexin V-FITC (ANX)/propidium iodide (PI) (+115 and +170%, respectively, vs. controls). Moreover, a significant increase in TMRE fluorescence was detected at 50 µg/ml (+44% with respect to controls). For oxidative stress parameters, MitoSOX and C-DCF fluorescence significantly increased at both concentrations (+25 and +115% for MitoSOX; +117 and +97%, for C-DCF, respectively, vs. controls), while a decrease in glutathione signal was detected (-35 and -39%, respectively, vs. controls) (**Figure 9**).

3 DISCUSSION

Cellular membranes are composed of several thousands of chemically different lipids that serve many functions, such as structural membrane components, signalling molecules, or platforms for protein recruitment (Harayama and Riezman, 2018). Lipids control these biological processes by regulating membrane properties, and alterations in membrane lipid homeostasis is consequently associated with various diseases (Horn and Jaiswal, 2019; Nishimura and Matsumori, 2020). In contrast to proteins that can be prone to mutations, lipids are structurally conserved and constitutive components of cell membranes. This feature makes membrane lipids and lipid domains, like membrane rafts, ideal targets for treatment of various diseases (e.g., neurodegeneration, neuropatic pain, atherosclerosis, and infection, including the one with Sars-CoV-2) (D'Angelo et al., 2018; Resnik et al., 2015; Sviridrov et al., 2020a; Sviridrov et al., 2020b), and for the development of new biopesticides (Panevska et al., 2019a).

Sphingolipids, together with glycerophospholipids and sterols, are the most abundant components of cell membranes, and their sphingosine-based degradation products are involved in many physiological processes, including signalling events (Panevska et al., 2019b). In mammalian cell membranes, interactions between sphingomyelin and Chol drive the formation of membrane rafts; heterogeneous, dynamic membrane nanodomains that serve as functional platforms that regulate various cellular processes (e.g., immune signalling, host-pathogen interactions, development and regulation of cardiovascular disease and cancer) as a result of the segregation of specific lipid-anchored proteins within raft domains (Pike, 2006; Michel and Bakovic, 2007; Lingwood and Simons 2010; Sezgin et al., 2012). While mammalian cell membranes contain sphingomyelin as the major sphingolipid, invertebrates, especially arthropods, synthesize its analogue with a phosphoethanolamine instead of phosphocholine polar head, the CPE. Complete understanding of

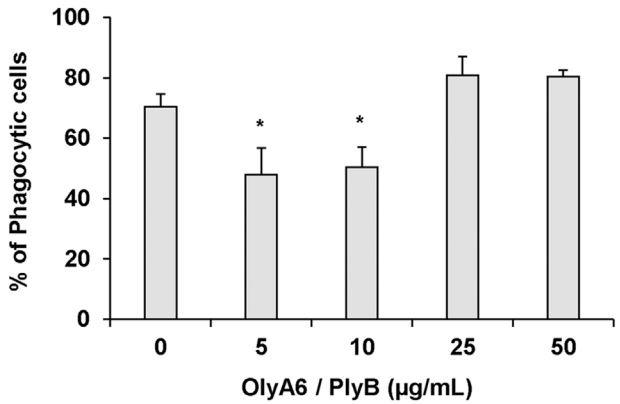

FIGURE 7 | Effects of the OlyA6/PlyB mixture on phagocytic activity of *M. galloprovincialis* hemocytes. Hemocytes were exposed to different concentrations of the protein mixture (5, 10, 25, 50 µg/ml; OlyA6/PlyB molar ratio 12.5/1). Data, representing the mean ± SD of four experiments in triplicate, were analysed by the Mann Whitney *U* test. *$p < 0.01$.

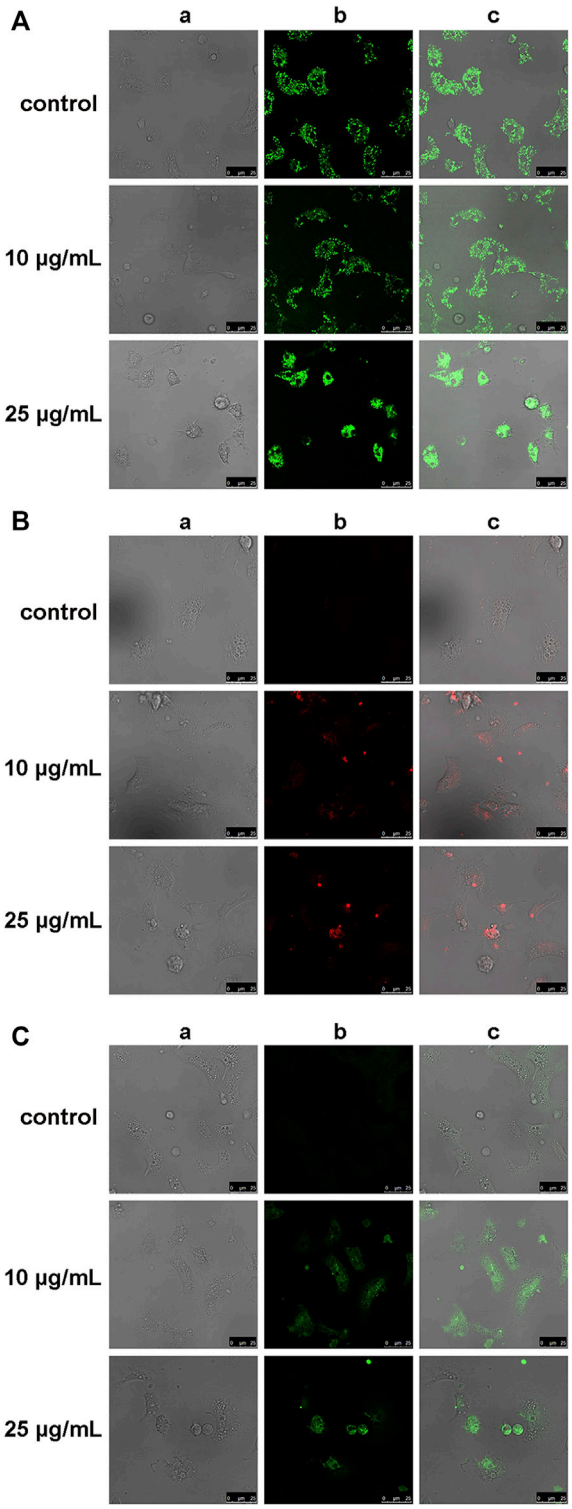

FIGURE 8 | Effects of the OlyA6/PlyB mixture on mitochondrial and oxidative stress parameters in *M. galloprovincialis* hemocytes evaluated by confocal laser scanning microscopy. Representative images of hemocytes exposed to different concentrations of the OlyA6/PlyB mixture at the OlyA6/PlyB molar ratio 12.5/1 and loaded with **(A)** tetramethylrhodamine ethyl ester (TMRE), for mitochondrial membrane potential; **(B)** MitoSOX Red for

(*Continued*)

FIGURE 8 | mitochondrial superoxide (O_2^-) production; **(C)** CM-H2DCFDA (C-DCF), for generation of intracellular H_2O_2. Rows correspond to different concentrations of the OlyA6/PlyB mixture (0, 10 and 25 µg/ml). Columns show: **(a)** brightfield, **(b)** fluorescence signals of TMRE, MitoSOX and C-DCF **(c)** merged channels. Scale bar: 25 µm.

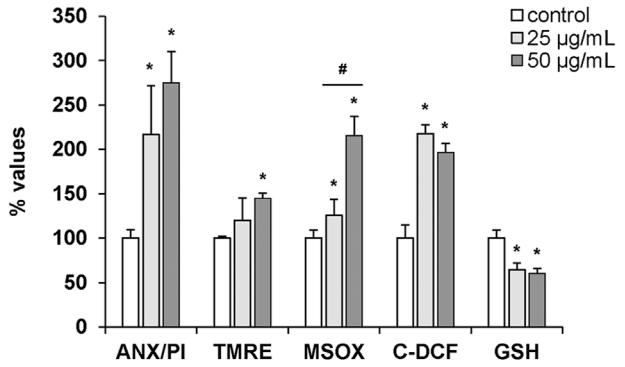

FIGURE 9 | Effects of the OlyA6/PlyB mixture on apoptotic and oxidative stress parameters in *M. galloprovincialis* hemocytes evaluated by flow cytometry. Hemocytes were exposed to the OlyA6/PlyB mixture (25 and 50 µg/ml; OlyA6/PlyB molar ratio 12.5/1) and apoptotic (ANX/PI, TMRE) and oxidative stress (MSOX, C-DCF and glutathione (GSH)) parameters were determined. ANX/PI staining is expressed as a percentage of positive cells in exposed hemocytes with respect to controls. TMRE, MSOX, C-DCF and GSH data are reported as Mean Fluorescence Intensities (MIF) with respect to controls. See methods for details. Data, representing the mean ± SD of 4 experiments, were analysed by ANOVA followed by Tukey's post-hoc test. *$p < 0.01$ (treatment vs. control); #$p < 0.05$ (25 vs. 50 µg/ml).

the physiological relevance of CPE and its biological role is still lacking, but recent experimental evidences suggest that this sphingolipid might be crucial for the early development of *Drosophila melanogaster*, where it has a key role in axonal ensheathment of peripheral nerves by glia (Ghosh et al., 2013), and it might be involved in the developmental stages of *Trypanosoma brucei* (Suttervala et al., 2008; Bhat et al., 2015). In contrast to sphingomyelin, the membrane behavior of CPE has been considerably less studied, but it was suggested that it does not induce the formation raft-like domains (Ramstedt and Slotte, 2006). The biological role of CAEP, a CPE analogue characteristic of marine invertebrates (Moschidis, 1984; Tomonaga et al., 2017; Imbs et al., 2019) bearing a phosphono rather than the usual phosphate group in its polar head, is even more obscure. Our lipidomic analyses of *M. galloprovincialis* hemocytes revealed the presence of 29.0 mol% CAEP among all the phospholipids, matching with the literature records of the whole mussel lipidome (Donato et al., 2018). This amount is considerably higher than the usual amount of CPE in insect cell membranes, where this lipid represents around 2–6 mol% (Guan et al., 2013) of total lipids.

Proteins from the aegerolysin family, such as OlyA6 from the edible oyster mushroom, were shown to specifically target sphingomyelin, that is the major sphingolipid in vertebrates,

and CPE, that dominates in invertebrates (Sepčić et al., 2004; Bhat et al., 2015; Panevska et al., 2019a). Further, OlyA6/PlyB complexes can efficiently permeabilize membranes enriched in sphingomyelin or CPE, acting as potent and species-selective bioinsecticides (Panevska et al., 2019b). Because of a distinctive difference in the affinity to insect-specific sphingolipid CPE, which is their high-affinity receptor, and due to the fact that they are immediately degraded by mammalian digestive enzymes (Kristina Sepčić, personal communication), insecticides based on OlyA6/PlyB complexes are safe for vertebrates. However, this might not be the case with other organisms which contain CPE or its analogues in their cell membranes.

Within this study, we showed that a CPE analogue characteristic for marine invertebrates, the CAEP, also acts as an OlyA6 high-affinity receptor. OlyA6 was able to strongly bind to artificial lipid vesicles supplemented with CAEP isolated from mussel hemocytes, and OlyA6/PlyB mixture efficiently permeabilized CAEP-supplemented lipid vesicles and induced the apoptosis of *Mytilus* haemocytes at submicromolar concentrations. Short-term exposure of mussel hemocytes to the OlyA6/PlyB mixture affected the function of lysosomal membranes, as indicated by the concentration-dependent decrease in lysosomal membrane stability, with an EC_{50} of 6.5 μg/ml (corresponding to 0.43 μM OlyA6). In the 5–10 μg/ml range, a significant decrease in phagocytic activity was observed, indicating a general disturbance of membrane function, that is probably the consequence of the formation of OlyA6/PlyB transmembrane pores (Lukoyanova et al., 2015; Ota et al., 2013; Milijaš Jotić, 2021). Higher concentrations were ineffective; however, since the phagocytosis assay is based on microscopic observations of internalized NR-conjugated zymosan, the lack of effect in these conditions was due to non-specific, passive particle uptake by dying cells (see also **Figure 6B**). Moreover, phagocytic activity, as other functional immune parameters in bivalves, often shows a non-monotonic dose-response curve to chemical exposure (Balbi et al., 2021).

At increasing concentrations, progressive lysosomal destabilization was associated with cell rounding (indicating colloid-osmotic mechanism of cell disruption), detachment and death. At the highest concentration tested, only plasma membranes could be detected ("ghost" hemocytes), with complete loss of cytoplasm and organelles. To our knowledge, such an effect has not been previously observed in mussel hemocytes exposed in the same experimental conditions to a variety of potentially toxic inorganic and organic chemicals.

The results of both confocal laser scanning microscopy and flow cytometry provided a further insight into the toxic effects of OlyA6/PlyB on mussel hemocytes in the range of 10–50 μg/ml. Increases in parameters related to apoptotic processes both at the plasma membrane (Annexin V binding) and at mitochondrial level (TMRE) were observed. Moreover, OlyA6/PlyB induced increased oxyradical production both at mitochondrial (MitoSOX) and cytosolic (C-DCF) level, and provoked a decrease in reduced glutathione, indicating oxidative stress conditions. Deregulation of mitochondrial activity, leading to the cell death, has been already described in nucleated cells exposed to higher concentrations of bacterial pore-forming toxins (Kennedy et al., 2009; Bischovberger et al., 2012). It is thus very likely that the above-described effects observed in mussel hemocytes treated with OlyA6/PlyB complexes, also derive from the ability of the tested proteins to induce the formation of bi-component multimeric pores in hemocyte membranes.

Taken together, the results presented in this study indicate the possible application of fluorescently tagged aegerolysins, such as OlyA6, as molecular markers for studying the biology and distribution of CAEP in membranes of living cells that synthesize this membrane sphingolipid. These molecular probes could be also used for biophysical studies of CAEP or CPE membrane dynamics, both in living cells and in artificial lipid systems. Finally, due to their specific binding to membrane CAEP, aegerolysin-based cytolytic complexes, such as OlyA6/PlyB, could be considered as potential agents for selective elimination of organisms that harbour this sphingolipid in their membranes. Such examples are bivalves and other fouling marine invertebrates, but also some important plant pathogen oomycetes (Moschidis, 1984).

4 MATERIALS AND METHODS

4.1 Materials

4.1.1 Chemicals

All chemicals used in the present study were from Merck (United States) unless specified otherwise. Wool grease Chol, POPC, and CPE were from Avanti Polar Lipids (United States). Cholesterol and POPC lipids were stored at −20°C and dissolved in chloroform prior to use. CPE was dissolved in 1 ml chloroform/methanol (9/1, v/v).

4.1.2 Proteins

The OlyA6 and Δ48PlyB (henceforth PlyB) recombinant proteins were produced as described previously (Ota et al., 2013; Panevska et al., 2019a) and stored in aliquots at −20°C prior to use. The lytic activity of the OlyA6/PlyB mixture (OlyA6/PlyB molar ratio, 12.5/1) on CPE-containing lipid vesicles prepared in artificial sea water (Lake Products Company LLC, United States) was tested prior to use and was found to be comparable to the activity on the same vesicles prepared in vesicle buffer (140 mM NaCl, 20 mM Tris, 1 mM EDTA, pH 7.4).

4.1.3 Target Organisms

Mussels (*M. galloprovincialis* Lam.), were purchased in 2021 from an aquaculture farm in the Ligurian Sea (La Spezia, Italy) and acclimatized in static tanks containing aerated artificial sea water at pH 7.9–8.1, 36 ppt salinity (1 L/animal), 16 ± 1°C, for 3 days. In order to assess hemocyte functional parameters, for each sample hemolymph was extracted from the adductor muscle of 8–10 individuals and pooled. Hemocyte monolayers were prepared as previously described (Balbi et al., 2018, 2019).

4.2 Methods

4.2.1 Lipid Extraction From *M. galloprovincialis* Hemocytes

Hemolymph was extracted from at least 150 animals and was immediately centrifuged at 800 × g for 10 min, at room temperature. The cell pellet obtained was resuspended in 700 µl of milliQ water in order to induce the cell lysis. Then, 3 ml of chloroform/methanol (2:1 v/v) were added to initiate the lipid extraction. The samples were placed on ice and sonicated with a Tip Sonicator (UP200S Hielscher Ultrasonic Technology, Germany) for 20 min, at 100 W, 50% on/off cycle. At the end of the sonication, the suspension was vortexed thoroughly and the sample was centrifuged at 6,000 × *g* for 10 min, at 4°C to separate the two phases. The lower phase was collected, and the inter-layer sediment and the aqueous phase were extracted again as described above. The lower phases, containing the lipids, were mixed together and dried by N_2 flux to avoid oxidation. Dried samples were weighted and stored at −80°C. Lipids were dissolved in 600 µl deuterated methanol and analysed by NMR and HPLC-coupled LCMS.

4.2.2 Lipidomic Analyses

4.2.2.1 Nuclear Magnetic Resonance Analysis

^{1}H-NMR (400 MHz) and ^{31}P-NMR (162 MHz) spectra of the lipid extract dissolved in MeOH-d_4 were recorded at 300 K on a nuclear magnetic resonance (NMR) spectrometer (400 MHz; Bruker-Avance, Bremen, Germany), with a 5-mm double resonance broadband observe probe with pulsed-gradient field utility. The 1H-90° proton pulse length was 9.3 µs, with transmission power of 0 db. The ^{31}P-90° proton pulse length was 17 µs, with transmission power of −3 db. The probe temperature was maintained at 300.0 K (±0.1 K) using a variable temperature unit (B-VT 1000; Bruker). Calibration of the chemical shift scale (δ) was performed on the residual proton signal of the MeOH-d_4 at δ_H 3.310 and δ_C 49.00 ppm, and the phosphatidylcholine (PC) signal at δ_P −0.550 ppm was used for calibration of the ^{31}P-NMR δ scale. The following measurements were performed: ^{1}H-NMR (i.e., proton chemical shifts, scalar couplings); ^{31}P-NMR composite pulse decoupling to remove any proton coupling in ^{31}P-NMR spectra, where generally 4,000 free induction decays were acquired and processed using exponential line broadening of 0.3 Hz prior to Fourier transformation. The resulting 1D-NMR spectra were analysed using TopSpin 3.6.1 (Bruker, Bremen, Germany). The lipid classes from the NMR data were identified through comparisons with our previous NMR measurements carried on commercially available lipid standards.

4.2.2.2 HPLC-Electrospray Ionization-Mass Spectrometry Analysis

The lipid extract was analysed by liquid chromatography-mass spectrometry (LC-MS) (Model 1,100 series; Hewlett-Packard) coupled to a quadrupole ion-trap mass spectrometer (Esquire LCTM; Bruker, Bremen, Germany) equipped with an electrospray ionisation source and in both positive and negative ion modes. Chromatographic separation of the phospholipids was carried out at 303 K on a thermostated C18 column (Kinetex 2.6 µ; length, 100 mm; particle size, 2.6 µm; internal diameter, 2.1 mm; pore size, 100 Å; Phenomenex, Torrence, CA, United States). The solvent system consisted of eluant A as MeOH/H2O (7:3, v/v) containing 10 mM ammonium acetate and eluant B as isopropanol/MeOH (10:90, v/v) containing 10 mM ammonium acetate. Samples were resuspended in 1 ml $CHCl_3$/MeOH (2:1, v/v), and 10 µl was run with a linear gradient from 65% eluant B to 100% B in 40 min, plus 20 min isocratic 100% B at 1 ml/min, to elute the diglycerides and triglycerides. The column was then re-equilibrated to 65% B for 10 min. The MS scan range was 13,000 U/s in the range of 50–1,500 m/z, with a mass accuracy of ~100 ppm. The nebuliser gas was high purity nitrogen at a pressure of 20–30 psi, at a flow rate of 6 L/min and at 300°C. The electrospray ionisation was operated in positive ion mode for the qualitative and quantitative analyses of PC, lyso-PC, and sphingomyelin, and in both positive and negative ion modes for phosphatidylinositol, PE and CAEP. For the structural assignments of the lipid species, the extracted ion chromatograms from the positive and/or negative ion full scan data were integrated using the DataAnalysis 3.0 software (Bruker Daltonik, Bremen, Germany).

4.2.2.3 CAEP Isolation

CAEP isolation was performed by HPLC (Agilent, model 1,100 series; Hewlett-Packard). Separation was achieved by isocratic gradient of 95% MeOH + ammonium acetate 10 mM and 5% ddH_2O on a C18 column (Kinetex 2.6 µ; length, 100 mm; particle size, 2.6 µm; internal diameter, 2.1 mm; pore size, 100 Å; Phenomenex, Torrence, CA, United States) at flow 1 ml/min. UV chromatograms were acquired at 232 nm.

4.2.3 Preparation of Lipid Vesicles

Equimolar multilamellar vesicles containing CEAP isolated from mussels' hemocytes (CAEP/POP/Chol) or commercial CPE (CPE/POPC/Chol) were prepared (final concentration 5 mg/ml) in 140 mM NaCl, 20 mM Tris, 1 mM EDTA, pH 7.4, as described previously (Sepčić et al., 2003). To prepare the LUVs, suspensions of multilamellar vesicles were subjected to five freeze-thaw cycles and then extruded through 0.1 µm polycarbonate filters (Millipore, Germany) at ~50°C. Equimolar small unilamellar vesicles CAEP/POPC/Chol and CPE/POPC/Chol loaded with calcein at the self-quenching concentration (80 mM) were prepared for the calcein release experiment as described previously (Sepčić et al., 2003).

4.2.4 Surface Plasmon Resonance-Based Binding Studies

The interaction of OlyA6 and OlyA6/PlyB with CAEP/POPC/Chol (1/1/1, mol/mol/mol) and CPE/POPC/Chol (1/1/1, mol/mol/mol) LUVs was monitored with a surface plasmon resonance-based refractometer (Biacore T200; GE Healthcare, United States) using an L1 sensor chip with 20 mM Tris, 140 mM NaCl, 1 mM EDTA, pH 7.4, as running buffer. After initial cleaning of the chip with regeneration solutions of sodium dodecyl sulphate and octyl-β-D-glucopyranoside with 1-min injections at a flow rate of 10 µl/min, LUVs were bound to the second flow cell of the sensor chip to reach responses of ~8,000

RU. The first flow cell was left empty to control for possible non-specific binding of the proteins to the dextran matrix of the chip. Non-specific binding of the proteins was minimized by a 1-min injection of 0.1 mg/ml bovine serum albumin at a flow rate of 30 µl/min. A single-cycle kinetics experiment was performed in which OlyA6 and OlyA6/PlyB (molar ratio 12.5/1) were injected at concentrations 0.03, 0.06, 0.12, 0.25, and 0.5 µM, with no dissociation in between and a dissociation time of 180 s at the end. Chip regeneration was achieved with 1-min injections of 0.5% sodium dodecyl sulphate and 40 mM β-D-glucopyranoside at a flow rate of 10 µl/min. Experiments were performed at 25°C. Data were processed using BIAevaluation software (GE Healthcare).

4.2.5 Permeabilization of the Small Unilamellar Vesicles

Vesicle permeabilization was determined using a fluorescence microplate reader (Tecan, Switzerland), with excitation and emission set at 485 and 535 nm, respectively. Calcein-loaded CAEP/POPC/Chol (1/1/1, mol/mol/mol) and CPE/POPC/Chol (1/1/1, mol/mol/mol) small unilamellar vesicles were exposed to OlyA6/PlyB (molar ratio 12.5/1) at concentrations ranging from 0.0039 to 0.5 µM. Experiments with OlyA6 or PlyB alone were run in parallel. The experiments were performed for 20 min at 25°C. The permeabilization induced by the lytic OlyA6/PlyB complex was expressed as a percentage of the maximum permeabilization obtained by adding the detergent Triton-X 100 at a final concentration of 1 mM.

4.2.6 Effect of Aegerolysin-Based Complexes on *Mytilus galloprovincialis* Hemocytes

4.2.6.1 Hemocyte Functional Parameters

Lysosomal membrane stability was evaluated by the Neutral Red retention time (NRR) assay as in Balbi et al. (2018), (2019). Hemocyte monolayers were pre-incubated with different concentrations of OlyA6 (5, 10, 25, 50, and 500 µg/ml) in combination with PlyB, at an OlyA6/PlyB molar ratio of 12.5/1 for 30 min. Cells were then incubated with 20 µl of Neutral Red (Sigma-Aldrich, Milan, Italy) solution (final concentration 40 µg/ml from a stock solution of neutral red 40 mg/ml in DMSO). Experiments with OlyA6 (25 µg/ml) or PlyB alone (2 µg/ml) were run in parallel. All incubations were performed at 16°C. After 15 min, excess of dye was washed out, 20 µl of artificial sea water was added, and slides were sealed with a coverslip. Every 15 min, slides were examined using an inverted Olympus IX53 microscope (Olympus, Milano, Italy), equipped with a CCD UC30 camera and a digital image acquisition software (cellSens Entry). The endpoint of the assay was defined as the time at which 50% of the cells showed signs of lysosomal leaking (the cytosol becoming red and the cells rounded). For each experiment, control hemocyte samples were run in parallel. Triplicate preparations were made for each sample. Data are expressed as % of control.

Phagocytosis of neutral red-stained zymosan by hemocyte monolayers was used to assess the phagocytic ability of hemocytes. Neutral red-stained zymosan in 0.05 M Tris-HCl buffer (TBS), pH 7.8, containing 2% NaCl was added to each monolayer at a concentration of about 1:30 hemocytes:zymosan in the presence or absence of OlyA6/PlyB mixture (5, 10, 25, and 50 µg/ml), and allowed to incubate for 60 min. Monolayers were then washed three times with TBS, fixed with Baker's formol calcium (4%, v/v, formaldehyde, 2% NaCl, 1% calcium acetate) for 30 min and mounted in Kaiser's medium for microscopical examination. For each slide, the percentage of phagocytic hemocytes was calculated from a minimum of 200 cells. All experiments were performed in quadruplicate samples (N = 4).

4.2.6.2 Confocal Laser Scanning Microscopy

For confocal live imaging, aliquots of hemolymph (500 µl) exposed to OlyA6/PlyB mixture (10 and 25 µg/ml, at an OlyA6/PlyB molar ratio of 12.5/1), were seeded for 30 min in glass bottom culture dish (MatTek, Ashland, MA) and stained with 1) tetramethylrhodamine ethyl ester (TMRE) (40 nM for 10 min), for determination mitochondrial membrane potential; 2) the mitochondrial reactive oxygen species-sensitive probe MitoSOX Red (5 µM, 10 min), and 3) 5-(and-6)-chloromethyl-20,70-dichlorodihydrofluorescein diacetate acetyl ester, CM-H2DCFDA (2 µM for 20 min), for generation of intracellular H_2O_2. All probes were diluted in artificial sea water. All reagents were from Molecular Probes Inc.

Fluorescence of TMRE (ex: 568 nm, em: 590–630 nm), MitoSOX Red (ex: 488 nm, em: 580 nm) and DCF (ex: 495 nm, em: 520 nm) were detected using a Leica TCS SP5 confocal setup mounted on a Leica DMI 6000 CS inverted microscope (Leica Microsystems, Heidelberg, Germany) using 63 ×1.4 oil objective (HCX PL APO ×63.0 1.40 OIL UV). Images were analysed by the Leica Application Suite Advanced Fluorescence (LASAF) and ImageJ Software (Wayne Rasband, Bethesda, MA).

4.2.6.3 Flow Cytometry

Aliquots (200 µl) of whole hemolymph (each containing about 1–2 × 10^6 cells/ml) were incubated with the OlyA6/PlyB mixture (25 and 50 µg/ml) for 30 min at 16°C. Control samples were run in parallel. Total hemocyte count was carried out using an Omnicyt flow cytometer (Cytognos SL, Salamanca, Spain). Samples were pelleted by centrifugation (100 × g for 10 min) and stained with different fluorophores. Annexin V-FITC (ANX)/propidium iodide (PI) and TMRE staining was carried out as previously described (Ciacci et al., 2012; Canesi et al., 2015); MitoSOX and CM-H2DCFDA staining was performed as described above for confocal scanning laser microscopy. Samples were also analysed by the Intracellular Glutathione Detection Assay Kit (Abcam) (at ex: 490, em: 520 nm). Sample acquisition and analyses were performed by means of a FACS Canto II flow cytometer and analysed with DiVa™ software collecting at least 10,000 events for each sample. Data, representing the mean ± standard deviation (SD) of at least three experiments, are expressed as Mean Fluorescence Intensities reported as percent changes with respect to controls, except for ANX/PI staining, where data are expressed as percent positive cells with respect to controls.

4.2.6.4 Statistics

Data are the mean ± SD of four independent experiments. Statistical analysis was performed using the non-parametric Mann-Whitney *U* test or ANOVA followed by Tukey's post hoc test. The EC_{50} for lysosomal membrane stability was

calculated from a regression model of the original data and analysed by one-way ANOVA at a 95% confidence interval. All statistic calculations were performed by the PRISM seven GraphPad software.

DATA AVAILABILITY STATEMENT

The original contributions presented in the study are included in the article/**Supplementary Material**, further inquiries can be directed to the corresponding authors.

AUTHOR CONTRIBUTIONS

TB, FT, CC, BC, GB, and AP conducted the experiments; LC, GG, and KS designed the experiments, TB, FT, AP, LC, GG, and KS wrote the paper. All authors reviewed the manuscript.

FUNDING

Financial support was provided by the Slovenian Research Agency (grants J4-1772, P1-0207), and by Fondi di Ricerca di Ateneo, University of Genoa (TB, 100022-2020-FRA2019-Balbi).

ACKNOWLEDGMENTS

The authors gratefully acknowledge Adriano Sterni for mass spectrometry measurements.

SUPPLEMENTARY MATERIAL

The Supplementary Material for this article can be found online at: https://www.frontiersin.org/articles/10.3389/fmolb.2022.902706/full#supplementary-material

REFERENCES

Balbi, T., Auguste, M., Ciacci, C., and Canesi, L. (2021). Immunological Responses of Marine Bivalves to Contaminant Exposure: Contribution of the -omics Approach. *Front. Immunol.* 12, 618726. doi:10.3389/fimmu.2021.618726

Balbi, T., Auguste, M., Cortese, K., Montagna, M., Borello, A., Pruzzo, C., et al. (2019). Responses of *Mytilus galloprovincialis* to Challenge with the Emerging Marine Pathogen *Vibrio coralliilyticus*. *Fish Shellfish Immunol.* 84, 352–360. doi:10.1016/j.fsi.2018.10.011

Balbi, T., Cortese, K., Ciacci, C., Bellese, G., Vezzulli, L., Pruzzo, C., et al. (2018). Autophagic Processes in *Mytilus galloprovincialis* Hemocytes: Effects of *Vibrio tapetis*. *Fish Shellfish Immunol.* 73, 66–74. doi:10.1016/j.fsi.2017.12.003

Batrakov, S. G., Mosezhnyi, A. E., Ruzhitsky, A. O., Sheichenko, V. I., and Nikitin, D. I. (2000). The Polar-Lipid Composition of the Sphingolipid-Producing Bacterium *Flectobacillus major*. *Biochim. Biophys. Acta.* 1484, 225–240. doi:10.1016/s1388-1981(00)00011-1

Bhat, H. B., Ishitsuka, R., Inaba, T., Murate, M., Abe, M., Makino, A., et al. (2015). Evaluation of Aegerolysins as Novel Tools to Detect and Visualize Ceramide Phosphoethanolamine, a Major Sphingolipid in Invertebrates. *FASEB J.* 29, 3920–3934. doi:10.1096/fj.15-272112

Bischofberger, M., Iacovache, I., and van der Goot, F. G. (2012). Pathogenic Pore-Forming Proteins: Function and Host Response. *Cell. Host Microbe* 2, 266–275. doi:10.1016/j.chom.2012.08.005

Broad, T. E., and Dawson, R. M. C. (1973). Formation of Ceramide Phosphorylethanolamine from Phosphatidylethanolamine in the Rumen Protozoon *Entodinium caudatum* (Short Communication). *Biochem. J.* 134, 659–662. doi:10.1042/bj1340659

Butala, M., Novak, M., Kraševec, N., Skočaj, M., Veranič, P., Maček, P., et al. (2017). Aegerolysins: Lipid-Binding Proteins with Versatile Functions. *Seminars Cell. & Dev. Biol.* 72, 142–151. doi:10.1016/j.semcdb.2017.05.002

Canesi, L., Ciacci, C., Bergami, E., Monopoli, M. P., Dawson, K. A., Papa, S., et al. (2015). Evidence for Immunomodulation and Apoptotic Processes Induced by Cationic Polystyrene Nanoparticles in the Hemocytes of the Marine Bivalve *Mytilus*. *Mar. Environ. Res.* 111, 34–40. doi:10.1016/j.marenvres.2015.06.008

Ciacci, C., Canonico, B., Bilaničová, D., Fabbri, R., Cortese, K., Gallo, G., et al. (2012). Immunomodulation by Different Types of N-Oxides in the Hemocytes of the Marine Bivalve *Mytilus galloprovincialis*. *PLoS One* 7, e36937. doi:10.1371/journal.pone.0036937

Crone, H., and Bridges, R. (1963). The Phospholipids of the Housefly, *Musca domestica*. *Biochem.* 89, 11–21. doi:10.1042/bj0890011

D'Angelo, G., Moorthi, S., and Luberto, C. (2018). Role and Function of Sphingomyelin Biosynthesis in the Development of Cancer. *Adv. Cancer Res.* 140, 61–96. doi:10.1016/bs.acr.2018.04.009

Donato, P., Micalizzi, G., Oteri, M., Rigano, F., Sciarrone, D., Dugo, P., et al. (2018). Comprehensive Lipid Profiling in the Mediterranean Mussel (*Mytilus galloprovincialis*) Using Hyphenated and Multidimensional Chromatography Techniques Coupled to Mass Spectrometry Detection. *Anal. Bioanal. Chem.* 410, 3297–3313. doi:10.1007/s00216-018-1045-3

Endapally, S., Frias, D., Grzemska, M., Gay, A., Tomchick, D. R., and Radhakrishnan, A. (2019). Molecular Discrimination between Two Conformations of Sphingomyelin in Plasma Membranes. *Cell.* 176, 1040–1053. doi:10.1016/j.cell.2018.12.042

Ghosh, A., Kling, T., Snaidero, N., Sampaio, J. L., Shevchenko, A., Gras, H., et al. (2013). A Global *In Vivo Drosophila* RNAi Screen Identifies a Key Role of Ceramide Phosphoethanolamine for Glial Ensheathment of Axons. *PLoS Genet.* 9, e1003980. doi:10.1371/journal.pgen.1003980

Grundner, M., Panevska, A., Sepčić, K., and Skočaj, M. (2021). What Can Mushroom Proteins Teach Us about Lipid Rafts? *Membranes* 11, 264. doi:10.3390/membranes11040264

Guan, X. L., Cestra, G., Shui, G., Kuhrs, A., Schittenhelm, R. B., Hafen, E., et al. (2013). Biochemical Membrane Lipidomics during *Drosophila* Development. *Dev. Cell.* 24, 98–111. doi:10.1016/j.devcel.2012.11.012

Harayama, T., and Riezman, H. (2018). Understanding the Diversity of Membrane Lipid Composition. *Nat. Rev. Mol. Cell. Biol.* 19, 281–296. doi:10.1038/nrm.2017.138

Hori, T., Arakawa, I., and Sugita, M. (1967). Distribution of Ceramide 2-Aminoethylphosphonate and Ceramide Aminoethylphosphate (Sphingoethanolamine) in Some Aquatic Animals. *Biochem.* 62, 67–70. doi:10.1093/oxfordjournals.jbchem.a128637

Horn, A., and Jaiswal, J. K. (2019). Structural and Signaling Role of Lipids in Plasma Membrane Repair. *Curr. Top. Membr.* 84, 67–98. doi:10.1016/bs.ctm.2019.07.001

Imbs, A. B., Dang, L. P. T., and Nguyen, K. B. (2019). Comparative Lipidomic Analysis of Phospholipids of Hydrocorals and Corals from Tropical and Cold-Water Regions. *PLoS ONE* 14, e0215759. doi:10.1371/journal.pone.0215759

Kaneshiro, E. S., Jayasimhulu, K., Sul, D., and Erwin, J. A. (1997). Identification and Initial Characterizations of Free, Glycosylated, and Phosphorylated Ceramides of *Paramecium*. *J. Lipid Res. Lipid Res.* 38, 2399–2410. doi:10.1016/s0022-2275(20)30025-0

Katsumiti, A., Nicolussi, G., Bilbao, D., Prieto, A., Etxebarria, N., and Cajaraville, M. P. (2019). *In Vitro* toxicity Testing in Hemocytes of the Marine Mussel *Mytilus galloprovincialis* (L.) to Uncover Mechanisms of Action of the Water Accommodated Fraction (WAF) of a Naphthenic North Sea Crude Oil without and with Dispersant. *Sci. Total Environ.* 670, 1084–1094. doi:10.1016/j.scitotenv.2019.03.187

Kellermann, M. Y., Schubotz, F., Elvert, M., Lipp, J. S., Birgel, D., Prieto-Mollar, X., et al. (2012). Symbiont-host Relationships in Chemosynthetic Mussels: A

Comprehensive Lipid Biomarker Study. *Org. Geochem.* 43, 112–124. doi:10.1016/j.orggeochem.2011.10.005

Kennedy, C. L., Smith, D. J., Lyras, D., Chakravorty, A., and Rood, J. I. (2009). Programmed Cellular Necrosis Mediated by the Pore-Forming α-Toxin from *Clostridium septicum*. *PLoS Pathog.* 5, e1000516. doi:10.1371/journal.ppat.1000516

Kraut, R. (2011). Roles of Sphingolipids in *Drosophila* Development and Disease. *J. Neurochem.* 116, 764–778. doi:10.1111/j.1471-4159.2010.07022.x

Lingwood, D., and Simons, K. (2010). Lipid Rafts as a Membrane-Organizing Principle. *Science* 327, 46–50. doi:10.1126/science.1174621

Lukoyanova, N., Kondos, S. C., Farabella, I., Law, R. H. P., reboul, C. F., Caradoc-Davies, T. T., et al. (2015). Conformational Changes during Pore Formation by the Perforin-Related Protein Pleurotolysin. *PLoS Biol.* 13, e1002049. doi:10.1371/journal.pbio.1002049

Masood, M. A., Yuan, C., Acharya, J. K., Veenstra, T. D., and Blonder, J. (2010). Quantitation of Ceramide Phosphorylethanolamines Containing Saturated and Unsaturated Sphingoid Base Cores. *Anal. Biochem.* 400, 259–269. doi:10.1016/j.ab.2010.01.033

Michel, V., and Bakovic, M. (2007). Lipid Rafts in Health and Disease. *Biol. Cell.* 99, 129–140. doi:10.1042/BC20060051

Milijaš Jotić, M., Panevska, A., Iacovache, I., Kostanjšek, R., Mravinec, M., Skočaj, M., et al. (2021). Dissecting Out the Molecular Mechanism of Insecticidal Activity of Ostreolysin A6/pleurotolysin B Complexes on Western Corn Rootworm. *Toxins* 13, 455. doi:10.3390/toxins13070455

Moreau, R. A., Young, D. H., Danis, P. O., Powell, M. J., Quinn, C. J., Beshah, K., et al. (1998). Identification of Ceramide-Phosphorylethanolamine in Oomycete Plant Pathogens: *Pythium Ultimum*, *Phytophthora Infestans*, and *Phytophthora Capsici*. *Lipids* 33, 307–317. doi:10.1007/s11745-998-0210-1

Moschidis, M. C. (1984). Phosphonolipids. *Prog. Lipid Res.* 23, 223–246. doi:10.1016/0163-7827(84)90012-2

Nishimura, S., and Matsumori, N. (2020). Chemical Diversity and Mode of Action of Natural Products Targeting Lipids in the Eukaryotic Cell Membrane. *Nat. Prod. Rep.* 37, 677–702. doi:10.1039/c9np00059c

Novak, M., Kraševec, N., Skočaj, M., Maček, P., Anderluh, G., and Sepčić, K. (2015). Fungal Aegerolysin-like Proteins: Distribution, Activities, and Applications. *Appl. Microbiol. Biotechnol.* 99, 601–610. doi:10.1007/s00253-014-6239-9

Novak, M., Krpan, T., Panevska, A., Shewell, L. K., Day, C. J., Jennings, M. P., et al. (2020). Binding Specificity of Ostreolysin A6 towards Sf9 Insect Cell Lipids. *Biochimica Biophysica Acta (BBA) - Biomembr.* 1862, 183307. doi:10.1016/j.bbamem.2020.183307

Ota, K., Leonardi, A., Mikelj, M., Skočaj, M., Wohlschlager, T., Künzler, M., et al. (2013). Membrane Cholesterol and Sphingomyelin, and Ostreolysin A Are Obligatory for Pore-Formation by a MACPF/CDC-like Pore-Forming Protein, Pleurotolysin B. *Biochimie* 95, 1855–1864. doi:10.1016/j.biochi.2013.06.012

Panevska, A., Hodnik, V., Skočaj, M., Novak, M., Modic, Š., Pavlic, I., et al. (2019a). Pore-forming Protein Complexes from *Pleurotus* Mushrooms Kill Western Corn Rootworm and Colorado Potato Beetle through Targeting Membrane Ceramide Phosphoethanolamine. *Sci. Rep.* 9, 5073. doi:10.1038/s41598-019-41450-4

Panevska, A., Skočaj, M., Križaj, I., Maček, P., and Sepčić, K. (2019b). Ceramide Phosphoethanolamine, an Enigmatic Cellular Membrane Sphingolipid. *Biochimica Biophysica Acta (BBA) - Biomembr.* 1861, 1284–1292. doi:10.1016/j.bbamem.2019.05.001

Panevska, A., Skočaj, M., Modic, Š., Razinger, J., and Sepčić, K. (2021). Aegerolysins from the Fungal Genus *Pleurotus* – Bioinsecticidal Proteins with Multiple Potential Applications. *J. Invert. Pathol.* 186, 107474. doi:10.1016/j.jip.2020.107474

Pike, L. J. (2006). Rafts Defined: a Report on the Keystone Symposium on Lipid Rafts and Cell Function. *J. Lipid Res.* 47, 1597–1598. doi:10.1194/jlr.E600002-JLR200

Ramstedt, B., and Slotte, J. P. (2006). Sphingolipids and the Formation of Sterol-Enriched Ordered Membrane Domains. *Biochimica Biophysica Acta (BBA) - Biomembr.* 1758, 1945–1956. doi:10.1016/j.bbamem.2006.05.020

Resnik, N., Repnik, U., Kreft, M. E., Sepčić, K., Maček, P., Turk, B., et al. (2015). Highly Selective Anti-cancer Activity of Cholesterol-Interacting Agents Methyl-β-Cyclodextrin and Ostreolysin A/Pleurotolysin B Protein Complex on Urothelial Cancer Cells. *PLoS One* 10, e0137878. doi:10.1371/journal.pone.0137878

Sepčić, K., Berne, S., Potrich, C., Turk, T., Macek, P., and Menestrina, G. (2003). Interaction of Ostreolysin, a Cytolytic Protein from the Edible Mushroom *Pleurotus ostreatus*, with Lipid Membranes and Modulation by Lysophospholipids. *Eur. J. Biochem.* 270, 1199–1210. doi:10.1046/j.1432-1033.2003.03480.x

Sepčić, K., Berne, S., Rebolj, K., Batista, U., Plemenitaš, A., Šentjurc, M., et al. (2004). Ostreolysin, a Pore-Forming Protein from the Oyster Mushroom, Interacts Specifically with Membrane Cholesterol-Rich Lipid Domains. *FEBS Lett.* 575, 81–85. doi:10.1016/j.febslet.2004.07.093

Sezgin, E., Kaiser, H.-J., Baumgart, T., Schwille, P., Simons, K., and Levental, I. (2012). Elucidating Membrane Structure and Protein Behavior Using Giant Plasma Membrane Vesicles. *Nat. Protoc.* 7, 1042–1051. doi:10.1038/nprot.2012.059

Skočaj, M., Resnik, N., Grundner, M., Ota, K., Rojko, N., Hodnik, V., et al. (2014). Tracking Cholesterol/Sphingomyelin-Rich Membrane Domains with the Ostreolysin A-mCherry Protein. *PLoS ONE* 9, e92783. doi:10.1371/journal.pone.0092783

Sutterwala, S. S., Hsu, F.-F., Sevova, E. S., Schwartz, K. J., Zhang, K., Key, P., et al. (2008). Developmentally Regulated Sphingolipid Synthesis in African Trypanosomes. *Mol. Microbiol.* 70, 281–296. doi:10.1111/j.1365-2958.2008.06393.x

Sviridov, D., Miller, Y. I., Ballout, R. A., Remaley, A. T., and Bukrinsky, M. (2020b). Targeting Lipid Rafts-A Potential Therapy for COVID-19. *Front. Immunol.* 11, e574508. doi:10.3389/fimmu.2020.574508

Sviridov, D., Mukhamedova, N., and Miller, Y. I. (2020a). Lipid Rafts as a Therapeutic Target. *J. Lipid Res.* 61, 687–695. doi:10.1194/jlr.TR120000658

Tomita, T., Noguchi, K., Mimuro, H., Ukaji, F., Ito, K., Sugawara-Tomita, N., et al. (2004). Pleurotolysin, a Novel Sphingomyelin-specific Two-Component Cytolysin from the Edible Mushroom *Pleurotus ostreatus*, Assembles into a Transmembrane Pore Complex. *J. Biol. Chem.* 279, 26975–26982. doi:10.1074/jbc.M402676200

Tomonaga, N., Manabe, Y., and Sugawara, T. (2017). Digestion of Ceramide 2-aminoethylphosphonate, a Sphingolipid from the Jumbo Flying Squid *Dosidicus gigas*, in Mice. *Lipids* 52, 353–362. doi:10.1007/s11745-017-4239-0

Vacaru, A. M., van den Dikkenberg, J., Ternes, P., and Holthuis, J. C. M. (2013). Ceramide Phosphoethanolamine Biosynthesis in Drosophila is Mediated by a Unique Ethanolamine Phosphotransferase in the Golgi Lumen. *J. Biol. Chem.* 288, 11520–11530. doi:10.1074/jbc.M113.460972

Wang, R., Chen, Q., Song, Y., Ding, Y., Cong, P., Xu, J., et al. (2020). Identification of Ceramide 2-aminoethylphosphonate Molecular Species from Different Aquatic Products by NPLC/Q-Exactive-MS. *Food Chem.* 304, 125425. doi:10.1016/j.foodchem.2019.125425

Conflict of Interest: The authors declare that the research was conducted in the absence of any commercial or financial relationships that could be construed as a potential conflict of interest.

Publisher's Note: All claims expressed in this article are solely those of the authors and do not necessarily represent those of their affiliated organizations, or those of the publisher, the editors and the reviewers. Any product that may be evaluated in this article, or claim that may be made by its manufacturer, is not guaranteed or endorsed by the publisher.

frontiers | Frontiers in Molecular Biosciences

PERSPECTIVE
published: 27 May 2022
doi: 10.3389/fmolb.2022.915301

Current Knowledge on the Role of Cardiolipin Remodeling in the Context of Lipid Oxidation and Barth Syndrome

Zhuqing Liang[†], *Michael W. Schmidtke*[†] *and Miriam L. Greenberg* *

Department of Biological Sciences, Wayne State University, Detroit, MI, United States

Barth syndrome (BTHS, OMIM 302060) is a genetic disorder caused by variants of the *TAFAZZIN* gene (G 4.5, OMIM 300394). This debilitating disorder is characterized by cardio- and skeletal myopathy, exercise intolerance, and neutropenia. TAFAZZIN is a transacylase that catalyzes the second step in the cardiolipin (CL) remodeling pathway, preferentially converting saturated CL species into unsaturated CLs that are susceptible to oxidation. As a hallmark mitochondrial membrane lipid, CL has been shown to be essential in a myriad of pathways, including oxidative phosphorylation, the electron transport chain, intermediary metabolism, and intrinsic apoptosis. The pathological severity of BTHS varies substantially from one patient to another, even in individuals bearing the same *TAFAZZIN* variant. The physiological modifier(s) leading to this disparity, along with the exact molecular mechanism linking CL to the various pathologies, remain largely unknown. Elevated levels of reactive oxygen species (ROS) have been identified in numerous BTHS models, ranging from yeast to human cell lines, suggesting that cellular ROS accumulation may participate in the pathogenesis of BTHS. Although the exact mechanism of how oxidative stress leads to pathogenesis is unknown, it is likely that CL oxidation plays an important role. In this review, we outline what is known about CL oxidation and provide a new perspective linking the functional relevance of CL remodeling and oxidation to ROS mitigation in the context of BTHS.

Keywords: cardiolipin remodeling, oxidation, apoptosis, barth syndrome, cardiolipin

OPEN ACCESS

Edited by:
Isabel María López-Lara, National Autonomous University of Mexico, Mexico

Reviewed by:
Patrice X. Petit, Centre National de la Recherche Scientifique (CNRS), France
Christopher McMaster, Dalhousie University, Canada
Grant M. Hatch, University of Manitoba, Canada

***Correspondence:**
Miriam L. Greenberg
mgreenberg@wayne.edu

[†]*These authors have contributed equally to this work*

Specialty section:
This article was submitted to Lipids, Membranes and Membranous Organelles, a section of the journal Frontiers in Molecular Biosciences

Received: *07 April 2022*
Accepted: *04 May 2022*
Published: *27 May 2022*

Citation:
Liang Z, Schmidtke MW and Greenberg ML (2022) Current Knowledge on the Role of Cardiolipin Remodeling in the Context of Lipid Oxidation and Barth Syndrome. Front. Mol. Biosci. 9:915301. doi: 10.3389/fmolb.2022.915301

INTRODUCTION

As the hallmark lipid of the mitochondrial inner membrane, cardiolipin (CL) is essential for a myriad of cellular functions. CL undergoes a unique and highly regulated remodeling process catalyzed in part by the enzyme TAFAZZIN (Vreken et al., 2000). Variations in TAFAZZIN lead to the life-threatening disease Barth syndrome (BTHS), underscoring the importance of CL homeostasis and remodeling for cellular and organismal fitness (D'Adamo et al., 1997; Xu et al., 2003).

Newly synthesized CL contains predominantly saturated fatty acid chains. The primary outcome of CL remodeling is the incorporation of polyunsaturated fatty acids (PUFAs) into CL molecules. Unlike saturated and monounsaturated fatty acids, PUFAs are susceptible to oxidation in the presence of elevated reactive oxygen species (ROS), and oxidation of PUFA-CL has been shown to underlie cellular sensitivity to apoptosis (Belikova et al., 2006). Recent studies have demonstrated that oxidized CL (CL_{ox}) forms a complex with the intermembrane space (IMS) protein cytochrome *c* (cyt *c*), and that this complex catalyzes the oxidation of additional PUFA-CL molecules (Kagan et al., 2005).

Here we describe a new perspective for understanding the evolutionarily conserved role of CL remodeling in the context of CL oxidation and BTHS. This model represents a paradigm shift for BTHS research by identifying a novel link between TAFAZZIN function and BTHS pathophysiology. Future studies should be aimed at improving our understanding of this model and evaluating the potential for treating BTHS by inhibiting this oxidation pathway.

WHAT IS CL?

CL is a uniquely dimeric phospholipid found almost exclusively in mitochondria. It is comprised of a glycerol backbone bridging two canonical phosphatidylglycerol molecules. The variable structure of the four associated fatty acid chains, along with the negative charge carried by the two phosphate head groups, are important for the many protein-lipid interactions attributed to CL (Planas-Iglesias et al., 2015). Following its initial synthesis, CL undergoes a remodeling process in which multiple cycles of deacylation and reacylation generate predominantly mono- and polyunsaturated fatty acid-containing CL (PUFA-CL). In mammals, this generally involves replacing oleic acid (18:1) acyl chains with linoleic acid (18:2) to form tetralinoleoyl-CL (Xu et al., 2006; Oemer et al., 2020). The importance of the CL remodeling pathway is underscored by the severe disease BTHS, in which patients bear variations in the CL-specific transacylase TAFAZZIN (Barth et al., 1999). At the cellular level, TAFAZZIN deficiency causes a decrease in total CL levels, an aberrant CL profile characterized by a decrease in unsaturated CL, and accumulation of monolyso-CL (mCL), biochemical hallmarks that have been observed in all BTHS models tested to date (Vreken et al., 2000; Valianpour et al., 2002; Schlame et al., 2003; Gu et al., 2004; Houtkooper et al., 2006; Acehan et al., 2011). Although the pathological consequences of TAFAZZIN deficiency have been well-characterized in BTHS patients, the exact mechanism(s) linking defective CL remodeling to these phenotypes remain elusive.

TAFAZZIN is the primary enzyme responsible for reacylation of CL in healthy cells, but two additional acyltransferases have been described in mammals. Similar to TAFAZZIN, both of these enymzes, acyl-CoA:lysocardiolipin acyltransferase 1 (ALCAT1) and monolysocardiolipin acyltransferase 1 (MLCL AT-1), preferentially transfer oleic and linoleic acid acyl chains to CL, generating predominantly unsaturated CL species (Ma et al., 1999; Taylor and Hatch, 2003; Cao et al., 2004; Cao et al., 2009). Interestingly, overexpression of ALCAT1 has been shown to promote ROS production whereas overexpression of MLCL AT-1 attenuates ROS production in BTHS lymphoblasts (Li et al., 2010; Mejia et al., 2018). Given their secondary role to TAFAZZIN, the physiological relevance of each of these enzymes remains unclear, and adding to this complexity, it has been shown that MLCL AT-1 expression is upregulated by TAFAZZIN knockdown in healthy cells but not in BTHS lymphoblasts (Mejia et al., 2018). Thus, further studies are needed to determine the relative contributions of these enzymes to PUFA-CL production in both healthy cells and BTHS tissues.

PUFA-CL LIKELY CONFERS A FITNESS ADVANTAGE IN MAMMALIAN CELLS

In mammalian cells, it is likely that remodeled CL confers a fitness advantage. Intact CL remodeling has been shown to be important for various aspects of cellular and mitochondrial homeostasis, including regulation of mitochondrial dynamics, induction of mitophagy and apoptosis, protein turnover, and calcium uptake (Chu et al., 2013; Hsu et al., 2015; Ban et al., 2017; de Taffin de Tilques et al., 2018; Kameoka et al., 2018; Petit et al., 2020; Bertero et al., 2021). In human heart and skeletal muscle mitochondria, 80% of all endogenous CL is tetralinoleoyl-CL, and decreased tetralinoleoyl-CL has been associated with aging and sarcopenia (Sparagna et al., 2007; Chu et al., 2013; Oemer et al., 2018; Semba et al., 2019; Zhang et al., 2022). Thus, defective CL remodeling in BTHS results in a broad range of cellular deficiencies that may contribute to the pathophysiology.

Although the above findings demonstrate the general importance of CL remodeling, the exact nature of how PUFA-CL benefits cells is not clear. One molecular hypothesis is that protein-lipid packing in the inner mitochondrial membrane (IMM) imposes mechanical stress that favors the accumulation of PUFA-CL, which can only be generated through remodeling. Due to its intrinsic negative curvature, membranes enriched with PUFA-CL can accommodate a higher density of electron transport chain (ETC) complexes and thereby act as more efficient sites for oxidative phosphorylation (OXPHOS) (Musatov, 2006; Schlame and Xu, 2020). However, due to the presence of multiple carbon-carbon double bounds, PUFA-CL is vulnerable to being oxidized by ROS produced by the ETC, and as detailed below, this susceptibility has important consequences for maintaining cellular homeostasis.

OXIDATION OF PUFA-CL IS DETRIMENTAL TO CELL HOMEOSTASIS

In healthy cells, energy production *via* OXPHOS relies on the electron shuttling activity of cyt *c*, an IMS protein whose localization is maintained, in part, by binding with CL. The interaction between CL and cyt *c* is a critical determinant of cell homeostasis. Cyt *c* contains two CL binding sites; loose binding of CL to the "A-site" is mediated by reversible electrostatic interactions between positively charged lysine residues 54/55, 72/73, 86/87, and the negatively charged head groups of CL, whereas tighter binding to the "C-site" involves hydrophobic residues in the fatty acyl chains of CL (Rytomaa et al., 1992; Rytomaa and Kinnunen, 1994; Kagan et al., 2005; Gonzalvez and Gottlieb, 2007; Elmer-Dixon and Bowler, 2018). In the loosely bound conformation mediated by site A, cyt *c* conducts its canonical function of transferring electrons from ETC complex III to complex IV. Conversely, when the C-site is bound, cyt *c* becomes partially unfolded. This exposes a ROS binding site on the associated heme, which effectively converts the CL-cyt *c* complex into a potent lipid peroxidase that preferentially oxidizes PUFA-CL to form CL_{ox} (Kagan et al., 2005; Belikova et al., 2006; Kagan et al., 2014). Due to its

localization in the IMM, CL is highly prone to oxidation, as ETC complex activity is a major source of ROS production even in healthy cells (Raha et al., 2000; Koopman et al., 2010; Holzerova and Prokisch, 2015).

Oxidation of CL facilitates apoptosis by disrupting binding and localization of cyt *c*. Binding between cyt *c* and CL has been shown to depend on the oxidation status of CL. Specifically, cyt *c* has a lower affinity for CL_{ox} than non-oxidized CL, and thus CL oxidation results in increased release of cyt *c* from the IMS, a key event that activates the mitochondria-mediated apoptosis pathway, and increased sensitivity to apoptotic stimuli (Nakagawa, 2004; Jiang et al., 2008; Tyurina et al., 2012). The release of cyt *c* from the IMS takes place in two steps: cyt *c* detachment from CL_{ox}, followed by the permeabilization of the outer mitochondria membrane (OMM). The reduced affinity of cyt *c* for CL_{ox} likely contributes to detachment of the former from the IMM, though the exact biochemistry of this process remains obscure. Subsequent translocation of cyt *c* into the cytosol requires permeabilization of the OMM. The mechanism(s) responsible for OMM permeabilization are the subject of much debate, but two potential explanations have received considerable attention (Robertson et al., 2003; Gogvadze et al., 2006). In the first scenario, calcium overload in the matrix promotes formation of a permeability transition pore in the IMM, which results in swelling and eventual rupture of the OMM (Gogvadze et al., 2006). In the second scenario, the Bcl-2 family protein Bax is recruited to the OMM by tBid where it then homo-oligomerizes to form a pore through which cyt *c* can diffuse. Regardless of the exact mechanism, cyt *c* released from the mitochondria stimulates apoptosis by triggering oligomerization of apoptosis protease activating factor-1 and subsequent activation of pro-caspase-9 (Yu et al., 2005). Interestingly, reduced levels of PUFA-CL in BTHS cells have been linked to a defect in induction of apoptosis, owing to diminished binding affinity between unremodeled CL and caspase-8 (Gonzalvez et al., 2008; Gonzalvez et al., 2013). This suggests that CL remodeling plays an important role in balancing sensitivity to apoptosis, as a decrease in PUFA-CL leads to deficient apoptotic induction while the production of CL_{ox} from PUFA-CL results in hypersensitivity to apoptosis.

The production of CL_{ox} has other important consequences. CL in the IMM acts to bind and stabilize ETC complexes, but when CL becomes oxidized, this interaction is diminished, leading to a concomitant reduction in ETC function (Musatov, 2006). Recent work has also shown that the yeast CL phospholipase Cld1 has a greater affinity for CL_{ox} than non-oxidized CL *in vitro* (Lou et al., 2018b), suggesting that repeated cycles of CL remodeling in the presence of CL_{ox} preferentially generate oxidized (vs non-oxidized) free fatty acids (FA_{ox}). FA_{ox}, and highly reactive aldehydes readily derived from them (Esterbauer et al., 1991; Gueraud et al., 2010), have a variety of secondary messenger signaling roles relating to apoptotic induction (Iuchi et al., 2019), inflammation (Ramakrishnan et al., 2014; Dennis and Norris, 2015), metabolism (Hauck and Bernlohr, 2016; Wenzel et al., 2017), vascular regulation (Sudhahar et al., 2010), and calcium homeostasis (Saraswathi et al., 2004) among other functions (Buland et al., 2016). In light of these primarily negative consequences, selection pressure should favor adaptive mechanisms for preventing or mitigating the production of CL_{ox} in cells.

DISCUSSION AND PERSPECTIVE

The pathologies associated with BTHS illustrate the global importance of CL remodeling. However, the capacity for oxidation in the presence of ROS represents a potential drawback to the production of PUFA-CL through the CL remodeling pathway, and thus a complete understanding of why remodeling has been maintained through evolution remains elusive. This has been highlighted by studies indicating that remodeled and unremodeled CL are functionally equivalent in yeast, and that the pathology of BTHS stems from an elevated mCL:CL ratio rather than a lack of PUFA-CL *per se* (Baile et al., 2014; Ye et al., 2014).

The predominance of PUFA-CL (most notably tetralinoleoyl-CL) suggests that it confers a fitness advantage in mammalian cells, and CL remodeling is often thought of solely as a mechanism for converting saturated CL into PUFA-CL. However, if CL remodeling only functions to generate PUFA-CL, why have cells not evolved to synthesize PUFA-CL directly, rather than depend on the additional multi-step process of converting nascent, primarily saturated CL to PUFA-CL through remodeling? Indeed, it has been shown that exogenously obtained PUFAs can be readily incorporated into newly synthesized CL, indicating that remodeling for the sole purpose of producing PUFA-CL would be redundant when PUFAs can be dietarily acquired (Tyurina et al., 2017). This suggests that the CL remodeling pathway may serve an additional function, and a hint regarding this comes from the study by Lou et al., showing that the yeast CL phospholipase Cld1, which mediates the first step in the CL remodeling pathway, exhibits a clear preference for removing oxidized acyl chains from CL_{ox} (Lou et al., 2018b). Furthermore, this study demonstrated that expression of the *CLD1* gene is upregulated in response to H_2O_2 treatment, suggesting that Cld1 function is regulated as a homeostatic response to elevated ROS (Lou et al., 2018b). Taken together, these findings support the novel hypothesis that CL remodeling may serve as a conserved, compensatory mechanism for removing oxidized fatty acid chains from CL_{ox} in order to mitigate oxidative damage and regenerate non-oxidized PUFA-CL in the second TAFAZZIN-catalyzed step of the remodeling process.

In view of this model, one point should be noted. The notion that CL remodeling has evolved as a mechanism to remove CL_{ox} and regenerate non-oxidized CL presupposes that the phenotype of having elevated CL_{ox} is more deleterious than generating FA_{ox} and associated reactive aldehyde species. This point is supported by the fact that cells have robust mechanisms for neutralizing FA_{ox}/aldehydes, including adduction with glutathione, reduction by aldo-keto reductases or alcohol dehydrogenases, and oxidation by aldehyde dehydrogenases (Gueraud et al., 2010; Pizzimenti et al., 2013), whereas the diminished function of CL_{ox} causes

widespread problems related to cell viability and bioenergetics that cannot be mitigated efficiently.

In the context of BTHS, this hypothesis may partially explain the deleterious consequences of TAFAZZIN deficiency. Although PUFA-CL is primarily produced through the CL remodeling pathway in healthy cells, it is important to note that PUFAs can be incorporated into nascent CL when PUFA-containing precursor lipids are available (e.g., from nutritionally-derived sources) (Tyurina et al., 2017; Lou et al., 2018b). This means that even in TAFAZZIN-deficient cells, oxidizable PUFA-CL will be present, albeit in relatively low abundance compared to wild type cells. Elevated ROS is a characteristic of BTHS models, and this likely facilitates oxidation of the existing PUFA-CL by CL-cyt *c* peroxidase complexes (Chen et al., 2008; Lou et al., 2018a; Liu et al., 2021). The key difference between wild type and TAFAZZIN-deficient cells would become apparent in the homeostatic response to elevated CL_{ox}. While wild type cells would be capable of upregulating their remodeling pathway by increasing iPLA2γ phospholipase expression and relying on TAFAZZIN to reacylate mCL with predominantly non-oxidized PUFAs, TAFAZZIN-deficient cells might still upregulate iPLA2γ phospholipase expression but would be incapable of regenerating PUFA-CL.

In summary, this novel paradigm posits that CL remodeling has been evolutionarily conserved as a means for mitigating the deleterious effects of CL_{ox} production. As an extension of this framework, a major pathophysiological outcome of TAFAZZIN deficiency in BTHS is the inability of cells to recycle CL_{ox} and regenerate non-oxidized PUFA-CL. Future studies should be aimed at testing this model, as it may suggest a new avenue for treating BTHS.

DATA AVAILABILITY STATEMENT

The original contributions presented in the study are included in the article/Supplementary Material, further inquiries can be directed to the corresponding author.

AUTHOR CONTRIBUTIONS

ZL: Conceptualization, Writing—Original Draft, Review, Editing; MS: Conceptualization, Writing—Original Draft, Review, Editing; MG: Conceptualization, Writing—Review and Editing, Supervision, Funding Acquisition.

FUNDING

This work was supported by the National Institutes of Health grant numbers R01 HL117880 and R01 GM134715 (to MG).

REFERENCES

Acehan, D., Vaz, F., Houtkooper, R. H., James, J., Moore, V., Tokunaga, C., et al. (2011). Cardiac and Skeletal Muscle Defects in a Mouse Model of Human Barth Syndrome. *J. Biol. Chem.* 286 (2), 899–908. doi:10.1074/jbc.M110.171439

Baile, M. G., Sathappa, M., Lu, Y.-W., Pryce, E., Whited, K., McCaffery, J. M., et al. (2014). Unremodeled and Remodeled Cardiolipin Are Functionally Indistinguishable in Yeast. *J. Biol. Chem.* 289 (3), 1768–1778. doi:10.1074/jbc.M113.525733

Ban, T., Ishihara, T., Kohno, H., Saita, S., Ichimura, A., Maenaka, K., et al. (2017). Molecular Basis of Selective Mitochondrial Fusion by Heterotypic Action between OPA1 and Cardiolipin. *Nat. Cell Biol.* 19 (7), 856–863. doi:10.1038/ncb3560

Barth, P. G., Wanders, R. J. A., Vreken, P., Janssen, E. A. M., Lam, J., and Baas, F. (1999). X-linked Cardioskeletal Myopathy and Neutropenia (Barth Syndrome) (MIM 302060). *J. Inherit. Metab. Dis.* 22 (4), 555–567. doi:10.1023/a:1005568609936

Belikova, N. A., Vladimirov, Y. A., Osipov, A. N., Kapralov, A. A., Tyurin, V. A., Potapovich, M. V., et al. (2006). Peroxidase Activity and Structural Transitions of Cytochrome C Bound to Cardiolipin-Containing Membranes. *Biochemistry* 45 (15), 4998–5009. doi:10.1021/bi0525573

Bertero, E., Nickel, A., Kohlhaas, M., Hohl, M., Sequeira, V., Brune, C., et al. (2021). Loss of Mitochondrial Ca 2+ Uniporter Limits Inotropic Reserve and Provides Trigger and Substrate for Arrhythmias in Barth Syndrome Cardiomyopathy. *Circulation* 144 (21), 1694–1713. doi:10.1161/CIRCULATIONAHA.121.053755

Buland, J. R., Wasserloos, K. J., Tyurin, V. A., Tyurina, Y. Y., Amoscato, A. A., Mallampalli, R. K., et al. (2016). Biosynthesis of Oxidized Lipid Mediators via Lipoprotein-Associated Phospholipase A2 Hydrolysis of Extracellular Cardiolipin Induces Endothelial Toxicity. *Am. J. Physiology-Lung Cell. Mol. Physiology* 311 (2), L303–L316. doi:10.1152/ajplung.00038.2016

Cao, J., Liu, Y., Lockwood, J., Burn, P., and Shi, Y. (2004). A Novel Cardiolipin-Remodeling Pathway Revealed by a Gene Encoding an Endoplasmic Reticulum-Associated Acyl-CoA:lysocardiolipin Acyltransferase (ALCAT1) in Mouse. *J. Biol. Chem.* 279 (30), 31727–31734. doi:10.1074/jbc.M402930200

Cao, J., Shen, W., Chang, Z., and Shi, Y. (2009). ALCAT1 Is a Polyglycerophospholipid Acyltransferase Potently Regulated by Adenine Nucleotide and Thyroid Status. *Am. J. Physiology-Endocrinology Metabolism* 296 (4), E647–E653. doi:10.1152/ajpendo.90761.2008

Cao, W., Ramakrishnan, R., Tuyrin, V. A., Veglia, F., Condamine, T., Amoscato, A., et al. (2014). Oxidized Lipids Block Antigen Cross-Presentation by Dendritic Cells in Cancer. *J. I.* 192 (6), 2920–2931. doi:10.4049/jimmunol.1302801

Chen, S., He, Q., and Greenberg, M. L. (2008). Loss of Tafazzin in Yeast Leads to Increased Oxidative Stress during Respiratory Growth. *Mol. Microbiol.* 68 (4), 1061–1072. doi:10.1111/j.1365-2958.2008.06216.x

Chu, C. T., Ji, J., Dagda, R. K., Jiang, J. F., Tyurina, Y. Y., Kapralov, A. A., et al. (2013). Cardiolipin Externalization to the Outer Mitochondrial Membrane Acts as an Elimination Signal for Mitophagy in Neuronal Cells. *Nat. Cell Biol.* 15 (10), 1197–1205. doi:10.1038/ncb2837

D'Adamo, P., Fassone, L., Gedeon, A., Janssen, E. A. M., Bione, S., Bolhuis, P. A., et al. (1997). The X-Linked Gene G4.5 Is Responsible for Different Infantile Dilated Cardiomyopathies. *Am. J. Hum. Genet.* 61 (4), 862–867. doi:10.1086/514886

de Taffin de Tilques, M., Lasserre, J.-P., Godard, F., Sardin, E., Bouhier, M., Le Guedard, M., et al. (2018). Decreasing Cytosolic Translation Is Beneficial to Yeast and Human Tafazzin-Deficient Cells. *Microb. Cell* 5 (5), 220–232. doi:10.15698/mic2018.05.629

Dennis, E. A., and Norris, P. C. (2015). Eicosanoid Storm in Infection and Inflammation. *Nat. Rev. Immunol.* 15 (8), 511–523. doi:10.1038/nri3859

Elmer-Dixon, M. M., and Bowler, B. E. (2018). Electrostatic Constituents of the Interaction of Cardiolipin with Site A of Cytochrome C. *Biochemistry* 57 (39), 5683–5695. doi:10.1021/acs.biochem.8b00704

Esterbauer, H., Schaur, R. J., and Zollner, H. (1991). Chemistry and Biochemistry of 4-hydroxynonenal, Malonaldehyde and Related Aldehydes. *Free Radic. Biol. Med.* 11 (1), 81–128. doi:10.1016/0891-5849(91)90192-6

Gogvadze, V., Orrenius, S., and Zhivotovsky, B. (2006). Multiple Pathways of Cytochrome C Release from Mitochondria in Apoptosis. *Biochimica Biophysica*

Acta (BBA) - Bioenergetics 1757 (5-6), 639–647. doi:10.1016/j.bbabio.2006.03.016

Gonzalvez, F., D'Aurelio, M., Boutant, M., Moustapha, A., Puech, J.-P., Landes, T., et al. (2013). Barth Syndrome: Cellular Compensation of Mitochondrial Dysfunction and Apoptosis Inhibition Due to Changes in Cardiolipin Remodeling Linked to Tafazzin (TAZ) Gene Mutation. *Biochimica Biophysica Acta (BBA) - Mol. Basis Dis.* 1832 (8), 1194–1206. doi:10.1016/j.bbadis.2013.03.005

Gonzalvez, F., and Gottlieb, E. (2007). Cardiolipin: Setting the Beat of Apoptosis. *Apoptosis* 12 (5), 877–885. doi:10.1007/s10495-007-0718-8

Gonzalvez, F., Schug, Z. T., Houtkooper, R. H., MacKenzie, E. D., Brooks, D. G., Wanders, R. J. A., et al. (2008). Cardiolipin Provides an Essential Activating Platform for Caspase-8 on Mitochondria. *J. Cell Biol.* 183 (4), 681–696. doi:10.1083/jcb.200803129

Gu, Z., Valianpour, F., Chen, S., Vaz, F. M., Hakkaart, G. A., Wanders, R. J. A., et al. (2004). Aberrant Cardiolipin Metabolism in the Yeast Taz1 Mutant: a Model for Barth Syndrome. *Mol. Microbiol.* 51 (1), 149–158. doi:10.1046/j.1365-2958.2003.03802.x

Guéraud, F., Atalay, M., Bresgen, N., Cipak, A., Eckl, P. M., Huc, L., et al. (2010). Chemistry and Biochemistry of Lipid Peroxidation Products. *Free Radic. Res.* 44 (10), 1098–1124. doi:10.3109/10715762.2010.498477

Hauck, A. K., and Bernlohr, D. A. (2016). Oxidative Stress and Lipotoxicity. *J. Lipid Res.* 57 (11), 1976–1986. doi:10.1194/jlr.R066597

Holzerová, E., and Prokisch, H. (2015). Mitochondria: Much Ado about Nothing? How Dangerous Is Reactive Oxygen Species Production? *Int. J. Biochem. Cell Biol.* 63, 16–20. doi:10.1016/j.biocel.2015.01.021

Houtkooper, R. H., Akbari, H., van Lenthe, H., Kulik, W., Wanders, R. J. A., Frentzen, M., et al. (2006). Identification and Characterization of Human Cardiolipin Synthase. *FEBS Lett.* 580 (13), 3059–3064. doi:10.1016/j.febslet.2006.04.054

Hsu, P., Liu, X., Zhang, J., Wang, H.-G., Ye, J.-M., and Shi, Y. (2015). Cardiolipin Remodeling by TAZ/tafazzin Is Selectively Required for the Initiation of Mitophagy. *Autophagy* 11 (4), 643–652. doi:10.1080/15548627.2015.1023984

Iuchi, K., Ema, M., Suzuki, M., Yokoyama, C., and Hisatomi, H. (2019). Oxidized Unsaturated Fatty Acids Induce Apoptotic Cell Death in Cultured Cells. *Mol. Med. Rep.* 19 (4), 2767–2773. doi:10.3892/mmr.2019.9940

Jiang, J., Huang, Z., Zhao, Q., Feng, W., Belikova, N. A., and Kagan, V. E. (2008). Interplay between Bax, Reactive Oxygen Species Production, and Cardiolipin Oxidation during Apoptosis. *Biochem. Biophysical Res. Commun.* 368 (1), 145–150. doi:10.1016/j.bbrc.2008.01.055

Kagan, V. E., Chu, C. T., Tyurina, Y. Y., Cheikhi, A., and Bayir, H. (2014). Cardiolipin Asymmetry, Oxidation and Signaling. *Chem. Phys. Lipids* 179, 64–69. doi:10.1016/j.chemphyslip.2013.11.010

Kagan, V. E., Tyurin, V. A., Jiang, J., Tyurina, Y. Y., Ritov, V. B., Amoscato, A. A., et al. (2005). Cytochrome C Acts as a Cardiolipin Oxygenase Required for Release of Proapoptotic Factors. *Nat. Chem. Biol.* 1 (4), 223–232. doi:10.1038/nchembio727

Kameoka, S., Adachi, Y., Okamoto, K., Iijima, M., and Sesaki, H. (2018). Phosphatidic Acid and Cardiolipin Coordinate Mitochondrial Dynamics. *Trends Cell Biol.* 28 (1), 67–76. doi:10.1016/j.tcb.2017.08.011

Koopman, W. J. H., Nijtmans, L. G. J., Dieteren, C. E. J., Roestenberg, P., Valsecchi, F., Smeitink, J. A. M., et al. (2010). Mammalian Mitochondrial Complex I: Biogenesis, Regulation, and Reactive Oxygen Species Generation. *Antioxidants Redox Signal.* 12 (12), 1431–1470. doi:10.1089/ars.2009.2743

Li, J., Romestaing, C., Han, X., Li, Y., Hao, X., Wu, Y., et al. (2010). Cardiolipin Remodeling by ALCAT1 Links Oxidative Stress and Mitochondrial Dysfunction to Obesity. *Cell Metab.* 12 (2), 154–165. doi:10.1016/j.cmet.2010.07.003

Liu, X., Wang, S., Guo, X., Li, Y., Ogurlu, R., Lu, F., et al. (2021). Increased Reactive Oxygen Species-Mediated Ca 2+/Calmodulin-dependent Protein Kinase II Activation Contributes to Calcium Handling Abnormalities and Impaired Contraction in Barth Syndrome. *Circulation* 143 (19), 1894–1911. doi:10.1161/CIRCULATIONAHA.120.048698

Lou, W., Reynolds, C. A., Li, Y., Liu, J., Hüttemann, M., Schlame, M., et al. (2018a). Loss of Tafazzin Results in Decreased Myoblast Differentiation in C2C12 Cells: A Myoblast Model of Barth Syndrome and Cardiolipin Deficiency. *Biochimica Biophysica Acta (BBA) - Mol. Cell Biol. Lipids* 1863 (8), 857–865. doi:10.1016/j.bbalip.2018.04.015

Lou, W., Ting, H.-C., Reynolds, C. A., Tyurina, Y. Y., Tyurin, V. A., Li, Y., et al. (2018b). Genetic Re-engineering of Polyunsaturated Phospholipid Profile of Saccharomyces cerevisiae Identifies a Novel Role for Cld1 in Mitigating the Effects of Cardiolipin Peroxidation. *Biochimica Biophysica Acta (BBA) - Mol. Cell Biol. Lipids* 1863 (10), 1354–1368. doi:10.1016/j.bbalip.2018.06.016

Ma, B. J., Taylor, W. A., Dolinsky, V. W., and Hatch, G. M. (1999). Acylation of Monolysocardiolipin in Rat Heart. *J. Lipid Res.* 40 (10), 1837–1845. doi:10.1016/s0022-2275(20)34900-2

Mejia, E. M., Zegallai, H., Bouchard, E. D., Banerji, V., Ravandi, A., and Hatch, G. M. (2018). Expression of Human Monolysocardiolipin Acyltransferase-1 Improves Mitochondrial Function in Barth Syndrome Lymphoblasts. *J. Biol. Chem.* 293 (20), 7564–7577. doi:10.1074/jbc.RA117.001024

Musatov, A. (2006). Contribution of Peroxidized Cardiolipin to Inactivation of Bovine Heart Cytochrome C Oxidase. *Free Radic. Biol. Med.* 41 (2), 238–246. doi:10.1016/j.freeradbiomed.2006.03.018

Nakagawa, Y. (2004). Initiation of Apoptotic Signal by the Peroxidation of Cardiolipin of Mitochondria. *Ann. N. Y. Acad. Sci.* 1011, 177–184. doi:10.1007/978-3-662-41088-2_18

Oemer, G., Koch, J., Wohlfarter, Y., Alam, M. T., Lackner, K., Sailer, S., et al. (2020). Phospholipid Acyl Chain Diversity Controls the Tissue-specific Assembly of Mitochondrial Cardiolipins. *Cell Rep.* 30 (12), 4281–4291. doi:10.1016/j.celrep.2020.02.115

Oemer, G., Lackner, K., Muigg, K., Krumschnabel, G., Watschinger, K., Sailer, S., et al. (2018). Molecular Structural Diversity of Mitochondrial Cardiolipins. *Proc. Natl. Acad. Sci. U.S.A.* 115 (16), 4158–4163. doi:10.1073/pnas.1719407115

Petit, P., Ardilla-Osorio, H., Penalvia, L., and Rainey, N. E. (2020). Tafazzin Mutation Affecting Cardiolipin Leads to Increased Mitochondrial Superoxide Anions and Mitophagy Inhibition in Barth Syndrome. *Cells* 9 (10), 2333. doi:10.3390/cells9102333

Pizzimenti, S., Ciamporcero, E., Daga, M., Pettazzoni, P., Arcaro, A., Cetrangolo, G., et al. (2013). Interaction of Aldehydes Derived from Lipid Peroxidation and Membrane Proteins. *Front. Physiol.* 4, 242. doi:10.3389/fphys.2013.00242

Planas-Iglesias, J., Dwarakanath, H., Mohammadyani, D., Yanamala, N., Kagan, V. E., and Klein-Seetharaman, J. (2015). Cardiolipin Interactions with Proteins. *Biophysical J.* 109 (6), 1282–1294. doi:10.1016/j.bpj.2015.07.034

Raha, S., McEachern, G. E., Myint, A. T., and Robinson, B. H. (2000). Superoxides from Mitochondrial Complex III: the Role of Manganese Superoxide Dismutase. *Free Radic. Biol. Med.* 29 (2), 170–180. doi:10.1016/s0891-5849(00)00338-5

Robertson, J. D., Zhivotovsky, B., Gogvadze, V., and Orrenius, S. (2003). Outer Mitochondrial Membrane Permeabilization: an Open-And-Shut Case? *Cell Death Differ.* 10 (5), 485–487. doi:10.1038/sj.cdd.4401218

Rytömaa, M., and Kinnunen, P. K. (1994). Evidence for Two Distinct Acidic Phospholipid-Binding Sites in Cytochrome C. *J. Biol. Chem.* 269 (3), 1770–1774. doi:10.1016/s0021-9258(17)42094-1

Rytömaa, M., Mustonen, P., and Kinnunen, P. K. (1992). Reversible, Nonionic, and pH-dependent Association of Cytochrome C with Cardiolipin-Phosphatidylcholine Liposomes. *J. Biol. Chem.* 267 (31), 22243–22248. doi:10.1016/s0021-9258(18)41661-4

Saraswathi, V., Wu, G., Toborek, M., and Hennig, B. (2004). Linoleic Acid-Induced Endothelial Activation. *J. Lipid Res.* 45 (5), 794–804. doi:10.1194/jlr.M300497-JLR200

Schlame, M., Kelley, R. I., Feigenbaum, A., Towbin, J. A., Heerdt, P. M., Schieble, T., et al. (2003). Phospholipid Abnormalities in Children with Barth Syndrome. *J. Am. Coll. Cardiol.* 42 (11), 1994–1999. doi:10.1016/j.jace.2003.06.01510.1016/j.jacc.2003.06.015

Schlame, M., and Xu, Y. (2020). The Function of Tafazzin, a Mitochondrial Phospholipid-Lysophospholipid Acyltransferase. *J. Mol. Biol.* 432, 5043–5051. doi:10.1016/j.jmb.2020.03.026

Semba, R. D., Moaddel, R., Zhang, P., Ramsden, C. E., and Ferrucci, L. (2019). Tetra-linoleoyl Cardiolipin Depletion Plays a Major Role in the Pathogenesis of Sarcopenia. *Med. Hypotheses* 127, 142–149. doi:10.1016/j.mehy.2019.04.015

Sparagna, G. C., Chicco, A. J., Murphy, R. C., Bristow, M. R., Johnson, C. A., Rees, M. L., et al. (2007). Loss of Cardiac Tetralinoleoyl Cardiolipin in Human and Experimental Heart Failure. *J. Lipid Res.* 48 (7), 1559–1570. doi:10.1194/jlr.M600551-JLR200

Sudhahar, V., Shaw, S., and Imig, J. (2010). Epoxyeicosatrienoic Acid Analogs and Vascular Function. *Cmc* 17 (12), 1181–1190. doi:10.2174/092986710790827843

Taylor, W. A., and Hatch, G. M. (2003). Purification and Characterization of Monolysocardiolipin Acyltransferase from Pig Liver Mitochondria. *J. Biol. Chem.* 278 (15), 12716–12721. doi:10.1074/jbc.M210329200

Tyurina, Y. Y., Lou, W., Qu, F., Tyurin, V. A., Mohammadyani, D., Liu, J., et al. (2017). Lipidomics Characterization of Biosynthetic and Remodeling Pathways of Cardiolipins in Genetically and Nutritionally Manipulated Yeast Cells. *ACS Chem. Biol.* 12 (1), 265–281. doi:10.1021/acschembio.6b00995

Tyurina, Y. Y., Tungekar, M. A., Jung, M.-Y., Tyurin, V. A., Greenberger, J. S., Stoyanovsky, D. A., et al. (2012). Mitochondria Targeting of Non-peroxidizable Triphenylphosphonium Conjugated Oleic Acid Protects Mouse Embryonic Cells against Apoptosis: Role of Cardiolipin Remodeling. *FEBS Lett.* 586 (3), 235–241. doi:10.1016/j.febslet.2011.12.016

Valianpour, F., Wanders, R. J., Barth, P. G., Overmars, H., and van Gennip, A. H. (2002). Quantitative and Compositional Study of Cardiolipin in Platelets by Electrospray Ionization Mass Spectrometry: Application for the Identification of Barth Syndrome Patients. *Clin. Chem.* 48 (9), 1390–1397. doi:10.1093/clinchem/48.9.1390

Vreken, P., Valianpour, F., Nijtmans, L. G., Grivell, L. A., Plecko, B., Wanders, R. J. A., et al. (2000). Defective Remodeling of Cardiolipin and Phosphatidylglycerol in Barth Syndrome. *Biochem. Biophysical Res. Commun.* 279 (2), 378–382. doi:10.1006/bbrc.2000.3952

Wenzel, S. E., Tyurina, Y. Y., Zhao, J., St. Croix, C. M., Dar, H. H., Mao, G., et al. (2017). PEBP1 Wardens Ferroptosis by Enabling Lipoxygenase Generation of Lipid Death Signals. *Cell* 171 (3), 628–641. doi:10.1016/j.cell.2017.09.044

Xu, Y., Kelley, R. I., Blanck, T. J. J., and Schlame, M. (2003). Remodeling of Cardiolipin by Phospholipid Transacylation. *J. Biol. Chem.* 278 (51), 51380–51385. doi:10.1074/jbc.M307382200

Xu, Y., Malhotra, A., Ren, M., and Schlame, M. (2006). The Enzymatic Function of Tafazzin. *J. Biol. Chem.* 281 (51), 39217–39224. doi:10.1074/jbc.M606100200

Ye, C., Lou, W., Li, Y., Chatzispyrou, I. A., Hüttemann, M., Lee, I., et al. (2014). Deletion of the Cardiolipin-specific Phospholipase Cld1 Rescues Growth and Life Span Defects in the Tafazzin Mutant. *J. Biol. Chem.* 289 (6), 3114–3125. doi:10.1074/jbc.M113.529487

Yu, X., Acehan, D., Ménétret, J.-F., Booth, C. R., Ludtke, S. J., Riedl, S. J., et al. (2005). A Structure of the Human Apoptosome at 12.8 Å Resolution Provides Insights into This Cell Death Platform. *Structure* 13 (11), 1725–1735. doi:10.1016/j.str.2005.09.006

Zhang, J., Liu, X., Nie, J., and Shi, Y. (2022). Restoration of Mitophagy Ameliorates Cardiomyopathy in Barth Syndrome. *Autophagy*, 1–16. doi:10.1080/15548627.2021.2020979

Conflict of Interest: The authors declare that the research was conducted in the absence of any commercial or financial relationships that could be construed as a potential conflict of interest.

Publisher's Note: All claims expressed in this article are solely those of the authors and do not necessarily represent those of their affiliated organizations, or those of the publisher, the editors and the reviewers. Any product that may be evaluated in this article, or claim that may be made by its manufacturer, is not guaranteed or endorsed by the publisher.

frontiers | Frontiers in Molecular Biosciences

ORIGINAL RESEARCH
published: 03 June 2022
doi: 10.3389/fmolb.2022.901062

Membrane Lipids in the Thyroid Comparing to Those in Non-Endocrine Tissues Are Less Sensitive to Pro-Oxidative Effects of Fenton Reaction Substrates

Jan Stępniak[1], *Aleksandra Rynkowska*[1] *and Małgorzata Karbownik-Lewińska*[1,2]*

[1]Department of Oncological Endocrinology, Medical University of Lodz, Lodz, Poland, [2]Polish Mother's Memorial Hospital—Research Institute, Lodz, Poland

OPEN ACCESS

Edited by:
Elena G. Govorunova,
University of Texas Health Science Center at Houston, United States

Reviewed by:
Rasim Mogulkoc,
Selçuk University, Turkey
José Joaquín García,
University of Zaragoza, Spain

***Correspondence:**
Małgorzata Karbownik-Lewińska
malgorzata.karbownik-lewinska@umed.lodz.pl
mkarbownik@hotmail.com

Specialty section:
This article was submitted to Lipids, Membranes and Membranous Organelles, a section of the journal Frontiers in Molecular Biosciences

Received: 21 March 2022
Accepted: 29 April 2022
Published: 03 June 2022

Citation:
Stępniak J, Rynkowska A and Karbownik-Lewińska M (2022) Membrane Lipids in the Thyroid Comparing to Those in Non-Endocrine Tissues Are Less Sensitive to Pro-Oxidative Effects of Fenton Reaction Substrates. Front. Mol. Biosci. 9:901062. doi: 10.3389/fmolb.2022.901062

Iron is an essential microelement for the proper functioning of many organs, among others it is required for thyroid hormone synthesis. However, its overload contributes to the increased formation of reactive oxygen species via Fenton chemistry ($Fe^{2+}+H_2O_2 \rightarrow Fe^{3+}+{}^{\bullet}OH + OH^-$), and it is potentially toxic. Individual organs/tissues are affected differently by excess iron. The excessive absorption of iron with subsequent deposition in various organs is associated with diseases such as hemochromatosis. Such an iron deposition also occurs in the thyroid gland where it can disturb thyroid hormone synthesis. In turn, melatonin is an effective antioxidant, which protects against oxidative damage. This study aims to check if lipid peroxidation resulting from oxidative damage to membrane lipids, is caused by Fenton reaction substrates, and if protective effects of melatonin differ between the thyroid and various non-endocrine porcine tissues (liver, kidney, brain cortex, spleen, and small intestine). To mimic the conditions of iron overload, Fe^{2+} was used in extremely high concentrations. Homogenates of individual tissues were incubated together with Fenton reaction substrates, i.e., $FeSO_4$ (9.375, 18.75, 37.5, 75, 150, 300, 600, 1,200, 1,800, 2,100, 2,400, 3,000, 3,600, 4,200, and 4,800 μM)+H_2O_2 (5 mM), either without or with melatonin (5 mM). The concentration of malondialdehyde+4-hydroxyalkenals (MDA+4-HDA), as the LPO index, was evaluated by a spectrophotometrical method. Fenton reaction substrates increased concentrations of LPO products in all chosen tissues. However, in the thyroid, compared to non-endocrine tissues, the damaging effect was generally weaker, it was not observed for the two lowest concentrations of iron, and the LPO peak occurred with higher concentrations of iron. Melatonin reduced experimentally induced LPO in all examined tissues (without differences between them), and these protective effects did not depend on iron concentration. In conclusion, membrane lipids in the thyroid compared to those in non-endocrine tissues are less sensitive to pro-oxidative effects of Fenton reaction substrates, without differences regarding protective effects of melatonin.

Keywords: Fenton reaction, lipid peroxidation, oxidative damage, thyroid, melatonin

INTRODUCTION

Iron is a critical micronutrient in mammalian organisms, and it is a cofactor for many biological reactions. As a redox-active transition metal, it acts as an electron donor and acceptor in a plethora of fundamental cellular processes, such as oxygen transport, DNA and RNA synthesis, cell proliferation, and energy metabolism. In mammals, all iron is obtained from digestion of food where it exists largely in two forms, i.e., non-heme iron in the relatively non-toxic ferric form (Fe^{3+}), derived mainly from plant-based foods and animal products, and heme iron in a more reactive and toxic form of ferrous ion (Fe^{2+}), derived from the breakdown of hemoglobin and myoglobin in animal tissues. Despite the fact that non-heme iron is usually much less well absorbed than heme iron, it constitutes most of the human dietary iron, even in meat-eating populations (Hurrell and Egli, 2010; Abbaspour et al., 2014).

The adult well-nourished human body contains approx. 3–5 g of iron. Under healthy conditions, most of it is bound to some form of a ligand. It is estimated that up to 80% of body iron is present in red blood cell hemoglobin, while another approximately 20% is stored in the form of ferritin and heme within hepatocytes and macrophages of the liver and spleen (Hentze et al., 2004). The remaining small amount (<1%) of the iron in the human body is found in various proteins such as cytochromes (Lane et al., 2015).

This iron compartmentalization is crucial for organism homeostasis since "free" (catalytically active) iron can react with hydrogen peroxide (H_2O_2) via the Fenton chemistry ($Fe^{2+} + H_2O_2 \rightarrow Fe^{3+} + {}^{\bullet}OH + OH^{-}$), the reaction directly related to the oxidative stress. The hydroxyl radical (${}^{\bullet}OH$) produced during this process is one of the most powerful oxidizing agents and can react—at a diffusion-controlled rate—with practically all subcellular components in the organism (Koppenol and Hider, 2019). The hydroxyl radical can react and consequently damage all biological macromolecules (lipids, proteins, nucleic acids, and carbohydrates) leading to cell dysfunction and death. It has been observed that the harmful effects of ${}^{\bullet}OH$ may contribute to pathogenesis of cancer, atherosclerosis, or neurodegenerative diseases (Lipinski, 2011).

Improper iron compartmentalization and subsequent elevated levels of oxidative stress are often the results of accumulation and overload of this element. The human organism does not have any specific mechanism to remove excess iron. Iron elimination occurs only via non-regulated ways such as cell desquamation or bleeding; hence, its concentration is controlled only at the level of iron absorption. A number of diseases and pathological factors can lead to iron overload. The most common causes of iron overload are overconsumption of iron when it is in excess in the environment (Aranda et al., 2016), congenital disturbances of iron metabolism (hemochromatosis) (Girelli et al., 2021), or secondary hemochromatosis resulting from repeated blood transfusions in patients with beta-thalassemia (Ali et al., 2021) or with sickle cell anemia (Badawy et al., 2016). The growing literature demonstrates that also chronic hepatitis C may cause iron overload (Zou and Sun, 2017).

Iron overload and enhanced oxidative stress can lead to adverse effects in all tissues; however, it can be, especially severe in the thyroid when we take into consideration the "oxidative nature" of this gland. Hydrogen peroxide (one of the Fenton reaction substrates) is indispensable for biosynthesis of thyroid hormones, in which it serves as an electron acceptor at each stage of this process (Song et al., 2007). Therefore, H_2O_2 is generated in the thyroid in high concentrations which, in turn, can create favorable conditions for the Fenton reaction to occur.

Until now, Fenton reaction substrates were used very commonly to experimentally induce oxidative damage to macromolecules in different tissues (e.g., ovary, thyroid, and skin) with very high Fe^{2+} concentrations (Rynkowska et al., 2020, 2021), equal to these used in the present study.

This study aims to check if lipid peroxidation (LPO) resulting from oxidative damage to membrane lipids caused by Fenton reaction substrates and protective effects of melatonin differs between the thyroid and various non-endocrine porcine tissues (liver, kidney, brain cortex, spleen, and small intestine). While it is currently known that certain hormones can be synthesized by and secreted from nontraditional endocrine organs, still specific organs classified as endocrine glands are separated. They are traditionally defined as ductless glandular structures that release their hormonal secretions into the extracellular space, from where they can eventually enter the bloodstream; examples of classic endocrine glands are the thyroid gland, the pituitary gland, the adrenal gland, and the ovary, etc. (Hsiao et al., 2017; Holt et al., 2021). Regarding tissues, such as liver, kidney, brain cortex, spleen, and small intestine, which are used in the present study, do not fulfill the criteria of an endocrine gland; therefore, they can be called non-endocrine tissues. In fact, experimental and clinical studies to describe various processes occurring in endocrine versus non-endocrine tissues have been published before (McCarthy et al., 2013; Xie et al., 2018). In the present study, we have chosen these non-endocrine tissues, which play important roles in iron absorption (intestine) and accumulation (liver and spleen) or iron overload. Iron overload plays a crucial role in the pathogenesis of diseases developing in the tissues, such as brain cortex (Belaidi and Bush, 2016) or kidney (Nakanishi et al., 2019). To simulate conditions of iron overload, Fe^{2+} ion was used in the present study in extremely high concentrations.

MATERIALS AND METHODS

Ethical Considerations

In accordance with the Polish Act on the Protection of Animals Used for Scientific or Educational Purposes from 15 January, 2015 (which implements Directive 2010/63/EU of the European Parliament and the Council of 22 September 2010 on the protection of animals used for scientific purposes)—the use of animals to collect organs or tissues does not require the approval of the Local Ethics Committee. These animals are only subjected to registration by the center in which the organs or tissues were taken. Additionally, we did not use experimental animals; instead, porcine tissues were collected from animals at a slaughterhouse during the routine process of slaughter carried out for consumption.

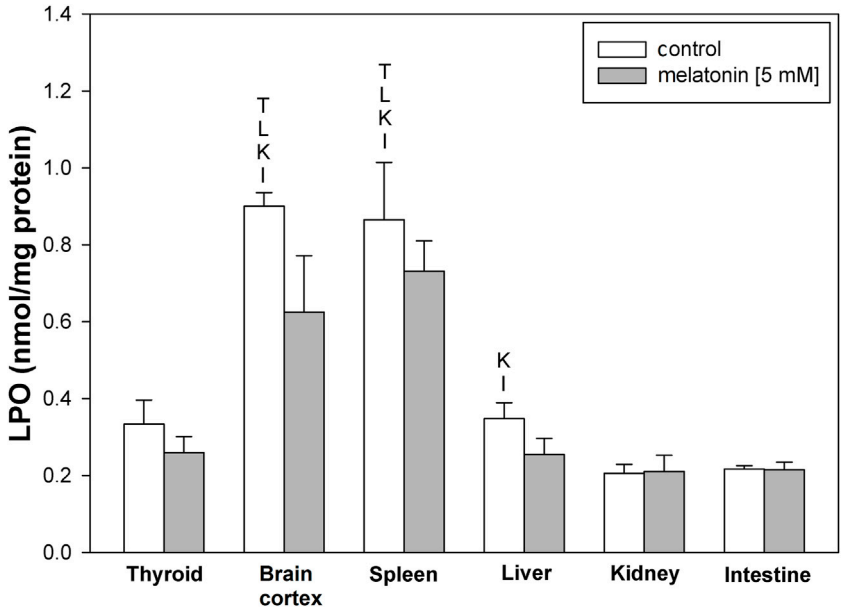

FIGURE 1 | Concentrations of lipid peroxidation products (MDA+4-HDA) in the homogenates of porcine tissues (thyroid, brain cortex, spleen, liver, kidney, and intestine) incubated without any substance (control; white bars) or with melatonin (5 mM) (gray bars). T–$p < 0.05$ vs. respective control in the thyroid; L–$p < 0.05$ vs. respective control in the liver; K–$p < 0.05$ vs. respective control in the kidney; I–$p < 0.05$ vs. respective control in the intestine. Differences in LPO levels between control and melatonin are not statistically significant in particular tissues. Statistical differences between particular tissues after melatonin exposure are not marked.

Chemicals

All chemicals applied in the study are of analytical grade and come from the following commercial sources: melatonin, ferrous sulfate ($FeSO_4$), and hydrogen peroxide (H_2O_2)—Sigma (St. Louis, MO, United States); the ALDetect Lipid Peroxidation Assay Kit–Enzo Life Sciences, Inc. (Zandhoven, Belgium).

Tissue Collection

Porcine tissues were collected from pigs slaughtered at the local slaughterhouse. Animals were treated according to the European Community Council Regulation (CE1099/2009) concerning protection of animals at the time of killing. All animals were sexually mature as determined by age (8–9 months) and body mass [118 ± 3.8 (SD) kg]. They were in good body condition and considered free of pathologies by the veterinary medical officer responsible for the health of animals and hygiene of the slaughterhouse. Immediately (in less than 5 min) after the slaughter, the tissues, i.e., thyroid, spleen, liver (from left lateral lobe), brain cortex, small intestine (jejunum and ileum), and kidney (renal cortex), were collected, frozen on solid CO_2, and stored at −80°C till experimental procedure. Each experiment was repeated three times.

Incubation of Tissue Homogenates

We homogenized individual tissues (thyroid, spleen, liver, brain cortex, small intestine, and kidney) in ice-cold 20 mM Tris–HCl buffer (pH 7.4) (10%, w/v), and then tissues were incubated (37°C, 30 min) in the presence of $FeSO_4$ (9.375, 18.75, 37.5, 75, 150, 300, 600, 1,200, 1,800, 2,100, 2,400, 3,000, 3,600, 4,200, and 4,800 μM)+H_2O_2 (5 mM) without melatonin or with the addition of melatonin in its highest achievable *in vitro* concentration (due to limited solubility), i.e., 5 mM. After incubation, the samples were cooled on ice to stop the reaction.

Assay of Lipid Peroxidation

The ALDetect Lipid Peroxidation Assay Kit was used to measure concentrations of malondialdehyde + 4-hydroxyalkenals (MDA+4-HDA), being the index of lipid peroxidation. To obtain supernatants, samples of homogenates were centrifuged (5,000×*g*, 10 min, 4°C). Next, 200 μL of supernatant was mixed with methanol: acetonitrile (1:3, v/v) solution (650 μL), containing N-methyl-2-phenylindole as a chromogenic reagent, and after that the sample was vortexed. In the next step, methanesulfonic acid (150 μL, 15.4 M) was added, and then incubation was conducted again (45°C, 40 min). The product of the reaction between MDA+4-HDA and N-methyl-2-phenylindole was a chromophore, which was measured by the spectrophotometrical method (at an absorbance of 586 nm) with the use of a 4-hydroxynonenal solution (10 mM) as the standard. The amount of protein was measured with the use of Bradford's method (the standard was bovine albumin) (Bradford, 1976). We expressed the level of lipid peroxidation as the concentration of MDA+4-HDA (nmol)/mg protein.

Statistical Analyses

We used the following statistical tests: one-way analysis of variance (ANOVA), followed by the Student–Neuman–Keuls test, or an unpaired *t*-test. $p < 0.05$ was accepted as the level of statistical significance. We presented the results as means ± SE.

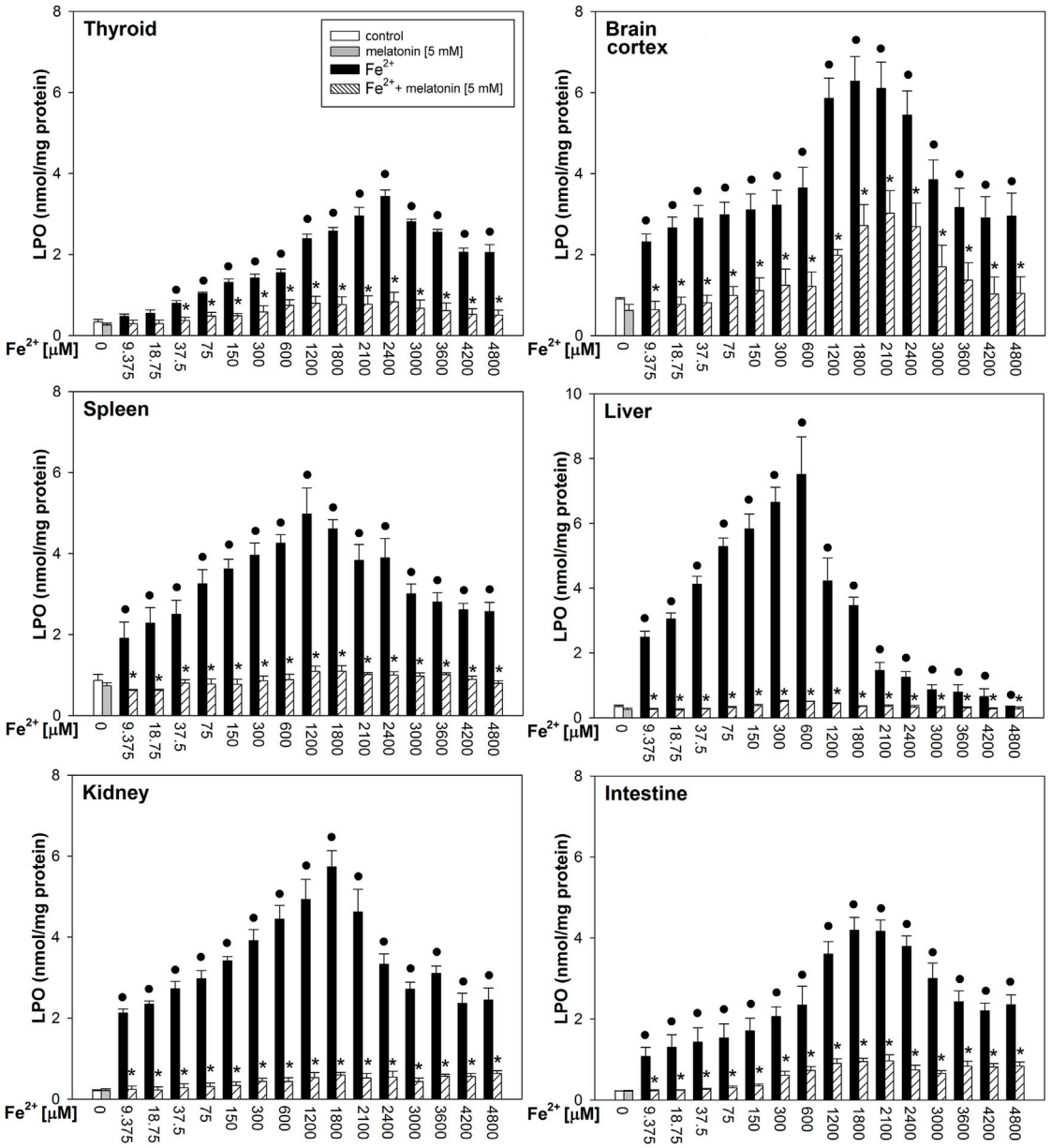

FIGURE 2 | Concentrations of lipid peroxidation products (MDA+4-HDA) in the homogenates of porcine tissues (thyroid, brain cortex, spleen, liver, kidney, and intestine), incubated without any substance (control; white bars) or with melatonin (5 mM) (gray bars) or with Fe^{2+} (9.375, 18.75, 37.5, 75, 150, 300, 600, 1,200, 1,800, 2,100, 2,400, 3,000, 3,600, 4,200, and 4,800 μM) + H_2O_2 (5 mM) (black bars) or with Fe^{2+} (9.375, 18.75, 37.5, 75, 150, 300, 600, 1,200, 1,800, 2,100, 2,400, 3,000, 3,600, 4,200, and 4,800 μM) + H_2O_2 (5 mM) with melatonin (5 mM) (striped bars). $p < 0.05$ vs. respective control (without any substance); *$p < 0.05$ vs. Fe^{2+} in the same concentration. Statistical differences between Fe^{2+}+H_2O_2+melatonin (stripped bars) vs. melatonin (gray bars) in particular tissues are not marked.

RESULTS

LPO levels under basal conditions were higher in the brain cortex and spleen than in other examined tissues (**Figure 1**). Incubation with melatonin did not change basal levels of LPO significantly in any of the examined tissues (**Figure 1**).

Fenton reaction substrates increased LPO levels in all examined tissues and—except for the thyroid—in all used concentrations of Fe^{2+} (**Figure 2**). Namely, in the thyroid, the damaging effect was not observed for the two lowest concentrations of iron (9.375 and 18.75 μM) (**Figure 2**). Additionally, compared to that in non-endocrine tissues, Fenton reaction-induced damage in the thyroid was weak for the increasing Fe^{2+} concentrations up to 1,800 μM; although with the increasing Fe^{2+} concentrations above 1,800 μM, these differences gradually disappeared (**Figure 3A**). Importantly, the LPO peak occurred "later," i.e., with higher concentrations of iron, whereas the LPO peak was observed in the thyroid at an

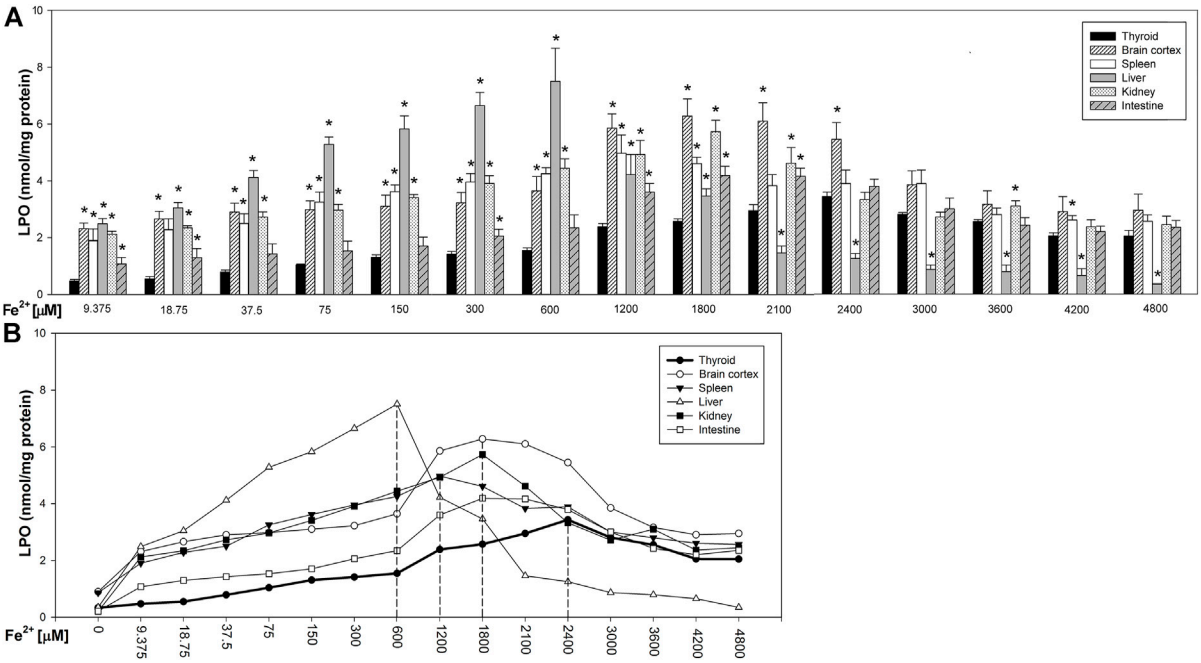

FIGURE 3 | (A) Concentrations of lipid peroxidation products (MDA+4-HDA) in the homogenates of porcine tissues (thyroid, brain cortex, spleen, liver, kidney, and intestine), incubated with Fe^{2+} (9.375, 18.75, 37.5, 75, 150, 300, 600, 1,200, 1,800, 2,100, 2,400, 3,000, 3,600, 4,200, and 4,800 μM) + H_2O_2 (5 mM). *$p < 0.05$ vs. respective concentration in the thyroid. **(B)** Line graph representing concentrations of lipid peroxidation products (MDA+4-HDA) in the homogenates of porcine tissues (thyroid, brain cortex, spleen, liver, kidney, and intestine), incubated with Fe^{2+} (9.375, 18.75, 37.5, 75, 150, 300, 600, 1,200, 1,800, 2,100, 2,400, 3,000, 3,600, 4,200, and 4,800 μM) + H_2O_2 (5 mM). Vertical dashed lines indicate that iron concentration at which the LPO peak occurs for each individual tissue. Data points represent mean values of independent experiments analogically to results presented in **Figure 3**.

Fe^{2+} concentration of 2,400 μM. In the liver, the LPO peak was recorded at an Fe^{2+} concentration of 600 μM (four times lower than that in the thyroid), in the spleen—at an Fe^{2+} concentration of 1,200 μM (two times lower than that in the thyroid), and in the kidney, brain cortex, and intestine—at an Fe^{2+} concentration of 1,800 μM (lower by 25% than that in the thyroid) (**Figures 3A,B**).

Melatonin reduced LPO levels induced by Fenton reaction substrates in all tissues; these protective effects did not significantly differ between tissues, and the protective effects of melatonin did not depend on iron concentration (**Figure 2**).

DISCUSSION

In our earlier studies, we have observed that the thyroid gland is less sensitive to the damaging effects of iron than the ovary which is also an endocrine gland (Rynkowska et al., 2020). We have also evaluated the damaging effect of KIO_3 and have found that KIO_3-induced LPO is significantly lower in the thyroidal tissue than non-endocrine tissues and the ovary (Iwan et al., 2021a). Our present results confirm the results cited previously and clearly indicate that membrane lipids in the thyroid are less sensitive to pro-oxidative events occurring in this gland. Such findings suggest that the thyroid gland has developed more effective (than other tissues) protective mechanisms for maintaining redox homeostasis.

The thyroid gland constitutes a specific organ in such a sense that oxidative reactions are absolutely required for thyroid hormone synthesis. Hydrogen peroxide is generated for the needs of thyroid hormone biosynthesis by NADPH oxidases, especially by dual oxidase 2 (DUOX2) (Pachucki et al., 2004), and it is synthesized in a higher amount than this which is required for proper iodide incorporation into thyroid hormones. This apparent discrepancy may be associated with the relatively high Michaelis–Menten constant of thyroperoxidase (TPO, a clue enzyme in thyroid hormone synthesis) for H_2O_2, resulting in relatively higher concentrations of H_2O_2 (as a substrate) indispensable for proper activation of TPO (Song et al., 2007). Interestingly, in our experimental study on sexual dimorphism, we have found that thyroid follicular cells from female thyroids are exposed to higher H_2O_2 concentrations than male thyroids, which probably results from the higher activity of NOX/DUOX enzymes in the female thyroid (Stepniak et al., 2018), and it is in agreement with the assumption that higher prevalence of thyroid diseases in women is associated with stronger oxidative stress. H_2O_2 is primarily a toxic compound with a relatively long half-life which, as a non-polar molecule, is able to diffuse across biological membranes. Because it is an oxidizing agent, it is in power to induce damage to biological macromolecules such as DNA, lipids, and proteins, consequently leading to mutagenesis and apoptosis (Song et al., 2007). Therefore, to ensure the proper functioning of the thyroid, sources of H_2O_2

and other potentially pro-oxidative compounds need to be under strict control. Therefore, some adaptive mechanisms have developed in the thyroid, such as specific localization of potentially dangerous processes (e.g., production of H_2O_2) and compartmentalization of potentially damaging elements (Szanto et al., 2019), as well as formation of antioxidants and ROS-scavenging systems. Regarding the last mentioned adaptive mechanism, responsible for this are mainly redox-controlling enzymes such as peroxiredoxins, glutathione peroxidases, and catalase. As catalase is rather weakly expressed in the thyroid, H_2O_2 degradation is carried out in this organ mainly by the enzymes from the glutathione peroxidases family (Song et al., 2007; Schweizer et al., 2008). This enzymatic antioxidative system is additionally supported by the contribution of molecules such as ascorbic acid, polyphenolic compounds, coenzyme Q10, β-carotene, retinol, and tocopherol (Kochman et al., 2021).

Under basal conditions, these thyroid systems effectively fulfill their antioxidant role. In our both studies (the present and the previous by Iwan et al., 2021a), we have observed that the basal level of LPO in the thyroid gland is not higher than that in other tissues. However, under any pathological condition associated either with endogenous abnormalities or exposure to exogenous pro-oxidants, this redox balance may be disrupted and, in consequence, the level of oxidative damage can be increased, resulting in various diseases (Valko et al., 2007), such as cancer (Ziech et al., 2011). A phenomenon that can definitely lead to disruption of redox homeostasis in the thyroid is iron overload. Consistently, we have shown earlier that Fe^{2+}, than H_2O_2, damages more strongly both nuclear DNA and membrane lipids (Stepniak et al., 2013). Hepatic iron concentration in patients with asymptomatic and symptomatic hemochromatosis is approximately 8 to 15 times higher than that in healthy subjects—36–550 μmol/g (36–550 mM) in dry weight tissue (Bacon et al., 2011). Whereas in healthy individuals blood iron concentration is below 150 μg/dl, it is 150–300 μg/dl (0.026–0.053 mM) in subjects with hemochromatosis (Bacon et al., 2011). To mimic conditions of iron overload, in the present study, we have used the range of iron concentrations from 0.009 to 4.8 mM, which corresponds to the aforementioned.

In case of disrupted redox homeostasis, different exogenous antioxidants can be considered to be used. One of the most famous antioxidants is melatonin (N-acetyl-5-methoxytryptamine), which is produced in the organism mostly by the pineal gland, but it is also available as an exogenous substance. This molecule is confirmed to be a very effective antioxidant and free radical scavenger which prevents oxidative damage not only in the thyroid (Lewinski and Karbownik, 2002; Karbownik et al., 2005; Kokoszko-Bilska et al., 2014; Zasada and Karbownik-Lewinska, 2015; Iwan et al., 2021a, 2021b; Stepniak et al., 2021) but also in many other tissues and organs (Karbownik et al., 2000, 2001a, 2001b, 2006; Gitto et al., 2001; Osuna et al., 2002; Mogulkoc et al., 2006; Reiter et al., 2017). In the current study, we have observed that melatonin reduced LPO induced by Fenton reaction substrates in all examined tissues, and this protective effect was independent of iron concentration. These results confirm a well-known fact that melatonin is very effective in protecting against even these effects of iron which are caused by its extremely high concentrations (corresponding to those iron concentrations found in patients with hemochromatosis). It should be underlined that in our study melatonin did not reduce LPO levels below the physiological threshold in control groups of any examined tissue. This additionally supports the statement that this indoleamine is a distinctive antioxidant, which does not affect physiological processes, whereas it is effective under conditions with additional oxidative abuse.

Our study is probably the first attempt to compare the damaging effects of high iron concentrations in the thyroid and in various non-endocrine tissues under *in vitro* conditions. It should be stressed that the lower sensitivity of thyroidal membrane lipids, compared to that of membrane lipids in non-endocrine tissues, in response to high iron concentrations, is similar to previously observed pro-oxidative effects of KIO_3 (Iwan et al., 2021a). Therefore, we suppose that membrane lipids (and possibly other biological macromolecules) in the thyroid reveal higher resistance to any external pro-oxidative agent than those in other tissues. These differences in sensitivities of given tissues to pro-oxidative factors result presumably from oxidative/antioxidative processes which normally (under physiological conditions) occur in the tissue. Because oxidative processes occur in the thyroid gland at a high level (Karbownik-Lewińska and Kokoszko-Bilska, 2012), this endocrine gland has developed an adaptive mechanism and, therefore, it is probably better prepared to protect against damaging effects of pro-oxidants.

This study has some limitations. First, our study was conducted using tissue homogenates, so our results may not be directly extrapolated under *in vivo* conditions, especially into the human organism. However, some directions of action of a given agent observed *in vitro* should be taken into account also under *in vivo* conditions. Second, we used only one experimental method to measure oxidative damage to membrane lipids, i.e., a spectrophotometric assay, evaluating lipid peroxidation by measuring MDA + 4-HDA. Although this experimental method has some disadvantages, it is very reliable and is commonly used in studies on oxidative stress.

DATA AVAILABILITY STATEMENT

The raw data supporting the conclusion of this article will be made available by the authors, without undue reservation.

AUTHOR CONTRIBUTIONS

Conceptualization: MK-L; methodology: MK-L; software: JS; validation: MK-L; formal analysis: JS and AR; investigation: AR; writing—original draft preparation: JS; writing—review and editing: MK-L and JS; visualization: JS and AR; supervision: MK-L.

FUNDING

This research was funded by the Medical University of Lodz (Project No. 503/1-168-01/503-11-001).

REFERENCES

Abbaspour, N., Hurrell, R., and Kelishadi, R. (2014). Review on Iron and its Importance for Human Health. *J. Res. Med. Sci.* 19, 164–174.

Ali, S., Mumtaz, S., Shakir, H. A., Khan, M., Tahir, H. M., Mumtaz, S., et al. (2021). Current Status of Beta-Thalassemia and its Treatment Strategies. *Mol. Genet. Genomic. Med.* 9, e1788. doi:10.1002/mgg3.1788

Aranda, N., Fernandez-Cao, J. C., Tous, M., and Arija, V. (2016). Increased Iron Levels and Lipid Peroxidation in a Mediterranean Population of Spain. *Eur. J. Clin. Invest.* 46, 520–526. doi:10.1111/eci.12625

Bacon, B. R., Adams, P. C., Kowdley, K. V., Powell, L. W., and Tavill, A. S. (2011). Diagnosis and Management of Hemochromatosis: 2011 Practice Guideline by the American Association for the Study of Liver Diseases. *Hepatology* 54, 328–343. doi:10.1002/hep.24330

Badawy, S. M., Liem, R. I., Rigsby, C. K., Labotka, R. J., DeFreitas, R. A., and Thompson, A. A. (2016). Assessing Cardiac and Liver Iron Overload in Chronically Transfused Patients with Sickle Cell Disease. *Br. J. Haematol.* 175, 705–713. doi:10.1111/bjh.14277

Belaidi, A. A., and Bush, A. I. (2016). Iron Neurochemistry in Alzheimer's Disease and Parkinson's Disease: Targets for Therapeutics. *J. Neurochem.* 139, 179–197. doi:10.1111/jnc.13425

Bradford, M. M. (1976). A Rapid and Sensitive Method for the Quantitation of Microgram Quantities of Protein Utilizing the Principle of Protein-Dye Binding. *Anal. Biochem.* 72, 248–254. doi:10.1016/0003-2697(76)90527-3

Girelli, D., Busti, F., Brissot, P., Cabantchik, I., Muckenthaler, M. U., and Porto, G. (2021). Hemochromatosis Classification: Update and Recommendations by the BIOIRON Society. *Blood* 139, 3018–3029. doi:10.1182/blood.2021011338

Gitto, E., Tan, D. X., Reiter, R. J., Karbownik, M., Manchester, L. C., Cuzzocrea, S., et al. (2001). Individual and Synergistic Antioxidative Actions of Melatonin: Studies with Vitamin E, Vitamin C, Glutathione and Desferrioxamine (Desferoxamine) in Rat Liver Homogenates. *J. Pharm. Pharmacol.* 53, 1393–1401. doi:10.1211/0022357011777747

Hentze, M. W., Muckenthaler, M. U., and Andrews, N. C. (2004). Balancing Acts. *Cell.* 117, 285–297. doi:10.1016/s0092-8674(04)00343-5

Holt, R. I. G., and Hanley, N. A. (2021). *Overview of Endocrinology" in Essential Endocrinology and Diabetes (Essentials)*. Hoboken, NJ: John Wiley & Sons, 1–39.

Hsiao, E. C., and Gardner, D. G. (2017). *Hormones and Hormone Action" in Greenspan's Basic and Clinical Endocrinology*. New York, NY: McGraw-Hill Education, 1–28.

Hurrell, R., and Egli, I. (2010). Iron Bioavailability and Dietary Reference Values. *Am. J. Clin. Nutr.* 91, 1461S–1467S. doi:10.3945/ajcn.2010.28674f

Iwan, P., Stepniak, J., and Karbownik-Lewinska, M. (2021b). Melatonin Reduces High Levels of Lipid Peroxidation Induced by Potassium Iodate in Porcine Thyroid. *Int. J. Vitam. Nutr. Res.* 91, 271–277. doi:10.1024/0300-9831/a000628

Iwan, P., Stepniak, J., and Karbownik-Lewinska, M. (2021a). Pro-Oxidative Effect of KIO3 and Protective Effect of Melatonin in the Thyroid-Comparison to Other Tissues. *Life* 11, 592. doi:10.3390/life11060592

Karbownik, M., Gitto, E., Lewiński, A., and Reiter, R. J. (2001a). Relative Efficacies of Indole Antioxidants in Reducing Autoxidation and Iron-Induced Lipid Peroxidation in Hamster Testes. *J. Cell. Biochem.* 81, 693–699. doi:10.1002/jcb.1100

Karbownik, M., Reiter, R. J., Cabrera, J., and Garcia, J. J. (2001b). Comparison of the Protective Effect of Melatonin with Other Antioxidants in the Hamster Kidney Model of Estradiol-Induced DNA Damage. *Mutat. Research/Fundamental Mol. Mech. Mutagen.* 474, 87–92. doi:10.1016/s0027-5107(00)00164-0

Karbownik, M., Reiter, R. J., Garcia, J. J., Tan, D. X., Qi, W., and Manchester, L. C. (2000). Melatonin Reduces Rat Hepatic Macromolecular Damage Due to Oxidative Stress Caused by δ-aminolevulinic Acid. *Biochimica Biophysica Acta (BBA) - General Subj.* 1523, 140–146. doi:10.1016/s0304-4165(00)00110-0

Karbownik, M., Stasiak, M., Zasada, K., Zygmunt, A., and Lewinski, A. (2005). Comparison of Potential Protective Effects of Melatonin, Indole-3-Propionic Acid, and Propylthiouracil against Lipid Peroxidation Caused by Potassium Bromate in the Thyroid Gland. *J. Cell. Biochem.* 95, 131–138. doi:10.1002/jcb.20404

Karbownik, M., Stasiak, M., Zygmunt, A., Zasada, K., and Lewiński, A. (2006). Protective Effects of Melatonin and Indole-3-Propionic Acid against Lipid Peroxidation, Caused by Potassium Bromate in the Rat Kidney. *Cell. biochem. Funct.* 24, 483–489. doi:10.1002/cbf.1321

Karbownik-Lewińska, M., and Kokoszko-Bilska, A. (2012). Oxidative Damage to Macromolecules in the Thyroid - Experimental Evidence. *Thyroid. Res.* 5, 25. doi:10.1186/1756-6614-5-25

Kochman, J., Jakubczyk, K., Bargiel, P., and Janda-Milczarek, K. (2021). The Influence of Oxidative Stress on Thyroid Diseases. *Antioxidants* 10, 1442. doi:10.3390/antiox10091442

Kokoszko-Bilska, A., Stepniak, J., Lewinski, A., and Karbownik-Lewinska, M. (2014). Protective Antioxidative Effects of Caffeic Acid Phenethyl Ester (CAPE) in the Thyroid and the Liver Are Similar to Those Caused by Melatonin. *Thyroid. Res.* 7, 5. doi:10.1186/1756-6614-7-5

Koppenol, W. H., and Hider, R. H. (2019). Iron and Redox Cycling. Do's and Don'ts. *Free Radic. Biol. Med.* 133, 3–10. doi:10.1016/j.freeradbiomed.2018.09.022

Lane, D. J. R., Merlot, A. M., Huang, M. L.-H., Bae, D.-H., Jansson, P. J., Sahni, S., et al. (2015). Cellular Iron Uptake, Trafficking and Metabolism: Key Molecules and Mechanisms and Their Roles in Disease. *Biochimica Biophysica Acta (BBA) - Mol. Cell. Res.* 1853, 1130–1144. doi:10.1016/j.bbamcr.2015.01.021

Lewinski, A., and Karbownik, M. (2002). REVIEW. Melatonin and the Thyroid Gland. *Neuro. Endocrinol. Lett.* 23 Suppl 1, 73–78.

Lipinski, B. (2011). Hydroxyl Radical and its Scavengers in Health and Disease. *Oxid. Med. Cell. Longev.* 2011, 809696. doi:10.1155/2011/809696

McCarthy, P. L., Paterno, G. D., and Gillespie, L. L. (2013). Protein Expression Pattern of Human MIER1 Alpha, a Novel Estrogen Receptor Binding Protein. *J. Mol. Hist.* 44, 469–479. doi:10.1007/s10735-012-9478-z

Mogulkoc, R., Baltaci, A. K., Oztekin, E., Aydin, L., and Sivrikaya, A. (2006). Melatonin Prevents Oxidant Damage in Various Tissues of Rats with Hyperthyroidism. *Life Sci.* 79, 311–315. doi:10.1016/j.lfs.2006.01.009

Nakanishi, T., Kuragano, T., Nanami, M., Nagasawa, Y., and Hasuike, Y. (2019). Misdistribution of Iron and Oxidative Stress in Chronic Kidney Disease. *Free Radic. Biol. Med.* 133, 248–253. doi:10.1016/j.freeradbiomed.2018.06.025

Osuna, C., Reiter, R. J., García, J. J., Karbownik, M., Tan, D. X., Calvo, J. R., et al. (2002). Inhibitory Effect of Melatonin on Homocysteine-Induced Lipid Peroxidation in Rat Brain Homogenates. *Pharmacol. Toxicol.* 90, 32–37. doi:10.1034/j.1600-0773.2002.900107.x

Pachucki, J., Wang, D., Christophe, D., and Miot, F. (2004). Structural and Functional Characterization of the Two Human ThOX/Duox Genes and Their 5′-flanking Regions. *Mol. Cell. Endocrinol.* 214, 53–62. doi:10.1016/j.mce.2003.11.026

Reiter, R., Rosales-Corral, S., Tan, D.-X., Acuna-Castroviejo, D., Qin, L., Yang, S.-F., et al. (2017). Melatonin, a Full Service Anti-cancer Agent: Inhibition of Initiation, Progression and Metastasis. *Ijms* 18, 843. doi:10.3390/ijms18040843

Rynkowska, A., Stępniak, J., and Karbownik-Lewińska, M. (2020). Fenton Reaction-Induced Oxidative Damage to Membrane Lipids and Protective Effects of 17β-Estradiol in Porcine Ovary and Thyroid Homogenates. *Ijerph* 17, 6841. doi:10.3390/ijerph17186841

Rynkowska, A., Stępniak, J., and Karbownik-Lewińska, M. (2021). Melatonin and Indole-3-Propionic Acid Reduce Oxidative Damage to Membrane Lipids Induced by High Iron Concentrations in Porcine Skin. *Membranes* 11, 571. doi:10.3390/membranes11080571

Schweizer, U., Chiu, J., and Köhrle, J. (2008). Peroxides and Peroxide-Degrading Enzymes in the Thyroid. *Antioxidants Redox Signal.* 10, 1577–1592. doi:10.1089/ars.2008.2054

Song, Y., Driessens, N., Costa, M., De Deken, X., Detours, V., Corvilain, B., et al. (2007). Roles of Hydrogen Peroxide in Thyroid Physiology and Disease. *J. Clin. Endocrinol. Metabolism* 92, 3764–3773. doi:10.1210/jc.2007-0660

Stępniak, J., Lewiński, A., and Karbownik-Lewińska, M. (2013). Membrane Lipids and Nuclear DNA Are Differently Susceptive to Fenton Reaction Substrates in Porcine Thyroid. *Toxicol. Vitro.* 27, 71–78. doi:10.1016/j.tiv.2012.09.010

Stepniak, J., Lewinski, A., and Karbownik-Lewinska, M. (2021). Oxidative Damage to Membrane Lipids in the Thyroid - No Differences between Sexes. *Drug Chem. Toxicol.* 44, 655–660. doi:10.1080/01480545.2019.1643878

Stepniak, J., Lewinski, A., and Karbownik-Lewinska, M. (2018). Sexual Dimorphism of NADPH Oxidase/H2O2 System in Rat Thyroid Cells; Effect of Exogenous 17β-Estradiol. *Ijms* 19, 4063. doi:10.3390/ijms19124063

Szanto, I., Pusztaszeri, M., and Mavromati, M. (2019). H2O2 Metabolism in Normal Thyroid Cells and in Thyroid Tumorigenesis: Focus on NADPH Oxidases. *Antioxidants* 8, 126. doi:10.3390/antiox8050126

Valko, M., Leibfritz, D., Moncol, J., Cronin, M. T. D., Mazur, M., and Telser, J. (2007). Free Radicals and Antioxidants in Normal Physiological Functions and Human Disease. *Int. J. Biochem. Cell. Biol.* 39, 44–84. doi:10.1016/j.biocel.2006.07.001

Xie, J., Li, Z., and Tang, Y. (2018). Successful Management of Multiple-Systemic Langerhans Cell Histiocytosis Involving Endocrine Organs in an Adult. *Med. Baltim.* 97, e11215. doi:10.1097/md.0000000000011215

Zasada, K., and Karbownik-Lewinska, M. (2015). Comparison of Potential Protective Effects of Melatonin and Propylthiouracil against Lipid Peroxidation Caused by Nitrobenzene in the Thyroid Gland. *Toxicol. Ind. Health.* 31, 1195–1201. doi:10.1177/0748233713491799

Ziech, D., Franco, R., Pappa, A., and Panayiotidis, M. I. (2011). Reactive Oxygen Species (ROS)--induced Genetic and Epigenetic Alterations in Human Carcinogenesis. *Mutat. Research/Fundamental Mol. Mech. Mutagen.* 711, 167–173. doi:10.1016/j.mrfmmm.2011.02.015

Zou, D.-M., and Sun, W.-L. (2017). Relationship between Hepatitis C Virus Infection and Iron Overload. *Chin. Med. J. Engl.* 130, 866–871. doi:10.4103/0366-6999.202737

Conflict of Interest: The authors declare that the research was conducted in the absence of any commercial or financial relationships that could be construed as a potential conflict of interest.

Publisher's Note: All claims expressed in this article are solely those of the authors and do not necessarily represent those of their affiliated organizations, or those of the publisher, the editors, and the reviewers. Any product that may be evaluated in this article, or claim that may be made by its manufacturer, is not guaranteed or endorsed by the publisher.

frontiers | Frontiers in Molecular Biosciences

MINI REVIEW
published: 29 June 2022
doi: 10.3389/fmolb.2022.923794

Librational Dynamics of Spin-Labeled Membranes at Cryogenic Temperatures From Echo-Detected ED-EPR Spectra

Rosa Bartucci[1*†] *and Erika Aloi*[2†]

[1]Department of Chemistry and Chemical Technologies, University of Calabria, Rende (CS), Italy, [2]Molecular Biophysics Laboratory, Department of Physics, University of Calabria, Rende (CS), Italy

OPEN ACCESS

Edited by:
Elena G. Govorunova,
University of Texas Health Science Center at Houston, United States

Reviewed by:
Vasily Oganesyan,
University of East Anglia, United Kingdom
Sergei Dzuba,
Institute of Chemical Kinetics and Combustion (RAS), Russia
Johann P. Klare,
Osnabrück University, Germany
Miroslav Peric,
California State University, Northridge, United States

***Correspondence:**
Rosa Bartucci
rosa.bartucci@fis.unical.it

[†]These authors have contributed equally to this work

Specialty section:
This article was submitted to Lipids, Membranes and Membranous Organelles, a section of the journal Frontiers in Molecular Biosciences

Received: 19 April 2022
Accepted: 19 May 2022
Published: 29 June 2022

Citation:
Bartucci R and Aloi E (2022) Librational Dynamics of Spin-Labeled Membranes at Cryogenic Temperatures From Echo-Detected ED-EPR Spectra. Front. Mol. Biosci. 9:923794. doi: 10.3389/fmolb.2022.923794

Methods of electron spin echo of pulse electron paramagnetic resonance (EPR) spectroscopy are increasingly employed to investigate biophysical properties of nitroxide-labeled biosystems at cryogenic temperatures. Two-pulse echo-detected ED-spectra have proven to be valuable tools to describe the librational dynamics in the low-temperature phases of both lipids and proteins in membranes. The motional parameter, $\alpha^2\tau_C$, given by the product of the mean-square angular amplitude, α^2, and the rotational correlation time, τ_C, of the motion, is readily determined from the nitroxide ED-spectra as well as from the *W*-relaxation rate curves. An independent evaluation of α^2 is obtained from the motionally averaged ^{14}N-hyperfine splitting separation in the continuous wave cw-EPR spectra. Finally, the rotational correlation time τ_C can be estimated by combining ED- and cw-EPR data. In this mini-review, results on the librational dynamics in model and natural membranes are illustrated.

Keywords: model membranes, Na, K-ATPase, spin label, electron paramagnetic resonance, electron spin echo, echo-detected ED-spectra, librations

INTRODUCTION

Steady-state, continuous wave electron paramagnetic resonance (cw-EPR) spectroscopy of nitroxide(NO)-labels ($S = 1/2$, $I = 1$) holds a prominent place in membrane biophysics (Berliner, 1976; Marsh, 1981; Berliner 1998; Hemminga and Berliner, 2007; Marsh, 2019). The success and relevance of spin-label EPR in biomembrane studies is due to the fact that its timescale is optimally sensitive to the nanoseconds and matches the timescale of various molecular motions occurring in membrane components. 9-GHz (X-band) spin-label cw-EPR has notably contributed to the study of the dynamics of proteins and lipids in membranes as well as in reconstituted lipid–protein complexes and in lipid model systems (Borbat et al., 2001; Marsh, 2008; Klare and Steinhoff, 2009; Guzzi and Bartucci, 2015; Sahu and Lorigan, 2021).

Insights into the dynamics of spin-labeled membrane components emerged from the use of electron spin echo (ESE) methods of time-resolved, pulse-EPR spectroscopy (Freed, 2000; Bartucci et al., 2006; Dzuba, 2007). ESE methods are based on the use of resonant microwave power pulse sequences of defined short-time duration, typically 12–64 ns, separated by time intervals in which the microwaves are off, that produce an echo signal at a given delay time (Kevan and Bowman, 1990; Schweiger and Jeschke, 2001). The standard two-pulse sequence, π/2-τ-π-τ-primary echo (**Figure 1A**), allows experiments on the time domain of the interpulse time spacing τ, determined by the transverse phase memory time T_{2M} of the spin-labels, and the two-pulse ESE

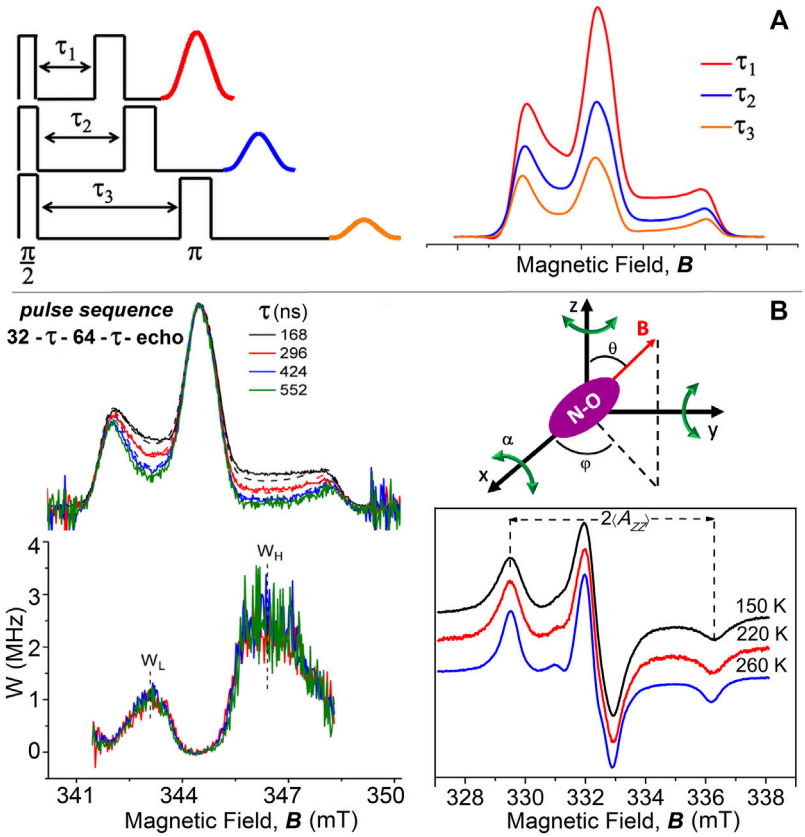

FIGURE 1 | (A) Two-pulse primary echo sequences and echo amplitudes decrease with increasing the interpulse delay time, τ; simulated examples of corresponding echo-detected ED-spectra of chain-labeled nitroxide in membranes. **(B)** Two-pulse (π/2-τ-π with microwave pulse widths of 32 and 64 ns) ED-EPR spectra of 5-PCSL in DPPC bilayers at T = 200 K recorded at incremented interpulse spacings τ (from top to bottom). Solid lines are the normalized experimental spectra, and dashed lines are simulations for isotropic librational motion. Underneath are reported the anisotropic part of the relaxation rate, *W*-spectra, obtained according to **Eq. 1** from pairs of spectra with interpulse separations of $\tau_1 = 168$ and $\tau_2 = 296$ ns, $\tau_1 = 168$ ns and $\tau_2 = 424$ ns, or $\tau_1 = 168$ ns and $\tau_2 = 552$ ns. Schematic illustration of isotropic librational motion: the nitroxide molecule performs oscillations of small angular amplitude, α, about the three nitroxide axes. cw-EPR spectra of 5-PCSL in DPPC bilayers at 150, 220, and 260 K. ED-, W-, and cw-EPR spectra are taken from Aloi et al. (2017).

technique is optimally sensitive to the spin-label dynamics in the nanoseconds timescale. The primary echo, recorded at 2τ from the first pulse, is the result of the refocusing of the spin magnetization after the action of the microwave pulses. The first π/2 pulse flips the magnetization by 90° into the X-Y plane perpendicular to the *Z* direction of the spectrometer magnetic field, B. The spins then dephase during τ, with the time constant T_{2M}, until the inverting *p* pulse reverses the magnetization that will refocus after a time τ producing the echo signal. By integrating the echo while sweeping the static magnetic field, an echo-detected ED-EPR absorption spectrum is obtained, the lineshape of which reflects the angular orientation of the spins. For spin relaxation, the echo amplitude decays exponentially when the interpulse separation τ is incremented, and the corresponding collected ED-spectra show variations in the lineshapes (**Figure 1A**). Such ED-spectra directly reflect the amplitude and the rate of motion of spin-labeled biosystems and contain all the information on their dynamics. Low, cryogenic temperatures are required for ESE-based measurements because spin-labeled T_{2M}-relaxation time is generally too fast to produce detectable echoes at an ambient temperature. Thus, ED-EPR spectra offer a convenient route to study the dynamics of spin-labeled biosystems at low temperatures, for samples cooled with liquid nitrogen down to 77 K or with helium below 77 K. Moreover, low-temperature studies are advantageous to reveal dynamical features that occur also at higher physiological temperatures where they cannot be resolved explicitly because they are hidden by large-amplitude motions.

Here, we review results obtained on the low-temperature dynamics of spin-labeled lipid bilayers and natural Na,K-ATPase membranes from two-pulse ED-EPR spectra.

Two-Pulse ED-EPR Spectra of Nitroxide Labels in Membranes

The pioneering work of Millhauser and Freed, (1984) showed the sensitivity of the two-pulse echo-induced EPR spectrum for each value of interpulse separation time τ to variation across the spectrum of the transverse relaxation time. With this ESE

technique, the structure and dynamics of cholestane spin-label in oriented lipid multilayers were studied (Kar et al., 1985). Two-pulse ED-spectra have been used by Dzuba et al. (1992), Dzuba (1996), Dzuba (2000), and Kirilina et al. (2001) to investigate the motion of spin-probes in glassy media. The lineshapes, revealing anisotropic phase relaxation, showed a decrease of the amplitudes in the intermediate spectral regions at low and high field with increasing τ. The ED-spectra have been simulated by assuming the occurrence of librational motion, that is, an orientational molecular motion consisting of fast, low-amplitude oscillations near an equilibrium position.

An analogous dependence on τ has been observed later for the ED-spectra of chain-labeled lipids in model membranes (Bartucci et al., 2003; Erilov et al., 2004a; Erilov et al., 2004b). In these spectra, the regions at intermediate low and high fields, which correspond to the maximum variation of spin orientation with the static magnetic field, relax faster than the others, and the intensities decrease systematically with increasing the interpulse spacing, τ. Minor changes are instead observed in the outer peaks, which correspond to stationary turning points (**Figure 1B**).

The ED-EPR spectra of lipid spin-labels in bilayers are successfully simulated according to the so-called "isotropic" model of librations (Erilov et al., 2004b). The model assumes that librations consist of independent and simultaneous rapid oscillations, each of small angular amplitude α and with correlation time τ_C, around each of the three perpendicular *X*-, *Y*-, and *Z*-axes of nitroxide (**Figure 1B**). For fast motion of small amplitude, that is, $\Delta\omega^2\tau_c^2 << 1$, and for a polar orientation θ, φ of the magnetic field, *B*, relative to the nitroxide *X*-, *Y*-, and *Z*-axes, the amplitude of a two-pulse echo decay is approximatively described by $E(2\tau,\theta,\varphi) \approx \exp(-2\tau/T_{2M}) \approx \exp(-2\Delta\omega^2(\theta,\varphi)\tau_C\tau)$, where $\Delta\omega$ is the shift in resonance frequency that is induced by the motion and τ_C is the rotational correlation time (Dzuba et al., 1992; Dzuba, 1996). This term is explicitly included as a factor in the echo-detected EPR lineshape, $ED(2\tau, B)$, details of which are reported in Erilov et al. (2004b). From spectral simulations, it is possible to extract the motional parameter, $\alpha^2\tau_C$, given by the product of the mean-square angular amplitude, α^2, and the rotational correlation time, τ_C, of the librational motion.

An alternative scheme of analyzing the dependence of the ED-EPR lineshapes on librational dynamics is given by the *W*-relaxation spectra. They are obtained from the experimental ED-spectra recorded at two different values, τ_1 and τ_2, of the interpulse delay by using the relation (Erilov et al., 2004b):

$$W(B,\tau_1,\tau_2) = \ln\left[\frac{ED(2\tau_1,B)}{ED(2\tau_2,B)}\right]\cdot\frac{1}{2(\tau_2-\tau_1)}. \quad (1)$$

The *W*-spectra evaluated for different pairs of τ-values coincide within the noise level (**Figure 1B**), showing exponential anisotropic spin relaxation as a function of τ (especially on the low-field side), as expected for the isotropic model of librations. The relaxation rate *W*-curves are characterized by the maximum values, W_L and W_H, determined in the low- and high-field regions, respectively, of the ED-spectra. The difference in intensity at the two positions arises simply from the different inherent sensitivities of the two spectral regions to spin relaxation.

The relaxation rate W_L or W_H can also be used to characterize the librational dynamics in membranes. Indeed, they are related to the motional parameter $\alpha^2\tau_c$ *via* the calibration constant, C_{cal}, established from simulations. For example, W_L or $W_H = (C_{cal}\ rad^{-2}s^{-2}) \times \alpha^2\tau_c$ (Erilov et al., 2004b).

To fully describe the librational motion of spin-labels in membranes, it is desirable to know the mean-square angular amplitude, α^2, and the rotational correlation time, τ_C, of the motion. An independent evaluation of α^2 is obtained by acquiring spin-label cw-EPR spectra at the same low temperatures as those of ED-spectra and measuring the motionally averaged ^{14}N-hyperfine splittings, $2A_{zz}$, that is, the separation between the two outer spectral peaks (**Figure 1B**). For small amplitude librations around the *X*-axis, α^2 can be obtained from the relation: $A_{zz} = A_{zz} - (A_{zz} - A_{xx})\alpha^2$, where A_{xx} and A_{zz} are the principal values of the hyperfine interaction tensor (Van et al., 1974; Dzuba, 2000). A_{xx} is obtained from the literature (Marsh, 2019), whereas A_{zz} is derived by linear extrapolation of $2A_{zz}$ vs. temperature data to zero temperature. From **Figure 1B**, it is evident that $2A_{zz}$ decreases with the temperature and, according to the aforementioned expression, to this corresponds an increase of α^2 due to librations. Finally, the correlation time τ_C of librations is evaluated from the quotient of the pulsed $\alpha^2\tau_c$ and the continuous wave α^2 data. In this way, combining two-pulse ED-EPR and cw-EPR spectra, the low-temperature librational dynamics has been fully characterized in a number of spin-labeled membranes and proteins (De Simone et al., 2007; Bartucci et al., 2008; Scarpelli et al., 2011; Guzzi et al., 2012).

An alternative approach to analyze ED-spectra is to evaluate the ratio of the echo amplitude at the two field positions with the largest and smallest anisotropies. For molecular librations, the resulting exponential decay rate W_{anis} is proportional to $\alpha^2\tau_C$ (Isaev and Dzuba, 2008; Golysheva et al., 2018; Golysheva and Dzuba, 2020).

Segmental Chain Librations of Lipids in Model Membranes

In this section, we present results on the segmental librations of chain-labeled lipids in the low-temperature phases of model membranes. Bilayers composed of the most prevalent types of lipids present in the cell membrane of the three domains of life, that is, *Eukarya*, *Bacteria*, and *Archaea*, are considered (van Meer et al., 2008; Lombard et al., 2012). They include bilayers of diacylglycerophosphocholine and dialkylglycerophosphocholine lipids which consist of a phosphocholine (PC) polar head group and an apolar region formed by two fatty acid chains covalently bound to a glycerol moiety through ester or ether linkages, respectively (**Figure 2A**). For the ester-linked diacyl-PC bilayer forming lipids, we used dipalmitoylphosphatidylcholine (DPPC) and the unsaturated palmitoyloleoylphosphatidylcholine (POPC) and dioleoylphosphatidylcholine (DOPC) lipids. For ether-linked lipids, we used dihexadecyl phosphocholine (DHPC), which is analogous to DPPC.

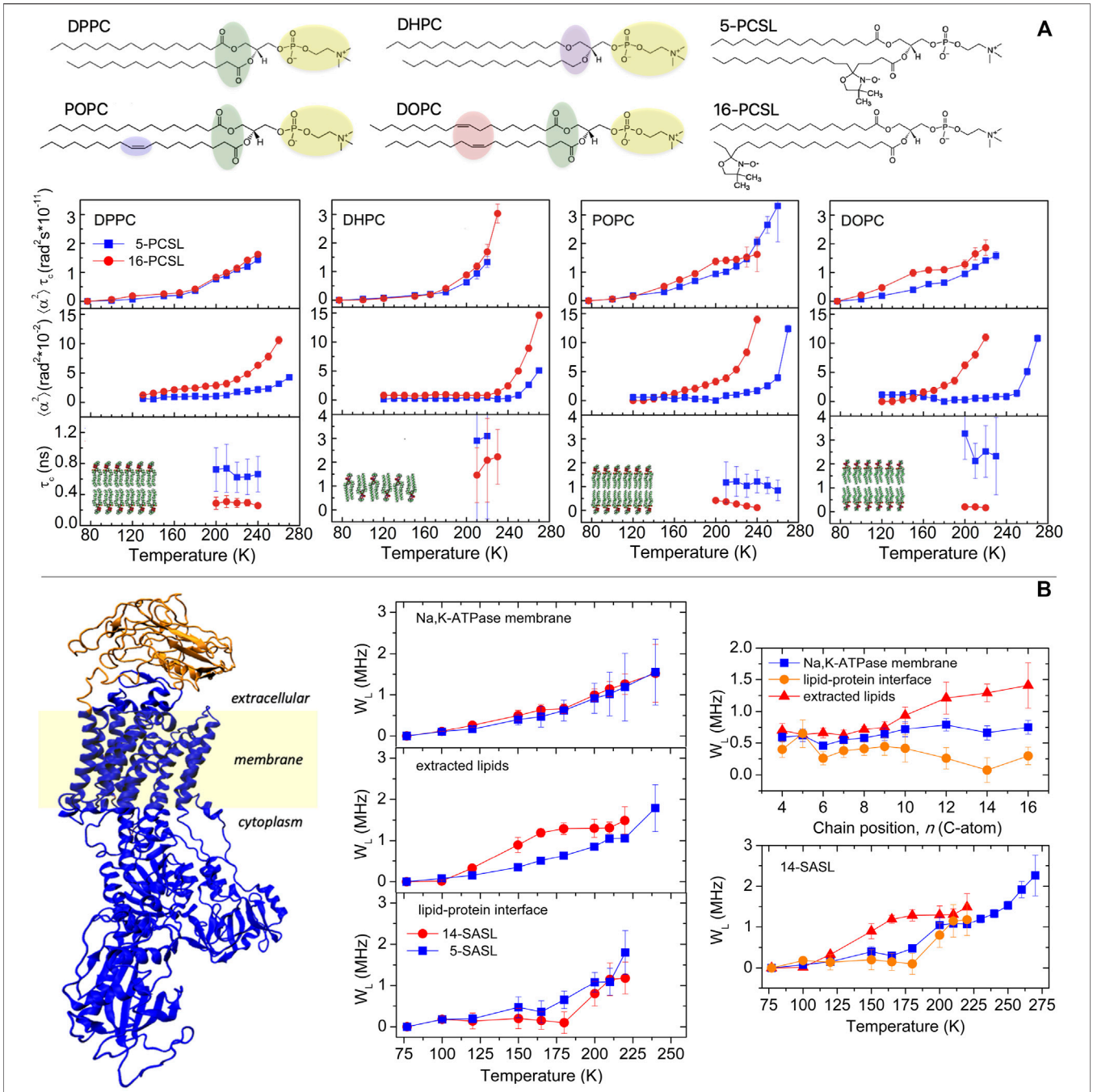

FIGURE 2 | (A) Chemical structure of the lipids DPPC, DHPC, POPC, and DOPC and of the chain-labeled phosphatidylcholine spin-label 5-PCSL and 16-PCSL. Characterization of the segmental librational motion in DPPC, DHPC, POPC, and DOPC membranes spin-labeled with 5- and 16-PCSL *via* the temperature dependence of the (i) amplitude-correlation time product, $\alpha^2\tau_C$, (ii) mean-square angular amplitude, α^2, and (iii) correlation time, τ_C. Error bars for α^2 are within the symbols. Data for DPPC and DHPC are adapted from Aloi et al. (2017), and those for POPC and DOPC are from Aloi et al. (2019). **(B)** Na,K-ATPase membrane: crystal structure of the enzyme (PDB ID 4RES (Laursen et al., 2015)) and schematic bilayer region. Temperature dependence of the relaxation rate W_L for 5- and 14-SASL in the Na,K-ATPase membrane, in bilayers of extracted lipids and at the lipid–protein interface. Chain positional profile, that is, W_L vs. n, at T = 180 K of n-SASL in Na,K-ATPase membranes, in bilayers of the extracted lipids and at the lipid–protein interface. Temperature dependence of W_L for 14-SASL in bilayers of extracted lipids and at the lipid–protein interface and for 5-MSL in the Na,K-ATPase protein. Data are adapted from Guzzi et al. (2015).

From a biophysical standpoint, the single species lipid membranes show different properties and thermotropic phase behavior (Marsh, 2012). Notably, DPPC and DHPC form bilayers with gel to fluid main phase transition temperature T_m ca. 315 K but DHPC spontaneously forms lamellae gel phase with interdigitated chains, whereas DPPC forms noninterdigitated

gel phase bilayers. POPC and DOPC, for the presence of cis-bonds in the lipid chain, form low-T_m bilayers, T_m being ca. 271 K for POPC and ca. 253 K for DOPC. For EPR measurements, the bilayers were spin-labeled with phosphatidylcholine lipids bearing the nitroxide group either at the 5th or at the 16th carbon atom positions of the *sn*-2 chain, namely, 5- and 16-PCSL, to probe, respectively, the first acyl chain segments and the terminal chain region of the hydrocarbon zone of the bilayers (**Figure 2A**). Lipids and spin-labeled lipids were purchased from Avanti Polar Lipids (Birmingham, AL).

Fast (τ_C from subnanoseconds to nanoseconds) librations of small amplitude ($\alpha < 20^{\circ}$) have been detected in DPPC, DHPC, POPC, and DOPC membranes in the low-temperature range of 77–270 K. However, the distinctive features of the lipid acyl chains and the different molecular chain packing between the membranes affect the characteristics of the librational motion.

A temperature-dependent increase of the motional parameter $\alpha^2\tau_C$ is seen in any lipid matrix, indicating that the segmental chain librations intensify with the temperature. In DPPC and DHPC assemblies, the librational oscillations acquire an appreciable intensity from 190 K onward, much more rapidly for interdigitated DHPC lamellae, especially for 16-PCSL. In unsaturated POPC and DOPC bilayers, the librational motion 1) is activated from the lowest temperatures; 2) is more intense in DOPC than in POPC bilayers; 3) in DOPC bilayers, it is more intense at the chain termini in the middle of the bilayers (probed by 16-PCSL) than at the first acyl chain segments close to the polar/apolar interfaces (probed by 5-PCSL) at any temperature (**Figure 2A**).

The linear and fully saturated acyl chains in DPPC and the interdigitated chains in DHPC impart a well compact and regular packing density to the lipid lamellae in the frozen state which restricts the librational dynamics, at least in the low-temperature regime. In contrast, the presence of double bonds in the hydrocarbon chain of the unsaturated lipids confers a loosened packing density to the bilayers which favors the segmental librations. In agreement with the results in **Figure 2A**, data on relaxation rates of stearic acid doxyl-labeled along the chain indicated more freedom of segmental chain librations in unsaturated POPC and DOPC bilayers compared to saturated DPPC bilayers (Surovtsev et al., 2012; Golysheva et al., 2018; Golysheva and Dzuba, 2020).

As seen for $\alpha^2\tau_C$, the mean-square angular amplitude also increases with temperature in all model membranes (**Figure 2A**). In frozen bilayers of DPPC, POPC, and DOPC with noninterdigitated chains, α^2 depends on the label position, n, along the lipid chain: the amplitude becomes larger on moving from the first acyl chain segments (probed by 5-PCSL) toward the chain termini at the bilayer midplane (probed by 16-PCSL). These results are expected for noninterdigitated lipid bilayers and are in agreement with pulsed EPR results in mixtures of DPPC and equimolar amount of cholesterol and in model membranes composed of lipids extracted from natural membranes (Bartucci et al., 2003; Erilov et al., 2004b; Isaev and Dzuba, 2008; Guzzi et al., 2015). The root-mean-square angular amplitudes in unsaturated bilayers are among the highest obtained. Recently, it has been evidenced by pulse-EPR that the high mobility of unsaturated bilayers is comparable to that of regions of intrinsically disordered proteins (Maslennikova et al., 2021).

In DHPC lamellae with interdigitated chains, the librations are restricted to small angular amplitude at both chain positions of labeling in the low-temperature regime. Only on entering the higher temperature regime, the angular amplitudes increase and are larger at the chain termini than at the beginning of the chain comparable to that in DPPC. Similar results have been obtained in lamellae with interdigitated chains formed by mixtures of DPPC and Lyso-palmitoilphosphatidylcholine or induced in DPPC by ethanol (Aloi and Bartucci, 2019). The behavior of the chain-labeled lipids in DHPC is consistent with the interdigitated phase in which the positional isomers at the chain termini are motionally restricted to an extent comparable to those in proximity of the polar/apolar interface (Boggs et al., 1989; Bartucci et al., 1993; Oranges et al., 2018). At highest temperatures, it is likely that 16-PCSL acquires significant freedom of motion relative to 5-PCSL since it is located in the interfacial region where the polar heads are spaced apart by interdigitation.

From **Figure 2A**, it can be seen that the rotational correlation time lies on the subnanosecond–nanosecond timescale, indicating that fast rapid segmental chain oscillations are detected in the considered model bilayers. On the whole, the differences in the librational dynamics in the various bilayers are attributable mostly to the variations in the angular amplitude rather than in the rotational correlation time. It is interesting to point out that the temperature dependence of α^2 shows close similarities with that of the mean-square atomic displacement r^2 measured in neutron studies (Fenimore et al., 2004; Dzuba, 2007; Golysheva et al., 2017; Peters et al., 2017; Golysheva et al., 2018; Aloi and Bartucci, 2022). Both curves show a rapid increase at a temperature in the range of 200 K ascribed to the dynamical transition from harmonic to anharmonic diffusive motion.

Librations in Na,K-ATPase Membranes

Membranous Na,K-ATPase is a complex transport system. The lipid bilayer sector is spanned by the sodium pump, a large integral protein (**Figure 2B**) that is responsible for maintenance of the electrochemical gradients of Na^+ and K^+ across the membrane in eukaryotes. Specific regions within the Na,K-ATPase membrane, including the protein, the cationic binding site, and the lipid bilayer environment, have been recently studied by cw- and pulse-EPR of spin-labels and spin-labeled lipids (Guzzi et al., 2009; Guzzi et al., 2015; Guo et al., 2018; Aloi et al., 2021).

The hydrophobic bilayer region of the sodium pump membrane has been investigated exploiting the affinity of ionized chain-labeled stearic acids (*n*-SASL) for the membrane (Bartucci et al., 2014; Guzzi et al., 2015). *n*-SASL was either purchased from Avanti Polar Lipids or synthesized as described elsewhere (Marsh and Watts, 1982). The studies in these samples include measurements of both the Na,K-ATPase membranes and the lipid model systems formed with the extracted membrane lipids and determination of the data at the lipid–protein interface as described in Bartucci et al. (2014) and Guzzi et al. (2015).

The temperature-dependent increase of the W_L-relaxation parameter in Na,K-ATPase membranes is rather similar to that at the lipid–protein interface: the mobility is more evident for T > 180 K and independent on the label position (**Figure 2B**). It differs notably from that in bilayers of extracted lipids, where mobility is evident from a lower temperature (120 K) and more intense at the end of the chain (i.e., data for 14-SASL) than at the top (i.e., data for 5-SASL) (Guzzi et al., 2015). These features have been confirmed by the positional dependence of the transmembrane librational dynamics. Indeed, the profile of W_L vs. label position is almost flat for lipid chains at the protein interface and in the Na,K-ATPase membrane where W_L remains at a relatively low level, comparable to that at the top of the chain in the bilayer lipids. In the lipid bilayers, W_L is larger toward the end of the chain, with a transition in the region of C10-C12.

Insights into the low-temperature dynamics of Na,K-ATPase have been gained from a comparison of the librational fluctuations of the extracted lipids and interfacial lipids with those of the protein alone studied with a maleimide spin-labels (5-MSL) covalently attached to cysteine–SH residues (Guzzi et al., 2009; Guzzi et al., 2015). The temperature dependence of the W_L-rates for interfacial lipids resembles that of protein side-chains, but not that for the bilayer lipids (**Figure 2B**). Librational motions of lipids at the protein interface are coupled both to those of the protein and to those of the bilayer lipids: protein and membrane lipids communicate *via* the interfacial lipids. It is most likely that these librational oscillations could drive transitions between the different conformational substates in Na,K-ATPase, which are frozen at lower temperatures but contribute to the pathways between the principal enzymatic intermediates at higher temperatures.

CONCLUSION

In this mini-review, we have illustrated the potential of ESE spectroscopy for the study of the nanosecond dynamics in bilayers and Na,K-ATPase membranes at cryogenic temperatures *via* two-pulse ED-spectra. Fast, low-amplitude librations that are readily detected and characterized at cryogenic temperatures must be present in the higher temperature phases of biomembranes, in addition to larger-scale rotational motions. The low, cryogenic temperatures contribute to highlight specific structural, dynamic, and kinetics features of biosystems, and spin-label pulse-EPR results deepen the biophysical characterization of membranes that are normally studied at higher temperatures. Therefore, ESE methods are increasingly used for studying complex macromolecular assemblies.

AUTHOR CONTRIBUTIONS

All authors listed have made a substantial, direct, and intellectual contribution to the work and approved it for publication.

REFERENCES

Aloi, E., and Bartucci, R. (2022). Influence of Hydration on Segmental Chain Librations and Dynamical Transition in Lipid Bilayers. *Biochimica Biophysica Acta (BBA) - Biomembr.* 1864, 183805. doi:10.1016/j.bbamem.2021.183805

Aloi, E., and Bartucci, R. (2019). Interdigitated Lamellar Phases in the Frozen State: Spin-Label CW- and FT-EPR. *Biophys. Chem.* 253, 106229. doi:10.1016/j.bpc.2019.106229

Aloi, E., Guo, J. -H., Guzzi, R., Jiang, R. -W., Ladefoged, L. K., Marsh, D., et al. (2021). Geometry and Water Accessibility of the Inhibitor Binding Site of Na^+-Pump: Pulse- and CW-EPR Study. *Biophys. J.* 120, 2679–2690.

Aloi, E., Guzzi, R., and Bartucci, R. (2019). Unsaturated Lipid Bilayers at Cryogenic Temperature: Librational Dynamics of Chain-Labeled Lipids from Pulsed and CW-EPR. *Phys. Chem. Chem. Phys.* 21, 18699–18705. doi:10.1039/c9cp03318a

Aloi, E., Oranges, M., Guzzi, R., and Bartucci, R. (2017). Low-Temperature Dynamics of Chain-Labeled Lipids in Ester- and Ether-Linked Phosphatidylcholine Membranes. *J. Phys. Chem. B* 121, 9239–9246. doi:10.1021/acs.jpcb.7b07386

Bartucci, R., Erilov, D. A., Guzzi, R., Sportelli, L., Dzuba, S. A., and Marsh, D. (2006). Time-resolved Electron Spin Resonance Studies of Spin-Labelled Lipids in Membranes. *Chem. Phys. Lipids* 141, 142–157. doi:10.1016/j.chemphyslip.2006.02.009

Bartucci, R., Guzzi, R., De Zotti, M., Toniolo, C., Sportelli, L., and Marsh, D. (2008). Backbone Dynamics of Alamethicin Bound to Lipid Membranes: Spin-Echo Electron Paramagnetic Resonance of TOAC-Spin Labels. *Biophysical J.* 94, 2698–2705. doi:10.1529/biophysj.107.115287

Bartucci, R., Guzzi, R., Esmann, M., and Marsh, D. (2014). Water Penetration Profile at the Protein-Lipid Interface in Na,K-ATPase Membranes. *Biophysical J.* 107, 1375–1382. doi:10.1016/j.bpj.2014.07.057

Bartucci, R., Guzzi, R., Marsh, D., and Sportelli, L. (2003). Chain Dynamics in the Low-Temperature Phases of Lipid Membranes by Electron Spin-Echo Spectroscopy. *J. Magnetic Reson.* 162, 371–379. doi:10.1016/s1090-7807(03)00049-1

Bartucci, R., Pali, T., and Marsh, D. (1993). Lipid Chain Motion in an Interdigitated Gel Phase: Conventional and Saturation Transfer ESR of Spin-Labeled Lipids in Dipalmitoylphosphatidylcholine-Glycerol Dispersions. *Biochemistry* 32, 274–281. doi:10.1021/bi00052a035

Berliner, L. J. (1976). *Theory and Applications*. New York: Academic Press.Spin Labeling

Berliner, L. J. (1998). Spin Labelling: The Next Millenium. *Biol. Magn. Reson.*, 14.

Boggs, J. M., Rangaraj, G., and Watts, A. (1989). Behavior of Spin Labels in a Variety of Interdigitated Lipid Bilayers. *Biochimica Biophysica Acta (BBA) - Biomembr.* 981, 243–253. doi:10.1016/0005-2736(89)90034-5

Borbat, P. P., Costa-Filho, A. J., Earle, K. A., Moscicki, J. K., and Freed, J. H. (2001). Electron Spin Resonance in Studies of Membranes and Proteins. *Science* 291, 266–269. doi:10.1126/science.291.5502.266

De Simone, F., Guzzi, R., Sportelli, L., Marsh, D., and Bartucci, R. (2007). Marsh., D., Bartucci, RElectron Spin-Echo Studies of Spin-Labelled Lipid Membranes and Free Fatty Acids Interacting with Human Serum Albumin. *Biochimica Biophysica Acta (BBA) - Biomembr.* 1768, 1541–1549. doi:10.1016/j.bbamem.2007.02.019

Dzuba, S. A. (2000). Libration Motion of Guest Spin Probe Molecules in Organic Glasses: CW EPR and Electron Spin Echo Study. *Spectrochimica Acta Part A Mol. Biomol. Spectrosc.* 56, 227–234. doi:10.1016/s1386-1425(99)00234-6

Dzuba, S. A. (1996). Librational Motion of Guest Spin Probe Molecules in Glassy Media. *Phys. Lett. A* 213, 77–84. doi:10.1016/0375-9601(96)00081-3

Dzuba, S. A. (2007). Pulsed EPR in the Method of Spin Labels and Probes. *Russ. Chem. Rev.* 76, 699–713. doi:10.1070/rc2007v076n08abeh003722

Dzuba, S. A., Tsvetkov, Y. D., Yu, A. G., and Maryasov, A. G. (1992). Echo-induced EPR Spectra of Nitroxides in Organic Glasses: Model of Orientational Molecular Motions Near Equilibrium Position. *Chem. Phys. Lett.* 188, 217–222. doi:10.1016/0009-2614(92)90012-c

Erilov, D. A., Bartucci, R., Guzzi, R., Marsh, D., Dzuba, S. A., and Sportelli, L. (2004a). Echo-detected Electron Paramagnetic Resonance Spectra of Spin-Labeled Lipids in Membrane Model Systems. *J. Phys. Chem. B* 108, 4501–4507. doi:10.1021/jp037249y

Erilov, D. A., Bartucci, R., Guzzi, R., Marsh, D., Dzuba, S. A., and Sportelli, L. (2004b). Librational Motion of Spin-Labeled Lipids in High-Cholesterol Containing Membranes from Echo-Detected EPR Spectra. *Biophysical J.* 87, 3873–3881. doi:10.1529/biophysj.104.046631

Fenimore, P. W., Frauenfelder, H., McMahon, B. H., and Young, R. D. (2004). Bulk-solvent and Hydration-Shell Fluctuations, Similar to α- and β-fluctuations in Glasses, Control Protein Motions and Functions. *Proc. Natl. Acad. Sci. U.S.A.* 101, 14408–14413. doi:10.1073/pnas.0405573101

Freed, J. H. (2000). New Technologies in Electron Spin Resonance. *Annu. Rev. Phys. Chem.* 51, 655–689. doi:10.1146/annurev.physchem.51.1.655

Golysheva, E. A., De Zotti, M., Toniolo, C., Formaggio, F., and Dzuba, S. A. (2018). Low-temperature Dynamical Transition in Lipid Bilayers Detected by Spin-Label ESE Spectroscopy. *Appl. Magn. Reson* 49. doi: doi:10.1007/s00723-018-1066-2

Golysheva, E. A., and Dzuba, S. A. (2020). Lipid Chain Mobility and Packing in DOPC Bilayers at Cryogenic Temperatures. *Chem. Phys. Lipids* 226, 104817. doi:10.1016/j.chemphyslip.2019.104817

Golysheva, E. A., Shevelev, G. Y., and Dzuba, S. A. (2017). Dynamical Transition in Molecular Glasses and Proteins Observed by Spin Relaxation of Nitroxide Spin Probes and Labels. *J. Chem. Phys.* 147, 064501. doi:10.1063/1.4997035

Guo, J. H., Jiang, R. W., Andersen, J. L., Esmann, M., and Fedosova, N. U. (2018). Spin-labeled Derivatives of Cardiotonic Steroids as Tools for Characterization of the Extracellular Entrance to the Binding Site on Na + ,K + - ATP Ase. *FEBS J.* 285, 2292–2305. doi:10.1111/febs.14480

Guzzi, R., and Bartucci, R. (2015). Electron Spin Resonance of Spin-Labeled Lipid Assemblies and Proteins. *Archives Biochem. Biophysics* 580, 102–111. doi:10.1016/j.abb.2015.06.015

Guzzi, R., Bartucci, R., Esmann, M., and Marsh, D. (2015). Lipid Librations at the Interface with the Na,K-ATPase. *Biophysical J.* 108, 2825–2832. doi:10.1016/j.bpj.2015.05.004

Guzzi, R., Bartucci, R., Sportelli, L., Esmann, M., and Marsh, D. (2009). Conformational Heterogeneity and Spin-Labeled –SH Groups: Pulsed EPR of Na,K-ATPase. *Biochemistry* 48, 8343–8354. doi:10.1021/bi900849z

Guzzi, R., Rizzuti, B., and Bartucci, R. (2012). Dynamics and Binding Affinity of Spin-Labeled Stearic Acids in β-Lactoglobulin: Evidences from EPR Spectroscopy and Molecular Dynamics Simulation. *J. Phys. Chem. B* 116, 11608–11615. doi:10.1021/jp3074392

Hemminga, M. A., and Berliner, L. J. (2007). *ESR Spectroscopy in Membrane Biophysics*. New York: Springer.

Isaev, N. P., and Dzuba, S. A. (2008). Fast Stochastic Librations and Slow Rotations of Spin Labeled Stearic Acids in a Model Phospholipid Bilayer at Cryogenic Temperatures. *J. Phys. Chem. B* 112, 13285–13291. doi:10.1021/jp805794c

Kar, L., Ney-Igner, E., and Freed, J. H. (1985). Electron Spin Resonance and Electron-Spin-Echo Study of Oriented Multilayers of L Alpha-Dipalmitoylphosphatidylcholine Water Systems. *Biophysical J.* 48, 569–595. doi:10.1016/s0006-3495(85)83814-5

Kevan, L., and Bowman, M. K. (1990). *Modern Pulsed and Continuous-Wave Electron Spin Resonance*. New York: Wiley.

Kirilina, E. P., Dzuba, S. A., Maryasov, A. G., and Tsvetkov, Y. D. (2001). Librational Dynamics of Nitroxide Molecules in a Molecular Glass Studied by Echo-Detected EPR. *Appl. Magn. Reson.* 21, 203–221. doi:10.1007/bf03162452

Klare, J. P., and Steinhoff, H.-J. (2009). Spin Labeling EPR. *Photosynth. Res.* 102, 377–390. doi:10.1007/s11120-009-9490-7

Laursen, M., Gregersen, J. L., Yatime, L., Nissen, P., and Fedosova, N. U. (2015). Structures and Characterization of Digoxin- and Bufalin-Bound Na + ,K + -ATPase Compared with the Ouabain-Bound Complex. *Proc. Natl. Acad. Sci. U.S.A.* 112, 1755–1760. doi:10.1073/pnas.1422997112

Lombard, J., López-García, P., and Moreira, D. (2012). The Early Evolution of Lipid Membranes and the Three Domains of Life. *Nat. Rev. Microbiol.* 10, 507–515. doi:10.1038/nrmicro2815

Marsh, D. (2012). *Handbook of Lipid Bilayers*. New York: Taylor & Francis.

Marsh, D. (2019). *Spin-Label Electron Paramagnetic Resonance Spectroscopy*. Boca Raton, FL: CRC Press.

Marsh, D. (2008). Electron Spin Resonance in Membrane Research: Protein-Lipid Interactions. *Methods* 46, 83–96. doi:10.1016/j.ymeth.2008.07.001

Marsh, D. (1981). "Electron Spin Resonance: Spin Labels," in *Biochemistry and Biophysics. Membrane SpectroscopyMolecular BiologyE. Grell* (Berlin, Heidelberg, New York: Springer-Verlag), 31, 51–142. doi:10.1007/978-3-642-81537-9_2

Marsh, D., and Watts, A. (1982). Spin-labeling and Lipid-Protein Interactions in Membranes. In *Lipid-Protein Interactions,*. Editors P. C. Jost and O. H. Griffith (New York: Wiley-Interscience), 2, 53–126.

Maslennikova, N. A., Golysheva, E. A., and Dzuba, S. A. (2021). Evidence for an Ordering Transition Near 120 K in an Intrinsically Disordered Protein, Casein. *Molecules* 26, 5971. doi:10.3390/molecules26195971

Millhauser, G. L., and Freed, J. H. (1984). Two-dimensional Electron Spin Echo Spectroscopy and Slow Motions. *J. Chem. Phys.* 81, 37–48. doi:10.1063/1.447316

Oranges, M., Guzzi, R., Marsh, D., and Bartucci, R. (2018). Ether-linked Lipids: Spin-Label EPR and Spin Echoes. *Chem. Phys. Lipids* 212, 130–137. doi:10.1016/j.chemphyslip.2018.01.010

Sahu, I. D., and Lorigan, G. A. (2021). Probing Structural Dynamics of Membrane Proteins Using Electron Paramagnetic Resonance Spectroscopic Techniques. *Biophysica* 1, 106–125. doi:10.3390/biophysica1020009

Scarpelli, F., Bartucci, R., Sportelli, L., and Guzzi, R. (2011). Solvent Effect on Librational Dynamics of Spin-Labelled Haemoglobin by ED- and CW-EPR. *Eur. Biophys. J.* 40, 273–279. doi:10.1007/s00249-010-0644-5

Schweiger, A., and Jeschke, G. (2001). *Principles of Pulse Electron Paramagnetic Resonance*. Oxford: Oxford University Press.

Surovtsev, N. V., Ivanisenko, N. V., Kirillov, K. Y., and Dzuba, S. A. (2012). Low-temperature Dynamical and Structural Properties of Saturated and Monounsaturated Phospholipid Bilayers Revealed by Raman and Spin-Label EPR Spectroscopy. *J. Phys. Chem. B* 116, 8139–8144. doi:10.1021/jp3038895

van Meer, G., Voelker, D. R., and Feigenson, G. W. (2008). Membrane Lipids: where They Are and How They Behave. *Nat. Rev. Mol. Cell. Biol.* 9, 112–124. doi:10.1038/nrm2330

Van, S. P., Birrell, G. B., and Griffith, O. H. (1974). Rapid Anisotropic Motion of Spin Labels. Models for Motion Averaging of the ESR Parameters. *J. Magnetic Reson. (1969)* 15, 444–459. doi:10.1016/0022-2364(74)90147-4

Conflict of Interest: The authors declare that the research was conducted in the absence of any commercial or financial relationships that could be construed as a potential conflict of interest.

Publisher's Note: All claims expressed in this article are solely those of the authors and do not necessarily represent those of their affiliated organizations, or those of the publisher, the editors, and the reviewers. Any product that may be evaluated in this article, or claim that may be made by its manufacturer, is not guaranteed or endorsed by the publisher.

frontiers | Frontiers in Molecular Biosciences

BRIEF RESEARCH REPORT
published: 15 July 2022
doi: 10.3389/fmolb.2022.895911

Toward a Topology-Based Therapeutic Design of Membrane Proteins: Validation of NaPi2b Topology in Live Ovarian Cancer Cells

Leisan Bulatova[1], Daria Savenkova[1], Alsina Nurgalieva[1], Daria Reshetnikova[1], Arina Timonina[1], Vera Skripova[1], Mikhail Bogdanov[1,2]† and Ramziya Kiyamova[1]*†*

[1]Research Laboratory "Biomarker", Institute of Fundamental Medicine and Biology, Kazan Federal University, Kazan, Russian Federation, [2]Department of Biochemistry and Molecular Biology, McGovern Medical School, the University of Texas Health Science Center, Houston, TX, United States

OPEN ACCESS

Edited by:
Isabel María López-Lara, National Autonomous University of Mexico, Mexico

Reviewed by:
Stéphanie Lebreton, Institut Pasteur, France
Shivani Sharda, Amity University, India
Russell Thomson, Hunter College (CUNY), United States

***Correspondence:**
Ramziya Kiyamova
kiyamova@mail.ru
Mikhail Bogdanov
mikhail.v.bogdanov@uth.tmc.edu

†These authors have contributed equally to this work and share senior authorship

Specialty section:
This article was submitted to Lipids, Membranes and Membranous Organelles, a section of the journal Frontiers in Molecular Biosciences

Received: 14 March 2022
Accepted: 22 June 2022
Published: 15 July 2022

Citation:
Bulatova L, Savenkova D, Nurgalieva A, Reshetnikova D, Timonina A, Skripova V, Bogdanov M and Kiyamova R (2022) Toward a Topology-Based Therapeutic Design of Membrane Proteins: Validation of NaPi2b Topology in Live Ovarian Cancer Cells. Front. Mol. Biosci. 9:895911. doi: 10.3389/fmolb.2022.895911

NaPi2b is a sodium-dependent phosphate transporter that belongs to the SLC34 family of transporters which is mainly responsible for phosphate homeostasis in humans. Although NaPi2b is widely expressed in normal tissues, its overexpression has been demonstrated in ovarian, lung, and other cancers. A valuable set of antibodies, including L2 (20/3) and MX35, and its humanized versions react strongly with an antigen on the surface of ovarian and other carcinoma cells. Although the topology of NaPi2b was predicted *in silico*, no direct experimental data are available for the orientation of NaPi2b extracellular domains in cancer cells. The presented results of antibody mapping of untagged NaPi2b in live ovarian carcinoma cells OVCAR-4 provide a platform for current and future epitope-based cancer therapies and serological diagnostics.

Keywords: SLC34A2, NaPi2b, MX35 antigen, topology, ECD, monoclonal antibody, ovarian cancer

INTRODUCTION

Membrane proteins represent at least 30% of all currently sequenced genomes and 60% of known drug targets and are therefore of great interest in understanding and treating diseases (Santos et al., 2017). Moreover, a majority of tumor-targeting compounds are directed against cell integral and membrane-bound proteins (Yin and Flynn, 2015). One of these very attractive targets for cancer therapy is the sodium-dependent phosphate transporter 2B (*SLC34A2*, NaPi2b, NaPi-IIb, and NPT2) which is overexpressed in several malignancies, including ovarian carcinomas (Rangel et al., 2003; Gryshkova et al., 2009), lung (Zhang et al., 2017), thyroid (Kim et al., 2010), and colorectal cancers (Liu et al., 2018). The sodium-dependent phosphate transporter NaPi2b belongs to the type II sodium-dependent phosphate transporter family SLC34 which also includes secondary transporters NaPi2a (NaPi-IIa) and NaPi2c (NaPi-IIc) (Levi et al., 2019). Although the main function in the maintenance of phosphate homeostasis in the human body belongs to the most-studied renal transporter NaPi2a, NaPi2b is involved in maintaining phosphate homeostasis by absorbing inorganic phosphates in the small intestine and a restricted number of other organs and tissues (Levi et al., 2019). Although the topology of renal NaPi2a (Lambert et al., 1999, 2000), as well as of the flounder NaPi2b (Kohl et al., 1998) with large extracellular domain/loop (ECD/ECL) and C- and N-termini facing the cytoplasm was predicted and verified by the heterologous expression of FLAG-tagged and untagged templates in *Xenopus laevis* oocytes, it is not known whether the topological arrangement of the largest extracellular domain facing outside and the N- and C-termini facing the

cytoplasm is conserved for all the SLC34 proteins, especially in cancer cells. Our preliminary bioinformatics analysis suggested that the protein encoded by the *SLC34A2* gene has at least 8 potential transmembrane domains (TMD), 5 putative intracellular domains, and 4 putative extracellular loops, with both the N- and C-terminal regions probably facing the cytoplasm (Yin et al., 2008). There are four potential disulfide-bond sites at positions 303, 322, 328, and 350 and six possible N-glycosylation sites at locations 295, 308, 313, 321, 335, and 340 in the putative largest extracellular domain of NaPi2b (Yin et al., 2008). The C-terminal domain is also predicted to have a palmitoylation site (McHaffie et al., 2007). The phosphate transporter NaPi2b was identified as an MX35 antigen by screening a phage cDNA library generated from the OVCAR-3 ovarian cancer cell line (Kiyamova R. G. et al., 2008) with MX35 antibodies (Mattes et al., 1987). Antibodies were generated by immunizing mice with a combination of ovarian cancer tumor cells, and recognized NaPi2b on the cell surface of 80–90% of ovarian carcinoma tumors (Mattes et al., 1987; Welshinger et al., 1997). Epitopes for the monoclonal antibodies (mAbs) MX35 and L2 (20/3) (Kiyamova R. et al., 2008) (epitope MX35) mapped originally within the ECD of the NaPi2b transporter in the frame of 311–340 amino acids by Western blot analysis of GST-fused overlapping recombinant truncated proteins were then narrowed down to 324–338 amino acids (aa) (Yin et al., 2008). A great variety of MX35-based therapeutic antibodies targeting the NaPi2b have then been developed including Rebmab200 (Santos et al., 2013), XMT-1535 (Mosher et al., 2019), XMT-1536 (Bodyak et al., 2021), and XMT-1592 (Fessler et al., 2020). Ultimately, almost all available anti-ECDs of NaPi2b antibodies including MX35, L2 (20/3), Rebmab200, XMT-1535, XMT-1536, and XMT-1592 recognize the same epitope of the NaPi2b protein between the 324 and 338 amino acid residues, however, only mAbs generated by Megale et al. are directed against the other part of the ECD of the NaPi2b protein (Megale et al., 2016).

The first evidence of surface localization of the MX35 epitope within NaPi2b extracellular loop has been obtained by the staining of unfixed ascite tumor cells of women with papillary poorly differentiated ovarian adenocarcinoma using monoclonal antibodies MX35 (Mattes et al., 1987). As mentioned previously, only the flounder NaPi2b topology was mapped previously using recombinant fragments with FLAG-tagged epitopes (Kohl et al., 1998) expressed in oocytes. However, the locations of the ECD, N, and C-terminal domains of the transporter expressed endogenously in cancer cells have not been studied experimentally. The N-terminal domains of membrane proteins are involved in ensuring the accuracy of the entire protein's insertion into the cell membrane rather than the elongation speed ramp at protein translational starts (Charneski and Hurst, 2014) and can contribute to the correct orientation of all subsequent transmembrane domains in the cell according to the model of sequential membrane protein topogenesis (Hartmann et al., 1989; Bogdanov et al., 2014). From the other side, the topology of N-terminal domains can be uncertain due to their unusual orientational dynamics (Seurig et al., 2019) and post-translational and even post-insertional reorientation (Nass et al., 2022). The C-terminal domain of NaPi2b is likely to be involved in signal transduction, intracellular trafficking, and the surface retention due to presence of multiple cysteine residues capable of reversible acylation (Chamberlain and Shipston, 2015), PDZ domain binding function of which is regulated by phosphorylation or allosterically by other binding partners (Gisler et al., 2001) as it was shown for NaPi2a and NaPi2c (NaPi2b protein counterparts) in renal proximal tubule cells (Levi et al., 2019).

A direct experimental determination of the membrane protein topology has been widely undertaken using confocal microscopy and foreign epitope insertion constructs or panels of monoclonal antibodies with known epitopes, where the assessment of their immunoreactivity has been made before and after cell permeabilization (Banerjee and Swaan, 2006; Nasie et al., 2013). However, we continue to favor mapping the topology of untagged proteins in living cells because foreign tags should be used with caution since such tags may affect the topology of adjacent TMDs with weak hydrophobic topological determinants (e.g. marginally hydrophobic), because their intrinsic flexibility makes them prone to various rearrangements (Bogdanov, 2017). Due to these dynamic, structural, and controversial predictive aspects and the fact that the NaPi2b transporter is an excellent target for anticancer therapy and immunodiagnostics, the aim of this work was to investigate the orientation of the aforementioned three domains (N-termini, largest ECD, and C-termini) in cancer cells by a bioinformatics approach and *in vivo* mapping with different mAbs by confocal microscopy. Despite advances in X-ray, and particularly, the development of advanced CryoEM technologies for acquiring high-resolution structures for membrane proteins, the necessity to identify low-resolution organizational information on membrane proteins in a natural membrane still persists. The structural basis for dynamic and transient topologies remains unapproachable by X-ray crystallography and CryoEM since membrane protein crystals and CryoEM structures of membrane proteins are static (Bogdanov et al., 2018). Although the membrane protein topology gives low-resolution structural information, it can serve as a starting point for various biochemical investigations or three-dimensional structure modeling (Bogdanov, 2017). The dynamic aspects of a protein structure as a function of the physiological state of the cell is best probed in whole intact cells and in a native microenvironment. The identification of specific epitopes for therapeutic antibodies continues to be a major challenge in molecular oncology and immunodiagnostics. NaPi2b may comprise of never been considered, established, continuous, and discontinuous epitopes and therefore represents a new family of potential cell surface markers and targets for the immunotherapy of several types of cancers.

MATERIALS AND METHODS

Cell Culture and Monoclonal Antibodies

The human ovarian carcinoma cell line OVCAR-4, which expresses the NaPi2b transporter endogenously, was purchased from Merck Millipore (United States). Cells were cultured in an RPMI-1640 medium (Paneco, Russia) containing 10% fetal

bovine serum, 4 mM L-glutamine, 100 U/mL penicillin, 100 µg/ml streptomycin at 37°C in an atmosphere of 5% CO_2.

Mouse mAbs against ECD of NaPi2b L2 (20/3) (Kiyamova R. et al., 2008), N-terminal domain of NaPi2b N-NaPi2b (15/1) (Gryshkova V. et al., 2011), and rabbit mAbs against C-terminal domain of NaPi2b (D3V3I, Cell Signaling, United States) were used as the primary antibodies. The goat anti-mouse IgG antibody with Alexa Fluor 488 (Thermo Fisher, United States) and the goat anti-rabbit IgG antibody with Alexa Fluor 488 (Thermo Fisher, United States) were used as secondary antibodies against the corresponding target in this indirect immunostaining approach.

Bioinformatics Analysis

The CCTOP server was used to predict the number of transmembrane domains in NaPi2b and the topology of its domains. This server allows many programs to create the NaPi2b topology, including HMMTOP, Memsat, Octopus, Phillius, Phobius, Pro, Provid, Scampi, ScampiMsa, and TMHMM (Dobson et al., 2015).

Confocal Microscopy

OVCAR-4 cells were used to visualize the ECD, N-terminal, and C-terminal domains of NaPi2b. Prior to the experiment, the cells were seeded onto glass bottom dishes (Mattek, United States). The cells were used alive or after being pre-fixed in 4% paraformaldehyde for 15 min and permeabilized in phosphate-buffered saline (PBS) containing 3% bovine serum albumin (BSA) and 0.1% Triton X-100 for 30 min. Cells were incubated with primary antibodies for 1 h at room temperature. Next, the cells were incubated with secondary antibodies for 1 h at room temperature. The nuclei were stained with Hoechst 33342 (Thermo Fisher Scientific, United States) and propidium iodide (PI) (Thermo Fisher Scientific, United States). Staining with PI served to control the membrane integrity of live cells. The fluorescent signal was detected using Z-stack mode on a Zeiss LSM 780 laser confocal microscope (Carl Zeiss AG, Germany). The provided Z-stacks were done using average intensity signals. The thickness of each section was 1 µm. The number of sections (the sample height) varied depending on the conditions of the sample preparation and ranged from 11 to 20 sections. The results were obtained using the Zen Analysis software (Carl Zeiss AG, Germany). The images were collected under the same conditions. Data are representative of multiple independent experiments. Particularly, up to 20 cells were analyzed for each image in three biological repeats.

RESULTS

Bioinformatics Analysis of NaPi2b Domain Orientation and Prediction of Its Transmembrane Regions

The CCTOP server (Dobson et al., 2015) was used to predict the topology of the largest ECD (ECL), N-terminal, and C-terminal domains of the NaPi2b in mammalian cells (**Supplementary Table S1**). Seven out of ten programs on the CCTOP server predicted extracellular localization for the largest ECD of NaPi2b. Seven out of ten programs predicted intracellular orientation of the N-terminal domain and six out of ten algorithms predicted the intracellular location for the C-terminal domain. The number of predicted transmembrane (TM) domains ranges from eight to thirteen membrane-spanning regions with N- and C-terminal domains potentially facing either the cytoplasm or outside. Since fine-tuning of the topological organization of hNaPi2b, including the orientation of re-entrant domains with serine rich QSSS stretches located centrally at the vertex of these mini loops containing Na-Pi-Na binding sites (Patti et al., 2016; Fenollar-Ferrer and Forrest, 2019) was out of scope, the predicted topological organization describes the only way a polypeptide chain is arranged in the membrane, i.e., the number of TMDs and their orientation in the membrane indicates the further verified sidedness of the three largest ECDs (N-termini, ECD, and C-termini). Although the common basic architectural principle of the structure of polytopic membrane proteins is the membrane topology, i.e., the number of TMDs and their orientation in the membrane which subsequently determines the orientation of ECDs, the number of predicted TMDs is very often different and uncertain due to presence of domains with insufficient hydrophobicity (Zhao and London, 2006) which are either underpredicted or not predicted as TMDs. Therefore, predicted entire NaPi2b topology lacks strong preference toward one or the other orientation of either the N-terminal or C-terminal domains or the total number of predicted TMDs. The N- and C-termini can end up either in the cytoplasm or in the extracellular environment. Statistically, if the number of TM segments is even, the N- and C-termini are localized on the same side of the membrane, if the number of TM segments is odd, the N- and C- termini face different sides (Bogdanov et al., 2014). Due to this uncertainty of prediction, an experimental validation of predicted orientation is required. The length of the largest ECD appears to vary from 117 to 128 amino acids within the polypeptide sequence located between positions 236 and 369 of the transporter polypeptide (**Supplementary Table S1**). It should be noted that the largest extracellular loop boundaries of NaPi2b were proposed to lie between 188 and 361 amino acid residues (Yin et al., 2008). The length of the N-terminal domain varies from 91 to 104 amino acids, and the length of the C-terminal domain varies to a greater extent (58–118 amino acid residues) (**Supplementary Table S1**). If the length of the C-terminal domain exceeds 100 amino acid residues according to the 6 programs, the C-terminal domain is orientated exclusively towards the cytoplasm (**Supplementary Table S1**). It can be at least partially supported by the identification of the putative palmitoylation site in the polycysteine region of the C-terminus adjacent to the hydrophobic amino acid stretch predicted to be the last TMD (618–645 amino acid residues) (Lituiev and Kiyamova, 2010). As a result, the effective hydrophobic length of this TMD is increased to trigger a positive mismatch within the membrane (Charollais and Goot, 2009) which usually favors the retention of the C-terminus in the cytoplasm (Dowhan and Bogdanov, 2009). The cysteine string in NaPi2b has been found to alter the sorting, possibly by limiting

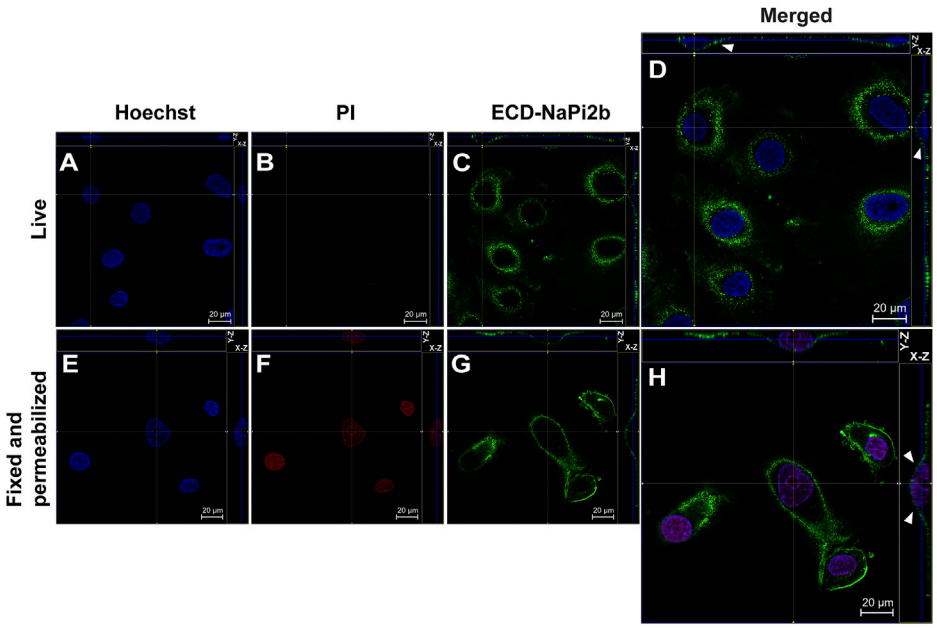

FIGURE 1 | Confocal microscopy analysis of the largest extracellular domain of NaPi2b in ovarian carcinomas cells OVCAR-4 that were either alive **(A–D)** or fixed and permeabilized **(E–H)** and imaged in the Z-stacking mode. **(A,E)** Blue channel (Hoechst); **(B,F)** Red channel (PI); and **(C,G)** Green channel (Alexa Fluor 488), ECD-NaPi2b–mAbs L2 (20/3) directed to ECD of NaPi2b; **(D,H)** Merged images; On the top (*Y*-axis and *Z*-axis combined) and right (*X*-axis and *Z*-axis combined) of each picture, a composite image comprising of numerous photographs obtained at various focus distances is shown. White arrows indicate the position of NaPi2b on the cell membrane.

the basolateral delivery (McHaffie et al., 2007). Furthermore, cysteine-rich palmitoylation motif could stabilize and anchor NaPi2b in biological membranes, as was shown for PLSCR1 (Posada et al., 2014; Herate et al., 2016).

Analysis of the Largest ECD, N- Terminal, and C- Terminal Domain Topologies of NaPi2b in Ovarian Cancer Cells by Confocal Microscopy

To determine the orientation of the largest ECD, N-, and C-terminal domains of NaPi2b in OVCAR-4 cells, the mAbs L2 (20/3) directed against the aforementioned ECD (Kiyamova R. et al., 2008), antibody N-NaPi2b (15/1) (Gryshkova V. et al., 2011), and mAbs (D3V3I, cell signaling) directed against the transporter's N-terminal and C-terminal domains, respectively, were used strategically in confocal microscopy experiments. To ensure that the observed immunofluorescence was entirely a result of the binding of antibodies to the outer leaflet of the OVCAR-4 plasma membrane, we routinely monitored cell integrity during antibody labeling by co-incubating cells with a cell membrane-impermeable probe, propidium iodide (PI). Live cells non-permeable to PI should be impermeable to Abs as well (Zhao et al., 2012). Orientation of the largest predicted ECD of NaPi2b in OVCAR-4 cells is shown in **Figure 1**.

The monoclonal antibodies L2 (20/3) detect the ECD of NaPi2b in live OVCAR-4 cells without using any reagents that disrupt membrane integrity (native conditions) (**Figure 1D**), as well as in cells that have been fixed with paraformaldehyde and permeabilized with Triton X-100 (**Figure 1H**). The Z-stacking (focus stacking) mode combines multiple images taken at different focal distances to provide a composite image with a greater depth of field and therefore enabled us to overlay maximum fluorescent intensities of the membrane over the cytoplasm and justify that the fluorescent signal predominantly derived from the cell membrane plane and therefore confidently confirm the membrane localization of NaPi2b. Live OVCAR-4 cells show the staining of the membrane with L2 (20/3) mAbs (**Figures 1C, D**) and no nuclear staining with PI confidently demonstrating the extracellular location of domain.

Membrane orientation of the N-terminal domain of the NaPi2b is estimated from the results shown in **Figure 2**. Live and intact OVCAR-4 cells showed no staining with mAbs (15/1) directed against the NaPi2b N-termini and no nuclear staining with PI (**Figures 2B, C**), whereas, fixed cells treated with a detergent to disrupt the plasma membrane showed both staining patterns (**Figures 2F, G**). Thus, monoclonal antibodies (15/1) recognize the N-terminal domain of the NaPi2b phosphate transporter exclusively in fixed and permeabilized cells (**Figure 2H**), but not in live cells (**Figure 2D**) confidently demonstrating that the N-terminal domain of NaPi2b is located intracellularly. The membrane localization of the NaPi2b was monitored due to fluorescence of Alexa Fluor 488 excited with the 488 nm laser (**Figure 2H** (X-Z), H (Y-Z) in this indirect immunostaining approach.

Membrane orientation of the C-terminal domain of NaPi2b is estimated from the results shown in **Figure 3**. Site-directed anti-

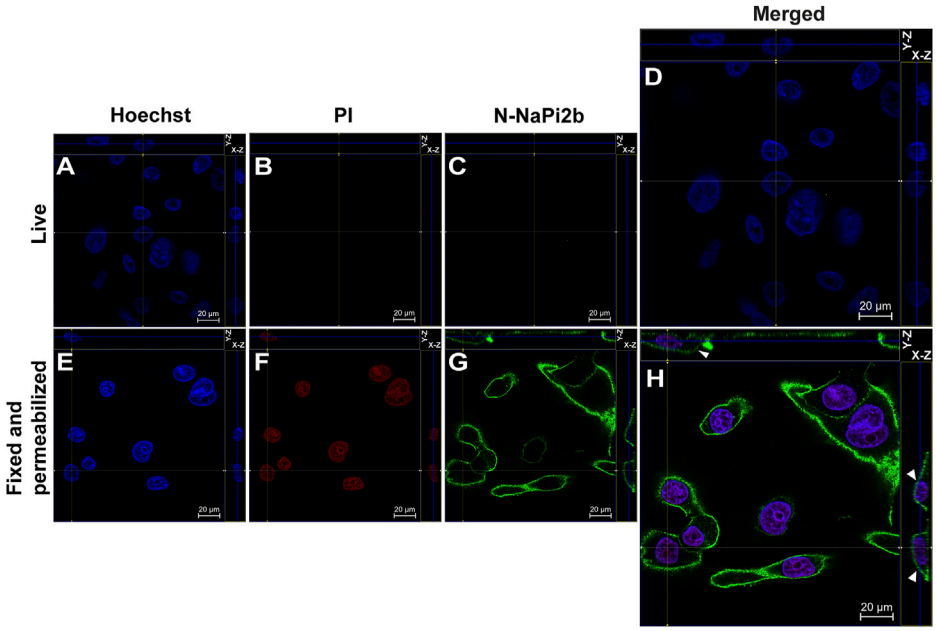

FIGURE 2 | Confocal microscopy analysis of the N-terminal domain of NaPi2b in ovarian carcinomas cells OVCAR-4 that were either intact **(A–D)** or fixed and permeabilized **(E–H)** and imaged in the Z-stacking mode. **(A,E)** Blue channel (Hoechst); **(B,F)** Red channel (PI); and **(C,G)** Green channel (Alexa Fluor 488), N-NaPi2b–mAbs N-NaPi2b (15/1) directed to the N-terminal domain of NaPi2b; **(D,H)** Merged images; On the top (*Y*-axis and *Z*-axis combined) and right (*X*-axis and *Z*-axis combined) of each picture, a composite image comprising of numerous photographs obtained at various focus distances is shown. White arrows indicate the position of NaPi2b on the cell membrane.

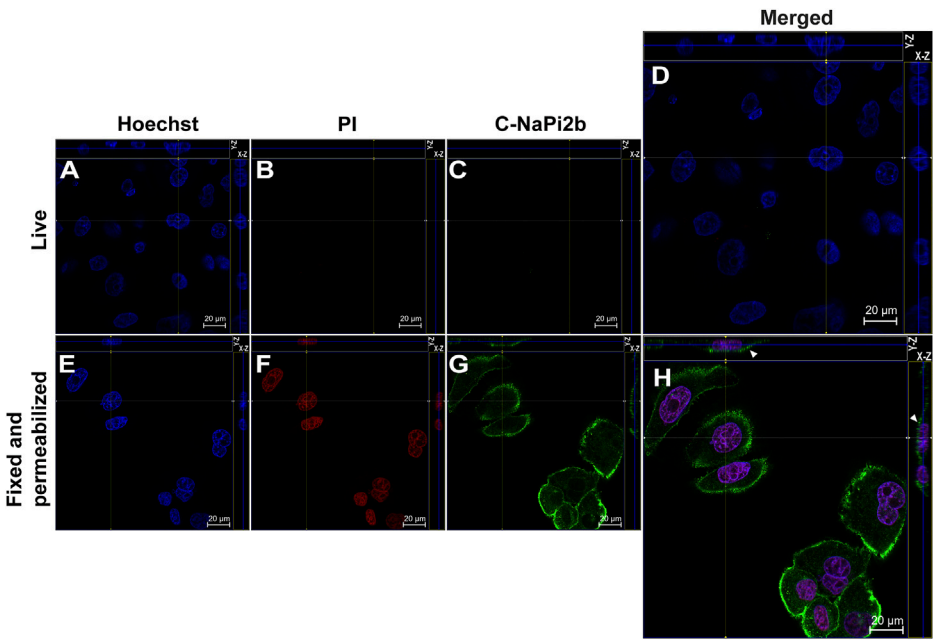

FIGURE 3 | Confocal microscopy analysis of the C-terminal domain of NaPi2b in ovarian carcinomas cells OVCAR-4 that were either alive **(A–D)** or fixed and permeabilized **(E–H)** and imaged in the Z-stacking mode. **(A,E)** Blue channel (Hoechst); **(B,F)** Red channel (PI); and **(C,G)** Green channel (Alexa Fluor 488), C-NaPi2b–mAbs D3V3I (Cell Signaling, United States) directed to the C-terminal domain of NaPi2b; **(D,H)** Merged Images; On the top (*Y*-axis and *Z*-axis combined) and right (*X*-axis and *Z*-axis combined) of each image, a composite image comprising of numerous photographs obtained at various focus distances is shown. White arrows indicate the position of NaPi2b on the cell membrane.

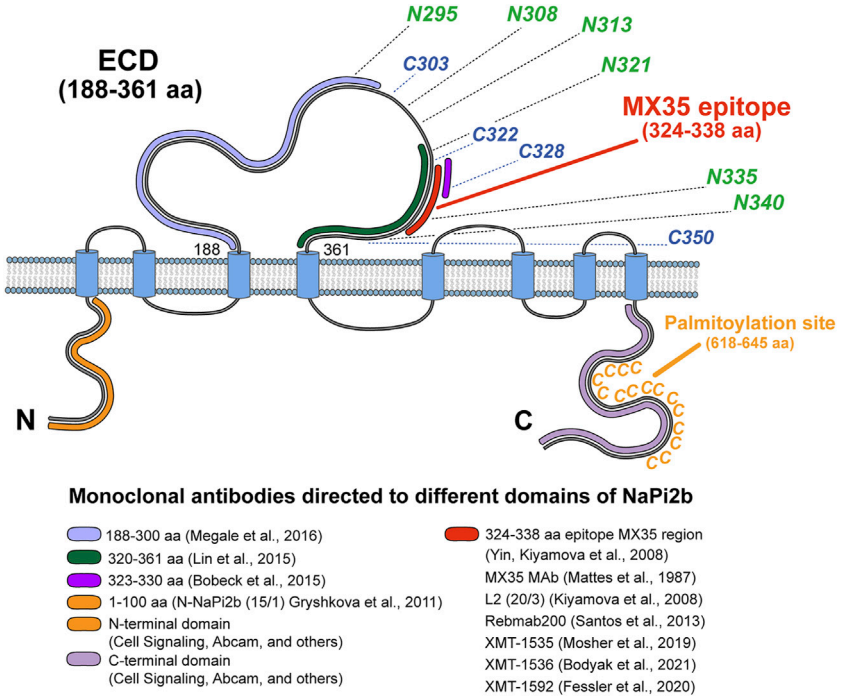

FIGURE 4 | Topological model of NaPi2b with color-coded antigenic regions recognized by available monoclonal analytical and therapeutic antibodies targeting different extramembrane domains. The epitope's region in ECD of NaPi2b for mAbs, generated by: Megale et al. (2016), 188–300 aa, marked in light purple; Lin et al. (2015), 320–361 aa, marked in green; Bobeck et al. (2015), 323–330 aa, marked in purple; Yin, Kiyamova et al. (2008), Mattes et al. (1987), Kiyamova et al. (2008), Santos et al. (2013), Mosher et al. (2019), Bodyak et al. (2021), Fessler et al. (2020), 324–338 aa, marked in red; Epitope region in N-termini and C-termini of NaPi2b for mAbs, generated by: Gryshkova et al. (2011), Cell Signaling, Abcam, and others against N-terminal domain of NaPi2b, 1–100 aa, marked in orange; Cell Signaling, Abcam, and others against C-terminal domain of NaPi2b, the region is unknown, marked in lavender. Positions of cysteine and asparagine amino acid residues potentially contributing to the oxidative folding and formation of disulfide bonds and N-linked glycosylation of the largest ECD, and palmytoilation site in C-terminal domain are also shown.

C-NaPi2b/SLC34A2 mAbs (D3V3I, cell signaling) detect the C-terminal domain of the NaPi2b phosphate transporter only in cells that are fixed and permeabilized (**Figure 3H**), but not in live PI-negative OVCAR-4 cells (**Figures 3A–D**). Permeabilizing the cells with Triton X-100 essentially made all cells positive, not only with PI, but also with these anti-C-termini antibodies, because the antibodies were then able to access the cytoplasmically oriented domain confidently confirming its intracellular orientation. The Alexa Fluor 488 that is excited with the 488 nm laser seen in the Z-stacking mode (**Figure 3H** (X-Z), H (Y-Z) (indicated by arrows) again confirms the membrane residence of NaPi2b.

This is the first report of the topological structure of NaPi2b obtained by confocal microscopy of live ovarian cancer cells with the set of available antibodies. The data obtained clearly indicate that the N-terminal and the C-terminal domains of NaPi2b are located inside the cell, and the largest extracellular loop of the transporter NaPi2b is located outside the OVCAR-4 cells. Orientation of the N- and C-termini can contribute to the overall topology of membrane proteins and predict whether the number of TMDs is odd or even (Bogdanov et al., 2014). Since both the N- and C-termini of NaPi2b are intracellularly exposed, NaPi2b must have an even number of TMDs in the plasma membrane. It is interesting to note that only the Octopus program of the CCTOP server predicted experimentally determined topology of the ECD, N-, and C-terminal domains of the NaPi2b transporter (**Supplementary Table S1**). It is important to mention that the Philius and Phobius programs also predict the even number of transmembrane domains (10) with the N- and C-termini in the cytoplasm, but the largest extracellular domain is predicted to be in the cytoplasm (**Supplementary Table S1**), which is not consistent with our experimental data. Therefore, the NaPi2b consists of eight transmembrane domains with the largest ECD located outside the cell, with both the N-terminal and the C-terminal domains facing the cytoplasm.

Scope for Mapping the Immunogenic Regions of NaPi2b With Available Monoclonal Antibodies

Membrane proteins, due to their localization, are attractive targets for targeted therapy of oncological diseases. For the moment, 127 therapeutic mAbs are represented on the market, and 77 of them are directed against membrane proteins (Salazar et al., 2021). Currently, several mAbs against the NaPi2b have been generated, including the humanized antibodies XMT-1536 (https://www.mersana.com/pipeline/xmt-1536/) and XMT-1592

(https://www.mersana.com/pipeline/xmt-1592/), which are undergoing clinical trials for the treatment of ovarian and lung cancers. All these antibodies are MX35-based antibodies and are directed against the epitope MX35 located within the largest extracellular loop of NaPi2b.

We analyzed all available data and provided a scope for the recognition of NaPi2b extracellular domains by all available arsenal of therapeutic and analytical Abs using the schematic model of human NaPi2b (**Figure 4**). The model includes positions of cysteines potentially engaged in disulfide bonds, putative asparagine-linked N-glycosylation sites, the location of the MX35 epitope, and the palmitoylation sites in the largest ECD, and the C-terminal domain of NaPi2b, respectively (**Figure 4**). Provided color-coded scheme rationalizes at first time antigenic regions within largest NaPi2b ECD recognized by available monoclonal antibodies. Both MX35 and L2 (20/3) are mouse mAbs-specific for the MX35 epitope of human sodium-dependent phosphate transporter NaPi2b. The monoclonal antibodies MX35 were generated from mice immunized with a cocktail of human ovarian carcinoma cells (Mattes et al., 1987), while L2 (20/3) mAbs were produced in mice immunized with the truncated recombinant NaPi2b protein (ECD, 188–361 aa) (Kiyamova R. et al., 2008). The monoclonal antibodies L2 (20/3) blocks the phosphate-mediated current driven by NaPi2b expressed in renal cancer cells SK-RC-18 (Kiyamova et al., 2011) while binding of MX35 mAbs to a largest ECD of NaPi2b inhibits the uptake of inorganic phosphate in HEK293 cells stably expressing WT protein (Gryshkova V. S. et al., 2011). As an approach toward elucidating the mechanism by which this ECD folds and affects phosphate transport, we have to undertake the definition of the binding sites and the specificity of these and other mAbs shown in **Figure 4**. Rebmab200, a humanized version of MX35 antibodies (Santos et al., 2013; Lindegren et al., 2015), was further renamed as XMT-1535 (Bodyak et al., 2021). Using dolaflexin-based conjugation technology, an antibody–drug conjugate (ADC) XMT-1536 was developed from XMT-1535 (Bodyak et al., 2021; Yurkovetskiy et al., 2021). Another ADC XMT-1592 was generated from XMT-1535 antibodies using dolasynthen conjugation technology (Fessler et al., 2020). It is important to state that despite the availability of various sets of mAbs directed to different regions of the large extracellular domain of the transporter, therapeutic effectiveness in clinical trials was so far demonstrated for only the mAbs-targeting MX35 epitope particularly in the first-in-human study of humanized XMT-1536 (https://clinicaltrials.gov/ct2/show/NCT03319628) and XMT-1592 (https://clinicaltrials.gov/ct2/show/NCT04396340) in patients with ovarian cancer and non-small cell lung cancer.

DISCUSSION

The identification of local and gross membrane protein misfoldings and stable structure- and cancer-type-specific epitopes for therapeutic antibodies such as the elucidation of their functions *in vivo* continue to be a major challenge in molecular oncology and immunodiagnostics. Exactly how this structural plasticity and dynamics of EMDs comprising such epitopes are achieved and controlled has not been clear. It should be noted that the topology of heterologously expressed renal NaPi2a was investigated predominantly in *Xenopus laevis* oocytes by different transmembrane mapping techniques including the immunohistochemical approach and N-glycosylation topology mapping with engineered glycosylation tags as topological probes (Lambert et al., 1999)). Although polyclonal anti-peptide antibodies against the N- and C-termini of NaPi2a were independently utilized for topology mapping, the insertion of the FLAG epitope (DYKDDDDK) location could affect the topology of NaPi2a due to the presence of five negatively charged residues in their sequences. The location of ECD, N-, and C-terminal domains of the NaPi2b transporter has been studied experimentally only on flounder NaPi2b recombinant fragments with FLAG-tagged epitopes (Kohl et al., 1998). In 2008, a topological model of NaPi2b consisting of at least eight potential transmembrane domains (TMD), five putative intracellular domains, and four putative extracellular loops, with both N- and C-terminal regions probably facing the cytoplasm in ovarian cancer cells was computationally predicted (Yin et al., 2008). Since cysteine and aspartate residues located in different extramembrane domains of NaPi2b (ECD and C-terminus) are functionally important, the Abs mapping approach provides a reasonable and perhaps the only one possible alternative to the substituted cysteine accessibility method (SCAM™) and N-glycosylation mapping technique (Bogdanov, 2017). Abs mapping represents one of the best available approaches so far for systematic topology mapping and topological analysis of untagged NaPi2b and other SCL34 proteins in live cancer cells.

Our results provide the first experimental evidence for the intracellular location of the N- and C-termini, and the extracellular location of the largest extracellular domain (loop) of the untagged NaPi2b transporter localized primarily in the plasma membrane, as demonstrated by confocal microscopy in cancer cells. Our model is consistent with the model of NaPi2b predicted by homology modeling (Patti et al., 2016) despite the limitations described below and the 3D structures of NaPi2b predicted computationally from the protein sequence with atomic accuracy by AlphaFold2. Correspondingly to the NaPi2a model (Fenollar-Ferrer et al., 2014), an outward and inward facing homology model of the Na-coupled phosphate co-transporter NaPi-IIb from flounder was generated using a repeat-swapped VcINDY model (Patti et al., 2016) and the modeled structure of hNaPi-IIa (Fenollar-Ferrer and Forrest, 2019) as templates. However, this model is missing its largest extracellular loop (ECD/ECL) connecting TMDIII and TMDIV, as well as the last two TMDs. These TMDs and ECD were intentionally omitted from the final homology model for "functional" reasons since no equivalent templates in VcINDY was respectively found suggesting that these TMDs are not part of the transport core fold despite the fact that a large extracellular loop can be associated with the transport function and postulated conformational changes (Patti et al., 2016). Nevertheless, Na1-site perturbing mutations were successfully mapped onto this homology model and supported by the positioning of probes

to examine transport dynamics and kinetics (Patti et al., 2016). The NaPi2b model for discrimination of continuous epitopes' regions mapped with various mAbs, including MX35 antibodies directed against different NaPi2b ECDs is presented on **Figure 4**, including cysteine residues potentially engaged in disulfide bonds, asparagine-linked N-glycosylation sites, the MX35 epitope, and the palmitoylation site within the NaPi2b C-terminal domain. We recently demonstrated that MX35 antibodies as well as L2 (20/3) antibodies recognize conformationally exposed epitope MX35 structurally constrained by disulfide bonds and carbohydrates attached at asparagine-linked glycosylation sites which can potentially contribute to the foldability of the largest ECD containing this epitope (Kiyamova et al., 2020; Bulatova et al., 2021).

Whether an epitope is conformationally constrained by disulfide bonds and whether N-glycosylation stabilizes structurally tethered conformation of the epitope is still unknown. Obviously, the epitope will be partially misfolded or folded differently if the disulfide bonds are unformed or mismatched. We suppose that an aberrant folding and/or transmembrane misassembly may determine bioavailability (immunogenicity) of this epitope and therefore "druggability" of membrane proteins as a target in cancer cells. We postulate that epitope MX35 recognition depends on its unique conformation specific only to cancer cells making it a potential cancer-specific epitope during co-translational oxidative folding and N-glycosylation events in cancer cells (Kiyamova et al., 2020; Bulatova et al., 2021). This assumption is supported by the fact that even though the transporter NaPi2b is expressed in several normal tissues, the MX35 mAbs are accumulated predominantly in cancer cells, as demonstrated during the first clinical trials involving the pharmacokinetics, biodistribution, and intraoperative radioimmunodetection of radiolabeled MX35 in patients with advanced epithelial ovarian cancer (Rubin et al., 1993). Digital images confirmed the specific uptake of radiolabeled mAbs MX35 F (ab') in tumor cell foci rather than the adjacent non-tumor tissues (Finstad et al., 1997). Intraperitoneal administration of 211At-MX35 F(ab9)2 achieves therapeutic absorbed doses in microscopic tumor clusters without significant toxicity indicating that antibodies do not accumulate in normal tissues (Andersson et al., 2009). Specific accumulation of MX35 mAbs in cancer cells may be explained by its overexpression in ovarian cancer cells (Gryshkova et al., 2009), but we cannot exclude the fact that MX35 antibodies and their humanized versions recognize the potential "cancer-specific" epitope of the transporter due to conformation provided only by cancer cells. This hypothesis is the subject of our current independent investigation.

Interestingly, recent attempts to generate antibodies to epitopes other than the MX35 epitope led to the production of several antibodies directed toward the largest ECD. These mAbs include those generated recently by Genentech derived from the sequence corresponding to the region between 320 and 361 amino acids of full-length human NaPi2b (Lin et al., 2015) and antibodies directed against synthetic peptides corresponding to an amino acid sequence of 188–300 residues in the non-overlapping portion of the NaPi2b protein epitope for MX35 Abs (Megale et al., 2016). Egg-yolk anti-h16 antibodies deposited in the avian egg and directed against the TSPSLCWT sequence (323–330 aa) within epitope MX35 of NaPi2b also were produced (Bobeck et al., 2015). It was shown that monomethyl auristatin E (MMAE) conjugated antibodies generated by Genentech inhibited tumor growth and caused tumor regression in xenograft animal tumor models, OVCAR-3-X2.1, and IGROV-1 derived from human ovarian cancer and from human non-small cell lung adenocarcinoma epithelial cells, respectively (Lin et al., 2015). Even though the antibodies generated by Genentech were evaluated in pre-clinical studies as an effective new therapy for the treatment of NSCLC and ovarian cancer, no additional information is available about the clinical studies of these antibodies. To date, only mAbs XMT-1536 (upifitamab rilsodotin (UpRi)) and XMT-1592 are under investigation in clinical trials for ovarian and lung cancers treatment in accordance with the www.clinicaltrials.gov server. UpRi, a first-in-class ADC-targeting NaPi2b, utilizes the Dolaflexin platform to deliver about 10 DolaLock payload molecules conjugated to auristatin (anti-tubulin agent) per antibody (Yurkovetskiy et al., 2021). UpRi is being studied in UPLIFT, a single-arm registration study in patients with platinum-resistant ovarian cancer (NCT03319628). In July 2021, UPGRADE, a Phase 1 umbrella study, combining UpRi with other ovarian cancer therapies in patients with platinum-sensitive high-grade serous ovarian cancer (NCT04907968), was initiated. Antibodies XMT-1592, based on the dolasynthen platform, are in phase 1 dose escalation trial (NCT04396340) in patients with tumors likely to express NaPi2b. Thus, NaPi2b represents a promising target for antitumor therapy due to its predominant membrane localization, existence of potential cancer-specific epitope, and increased expression in several tumors. However, we have shown recently that neo-adjuvant therapy with carboplatin and paclitaxel reduces the protein expression of the NaPi2b transporter in tumors of ovarian carcinoma, which calls into question the use of correspondent antibodies for ovarian cancer patients' treatment (Nurgalieva et al., 2021).

Site-directed antibodies' transmembrane topology mapping of untagged NaPi2b in live and intact ovarian cancer cells allowed us to experimentally validate a previously predicted model for the transmembrane organization of extramembrane domains (Yin et al., 2008) and provide an up-to date experimental platform for NaPi2b epitope-based cancer immunodiagnostics and immunotherapy. The establishment of the sidedness of surface-hidden N-terminal and C-terminal domains and demarcation of the robustness of the topology of NaPi2b in a normoxic condition is critically important for current and future studies aimed at understanding the roles of defined regions in function, folding, and antigenicity as well as the development of a new immunotherapeutic approaches.

An effective design of therapeutic monoclonal antibodies is dependent on understanding the membrane protein structure and the rules that govern the folding and topogenesis of native membrane proteins in healthy and cancer cells. These structural features appear to be crucial factors for the development of recombinant potent therapeutic monoclonal antibodies acting

by specifically binding an extracellular epitope on the surface of a membrane protein with high affinity. Therefore, an actual hallmark of the membrane protein's "druggability" with mAbs is the requirement for the extent of solvent exposure of folded extramembrane domains making it fully accessible to therapeutic antibodies. This view challenges the dogma that a solvent-accessible active site of an enzyme is only the "Achilles' Heel" of membrane proteins which should serve as the primary target for different drugs.

DATA AVAILABILITY STATEMENT

The original contributions presented in the study are included in the article/**Supplementary Material**; further inquiries can be directed to the corresponding authors.

AUTHOR CONTRIBUTIONS

RK and MB contributed equally and substantially to the conception and study design, writing of original draft, and subsequent editing of the manuscript. LB, DS, AN, DR, AT, and VS performed the experiments and contributed to the design of all the experiments. LB carried out the topology prediction, conceived the study, designed experiments, and supervised the research. LB, VS, RK, and MB analyzed the data and wrote the manuscript. All authors contributed to the data analysis and interpretation of the results. All authors reviewed the results and approved the final version of the manuscript.

FUNDING

This manuscript has been supported by the Kazan Federal University Strategic Academic Leadership Program (PRIORITY-2030). Analysis of the NaPi2b topology by confocal microscopy was supported by Russian Science Foundation Grant RCF 20-14-00166.

ACKNOWLEDGMENTS

We are very grateful M. Zhuravleva for confocal microscopy training.

SUPPLEMENTARY MATERIAL

The Supplementary Material for this article can be found online at: https://www.frontiersin.org/articles/10.3389/fmolb.2022.895911/full#supplementary-material

REFERENCES

Andersson, H., Cederkrantz, E., Bäck, T., Divgi, C., Elgqvist, J., Himmelman, J., et al. (2009). Intraperitoneal α-Particle Radioimmunotherapy of Ovarian Cancer Patients: Pharmacokinetics and Dosimetry of 211At-MX35 F(ab′)2-A Phase I Study. *J. Nucl. Med.* 50, 1153–1160. doi:10.2967/jnumed.109.062604

Banerjee, A., and Swaan, P. W. (2006). Membrane Topology of Human ASBT (SLC10A2) Determined by Dual Label Epitope Insertion Scanning Mutagenesis. New Evidence for Seven Transmembrane Domains. *Biochemistry* 45, 943–953. doi:10.1021/bi052202j

Bobeck, E. A., Hellestad, E. M., Sand, J. M., Piccione, M. L., Bishop, J. W., Helvig, C., et al. (2015). Oral Peptide Specific Egg Antibody to Intestinal Sodium-dependent Phosphate Co-transporter-2b Is Effective at Altering Phosphate Transport *In Vitro* and *In Vivo*. *Poult. Sci.* 94, 1128–1137. doi:10.3382/ps/pev085

Bodyak, N. D., Mosher, R., Yurkovetskiy, A. V., Yin, M., Bu, C., Conlon, P. R., et al. (2021). The Dolaflexin-Based Antibody-Drug Conjugate XMT-1536 Targets the Solid Tumor Lineage Antigen SLC34A2/NaPi2b. *Mol. Cancer Ther.* 20, 896–905. doi:10.1158/1535-7163.mct-20-0183

Bogdanov, M., Dowhan, W., and Vitrac, H. (2014). Lipids and Topological Rules Governing Membrane Protein Assembly. *Biochimica Biophysica Acta (BBA) - Mol. Cell. Res.* 1843, 1475–1488. doi:10.1016/j.bbamcr.2013.12.007

Bogdanov, M. (2017). Mapping of Membrane Protein Topology by Substituted Cysteine Accessibility Method (SCAM). *Methods Mol. Biol. Clifton N. J.* 1615, 105–128. doi:10.1007/978-1-4939-7033-9_9

Bogdanov, M., Vitrac, H., and Dowhan, W. (2018). Flip-Flopping Membrane Proteins: How the Charge Balance Rule Governs Dynamic Membrane Protein Topology. 1, 28. doi: doi:10.1007/978-3-319-43676-0_62-1

Bulatova, L. F., Skripova, V., Nurgalieva, A., Reshetnikova, D., Savenkova, D. V., Timonina, A., et al. (2021). 26P Structurally Constrained Tumor-specific Epitope within the Largest Extracellular Domain of Sodium-dependent Phosphate Transporter NaPi2b. *Ann. Oncol.* 32, S368–S369. doi:10.1016/j.annonc.2021.08.304

Chamberlain, L. H., and Shipston, M. J. (2015). The Physiology of ProteinS-Acylation. *Physiol. Rev.* 95, 341–376. doi:10.1152/physrev.00032.2014

Charneski, C. A., and Hurst, L. D. (2014). Positive Charge Loading at Protein Termini Is Due to Membrane Protein Topology, Not a Translational Ramp. *Mol. Biol. Evol.* 31, 70–84. doi:10.1093/molbev/mst169

Charollais, J., and Van Der Goot, F. G. (2009). Palmitoylation of Membrane Proteins (Review). *Mol. Membr. Biol.* 26, 55–66. doi:10.1080/09687680802620369

Dobson, L., Reményi, I., and Tusnády, G. E. (2015). CCTOP: a Consensus Constrained TOPology Prediction Web Server. *Nucleic Acids Res.* 43, W408–W412. doi:10.1093/nar/gkv451

dos Santos, M. L., Yeda, F. P., Tsuruta, L. R., Horta, B. B., Pimenta, A. A., Degaki, T. L., et al. (2013). Rebmab200, a Humanized Monoclonal Antibody Targeting the Sodium Phosphate Transporter NaPi2b Displays Strong Immune Mediated Cytotoxicity against Cancer: A Novel Reagent for Targeted Antibody Therapy of Cancer. *Plos One* 8, e70332. doi:10.1371/journal.pone.0070332

Dowhan, W., and Bogdanov, M. (2009). Lipid-Dependent Membrane Protein Topogenesis. *Annu. Rev. Biochem.* 78, 515–540. doi:10.1146/annurev.biochem.77.060806.091251

Fenollar-Ferrer, C., and Forrest, L. R. (2019). Structural Models of the NaPi-II Sodium-Phosphate Cotransporters. *Pflugers Arch. - Eur. J. Physiol.* 471, 43–52. doi:10.1007/s00424-018-2197-x

Fenollar-Ferrer, C., Patti, M., Knöpfel, T., Werner, A., Forster, I. C., and Forrest, L. R. (2014). Structural Fold and Binding Sites of the Human Na+-Phosphate Cotransporter NaPi-II. *Biophysical J.* 106, 1268–1279. doi:10.1016/j.bpj.2014.01.043

Fessler, S., Dirksen, A., Collins, S. D., Xu, L., Lee, W., Wang, J., et al. (2020). Abstract 2894: XMT-1592, a Site-specific Dolasynthen-Based NaPi2b-Targeted Antibody-Drug Conjugate for the Treatment of Ovarian Cancer and Lung Adenocarcinoma. *Exp. Mol. Ther.* 80, 2894. doi:10.1158/1538-7445.am2020-2894

Finstad, C. L., Lloyd, K. O., Federici, M. G., Divgi, C., Venkatraman, E., Barakat, R. R., et al. (1997). Distribution of Radiolabeled Monoclonal Antibody MX35 F(ab')2 in Tissue Samples by Storage Phosphor Screen Image

Analysis: Evaluation of Antibody Localization to Micrometastatic Disease in Epithelial Ovarian Cancer. *Clin. Cancer Res.* 3, 1433–1442.

Gisler, S. M., Stagljar, I., Traebert, M., Bacic, D., Biber, J., and Murer, H. (2001). Interaction of the Type IIa Na/Pi Cotransporter with PDZ Proteins. *J. Biol. Chem.* 276, 9206–9213. doi:10.1074/jbc.m008745200

Gryshkova, V., Goncharuk, I., Gurtovyy, V., Khozhayenko, Y., Nespryadko, S., Vorobjova, L., et al. (2009). The Study of Phosphate Transporter NAPI2B Expression in Different Histological Types of Epithelial Ovarian Cancer. *Exp. Oncol.* 31, 37–42.

Gryshkova, V., Lituiev, D., Savinska, L., Ovcharenko, G., Gout, I., Filonenko, V., et al. (2011a). Generation of Monoclonal Antibodies against Tumor-Associated Antigen MX35/sodium-dependent Phosphate Transporter NaPi2b. *Hybridoma* 30, 37–42. doi:10.1089/hyb.2010.0064

Gryshkova, V. S., Filonenko, V. V., and Kiyamova, R. G. (2011b). Inhibition of Sodium-dependent Phosphate Transporter NaPi2b Function with MX35 Antibody. *Biopolym. Cell.* 27, 193–198. doi:10.7124/bc.0000b9

Hartmann, E., Rapoport, T. A., and Lodish, H. F. (1989). Predicting the Orientation of Eukaryotic Membrane-Spanning Proteins. *Proc. Natl. Acad. Sci. U.S.A.* 86, 5786–5790. doi:10.1073/pnas.86.15.5786

Herate, C., Ramdani, G., Grant, N. J., Marion, S., Gasman, S., Niedergang, F., et al. (2016). Phospholipid Scramblase 1 Modulates FcR-Mediated Phagocytosis in Differentiated Macrophages. *Plos One* 11, e0145617. doi:10.1371/journal.pone.0145617

Kim, H. S., Kim, D. H., Kim, J. Y., Jeoung, N. H., Lee, I. K., Bong, J. G., et al. (2010). Microarray Analysis of Papillary Thyroid Cancers in Korean. *Korean J. Intern Med.* 25, 399–407. doi:10.3904/kjim.2010.25.4.399

Kiyamova, R. G., Gryshkova, V. S., Usenko, V. S., Khozaenko, Y. S., Gurtovyy, V. A., Yin, B., et al. (2008a). Identification of Phosphate Transporter NaPi2b as MX35 Cancer Antigen by Modified SEREX Approach. *Biopolym. Cell.* 24, 218–224. doi:10.7124/bc.0007a3

Kiyamova, R., Gryshkova, V., Ovcharenko, G., Lituyev, D., Malyuchik, S., Usenko, V., et al. (2008b). Development of Monoclonal Antibodies Specific for the Human Sodium-dependent Phosphate Co-transporter NaPi2b. *Hybridoma* 27, 277–284. doi:10.1089/hyb.2008.0015

Kiyamova, R. G., Savchenko, G. A., Gryshkova, V. S., Ovcharenko, G. V., Boychuk, Y. A., Krishtal, O. O., et al. (2011). Effect of Anti-NaPi2b Monoclonal Antibody on Phosphate Transport in Renal Cancer Cell Line SK-RC-18. *Int. J. Phys. Pathophys* 2, 279–289. doi:10.1615/intjphyspathophys.v2.i3.80

Kiyamova, R., Minigulova, L. F., Skripova, V., Nurgalieva, A., Reshetnikova, D., Savinska, L., et al. (2020). 34P N-Glycosylation Status of Membrane Phosphate Transporter NaPi2b Is Crucial for its Epitope Recognition by Monoclonal Antibody in Tumour Cells. *Ann. Oncol.* 31, S1227–S1228. doi:10.1016/j.annonc.2020.08.2193

Kohl, B., Wagner, C. A., Huelseweh, B., Busch, A. E., and Werner, A. (1998). The Na+-Phosphate Cotransport System (NaPi-II) with a Cleaved Protein Backbone: Implications on Function and Membrane Insertion. *J. Physiol.* 508, 341–350. doi:10.1111/j.1469-7793.1998.341bq.x

Lambert, G., Traebert, M., Biber, J., and Murer, H. (2000). Cleavage of Disulfide Bonds Leads to Inactivation and Degradation of the Type IIa, but Not Type IIb Sodium Phosphate Cotransporter Expressed in *Xenopus laevis* Oocytes. *J. Membr. Biol.* 176, 143–149. doi:10.1007/s00232001083

Lambert, G., Traebert, M., Hernando, N., Biber, J., and Murer, H. (1999). Studies on the Topology of the Renal Type II NaPi-Cotransporter. *Pfl gers Archiv Eur. J. Physiology* 437, 972–978. doi:10.1007/s004240050869

Levi, M., Gratton, E., Forster, I. C., Hernando, N., Wagner, C. A., Biber, J., et al. (2019). Mechanisms of Phosphate Transport. *Nat. Rev. Nephrol.* 15, 482–500. doi:10.1038/s41581-019-0159-y

Lin, K., Rubinfeld, B., Zhang, C., Firestein, R., Harstad, E., Roth, L., et al. (2015). Preclinical Development of an Anti-NaPi2b (SLC34A2) Antibody-Drug Conjugate as a Therapeutic for Non-small Cell Lung and Ovarian Cancers. *Clin. Cancer Res. Off. J. Am. Assoc. Cancer Res.* 21, 5139–5150. doi:10.1158/1078-0432.ccr-14-3383

Lindegren, S., Andrade, L. N. S., Bäck, T., Machado, C. M. L., Horta, B. B., Buchpiguel, C., et al. (2015). Binding Affinity, Specificity and Comparative Biodistribution of the Parental Murine Monoclonal Antibody MX35 (Anti-NaPi2b) and its Humanized Version Rebmab200. *Plos One* 10, e0126298. doi:10.1371/journal.pone.0126298

Lituiev, D. S., and Kiyamova, R. G. (2010). Mutations in the Gene of Human Type IIb Sodium-Phosphate Cotransporter SLC34A2. *Biopolym. Cell.* 26, 13–22. doi:10.7124/bc.00013f

Liu, L., Yang, Y., Zhou, X., Yan, X., and Wu, Z. (2018). Solute Carrier Family 34 Member 2 Overexpression Contributes to Tumor Growth and Poor Patient Survival in Colorectal Cancer. *Biomed. Pharmacother.* 99, 645–654. doi:10.1016/j.biopha.2018.01.124

Mattes, M. J., Look, K., Furukawa, K., Pierce, V. K., Old, L. J., Lewis, J. L., et al. (1987). Mouse Monoclonal Antibodies to Human Epithelial Differentiation Antigens Expressed on the Surface of Ovarian Carcinoma Ascites Cells. *Cancer Res.* 47, 6741–6750.

McHaffie, G. S., Graham, C., Kohl, B., Strunck-Warnecke, U., and Werner, A. (2007). The Role of an Intracellular Cysteine Stretch in the Sorting of the Type II Na/phosphate Cotransporter. *Biochimica Biophysica Acta (BBA) - Biomembr.* 1768, 2099–2106. doi:10.1016/j.bbamem.2007.05.017

Megale, Â. A. A., Júnior, J. M. d. C. F., Rangel, L. B. A., Diz, M. D. P. E., Mano, M. S., Hoff, P. M. G., et al. (2016). Novel Immunogenic Epitopes in the NaPi-IIb Protein: Production of Monospecific Antibodies Using Synthetic Peptides Outlined on Isoform Specific Regions of the Type IIb Sodium-dependent Phosphate Transporter (NaPi-IIb). *Jct* 07, 129–151. doi:10.4236/jct.2016.72015

Mosher, R., Poling, L. L., and Bergstrom, D. A. (2019). *Compositions and Methods for Predicting Response to NaPi2b-Targeted Therapy*. WO Patent No 060542. World Intellectual Property Organization.

Nasie, I., Steiner-Mordoch, S., and Schuldiner, S. (2013). Topology Determination of Untagged Membrane Proteins. *Methods Mol. Biol. Clifton N. J.* 1033, 121–130. doi:10.1007/978-1-62703-487-6_8

Nass, K. J., Ilie, I. M., Saller, M. J., Driessen, A. J. M., Caflisch, A., Kammerer, R. A., et al. (2022). The Role of the N-Terminal Amphipathic Helix in Bacterial YidC: Insights from Functional Studies, the Crystal Structure and Molecular Dynamics Simulations. *Biochimica Biophysica Acta (BBA) - Biomembr.* 1864, 183825. doi:10.1016/j.bbamem.2021.183825

Nurgalieva, A. K., Popov, V. E., Skripova, V. S., Bulatova, L. F., Savenkova, D. V., Vlasenkova, R. A., et al. (2021). Sodium-dependent Phosphate Transporter NaPi2b as a Potential Predictive Marker for Targeted Therapy of Ovarian Cancer. *Biochem. Biophysics Rep.* 28, 101104. doi:10.1016/j.bbrep.2021.101104

Patti, M., Fenollar-Ferrer, C., Werner, A., Forrest, L. R., and Forster, I. C. (2016). Cation Interactions and Membrane Potential Induce Conformational Changes in NaPi-IIb. *Biophysical J.* 111, 973–988. doi:10.1016/j.bpj.2016.07.025

Posada, I. M. D., Busto, J. V., Goñi, F. M., and Alonso, A. (2014). Membrane Binding and Insertion of the Predicted Transmembrane Domain of Human Scramblase 1. *Biochimica Biophysica Acta (BBA) - Biomembr.* 1838, 388–397. doi:10.1016/j.bbamem.2013.09.018

Rangel, L. B. A., Sherman-Baust, C. A., Wernyj, R. P., Schwartz, D. R., Cho, K. R., and Morin, P. J. (2003). Characterization of Novel Human Ovarian Cancer-specific Transcripts (HOSTs) Identified by Serial Analysis of Gene Expression. *Oncogene* 22, 7225–7232. doi:10.1038/sj.onc.1207008

Rubin, S. C., Kostakoglu, L., Divgi, C., Federici, M. G., Finstad, C. L., Lloyd, K. O., et al. (1993). Biodistribution and Intraoperative Evaluation of Radiolabeled Monoclonal Antibody MX 35 in Patients with Epithelial Ovarian Cancer. *Gynecol. Oncol.* 51, 61–66. doi:10.1006/gyno.1993.1247

Santos, R., Ursu, O., Gaulton, A., Bento, A. P., Donadi, R. S., Bologa, C. G., et al. (2017). A Comprehensive Map of Molecular Drug Targets. *Nat. Rev. Drug Discov.* 16, 19–34. doi:10.1038/nrd.2016.230

Seurig, M., Ek, M., von Heijne, G., and Fluman, N. (2019). Dynamic Membrane Topology in an Unassembled Membrane Protein. *Nat. Chem. Biol.* 15, 945–948. doi:10.1038/s41589-019-0356-9

To'a Salazar, G., Huang, Z., Zhang, N., Zhang, X.-G., and An, Z. (2021). Antibody Therapies Targeting Complex Membrane Proteins. *Engineering* 7, 1541–1551. doi:10.1016/j.eng.2020.11.013

Welshinger, M., Yin, B. W. T., and Lloyd, K. O. (1997). Initial Immunochemical Characterization of MX35 Ovarian Cancer Antigen. *Gynecol. Oncol.* 67, 188–192. doi:10.1006/gyno.1997.4846

Yin, B. W., Kiyamova, R., Chua, R., Caballero, O. L., Gout, I., Gryshkova, V., et al. (2008). Monoclonal Antibody MX35 Detects the Membrane Transporter NaPi2b (SLC34A2) in Human Carcinomas. *Cancer Immun.* 8, 3.

Yin, H., and Flynn, A. D. (2016). Drugging Membrane Protein Interactions. *Annu. Rev. Biomed. Eng.* 18, 51–76. doi:10.1146/annurev-bioeng-092115-025322

Yurkovetskiy, A. V., Bodyak, N. D., Yin, M., Thomas, J. D., Clardy, S. M., Conlon, P. R., et al. (2021). Dolaflexin: A Novel Antibody-Drug Conjugate Platform Featuring High Drug Loading and a Controlled Bystander Effect. *Mol. Cancer Ther.* 20, 885–895. doi:10.1158/1535-7163.mct-20-0166

Zhang, Z., Ye, S., Zhang, M., Wu, J., Yan, H., Li, X., et al. (2017). High Expression of SLC34A2 Is a Favorable Prognostic Marker in Lung Adenocarcinoma Patients. *Tumour Biol.* 39, 101042831772021. doi:10.1177/1010428317720212

Zhao, G., and London, E. (2006). An Amino Acid "Transmembrane Tendency" Scale that Approaches the Theoretical Limit to Accuracy for Prediction of Transmembrane Helices: Relationship to Biological Hydrophobicity. *Protein Sci.* 15, 1987–2001. doi:10.1110/ps.062286306

Zhao, Y. J., Lam, C. M. C., and Lee, H. C. (2012). The Membrane-Bound Enzyme CD38 Exists in Two Opposing Orientations. *Sci. Signal.* 5, ra67. doi:10.1126/scisignal.2002700

Conflict of Interest: The authors declare that the research was conducted in the absence of any commercial or financial relationships that could be construed as a potential conflict of interest.

Publisher's Note: All claims expressed in this article are solely those of the authors and do not necessarily represent those of their affiliated organizations, or those of the publisher, the editors, and the reviewers. Any product that may be evaluated in this article, or claim that may be made by its manufacturer, is not guaranteed or endorsed by the publisher.

frontiers | Frontiers in Molecular Biosciences

TYPE Original Research
PUBLISHED 15 August 2022
DOI 10.3389/fmolb.2022.958537

OPEN ACCESS

EDITED BY
Isabel María López-Lara,
National Autonomous University of Mexico, Mexico

REVIEWED BY
Christopher Garvey,
Technical University of Munich, Germany
Ravi K. Shukla,
DIT University, India

*CORRESPONDENCE
Marta Pasenkiewicz-Gierula,
marta.pasenkiewicz-gierula@uj.edu.pl
Michal Markiewicz,
m.markiewicz@uj.edu.pl

SPECIALTY SECTION
This article was submitted to Lipids, Membranes and Membranous Organelles,
a section of the journal
Frontiers in Molecular Biosciences

RECEIVED 31 May 2022
ACCEPTED 11 July 2022
PUBLISHED 15 August 2022

CITATION
Hryc J, Szczelina R, Markiewicz M and Pasenkiewicz-Gierula M (2022), Lipid/water interface of galactolipid bilayers in different lyotropic liquid-crystalline phases.
Front. Mol. Biosci. 9:958537.
doi: 10.3389/fmolb.2022.958537

Lipid/water interface of galactolipid bilayers in different lyotropic liquid-crystalline phases

Jakub Hryc[1], Robert Szczelina[2], Michal Markiewicz[1]* and Marta Pasenkiewicz-Gierula[1]*

[1]Faculty of Biochemistry, Biophysics and Biotechnology, Jagiellonian University, Krakow, Poland, [2]Faculty of Mathematics and Computer Science, Jagiellonian University, Krakow, Poland

In this study, carried out using computational methods, the organisation of the lipid/water interface of bilayers composed of galactolipids with both α-linolenoyl acyl chains is analysed and compared in three different lyotropic liquid-crystalline phases. These systems include the monogalactosyldiglyceride (MGDG) and digalactosyldiglyceride (DGDG) bilayers in the lamellar phase, the MGDG double bilayer during stalk phase formation and the inverse hexagonal MGDG phase. For each system, lipid-water and direct and water-mediated lipid-lipid interactions between the lipids of one bilayer leaflet and those of two apposing leaflets at the onset of new phase (stalk) formation, are identified. A network of interactions between DGDG molecules and its topological properties are derived and compared to those for the MGDG bilayer.

KEYWORDS

monogalactolipid, digalactolipid, bilayer, stalk structure, inverse hexagonal phase, inter-lipid interactions, interaction network

1 Introduction

Biological membranes (biomembranes) surround each cell and cell organelle. Their fundamental structural element is a lipid matrix that also plays the role of a selective permeability barrier. The biological functions that biomembranes can fulfil depend on the lipid composition of the matrix. The composition can vary within a wide range and determines the types and strength of intermolecular interactions and the molecular dynamics of lipids. Subsequently, it determines the physicochemical, biophysical, mechanical and other properties of the matrix and thus of the biomembrane. As the lipid matrix is an intricate system, experimental and computational studies are carried out on much simpler model membranes. Model membranes are hydrated lipid bilayers of a controlled lipid composition typical of the specific biomembrane. Lipid bilayers have three distinct regions, namely the bulk water region, the polar interface consisting of the lipid heads and water molecules, and the nonpolar bilayer core consisting of the lipid hydrocarbon chains. The interfacial region separates the other two regions and constitutes the first barrier preventing free movement of molecules across the bilayer. Moreover,

many important processes occur there (Bondar and Lemieux, 2019). The interface thus plays an essential role in the functioning of the biomembrane.

Even in simple model membranes the lipid/water interface is structurally and dynamically complex. Structurally, because it consists of different types of polar, nonpolar and charged chemical groups and water molecules; dynamically, because the groups are in constant motion and the interfacial water molecules, even though predominantly bound to the lipid head groups (Markiewicz et al., 2015; Calero and Franzese, 2019), undergo rotational and translational motion and exchange with bulk water fast (Rog et al., 2009). Intermolecular interactions, dynamics and spatial organisation of the lipid head groups and water molecules at the interface are strongly interrelated, and this mutual dependence regulates the properties of the interface and thus of the membrane (Disalvo and Disalvo, 2015; Nickels et al., 2015; Frias and Disalvo, 2021).

The lipid composition of the matrix depends on the type of biomembrane within the cell and the function of the cell within the organism. The matrix of the mammalian plasma membrane consists primarily of glycerophospholipids (PL), i.e. phosphatidylcholine (PC), phosphatidylethanolamine (PE), phosphatidylserine (PS), and sphingomyelin (SM), with one saturated and the other mono-*cis*-unsaturated acyl chains (van Meer et al., 2008). PE together with phosphatidylglycerol are the main lipid representatives of the inner bacterial membranes (Dowhan, 1997). The main constituents of thylakoid membranes of chloroplasts are glycolipids with the galactose moieties and the glycerol backbone as the head group, i.e. monogalactosyldiglyceride (MGDG) and digalactosyldiglyceride (DGDG), and both α-linolenoyl (di-18:3, *cis*) acyl chains (Dormann and Benning, 2002). Poly-unsaturation of galactolipid acyl chains is indispensable for proper functioning of thylakoid membranes as summarised in Bratek et al., 2019 (Bratek et al., 2019) and citations therein. Lipopolysaccharides and lipid A are the main constituents of the outer membrane of Gram-negative (G^-) bacteria (Brandenburg et al., 2016).

Due to the importance of the mammalian plasma membrane and the fact that they are relatively straightforward to handle, single or binary mixed PL bilayers as well as those also containing other natural membrane components have been extensively studied and much is known about their interfaces. The lipid/water interface of PL bilayers has been studied using experimental methods e.g. (Gawrisch et al., 1978; Volkov et al., 2007a; Volkov et al., 2007b; Disalvo et al., 2008; Zhao et al., 2008; Beranova et al., 2012; Cheng et al., 2014; Pokorna et al., 2014), although more detailed information about its properties has been provided by computer modelling, e.g. (Rog et al., 2009; Berkowitz and Vacha, 2012; Disalvo et al., 2014; Nickels et al., 2015; Pasenkiewicz-Gierula et al., 2016; Laage et al., 2017; Elola and Rodriguez, 2018; Martelli et al., 2018; Srivastava and Debnath, 2018; Tian and Chiu, 2018; Calero and Franzese, 2019; Kucerka et al., 2019; Srivastava et al., 2019; Deplazes et al., 2020; Luo et al., 2020; Szczelina et al., 2020; Hande and Chakrabarty, 2022).

In contrast to phospholipids, glycolipids are relatively less frequently studied in spite of their widespread occurrence. Publications on the lipid/water interface of galactolipid bilayers either in the lamellar or non-lamellar phases are rather scarce. Experimental studies were carried out on bilayers consisting of galactolipids with 18:3, 18:2 18:1, 18:0 and 16:0 acyl chains, e.g., (Shipley et al., 1973; Marra, 1986; Mcdaniel, 1988; Webb and Green, 1991; Bottier et al., 2007) whereas computational studies were carried out on di-18:3 MGDG, e.g., (Markiewicz et al., 2015; Baczynski et al., 2018; Szczelina et al., 2020), 80% di-18:3 DGDG and 20% 18:3–16:0 DGDG (Kanduc et al., 2017) and di-16:0 glucolipid and di-16:0 galactolipid (Rog et al., 2007) bilayers. Also publications on the interface of lipopolysaccharide and lipid A bilayers are not numerous, e.g. (Snyder et al., 1999; Wu et al., 2013; Murzyn and Pasenkiewicz-Gierula, 2015; Kim et al., 2016; Luna et al., 2021; Paracini et al., 2022).

Whereas di-18:3-*cis* DGDG is a bilayer-forming lipid (Deme et al., 2014), di-18:3-*cis* MGDG is not (Deme et al., 2014); due to the cone shape under ambient conditions it forms an inverse hexagonal (H_{II}) phase in water spontaneously (Sanderson and Williams, 1992). In this study, the organisation of the lipid/water interface of di-18:3-*cis* MGDG bilayers in different lyotropic phases and of the di-18:3-*cis* DGDG lamellar bilayer are analysed and compared. In particular, lipid-water as well as direct and water-mediated lipid-lipid interactions are identified. These interactions take place within the same bilayer interface but also between lipids belonging to the interfaces of apposing leaflets when a new phase begins to form. The strength and branching of inter-lipid interactions at the DGDG bilayer interface are analysed using a formal network analysis approach. The analysis demonstrates that the interactions together with the lipid head groups form a dynamic but stable and extended network. The topological properties of the network are determined and compared with those of the MGDG bilayer (Szczelina et al., 2020).

2 Systems and methods

2.1 Simulation systems

In this molecular modelling study, the lipid/water interface of galactolipid systems in three different lyotropic liquid-crystalline phases is investigated. The galactolipids used to build the systems are monogalactosyldiglyceride (MGDG) and digalactosyldiglyceride (DGDG), each with both α-linolenoyl (di-18:3, *cis*) acyl chains (Figure 1). The investigated phases are MGDG and DGDG lamellar bilayers (Figure 2); the MGDG double bilayer, which forms the stalk phase

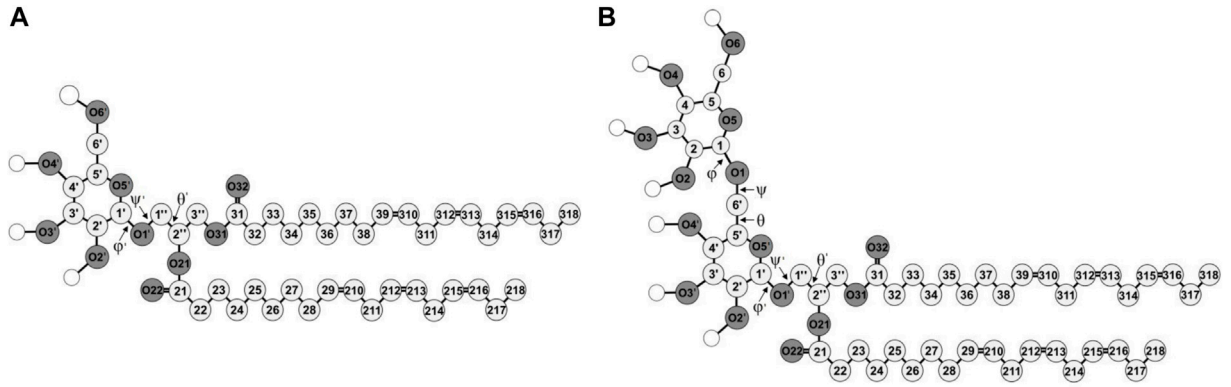

FIGURE 1
Molecular structures of di-18:3-*cis* **(A)** MGDG and **(B)** DGDG. The numbering of the acyl chains and glycerol backbone atoms is according to Sundaralingam's nomenclature (Sundaralingam, 1972), with an exception for the C1″ and C3″ carbon atoms that are swapped here. The numbering of the galactose ring atoms is according to IUPAC convention (McNaught, 1996). The numbers of the carbon and oxygen atoms of the β ring are marked with ′ and the C1, C2 and C3 atoms of the glycerol backbone are marked with ″ to distinguish the atoms of the α and β galactose rings and of the glycerol. The chemical symbol for carbon atoms, C, is omitted and the hydrogen atoms are not shown except for the polar ones shown as empty circles. Oxygen (O) atoms are dark and the carbon atoms are light *grey* circles, respectively.

(Figure 2); and the MGDG inverse hexagonal phase (H_{II}) (Bratek et al., 2019).

The construction and conformational analysis of the computer model of the di-18:3-*cis* MGDG molecule (Figure 1) are described in Refs (Baczynski et al., 2015; Baczynski et al., 2018) and those of di-18:3-*cis* DGDG molecule (Figure 1) are described in Supporting Information (SI). MGDG and DGDG with poly-unsaturated acyl chains were chosen because of their widespread occurrence in Nature and the role they play in photosynthetic membranes (Dormann and Benning, 2002). MGDG and DGDG lamellar bilayers were built from scratch using the Packmol package (Martinez et al., 2009). The MGDG bilayer consisted of 450 MGDG molecules (15 × 15 in each leaflet); the DGDG bilayer consisted of 200 DGDG molecules (10 × 10 in each leaflet). The bilayers were hydrated with 30 H_2O/lipid, i.e. with 13,500 and 6,000 H_2O molecules, respectively, and MD simulated; the MGDG bilayer for 320 ns (Figure 2A), and the DGDG bilayer for 1,050 ns (Figure 2B). 30 H_2O/lipid in the MGDG and DGDG bilayers is more than required for their full hydration. The hydration of DGDG in the lamellar phase and MGDG in hexagonal phase is similar (Brentel et al., 1985) and is 16 H_2O/DGDG (Crowe et al., 1990) and ~19 H_2O/DGDG (Rand and Parsegian, 1989) and 13–14 H_2O/MGDG (Brentel et al., 1985; Crowe et al., 1990; Selstam et al., 1990). This hydration corresponds to about 22% water by weight in both bilayers (Shipley et al., 1973).

The MGDG bilayer was validated in Ref. (Baczynski et al., 2015). Because a pure di-18:3-*cis* MGDG bilayer does not form in water spontaneously, e.g. (Dormann and Benning, 2002) there are no experimental data for this bilayer. Therefore, the MGDG bilayer was validated indirectly by comparing its structural properties with those of a pure di-16:0 MGDG bilayer (Rog et al., 2007; Lopez et al., 2013) and binary di-18:3 MGDG-DMPC bilayers (Kapla et al., 2012); also, with the help of a well-studied dioleoylPC (DOPC) bilayer, e.g., (Liu and Nagle, 2004; Kucerka et al., 2005; Kucerka et al., 2008). The DGDG bilayer is validated in the Results section.

A stalk is a crucial intermediate in the membrane fusion mechanism (Kozlovsky et al., 2004; Kasson and Pande, 2007). This is a local connection of lipids that belong to the inner leaflets of two bilayers which come into close contact (Figures 2D,E) as a result of their partial dehydration, and involves lipid mixing between these leaflets (Kozlov et al., 1989; Ohta-Iino et al., 2001; Salditt and Aeffner, 2016). The MGDG stalk was generated in MD simulation of the double bilayer system. The double bilayer was constructed by duplicating the MGDG bilayer after 300 ns of MD simulation and placing one bilayer on top of the other (Figure 2C and film Supplementary Video S1). The intra-bilayer water layer contained 6,750 H_2O molecules (15 H_2O/MGDG) and the outer water layer contained 13,500 H_2O molecules (30 H_2O/MGDG). The double bilayer (W15 system) was MD simulated for nearly 2,000 ns (Figure 2D). The first vertical connection between the head groups of two galactolipid molecules across the "inner" water layer formed spontaneously (Kozlovsky et al., 2004) within 1 ns of MD simulation (Supplementary Figure S3). A detailed description of the simulation and stalk formation will be presented elsewhere.

The construction of the MGDG H_{II} phase, its MD simulation and validation were described in detail in Ref. (Bratek et al., 2019). Several structures of the phase were tested before its stable computer model was achieved. The stable H_{II} phase consisted of sixteen cylinders, each

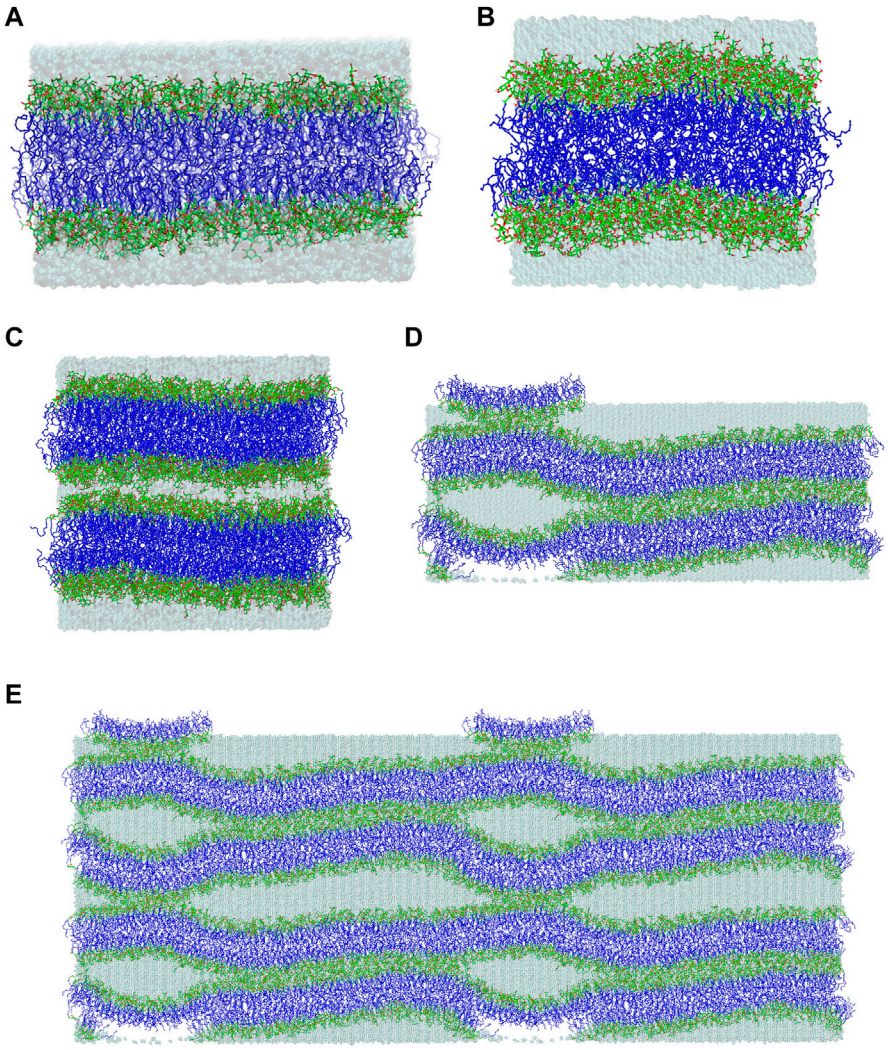

FIGURE 2
Final structures of the **(A)** MGDG and **(B)** DGDG bilayers after 320 and 1,050 ns of MD simulations, respectively. **(C)** Initial and **(D)** final (after ~1,800 ns of MD simulation) structures of the double MGDG bilayer (W15). **(E)** The image of W15 in **(D)** was replicated along the *x*- and *z*-axis over periodic boundaries. The atoms are represented in standard colours, except for acyl chain carbon atoms, which are dark *blue*. The water is shown as a transparent *blue* surface. The hydrogen atoms are not shown.

containing 5,400 water molecules, which corresponded to 30 H_2O/MGDG. The MGDG H_{II} phase generated in 3-μs MD simulation was analysed to obtain such basic structural parameters as hexagonal lattice constant, circular and effective radii of the water channel, surface area/MGDG, and order parameter profiles for the MGDG acyl chains (Bratek et al., 2019). To validate the computer model, experimental data for mainly di-18:3 MGDG (Shipley et al., 1973), mainly di-18:2 MGDG (Bottier et al., 2007), dioleoylPE (DOPE) (Rand and Fuller, 1994) and palmitoyloleoylPE (POPE) (Rappolt et al., 2003) H_{II} phases, were used. The comparison with experimental data was performed by extrapolating the linear dependence of the experimental parameters on the H_{II} phase hydration level, to a hydration level of 30 H_2O/MGDG in the computer-generated H_{II} phase.

2.2 Simulation parameters and conditions

Force field parameters for the α-linolenic chain, and the glycerol moiety of the galactolipids, were taken directly from the all-atom optimised potentials for liquid simulations (OPLS-AA) force field associated with the software package GROMACS 5.05 (Abraham et al., 2015) and supplemented with the partial charges on the glycerol backbone of galactolipids from Ref. (Maciejewski et al., 2014).

The head group of MGDG comprises a single β-D-galactose and the glycerol backbone to which the galactose is attached by an O-glycosidic bond called here β-1′-1″ linkage (cf. Figure 1). The head group of DGDG comprises two galactose moieties, α-D-galactose and β-D-galactose linked by an O-glycosidic bond called here α-1-6 linkage (cf. Figure 1), also attached to the glycerol backbone by the β-1′-1″ linkage. For the galactose moieties of MGDG and DGDG, OPLS-AA parameters for carbohydrates (Damm et al., 1997) were used. The parameters for MGDG and other mono-glycoglycerolipids have been tested successfully in previous atomistic MD-simulation studies (Rog et al., 2007; Baczynski et al., 2015; Markiewicz et al., 2015; Baczynski et al., 2018; Bratek et al., 2019; Szczelina et al., 2020). The DGDG bilayer is validated in the Results section. For water, the transferable intermolecular potential three-point model (TIP3P) was used (Jorgensen et al., 1983).

MD simulations of the lamellar galactolipid bilayers were carried out in the *NPT* ensemble, under a pressure of 1 atm and at a temperature of 295 K (22°C) using the software package GROMACS (Abraham et al., 2015). To control the temperature and pressure, for the first 20 ns of MD simulation, the Berendsen thermostat and barostat (Berendsen et al., 1984) were used, and then the Nosé-Hoover (Nose, 1984; Hoover, 1985) and the Parrinello-Rahman (Parrinello and Rahman, 1981) methods were used, respectively. The relaxation time for the temperature was 0.6 ps and for the pressure 1.0 ps. The temperatures of the solute and solvent were controlled independently, and the pressure was controlled anisotropically.

The linear constraint solver (LINCS) algorithm (Hess et al., 1997) was used to preserve the length of any covalent bond with a hydrogen atom, and the time step was set to 2 fs. The van der Waals interactions were cut-off at 1.0 nm. The long-range electrostatic interactions were evaluated using the particle-mesh Ewald summation method with a β spline interpolation order of 5, and a direct sum tolerance of 10^{-5} (Essmann et al., 1995). For the real space, a cut-off of 1.0 nm, three-dimensional periodic boundary conditions (PBC), and the usual minimum image convention, were used (Essmann et al., 1995). The list of non-bonded pairs was updated every 5 time steps.

The W15 system was MD simulated at 295 K for 320 ns (film SF1, SI). Then, to speed up the process of the MGDG stalk structure formation, the following ~1.4-μs simulation was carried out at 333 K (60°C) with the time step of 1.5 fs. After that, the temperature was gradually lowered to 295 K and after reaching this temperature, MD simulation was continued for 100 ns with a 2-fs time step. The temperature profile of this simulation is shown in Supplementary Figure S4. All other simulation parameters and conditions as well as the simulation programme were the same as in the case of the lamellar systems.

All trajectories analysed in this paper were recorded every 1 ps.

The MGDG H_{II} phase was generated in a 3-μs MD simulation, also at 295 K (22°C) and the trajectory was recorded every 2 ps (Bratek et al., 2019).

Visualisation of the results was done with the VMD 1.9.3 (Humphrey et al., 1996) and PyMOL 1.8.4 (DeLano, 2010) programmes.

2.3 Network analysis

The methodology used to analyse the interaction network at the bilayer interface is described in detail in Ref. (Szczelina et al., 2020). The basis of network analysis and the main weighted network parameters are summarised here only briefly. Mathematically, a network can be described and modelled by means of graph theory. In the following, the terms "network" and "graph" are interchangeable. Here, the objects of the graph are lipid molecules (centres-of-mass) in one bilayer leaflet (nodes) and intermolecular interactions between them are the graph edges. Consecutive pairs of nodes connected by edges form a path. A cluster is a set of interconnected nodes where each node has a path to all other nodes. A cluster size is the number of nodes which make a particular cluster. A graph is connected when it is made of only one cluster. The node degree is the number of edges connecting this node to other nodes. The node strength is determined by the number of individual interactions that account for each edge of the node, the average energy of each type of interaction and lifetime of the edge. A network bridge is an edge removing which disconnects the graph.

Network analysis was carried out using NetworkX (Hagberg et al., 2008), a Python language software package for creating, manipulating, and studying the structure, dynamics, and functions of complex networks. Network bridges were identified using a bridge-finding algorithm that employs the chain decompositions described in Ref. (Schmidt, 2013). The network at the DGDG bilayer was visualised using Cytoscape (Shannon et al., 2003).

3 Results

3.1 Systems equilibration and validation

Time profiles of the potential energy (Ep), the average surface area per lipid (A_L) and the bilayer width (D_{RR}) of the MGDG and DGDG bilayers are shown in Figure 3. The average A_L was obtained by dividing the simulation box surface area by the number of lipids in one bilayer leaflet. The average D_{RR} was defined and calculated as the distance between the average positions of the centres-of-mass of the single galactose rings (MGDG) or of the double galactose rings (DGDG), in the opposite bilayer leaflets, in a similar fashion to Ref. (Baczynski et al., 2015). Each of the three bilayer parameters converged to

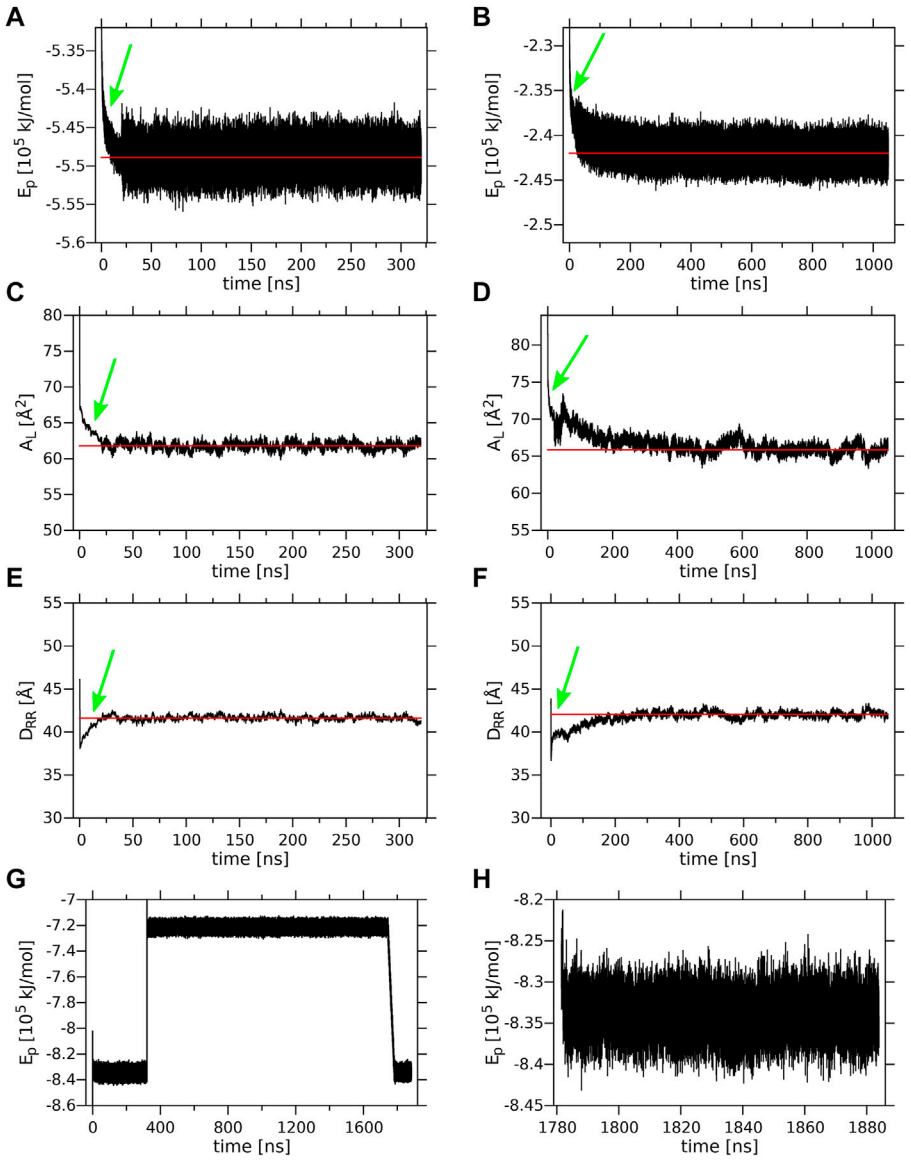

FIGURE 3
Equilibration of the lamellar MGDG and DGDG bilayers and the W15 system. Time profiles of the **(A)** MGDG and **(B)** DGDG potential energy (Ep); **(C)** MGDG and **(D)** DGDG average surface area per lipid (A_L); **(E)** MGDG and **(F)** DGDG average bilayer width (D_{RR}), during 320 and 1,050 ns, respectively, of MD simulations at 295 K. **(A–F)** The time (20 ns) when the *T* and *p* control methods were switched (cf. sec. 2.2) is marked with a *green* arrow; the *red* line shows the average value of a given parameter. Time profiles of Ep **(G)** for the whole ~1,800-ns and **(H)** for the last 100-ns (when the system's temperature was 295 K) of MD simulation of the W15 system.

some constant value (Figure 3). The time profiles for the MGDG bilayer (Figures 3A,C,E) indicated that the bilayer equilibrated within ~50 ns of MD simulation. However, the equilibration time of the DGDG bilayer was difficult to assess on the basis of the time profiles in Figure 3; therefore, the average values of Ep, A_L and D_{RR} were calculated at three time segments (400–500, 500–600, 600–1,050, Supplementary Table S2), which indicated that the DGDG bilayer equilibrated within ~500 ns of MD simulation. The average values of Ep, A_L and D_{RR} for the MGDG and the DGDG bilayer are given in Table 1 and are marked in Figure 3 as straight *red* lines. Additionally, to compare with some experimental values, the average D_{CC} bilayer width was calculated as the distance between the average positions of the C2″ atoms (cf. Figure 1) in the opposite leaflets of the MGDG and DGDG bilayers (Table 1). For the MGDG bilayer the averages presented below were obtained for the time range 200–300 ns, while for the DGDG bilayer they were obtained for the range 900–1,000 ns of the respective MD simulations.

TABLE 1 Mean values of the simulated systems parameters.

System	Ep [10^5 kJ/mol]	A_L [Å^2]	D_{RR} [Å]	D_{CC} [Å]	Tilt [°]
MGDG	−5.488 ± 0.02	61.77 ± 0.50	41.60 ± 0.28	34.59 ± 0.25	β: 32
DGDG	−2.420 ± 0.01	65.84 ± 0.63	42.04 ± 0.33	33.39 ± 0.31	α: 30 β: 36
W15	−8.340 ± 0.02	64.26 ± 0.72	40.39 ± 0.39	33.80 ± 0.40	β: 42

Time average values of the potential energy (Ep), surface area per lipid (A_L) and bilayer width (D_{RR}, and D_{CC}) (see text) as well as the preferred tilt angle (maximum of the ω angle probability distribution in Supplementary Figure S5) of the β and α rings for the MGDG, and DGDG, bilayers and the W15 system, MD, simulated at 295 K. The W15 system was cooled from 333 to 295 K and MD, simulated at this temperature for 100 ns (see Figure 3G); the average value of Ep was calculated for the whole W15 system and those for A_L, D_{RR}, and D_{CC}, for its "flat" part (marked with a *black* frame in Figure 4A) over the last 60 ns. The errors are standard deviation estimates.

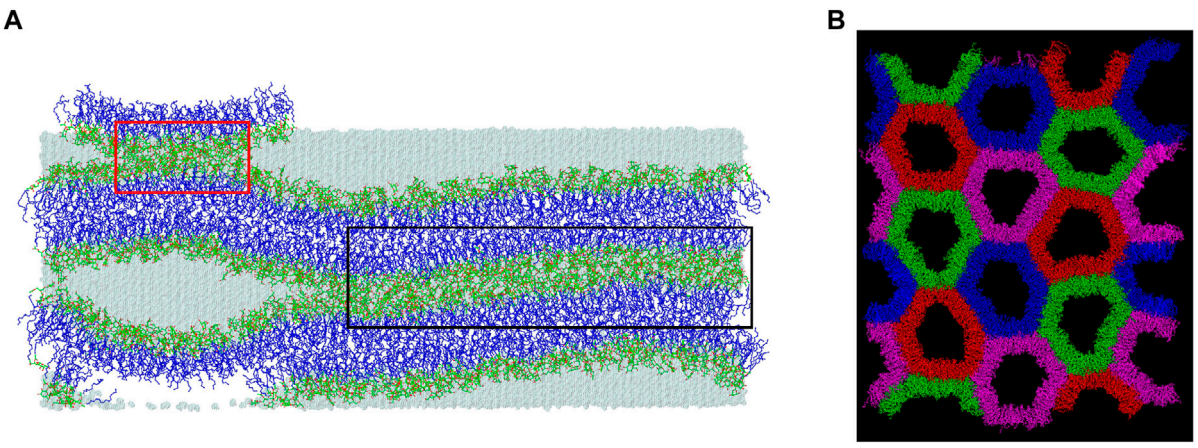

FIGURE 4
Three regions of W15 and top view of the H_{II} phase. **(A)** The concave region is not marked; the larger connect-15 region formed through the "inner" water layer (15 H_2O/MGDG) is marked with a *black* frame and the smaller connect-30 region newly forming over the PBC through the "outer" water layer (30 H_2O/MGDG) is marked with a *red* frame. The atoms are represented in standard colours, except for the acyl chain carbon atoms which are dark *blue*. The water is shown as a transparent *blue* surface. The hydrogen atoms are not shown. **(B)** Top view of the H_{II} phase generated Ref. (Bratek et al., 2019) after 3 μs of MD simulation. The water-filled cylinders are in different colours to show the H_{II} phase structure better. The water molecules are not shown.

Errors in the average values derived are standard deviation estimates.

The equilibrated lamellar MGDG and DGDG bilayers are shown in Figures 2A,B, respectively.

The values for A_L of 61.77 ± 0.50 Å^2 and D_{RR} of 41.60 ± 0.28 Å obtained in this study for the MGDG bilayer are very close to those obtained in Ref. (Baczynski et al., 2015), where the MGDG bilayer was validated (cf. sections 2.1).

The values for A_L of 65.84 ± 0.63 Å^2 and D_{RR} of 42.04 ± 0.33 Å obtained in this study for the DGDG bilayer MD simulated for 1 μs can be compared with those published in the literature—for A_L they range between 63 and 78 Å^2 and for D_{RR} between 41 and 44 Å. Most of the published values of A_L and D_{RR} were obtained from MD simulations, either coarse grained of 64 ± 1 Å^2 and of 41 Å, respectively, for the di-16:0 DGDG bilayer (Lopez et al., 2013) and 63 ± 1 Å^2 and 44 ± 3 Å, respectively, for the di-18:3 DGDG bilayer (Navarro-Retamal et al., 2018), atomistic united-atom of ~78 Å^2 and 41.7 Å, respectively, for the mixed DGDG bilayer containing 80% di-18:3 DGDG and 20% 18:3–16:0 (Kanduc et al., 2017) or atomistic all-atom of 67 Å^2 and 42 Å, respectively, for the di-16:0 DGDG bilayer (Lopez et al., 2013). The experimental values of A_L and D_{RR} obtained using X-ray diffraction are ~75 Å^2 and 41.6 Å, respectively (Shipley et al., 1973), and of D_{RR} obtained using neutron diffraction is 41 Å (Mcdaniel, 1988), for the bilayers consisting of DGDG with 18:3, 16:0, 18:4, 18:2, and smaller amounts of 16:1, 18:0, 18:1 acyl chains, but mainly of di-18:3 DGDG (Shipley et al., 1973).

The results of MD simulations show some dependence of the acyl chain unsaturation on the bilayer structural properties, although it should be remembered that the computer models of the DGDG molecule used in those studies had different resolutions, thus the structural parameters derived may somewhat differ from one another. Other differences in the

TABLE 2 Number of lipid-water interactions in the MGDG and DGDG lamellar bilayers.

Bilayer	MGDG	DGDG
# H-bonds/head	9.37 ± 0.10	12.83 ± 0.19
# H-bonds/rings (H; O)	6.34 ± 0.08 (2.54 ± 0.05; 3.81 ± 0.05)	9.95 ± 0.17 (3.88 ± 0.08; 6.06 ± 0.12)
# H-bonds/α ring	–	5.81 ± 0.12
# H-bonds/β ring	–	4.14 ± 0.10
# H-bonds/gly	3.02 ± 0.06	2.88 ± 0.06
# H-bonded H_2O/head	7.14 ± 0.09	9.07 ± 0.15
# WB/head	1.70 ± 0.06	2.89 ± 0.15
# ring-ring WB/head	0.80 ± 0.04	1.81 ± 0.12
#α ring-α ring WB/head	–	0.59 ± 0.06
#α ring-β ring WB/head	–	0.82 ± 0.07
#β ring-β ring WB/head	–	0.40 ± 0.05
# gly-gly WB/head	0.26 ± 0.02	0.24 ± 0.03
# gly-ring WB/head	0.63 ± 0.04	0.84 ± 0.06

Average numbers of lipid-water H-bonds (# H-bonds); H-bonded water molecules (#H bonded H_2O) and water bridges (# WB) per lipid head, rings and glycerol backbone (gly) and additionally per α and β rings of DGDG, at the interface of the MGDG, and DGDG, bilayers. In parenthesis are the numbers of interactions via H (H-bond donor) and O (H-bond acceptor) atoms of the ring moieties. The glycerol backbone includes the O1' atom (cf. Figure 1).

results may stem from the differing acyl chain compositions of the bilayers, e.g. (Shipley et al., 1973; Kanduc et al., 2017). Besides, the surface area/DGDG in the bilayer in Ref. (Kanduc et al., 2017), after initial equilibration, was kept constant, so its value may be not accurate.

The above comparisons demonstrate that the DGDG bilayer generated in this MD simulation study is effective in reproducing the basic bilayer properties determined in previous studies. Furthermore, the entries in Supplementary Table S1 imply that the conformational states of the DGDG head group concur well with experimental, e.g. (Hirotsu and Higuchi, 1976; Wormald et al., 2002; Ziolkowska et al., 2007; Nakae et al., 2018) and computer simulation, e.g. (Peric-Hassler et al., 2010) data for other disaccharides (cf. SI). Thus, the conclusion that the DGDG bilayer is positively validated is justified.

The initial and final structures of the W15 system are shown in Figures 2C,D. W15 is in the process of stalk phase formation (film Supplementary Video S1) and thus is not at equilibrium. Nevertheless, its energy profile (Figure 3G) was calculated for the whole MD simulation time of ~1,800 nsas well as for the last 100 ns (Figure 3H), when the temperature, after lowering from 333 to 295 K, was stable at 295 K (cf. Methods). The average value of the whole system's Ep, as well as the values of A_L, D_{RR} and D_{CC} for its "flat" part (marked with a *black* frame in Figure 4A) calculated over the last 60 ns of MD simulation of the W15 systems equilibrated at 295 K, are given in Table 1.

3.2 Lipid-water H-bonds

MGDG has four OH groups that are both donors and acceptors of hydrogen bonds (H-bond) and six O atoms that are only acceptors of H-bonds (Figure 1) can thus make numerous H-bonds with water molecules. The average numbers of particular types of the MGDG-water interactions are given in Table 2.

DGDG has seven OH groups that are both donors and acceptors of H-bonds and eight O atoms that are only acceptors of H-bonds (Figure 1). Accordingly, the average numbers of DGDG-water interactions (Table 2) are greater than those of MGDG, although somewhat smaller than expected.

Water molecules bind preferentially to the MGDG and DGDG rings and are 50% more often H-bond donors than acceptors (Table 2). In the water-glycerol H-bonding, water is the only H-bond donor. The number of water-glycerol H-bonds is only slightly smaller in the DGDG than the MGDG bilayer (Table 2).

The smaller than expected number of H-bonds with water and H-bonded water molecules in the DGDG than the MGDG bilayer is to some extent compensated by the larger number of water bridges (WB) (Pasenkiewicz-Gierula et al., 1997), which link pairs of galactolipid head groups. WBs form predominantly between galactolipid rings, although the number of glycerol-ring WBs in both bilayers is also quite significant (Table 2).

From Figures 2D, 4A it is apparent that the W15 system has two distinct regions—"region of full hydration" and "region of reduced hydration" (Figure 4A). The "full hydration region", which is called concave is not marked in Figure 4A. The larger "reduced hydration" region forms as a result of the local cross-water connection of two inner leaflets of the double bilayer that were originally separated by the thinner "inner" water layer (15 H_2O/MGDG). It is marked with a *black* frame in Figures 4A and is called connect-15. The smaller "reduced hydration" region is still forming over the PBC as a result of the local

TABLE 3 Number of lipid-water interactions in the MGDG lamellar and non-lamellar systems.

System	#H_2O-lipid H-bond/head	#H Bonded H_2O/head	WB/head horizontal	WB/head vertical	WB/head total
MGDG bilayer	9.37 ± 0.10	7.14 ± 0.09	1.70 ± 0.06	–	–
W15; concave	9.18 ± 0.18	6.99 ± 0.15	1.69 ± 0.10	–	–
W15; connect-15	8.13 ± 0.14	5.51 ± 0.07	1.57 ± 0.09	0.72 ± 0.06	2.28 ± 0.11
W15; connect-30	8.64 ± 0.23	6.25 ± 0.23	1.41 ± 0.16	0.56 ± 0.11	1.97 ± 0.20
H_{II}	8.23 ± 0.04	6.01 ± 0.03	1.90 ± 0.03	–	–

Concave is the region of W15 that contains excess water (not marked in Figure 4A); connect-15, and connect-30 (cf. Main text) are regions of W15 that are marked with *black* and *red* frames, respectively, in Figure 4A. The inverse hexagonal MGDG, phase (H_{II}) was generated in Ref. (Bratek et al., 2019). In the connect-15, and connect-30 regions, the numbers of the horizontal and vertical WBs (see text) are given. To make comparison easier, some data for the MGDG, bilayer from Table 2 were added to Table 3.

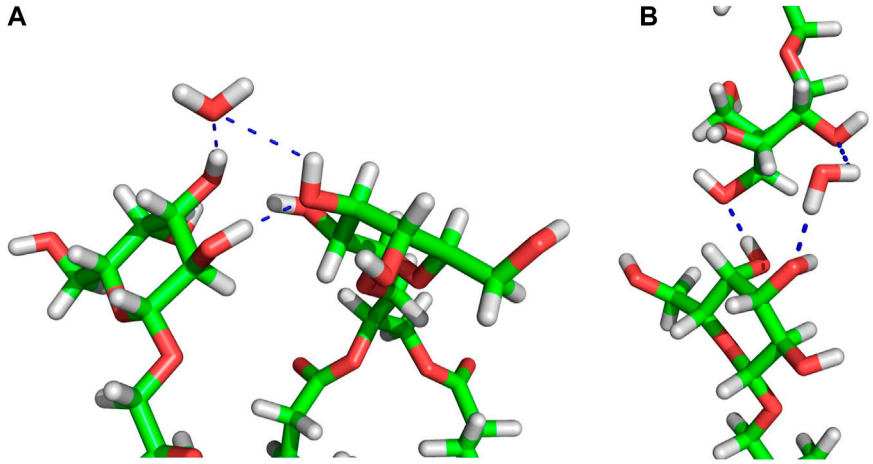

FIGURE 5
Examples of MGDG-MGDG H-bonds and water bridges at the interface of the W15 connect-15 region. **(A)** Horizontal (between lipids belonging to the same bilayer leaflet) interactions; **(B)** vertical (between lipids belonging to the apposing leaflets) interactions. The molecules are shown as sticks in standard colours (acyl chains are cut off). The dotted *blue* lines represent intermolecular interactions. In **(A)** the water molecule is an acceptor of two H-bonds, in **(B)** the water molecule is a donor of two H-bonds.

cross-water connection of two outer leaflets of the double bilayer that were originally separated by the thicker "outer" water layer (30 H_2O/MGDG). It is marked with a *red* frame in Figures 4A and is called connect-30. The connections are more visible in Figure 2E.

The average number of each type of MGDG-water interaction in a specified region of the W15 system and in the MGDG H_{II} channels is given in Table 3. The numbers of MGDG-water H-bonds and water bridges (horizontal) as well as H_2O molecules H-bonded by MGDG in the concave region of W15 are very similar to those in the MGDG lamellar bilayer, but those in the connect regions, particularly in the connect-15, are smaller (Tables 2, 3). The numbers of H-bonds and H-bonded H_2O molecules in the MGDG H_{II} phase are smaller than those in the concave region, but are similar to those in the connect regions of W15 (Table 3).

In the connect-15 and connect-30 regions, the horizontal and vertical WBs can be distinguished. The horizontal WBs are between lipids of the same bilayer leaflet (Figure 5A) and the vertical are between lipids of the apposing leaflets (Figure 5B). In both regions, the number of horizontal WBs is larger than that of the vertical ones but somewhat smaller than the number of them in the MGDG lamellar bilayer and the concave region. This could indicate that there is some competition between the horizontal and vertical WBs. Nevertheless, the total number of WBs (horizontal and vertical) in each connect region is larger than the number of those in the concave region and the lamellar bilayer. The number of water bridges (horizontal) in the MGDG H_{II} phase is higher than in the MGDG bilayer and any W15 region (Table 3).

3.3 Lipid-lipid interactions

The MGDG and DGDG heads have both H-bond acceptor and donor groups. Therefore, they can be linked by direct inter-

TABLE 4 Number of lipid-lipid interactions.

System	# Head-head H-bonds/head	# Head-head WB/head
MGDG bilayer	0.87 ± 0.04	1.70 ± 0.06
#β ring-β ring/MGDG	0.57 ± 0.03	0.80 ± 0.04
DGDG bilayer	1.97 ± 0.08	2.89 ± 0.15
#α ring-α ring/DGDG	0.46 ± 0.03	0.59 ± 0.06
#α ring-β ring/DGDG	0.32 ± 0.03	0.82 ± 0.07
#β ring-β ring/DGDG	0.69 ± 0.07	0.40 ± 0.05
W15; concave	0.94 ± 0.06	1.69 ± 0.10
W15; connect-15	H: 0.90 ± 0.05	H: 1.57 ± 0.09
	V: 0.41 ± 0.04	V: 0.72 ± 0.06
	T: 1.31 ± 0.07	T: 2.28 ± 0.11
W15; connect-30	H: 0.81 ± 0.09	H: 1.41 ± 0.16
	V: 0.31 ± 0.16	V: 0.56 ± 0.11
	T: 1.12 ± 0.12	T: 1.97 ± 0.20
H_{II}	1.33 ± 0.02	1.90 ± 0.03

Average numbers of direct lipid-lipid H-bonds (second column) in the MGDG, and DGDG, lamellar bilayers per head and per the α and β rings of DGDG; the concave, connect-15, and connect-30 regions of W15 (cf. Figure 4A) as well as in the inverse hexagonal MGDG, phase (H_{II}). For comparison, the average numbers of WBs, from Table 2 and 3 are also given (third column). H, V and T stand for the horizontal, vertical and total direct H-bonds and WBs, respectively (see text).

lipid H-bonds at the lipid/water interface, in addition to water bridges, which are water-mediated lipid-lipid interactions (Table 2, 3). The numbers of direct H-bonds in the MGDG and DGDG lamellar bilayers, the W15 system and its specified regions, as well as in the MGDG H_{II} phase, are given in Table 4. The number of H-bond acceptor and donor groups of DGDG is 50% larger than that of MGDG; however, the number of DGDG-water H-bonds is only ~37% greater, whereas the numbers of WBs and direct H-bonds are 70 and ~130%, respectively, greater than those of MGDG (Tables 2, 4). This indicates that at the bilayer interface the head groups of DGDG interact preferentially with one another, rather than with water, whereas interactions between the MGDG head groups and water are relatively numerous.

To obtain a better insight, the numbers of ring-water and ring-ring interactions in the DGDG bilayer were calculated for the α and β galactose rings separately. The results given in Tables 2, 4 show that the number of intermolecular interactions of each DGDG ring is different.

In the connect regions of W15, the MGDG head groups form both horizontal and vertical inter-lipid H-bonds (Figure 5), as in the case of WBs. The average numbers of horizontal H-bonds in the three regions of W15 are similar to each other and also similar to the number of them in the MGDG lamellar bilayer. This implies that, in contrast to WBs, different H-bond donor and acceptor groups of MGDG are involved in formation of the horizontal and the vertical direct H-bonds.

The number of lipid-lipid H-bonds in the MGDG H_{II} phase is higher than in the MGDG bilayer or any W15 region (Table 4), as is the number of WBs.

3.4 Orientation of the galactolipid head group

The orientation of the MGDG head group in the bilayer is determined here, as in Ref. (Baczynski et al., 2018), by angle ω between the MGDG head group vector, which connects the C2″ atom in the glycerol and the O4' atom in the galactose ring (Figure 1A), and the bilayer normal. Ref. (Baczynski et al., 2018) correlations between angle ω and the conformation of the torsion angles of the glycosidic linkages, and also between angle ω and the numbers of head-water and head-head interactions at the MGDG bilayer interface, were calculated. Significant conclusions of those calculations were that there was virtually no correlation between the orientation of the MGDG head group and the conformation of its glycosidic linkage, and that there was only a weak correlation between the MGDG head group orientation and the number of intermolecular interactions of the head.

The most probable (preferred) orientation, called here tilt, of the head group is angle ω, for which the ω distribution has the main maximum. The distributions of ω and tilts for MGDG in the bilayer and in the connect-15 region of W15 obtained in this study are shown in Supplementary Figure S5A, B and are given in Table 1, respectively. In the MGDG bilayer the ω distribution is smooth and the vector tilt is 32°. Both are similar to those in Ref. (Baczynski et al., 2018). In the connect-15 region the ω distribution has a long tail and the vector tilt is 42°. These results can possibly be linked to the somewhat uneven surface of the connect-15 region (Figure 4A) and to the onset of the rotation of some of the MGDG molecules in the process of formation of the stalk structure.

The tilt of the DGDG α ring in the bilayer was obtained from the distribution of angle ω between the α ring vector (C2″-O4 vector, Figure 1B) and the bilayer normal (Supplementary Figure S5C), and that of the DGDG β ring was obtained from the distribution of the ω angle between the β ring vector (C2″-O4' vector, Figure 1B) and the bilayer normal (Supplementary Figure S5D); both tilts are given in Table 1. The tilt of the DGDG α ring of 30° is almost the same as that of the MGDG β ring of 32°. However, their ω distributions differ. In addition to the main maximum in the ω distribution of the α ring vector at 30°, there are smaller but clear maxima at ~60°, ~80° and the last one at ~140°. These maxima indicate that the α ring may have three additional less populated but stable orientations.

The tilt of the DGDG β ring is 36°. Even though the tilts of the DGDG α and β ring vectors are similar, the rings belong to different planes (Supplementary Figure S6). The distribution of the angle between the planes of the α and β rings shown in Supplementary Figure S7 has two maxima. The higher, relatively narrow maximum is at 82° and the significantly lower one is at 162°. The angles are most likely determined by the preferred populations of the torsion angles of the α-1-6 and β-1′-1″ glycosidic linkages. On the basis of the results of Ref. (Baczynski et al., 2018) it is justified to assume the angles between the α and β ring planes do not depend on the α and β ring tilts.

3.5 Density profile of the terminal CH_3 groups of galactolipid acyl chains

The density profiles of the terminal CH_3 groups of the poly-*cis*-unsaturated α-linolenoyl acyl chains of MGDG and DGDG across the bilayer were calculated to estimate the probability of finding the groups in the interfacial region of each bilayer, and to compare this probability with the results of previous experimental, e.g. (Feix et al., 1984; Mihailescu et al., 2011) and computer simulation, e.g. (Mihailescu et al., 2011) studies. The profiles across the MGDG and DGDG bilayers and connect-15 region are shown in Supplementary Figure S8. The probability was calculated for each leaflet of the bilayers from the area under the fragment of the CH_3 profile where the electron density of water is non-zero (Supplementary Figure S8). The estimated probability (averaged over both leaflets) of finding a CH_3 group at the bilayer interface is ~15% in the MGDG bilayer and ~16% in the DGDG bilayer.

3.6 Network analysis of the DGDG bilayer

At the bilayer interface, the galactolipid head groups and interactions (H-bonds and water bridges) between them create a network of interactions. In Ref. (Szczelina et al., 2020) several topological properties of the network in the MGDG bilayers were determined. Here, the same methodology (cf. section 2.3) is used to analyse the interaction network in the DGDG bilayer. The values of the network parameters (cf. section 2.3), averaged over the last 50 ns of MD simulation of the DGDG bilayer, are given in Table 5, together with those obtained for the MGDG bilayers in Ref. (Szczelina et al., 2020). As the interacting groups of MGDG and DGDG head groups are the same, in this calculation the average energies of H-bonding and water bridging of DGDG are assumed to be the same as those of MGDG calculated in Ref. (Szczelina et al., 2020). The interaction network in the DGDG bilayer is presented in Figure 6 and its time changes are shown in film Supplementary Video S2.

The values given in Table 5 are graphically presented in Supplementary Figures S9,S10. These figures also provide additional information. The distribution of the node degrees shown in Supplementary Figure S9A indicates that the most probable degree in the DGDG bilayer is 5. This means that two DGDG head groups are most often connected by five individual inter-lipid interactions, and the smallest number of such interactions is two. The results shown in Supplementary Figure S9C demonstrate that only clusters of sizes 1, 2, 98, 99 and 100 have non-zero probability of forming and the probability of forming a cluster of size 100 is at least two orders of magnitude larger than that of the remaining ones. Time profiles of the average number of clusters and the average sizes of the smallest and the largest clusters are shown in Supplementary Figure S10; the averages are over two networks, each in one bilayer leaflet. Supplementary Figure S10A reveals that in each bilayer leaflet the network is connected for most of the time. However, from time to time one of the connected networks breaks for a short while into two clusters and the average number of clusters is then 1.5. Only in one case does the network break into three clusters (of sizes 1, 1 and 98) and the average number of clusters is then 2 (Supplementary Figure S10A). The average size of the smallest cluster is either 100 or nearly 50 (Supplementary Figure S10B) and that of the largest is either 100 or nearly 100 (Supplementary Figure S10C). For most of the time, the sizes of the smallest and the largest clusters are 100. The time profile of the average node strength plotted in Supplementary Figure S10D only fluctuates around the average value, and this indicates that the average node strength is stable during the simulation time.

4 Discussion

4.1 MGDG and DGDG bilayers

An interesting result of this study is that the DGDG bilayer equilibrated after a much longer time than the MGDG bilayer. This effect was previously noticed by Kanduč et al. (Kanduc et al., 2017) and explained as arising from the "pronounced hydrogen-bonding capabilities" of DGDG (Kanduc et al.,

TABLE 5 Mean values of the network parameters.

Bilayer (# lipids in a leaflet)	MGDG* (8 × 8)	4 MGDG* (16 × 16)	DGDG (10 × 10)
# H-bonds	1.04 ± 0.08	1.03 ± 0.04	1.90 ± 0.06
# water bridges	1.74 ± 0.13	1.69 ± 0.06	3.11 ± 0.12
# clusters	1.52 ± 0.53	3.27 ± 1.09	1.01 ± 0.06
size smallest	39.05 ± 21.78	28.83 ± 56.23	99.30 ± 5.86
size largest (%)	63.25 ± 0.99 (98.8)	252.80 ± 2.02 (98.7)	99.99 ± 0.06 (100)
# network bridges	5.12 ± 2.19	21.11 ± 4.44	0.21 ± 0.33
node strength	35.25 ± 2.03	34.86 ± 0.95	34.47 ± 1.09
Edge lifetime [ps]			
Direct H-bonds	1.73 ± 0.006	1.73 ± 0.004	0.86 ± 0.003
Water bridges	1.44 ± 0.007	1.43 ± 0.005	0.80 ± 0.004
Interaction energy [kcal/mol]			
Direct H-bonds	−5.12 ± 2.75	−5.12 ± 2.75	−5.12 ± 2.75
Water bridges	−14.23 ± 7.80	−14.23 ± 7.80	−14.23 ± 7.80

Average numbers (#) of lipid-lipid H-bonds and water bridges; average number of clusters (# clusters); average size of the smallest (size smallest) and largest (size largest) clusters (in parenthesis, % of the lipid molecules in one bilayer leaflet); average number of network bridges (# network bridges); average node strength; average lifetimes of inter-node edges (Edge lifetime) in networks via H-bonds (Direct H-bond) and via water bridges; average energy of the H-bond (Direct H-bond) and the water bridge interaction (Interaction energy) for the MGDG*, 4 MGDG* (Szczelina et al., 2020) and DGDG, bilayers MD, simulated at 295 K. The numbers for the DGDG bilayer are averages over the last 50 ns of the 1,050-ns MD simulation. The errors are standard deviation estimates, except for the errors in edge lifetimes, which are estimated as in Ref. (Szczelina et al., 2020).

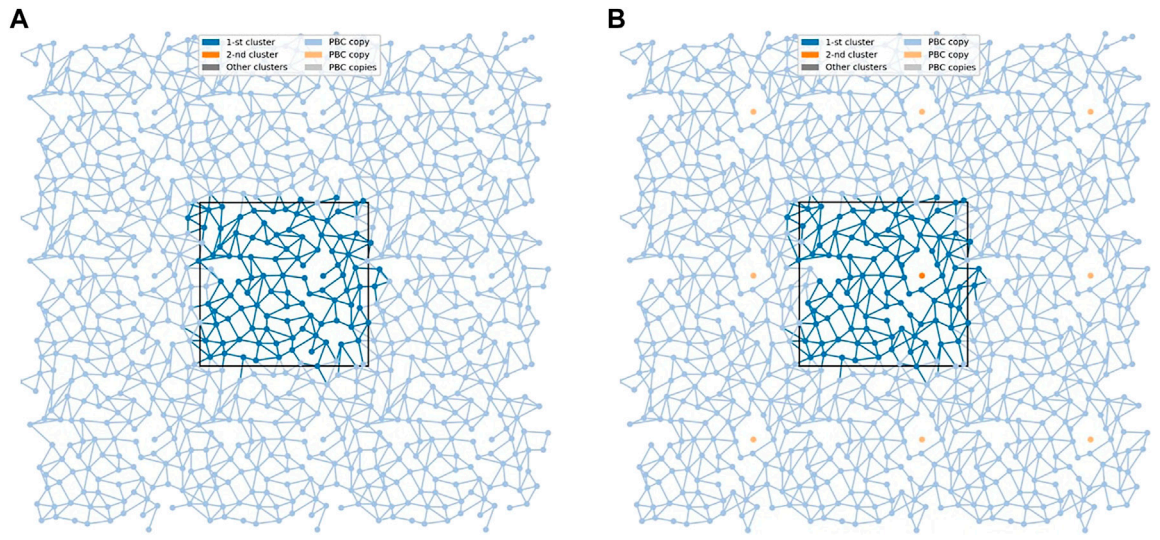

FIGURE 6
The networks of lipid interconnections at the interfaces of the DGDG bilayer at two time frames 1 ps apart. **(A)** The network is connected and **(B)** the connected network is broken into two clusters. The *black* rectangle depicts the basic simulation box. Nodes (centres-of-mass of the lipids) are presented as dots in the *x,y*-plane, and edges as lines connecting respective nodes. The largest cluster is in *blue* and a single-node cluster is in *orange*. To avoid problems with edges crossing PBC, 9 copies of each node are presented (strong colour tone for the cluster, soft colour tones for its 8 PBC copies); the edges are drawn in the basic simulation box and all its copies.

2017). Our results indicate that direct DGDG-DGDG H-bonds as well as WBs at the DGDG bilayer interface are indeed numerous (Table 4). The detailed spatial organisation of these inter-lipid links is revealed by network analysis (Hagberg et al., 2008) (cf. Section 3.6). The network of the connections (H-bonds and WBs) is shown in Figure 6 and its dynamics in film Supplementary Video S2. The figure, the film and the network parameters in Table 5 as well as Supplementary Figures S9,S10 demonstrate that the connections are not only numerous, but also extended, and

branched and for most of the time encompass all DGDG molecules in each bilayer leaflet.

The interaction network in the DGDG bilayer is qualitatively similar to those in the MGDG bilayers (Szczelina et al., 2020), but is considerably more stable. It also differs in some other aspects. The most probable node degree in the DGDG bilayer is 5 (Supplementary Figure S9A), whereas in the MGDG bilayer it is 3 (Szczelina et al., 2020). The average number of clusters is ~1 (Table 5; Supplementary Figures S9B,S10A), whereas in the MGDG bilayer, depending on its size, it is ~1.5 or ~3 (Table 5). The number of network bridges (0.21) is much smaller than in the MGDG bilayers (Table 5). The small number of network bridges in the DGDG bilayer indicates that the connected network disconnects rarely (Supplementary Figure S10A) and much less often than in the 4 MGDG bilayer, cf. Supporting Information of Ref. (Szczelina et al., 2020).

Probably due to the greater A_L (65.8 vs. 61.8 Å^2), the lifetimes of network edges consisting of only H-bond interactions and of only water bridge interactions in the DGDG bilayer are about half the length of those in the MGDG bilayers (Table 5). However, because the numbers of individual inter-lipid interactions are about twice as great and the energies of the interactions are the same, the node strength in the DGDG and MGDG bilayers are similar.

In the DGDG bilayer, as in the MGDG bilayers (Szczelina et al., 2020), the average node strength is stable during the analysis time (Supplementary Figure S10D). This indicates that the pattern of lipid interconnections at the bilayer interface is also stable in spite of the relatively short lifetimes of the network edges (Table 5), their fast rearrangements (film Supplementary Video S2) and the overall dynamics of the bilayer interfacial region.

Despite the fact that the network of interconnections at the DGDG bilayer interface is more stable, extended and branched than that at the MGDG bilayer interface, the large head group and cylindrical shape of the DGDG molecule prevent formation of non-bilayer phases, as is the case with the MGDG aggregates.

An apparent disproportion in the number of inter-lipid links at the bilayer interface between the DGDG and the MGDG bilayer (cf. section 3.3) can possibly be explained as follows. The tilt of the MGDG β galactose rings relative to the bilayer normal is 32° (Table 1), thus their polar groups are quite exposed to the water phase. In contrast, the DGDG β rings are screened from water by the α rings so they make fewer H-bonds with water than those of MGDG (Table 2). Due to smaller hydration, the polar groups of the DGDG β ring make fewer ring-ring WBs but more direct ring-ring H-bonds than those of the MGDG β ring and the DGDG α ring (Table 4). As a consequence of the hydration disparity of the DGDG α and β rings, the β-α WBs are more numerous and the β-α H-bonds are less numerous than those of the α-α rings (Tables 2, 4).

The tilt of the DGDG α galactose rings (O4-C2″ vector) is 30° and is practically the same as that of the MGDG β galactose rings, which is 32° (Table 1). However, the average numbers of ring-water H-bonds and ring-ring H-bonds and WBs made by the DGDG α ring are smaller than those made by the MGDG β ring (Tables 2, 4). This is because in addition to the α ring-water and α-α rings interactions, the α ring also interacts with the DGDG β ring. These interactions can be seen in the ω angle distribution in Supplementary Figure S5 as secondary maxima. They indicate that the DGDG α ring, on top of the preferred one, has three other less populated but stable orientations. Two of these orientations (~60° and ~80°) are possibly stabilised by its interactions with the β ring (particularly WBs) and one (~140°) with the glycerol backbone (Tables 2, 4). The values obtained for the DGDG α ring orientation are only in partial agreement with conclusions derived on the basis of experimental data that "the polar head group of this lipid (DGDG) is oriented parallel to the plane of the bilayer" (Marra, 1986; Mcdaniel, 1988). The distribution of angle ω in Supplementary Figure S5 indicates that only a small fraction of the DGDG α rings is oriented parallel to the bilayer plane.

Previous experimental, e.g. (Feix et al., 1984; Mihailescu et al., 2011) and computer simulation, e.g. (Mihailescu et al., 2011) studies have revealed that the terminal CH_3 groups of PL acyl chains can locate in the bilayer interfacial region. Using the electron-electron double-resonance methodology Felix et al. (Feix et al., 1984) showed that the probability of finding the CH_3 group of a saturated acyl chain at the interface is 14%. While using the neutron diffraction methodology Mihailescu et al. (Mihailescu et al., 2011) showed that the probability of finding the CH_3 group of a mono-*cis*-unsaturated acyl chain at the bilayer interface is 20%. This location of the CH_3 groups was also found in an MD simulation study (Mihailescu et al., 2011). In this study the probability of finding the CH_3 group of a poly-*cis*-unsaturated acyl chain was calculated from the electron densities of the CH_3 groups and the water of each bilayer leaflet (Supplementary Figure S8), and was found to be ~15% in the MGDG bilayer and ~16% in the DGDG bilayer. Thus, these results predict that the terminal CH_3 group not only of a saturated and a mono-unsaturated acyl chain of PC but also of a poly-unsaturated acyl chain of MGDG and DGDG can be found in the interfacial bilayer region.

4.2 W15 system

In the W15 system, two MGDG bilayers were initially placed parallel to each other and separated by two water layers, namely, the thinner "inner" water layer containing 6,750 H_2O molecules (15 H_2O/MGDG) and the thicker "outer" water layer containing 13,500 H_2O molecules (30 H_2O/MGDG) (Figure 2). In the course of MD simulation, the distance between the bilayers decreased in some places and increased in some others, indicating the onset of stalk structure formation (film Supplementary Video S1). The first vertical lipid-lipid contact across the "inner" water layer formed

within the initial 1 ns of MD simulation at 295 K (Supplementary Figure S3). Local partial dehydration leading to formation of the connect-15 region can be seen in film SF1 (SI). In this dehydration process, each MGDG molecule loses on average approximately one H-bond with water and ~1.5 H-bonded water molecules, but gains ~0.6 WBs and ~0.4 inter-lipid H-bonds (Table 3). Thus, interactions with water are replaced by lipid-lipid interaction. Water molecules move from the connect to the concave regions; this process is relatively fast as can be deduced from film Supplementary Video S1.

Hydration of MGDG molecules as well as the number of inter-lipid interactions in the W15 concave region are practically the same as in the MGDG bilayer. This might be because the W15 is in the process of stalk structure formation. The stalk structure involves lipid mixing between apposing leaflets (Kozlov et al., 1989; Ohta-Iino et al., 2001; Salditt and Aeffner, 2016), which requires rotation of lipid molecules so as to transform the concave region into a water-filled tube, whose inner surface consists of lipid heads. This rotation only started in the connect-15 region of W15, so the properties of the concave region are more like those of the MGDG bilayer than of the MGDG H_{II} phase. The onset of rotation of some of the MGDG molecules in W15 can be deduced from the long tail in the ω distribution for the MGDG ring vector in the connect-15 region (Supplementary Figure S5B), and the relatively high value of the MGDG tilt, being 42° (Table 1).

4.3 H_{II} phase

Details of the construction and MD simulation of the MGDG H_{II} phase are described in Ref. (Bratek et al., 2019). The MGDG H_{II} phase consisted of sixteen cylinders (Figure 4B), each filled with 5,400 water molecules (30 H_2O/MGDG). In that paper, the basic structural parameters of the H_{II} phase were identified (cf. section 2.1). In this paper, the average hydration and the average number of inter-lipid interactions of the MGDG head groups are calculated. Compared to the MGDG bilayer and the concave region of W15, the MGDG head groups in the H_{II} phase are less hydrated than in the bilayer, but their hydration is similar to that in the connect regions of W15, whereas their mutual interactions are more numerous than in the bilayer and W15.

4.4 Effect of acyl chains on the H_{II} phase structure

Combined X-ray, neutron scattering and MD simulation studies indicate that the length and mono- and poly-unsaturation of PL acyl chains have an impact, among others, on the lipid surface area in PC, e.g. (Pabst et al., 2010; Marquardt et al., 2020) and PE, e.g. (Kucerka et al., 2015) bilayers. Using a different experimental approach, the effect of the length and unsaturation of the acyl chains on lipid hydration in PC and PE monolayers is revealed (Maltseva et al., 2022). Yet, our previous MD simulation study on *cis*- and *trans*-mono-unsaturated PC bilayers indicates that the conformation of the double bond does not have much impact on the lipid surface area (Murzyn et al., 2001).

The results for the H_{II} phase are in contrast with those for lamellar PL bilayers. The experimentally derived structural parameters such as hexagonal lattice constant (*dhex*) and radius of the water channel (*r*), as a function of the hydration level for mainly di-18:3 MGDG, mainly di-18:2 MGDG, di-18:1 DOPE and 16:0–18:1 POPE H_{II} phases, either in the case of *dhex* or *r*, lie on one straight line, irrespectively of the degree of the acyl chains (Ref. (Bratek et al., 2019) and explanations therein). Moreover, the values of the average surface area/MGDG in the cylinders of the H_{II} phases as a function of the hydration level also lie on one curve, irrespectively of the type of acyl chains (Ref. Bratek et al., 2019), SI). Thus, these structural parameters depend predominantly on the hydration level of the phase and not on the degree of the unsaturation of the acyl chains.

5 Conclusion

The analyses presented in this paper revealed:

(1) In the interfacial region of the MGDG and DGDG bilayers, the galactolipid and water molecules interact via direct H-bonds and water bridges.
(2) At the bilayer/water interface MGDG interacts with water more readily than DGDG.
(3) At the bilayer/water interface the lipid-lipid interactions are more readily formed in the DGDG than the MGDG bilayer.
(4) The disproportionally higher number of DGDG-DGDG interactions relative to the number of the DGDG H-bond donor and acceptor groups can be explained by screening the DGDG β rings from the water by the α rings. This screening results in the hydration disparity of the DGDG α and β rings and the different preferences of the rings to interact via H-bonds and water bridges.
(5) The network of inter-lipid interactions at the DGDG bilayer interface is more stable and extended than that in the MGDG bilayer. Nevertheless, a DGDG aggregate under ambient conditions does not form H_{II} phase in water spontaneously; this is most likely due to the cylindrical shape of the DGDG molecule and its large head group.
(6) In the system consisting of two MGDG bilayers separated by a water layer containing 6,750 H_2O molecules (15 H_2O/MGDG) a MGDG stalk structure begins to form; the structure is visible as local vertical contacts of MGDG head groups from the apposing bilayer leaflets separated by water-filled tunnels (W15 system).
(7) The number of lipid-lipid and lipid-water interactions at the interface of the water-filled tunnel of the MGDG stalk structure is similar to that of the MGDG bilayer.

(8) The number of lipid-water interactions in the locally connected regions of the MGDG stalk structure is smaller than that at the interface of the MGDG bilayer.
(9) In the locally connected regions of the MGDG stalk structure both horizontal (between lipids from the same bilayer leaflet) and vertical (between lipids from apposing bilayer leaflets) inter-lipid H-bonds and water bridges are formed.
(10) The total number of lipid-lipid horizontal and vertical interactions in the locally connected regions of the MGDG stalk structure is greater than the number of horizontal lipid-lipid interactions in the MGDG bilayer.
(11) The number of lipid-water interactions in the MGDG H_{II} phase is similar to that in the locally connected regions of the stalk structure and smaller than that in the MGDG bilayer.
(12) The number of inter-lipid H-bonds (horizontal) in the MGDG H_{II} phase is greater than in the MGDG bilayer (horizontal) and similar to the total (horizontal and vertical) number of inter-lipid H-bonds in the locally connected regions of the MGDG stalk structure. The number of water bridges in the MGDG H_{II} phase is greater than in the MGDG bilayer and moderately similar to the total (horizontal and vertical) number of water bridges in the locally connected regions of the MGDG stalk structure.
(13) From 11 to 12 one can conclude that when the nonlamellar phase is formed, the lipid-water interactions are, to some extent, replaced by lipid-lipid interactions.

Data availability statement

The original contributions presented in the study are included in the article/Supplementary Material, further inquiries can be directed to the corresponding author.

Author contributions

MP-G conceived the study. JH, MM and MPG designed the study. JH carried out all MD simulations and analyses. RS performed all network analyses. MM supervised the computations. JH and RS created all figures and films. MP-G wrote the final version of the manuscript with input from all authors. All authors discussed the results, read, and approved the submitted version.

References

Abraham, M. J., Murtola, T., Schulz, R., Pall, S., Smith, J. C., Hess, B., et al. (2015). Gromacs: High performance molecular simulations through multi-level parallelism from laptops to supercomputers. *SoftwareX* 1-2, 19–25. doi:10.1016/j.softx.2015.06.001

Baczynski, K., Markiewicz, M., and Pasenkiewicz-Gierula, M. (2018). Is the tilt of the lipid head group correlated with the number of intermolecular interactions at the bilayer interface? *FEBS Lett.* 592 (9), 1507–1515. doi:10.1002/1873-3468.13048

Baczynski, K., Markiewicz, M., and Pasenkiewicz-Gierula, M. (2015). A computer model of a polyunsaturated monogalactolipid bilayer. *Biochimie* 118, 129–140. doi:10.1016/j.biochi.2015.09.007

Beranova, L., Humpolickova, J., Sykora, J., Benda, A., Cwiklik, L., Jurkiewicz, P., et al. (2012). Effect of heavy water on phospholipid membranes: Experimental confirmation of molecular dynamics simulations. *Phys. Chem. Chem. Phys.* 14 (42), 14516–14522. doi:10.1039/c2cp41275f

Funding

This research was supported in part by PL-Grid Infrastructure. The work has been partly performed under the Project HPC-EUROPA3 (INFRAIA-2016-1–730,897), with the support of the EC Research Innovation Action under the H2020 Programme. The open-access publication of this article was funded by the Department of Computational Biophysics and Bioinformatics, Jagiellonian University, Krakow, Poland.

Acknowledgments

J.H. gratefully acknowledges the support of Waldemar Kulig, University of Helsinki, and the computer resources and technical support provided by CSC, also the support by the project for PhD students and Young Scientists FBBB N19/MNW/000014.

Conflict of interest

The authors declare that the research was conducted in the absence of any commercial or financial relationships that could be construed as a potential conflict of interest.

Publisher's note

Supplementary material

The Supplementary Material for this article can be found online at: https://www.frontiersin.org/articles/10.3389/fmolb.2022.958537/full#supplementary-material

Berendsen, H. J. C., Postma, J. P. M., Vangunsteren, W. F., Dinola, A., and Haak, J. R. (1984). Molecular-dynamics with coupling to an external bath. *J. Chem. Phys.* 81 (8), 3684–3690. doi:10.1063/1.448118

Berkowitz, M. L., and Vacha, R. (2012). Aqueous solutions at the interface with phospholipid bilayers. *Acc. Chem. Res.* 45 (1), 74–82. doi:10.1021/ar200079x

Bottier, C., Gean, J., Artzner, F., Desbat, B., Pezolet, M., Renault, A., et al. (2007). Galactosyl headgroup interactions control the molecular packing of wheat lipids in Langmuir films and in hydrated liquid-crystalline mesophases. *Biochim. Biophys. Acta* 1768 (6), 1526–1540. doi:10.1016/j.bbamem.2007.02.021

Bondar, A. N., and Lemieux, M. J. (2019). Reactions at biomembrane interfaces. *Chem. Rev.* 119 (9), 6162–6183. doi:10.1021/acs.chemrev.8b00596

Brandenburg, K., Heinbockel, L., Correa, W., Fukuoka, S., Gutsmann, T., Zahringer, U., et al. (2016). Supramolecular structure of enterobacterial wild-type lipopolysaccharides (LPS), fractions thereof, and their neutralization by Pep19-2.5. *J. Struct. Biol.* 194 (1), 68–77. doi:10.1016/j.jsb.2016.01.014

Bratek, L., Markiewicz, M., Baczynski, K., Jalocha-Bratek, J., and Pasenkiewicz-Gierula, M. (2019). Inverse hexagonal phase of poly-unsaturated monogalactolipid: A computer model and analysis. *J. Mol. Liq.* 290, 111189. doi:10.1016/j.molliq.2019.111189

Brentel, I., Selstam, E., and Lindblom, G. (1985). Phase-equilibria of mixtures of plant galactolipids - the formation of a bicontinuous cubic phase. *Biochimica Biophysica Acta - Biomembr.* 812 (3), 816–826. doi:10.1016/0005-2736(85)90277-9

Calero, C., and Franzese, G. (2019). Membranes with different hydration levels: The interface between bound and unbound hydration water. *J. Mol. Liq.* 273, 488–496. doi:10.1016/j.molliq.2018.10.074

Cheng, C. Y., Olijve, L. L. C., Kausik, R., and Han, S. G. (2014). Cholesterol enhances surface water diffusion of phospholipid bilayers. *J. Chem. Phys.* 141 (22), 22D513. doi:10.1063/1.4897539

Crowe, J. H., and Crowe, L. M. (1990). "Lyotropic effects of water on phospholipids," in *Water science reviews 5*. Editor F. Franks (Cambridge: Cambridge University Press), 1–21.

Damm, W., Frontera, A., TiradoRives, J., and Jorgensen, W. L. (1997). OPLS all-atom force field for carbohydrates. *J. Comput. Chem.* 18 (16), 1955–1970. doi:10.1002/(sici)1096-987x(199712)18:16<1955::aid-jcc1>3.0.co;2-l

DeLano, W. L. (2010). *The PyMOL molecular graphics system*, Version 1.8. Schrödinger, LLC.

Deme, B., Cataye, C., Block, M. A., Marechal, E., and Jouhet, J. (2014). Contribution of galactoglycerolipids to the 3-dimensional architecture of thylakoids. *Faseb J.* 28 (8), 3373–3383. doi:10.1096/fj.13-247395

Deplazes, E., Sarrami, F., and Poger, D. (2020). Effect of H3O+ on the structure and dynamics of water at the interface with phospholipid bilayers. *J. Phys. Chem. B* 124 (8), 1361–1373. doi:10.1021/acs.jpcb.9b10169

Disalvo, E. A., Lairion, F., Martini, F., Tymczyszyn, E., Frias, M., Almaleck, H., et al. (2008). Structural and functional properties of hydration and confined water in membrane interfaces. *Biochim. Biophys. Acta* 1778 (12), 2655–2670. doi:10.1016/j.bbamem.2008.08.025

Disalvo, E. A., Martini, M. F., Bouchet, A. M., Hollmann, A., and Frias, M. A. (2014). Structural and thermodynamic properties of water-membrane interphases: Significance for peptide/membrane interactions. *Adv. Colloid Interface Sci.* 211, 17–33. doi:10.1016/j.cis.2014.05.002

Disalvo, E. A. (2015). "Membrane hydration: A hint to a new model for biomembranes," in *Membrane hydration the role of water in the structure and function of biological membranes. Subcellular biochemistry. 71*. Editor E. A. Disalvo (Cham: Springer), 1–16.

Dormann, P., and Benning, C. (2002). Galactolipids rule in seed plants. *Trends Plant Sci.* 7 (3), 112–118. doi:10.1016/s1360-1385(01)02216-6

Dowhan, W. (1997). Molecular basis for membrane phospholipid diversity: Why are there so many lipids? *Annu. Rev. Biochem.* 66, 199–232. doi:10.1146/annurev.biochem.66.1.199

Elola, M. D., and Rodriguez, J. (2018). Influence of cholesterol on the dynamics of hydration in phospholipid bilayers. *J. Phys. Chem. B* 122 (22), 5897–5907. doi:10.1021/acs.jpcb.8b00360

Essmann, U., Perera, L., Berkowitz, M. L., Darden, T., Lee, H., Pedersen, L. G., et al. (1995). A smooth particle mesh Ewald method. *J. Chem. Phys.* 103 (19), 8577–8593. doi:10.1063/1.470117

Feix, J. B., Popp, C. A., Venkataramu, S. D., Beth, A. H., Park, J. H., Hyde, J. S., et al. (1984). An electron-electron double-resonance study of interactions between [14N]- and [15N]stearic acid spin-label pairs: Lateral diffusion and vertical fluctuations in dimyristoylphosphatidylcholine. *Biochemistry* 23 (10), 2293–2299. doi:10.1021/bi00305a032

Frias, M. A., and Disalvo, E. A. (2021). Breakdown of classical paradigms in relation to membrane structure and functions. *Bba-Biomembranes.* 1863 (2), 183512. doi:10.1016/j.bbamem.2020.183512

Gawrisch, K., Arnold, K., Gottwald, T., Klose, G., and Volke, F. (1978). D-2 NMR-studies of phosphate - water interaction in dipalmitoyl phosphatidylcholine - water-systems. *Stud. Biophys.* 74, 13–14.

Hagberg, A. A., Schult, D. A., and Swart, P. J. (Editors) (2008). "Exploring network structure, dynamics, and function using NetworkX," *Proceedings of the 7th Python in science conference (SciPy2008)* (Pasadena, CA USA.

Hande, V. R., and Chakrabarty, S. (2022). How far is "bulk water" from interfaces? Depends on the nature of the surface and what we measure. *J. Phys. Chem. B* 126, 1125–1135. doi:10.1021/acs.jpcb.1c08603

Hess, B., Bekker, H., Berendsen, H. J. C., and Fraaije, J. G. E. M. (1997). Lincs: A linear constraint solver for molecular simulations. *J. Comput. Chem.* 18 (12), 1463–1472. doi:10.1002/(sici)1096-987x(199709)18:12<1463::aid-jcc4>3.0.co;2-h

Hirotsu, K., and Higuchi, T. (1976). The conformations of oligosaccharides. III. The crystal and molecular structure of melibiose monohydrate. *Bull. Chem. Soc. Jpn.* 49 (5), 1240–1245. doi:10.1246/bcsj.49.1240

Hoover, W. (1985). Canonical dynamics: Equilibrium phase-space distributions. *Phys. Rev. A Gen. Phys.* 31 (3), 1695–1697. doi:10.1103/physreva.31.1695

Humphrey, W., Dalke, A., and Schulten, K. (1996). Vmd: Visual molecular dynamics. *J. Mol. Graph.* 14 (1), 33–38. doi:10.1016/0263-7855(96)00018-5

Jorgensen, W. L., Chandrasekhar, J., Madura, J. D., Impey, R. W., and Klein, M. L. (1983). Comparison of simple potential functions for simulating liquid water. *J. Chem. Phys.* 79 (2), 926–935. doi:10.1063/1.445869

Kanduc, M., Schlaich, A., de Vries, A. H., Jouhet, J., Marechal, E., Deme, B., et al. (2017). Tight cohesion between glycolipid membranes results from balanced water-headgroup interactions. *Nat. Commun.* 8, 14899. doi:10.1038/ncomms14899

Kapla, J., Stevensson, B., Dahlberg, M., and Maliniak, A. (2012). Molecular dynamics simulations of membranes composed of glycolipids and phospholipids. *J. Phys. Chem. B* 116 (1), 244–252. doi:10.1021/jp209268p

Kasson, P. M., and Pande, V. S. (2007). Control of membrane fusion mechanism by lipid composition: Predictions from ensemble molecular dynamics. *PLoS Comput. Biol.* 3 (11), e220. doi:10.1371/journal.pcbi.0030220

Kim, S., Patel, D. S., Park, S., Slusky, J., Klauda, J. B., Widmalm, G., et al. (2016). Bilayer properties of lipid A from various gram-negative bacteria. *Biophys. J.* 111 (8), 1750–1760. doi:10.1016/j.bpj.2016.09.001

Kozlov, M. M., Leikin, S. L., Chernomordik, L. V., Markin, V. S., and Chizmadzhev, Y. A. (1989). Stalk mechanism of vesicle fusion - intermixing of aqueous contents. *Eur. Biophys. J.* 17 (3), 121–129. doi:10.1007/BF00254765

Kozlovsky, Y., Efrat, A., Siegel, D. A., and Kozlov, M. M. (2004). Stalk phase formation: Effects of dehydration and saddle splay modulus. *Biophys. J.* 87 (4), 2508–2521. doi:10.1529/biophysj.103.038075

Kucerka, N., Gallova, J., and Uhrikova, D. (2019). The membrane structure and function affected by water. *Chem. Phys. Lipids* 221, 140–144. doi:10.1016/j.chemphyslip.2019.04.002

Kucerka, N., Nagle, J. F., Sachs, J. N., Feller, S. E., Pencer, J., Jackson, A., et al. (2008). Lipid bilayer structure determined by the simultaneous analysis of neutron and x-ray scattering data. *Biophys. J.* 95 (5), 2356–2367. doi:10.1529/biophysj.108.132662

Kucerka, N., Tristram-Nagle, S., and Nagle, J. F. (2005). Structure of fully hydrated fluid phase lipid bilayers with monounsaturated chains. *J. Membr. Biol.* 208 (3), 193–202. doi:10.1007/s00232-005-7006-8

Kucerka, N., van Oosten, B., Pan, J. J., Heberle, F. A., Harroun, T. A., Katsaras, J., et al. (2015). Molecular structures of fluid phosphatidylethanolamine bilayers obtained from simulation-to-experiment comparisons and experimental scattering density profiles. *J. Phys. Chem. B* 119 (5), 1947–1956. doi:10.1021/jp511159q

Laage, D., Elsaesser, T., and Hynes, J. T. (2017). Water dynamics in the hydration shells of biomolecules. *Chem. Rev.* 117 (16), 10694–10725. doi:10.1021/acs.chemrev.6b00765

Liu, Y. F., and Nagle, J. F. (2004). Diffuse scattering provides material parameters and electron density profiles of biomembranes. *Phys. Rev. E Stat. Nonlin. Soft Matter Phys.* 69 (4), 040901. doi:10.1103/PhysRevE.69.040901

Lopez, C. A., Sovova, Z., van Eerden, F. J., de Vries, A. H., and Marrink, S. J. (2013). Martini force field parameters for glycolipids. *J. Chem. Theory Comput.* 9 (3), 1694–1708. doi:10.1021/ct3009655

Luna, E., Kim, S., Gao, Y., Widmalm, G., and Im, W. (2021). Influences ofVibrio choleraeLipid A types on lps bilayer properties. *J. Phys. Chem. B* 125, 2105–2112. doi:10.1021/acs.jpcb.0c09144

Luo, Y., Zhou, G. B., Li, L., Xiong, S. Y., Yang, Z., Chen, X. S., et al. (2020). Hydrogen bond-induced responses in mid- and far-infrared spectra of interfacial

water at phospholipid bilayers. *Fluid Phase Equilibr* 518, 112626. doi:10.1016/j.fluid.2020.112626

Maciejewski, A., Pasenkiewicz-Gierula, M., Cramariuc, O., Vattulainen, I., and Rog, T. (2014). Refined OPLS all-atom force field for saturated phosphatidylcholine bilayers at full hydration. *J. Phys. Chem. B* 118 (17), 4571–4581. doi:10.1021/jp5016627

Maltseva, D., Gonella, G., Ruysschaert, J-M., and Bonn, M. (2022). Phospholipid acyl tail affects lipid headgroup orientation and membrane hydration. *J. Chem. Phys.* 156, 234706–234710. doi:10.1063/5.0092237

Markiewicz, M., Baczynski, K., and Pasenkiewicz-Gierula, M. (2015). Properties of water hydrating the galactolipid and phospholipid bilayers: A molecular dynamics simulation study. *Acta Biochim. Pol.* 62 (3), 475–481. doi:10.18388/abp.2015_1077

Marquardt, D., Heberle, F. A., Pan, J. J., Cheng, X. L., Pabst, G., Harroun, T. A., et al. (2020). The structures of polyunsaturated lipid bilayers by joint refinement of neutron and X-ray scattering data. *Chem. Phys. Lipids* 229, 104892. doi:10.1016/j.chemphyslip.2020.104892

Marra, J. (1986). Direct measurements of attractive vanderwaals and adhesion forces between uncharged lipid bilayers in aqueous-solutions. *J. Colloid Interface Sci.* 109 (1), 11–20. doi:10.1016/0021-9797(86)90276-6

Martelli, F., Ko, H. Y., Borallo, C. C., and Franzese, G. (2018). Structural properties of water confined by phospholipid membranes. *Front. Phys. (Beijing).* 13 (1), 136801. doi:10.1007/s11467-017-0704-8

Martinez, L., Andrade, R., Birgin, E. G., and Martinez, J. M. (2009). Packmol: A package for building initial configurations for molecular dynamics simulations. *J. Comput. Chem.* 30 (13), 2157–2164. doi:10.1002/jcc.21224

Mcdaniel, R. V. (1988). Neutron-diffraction studies of digalactosyldiacylglycerol. *Biochim. Biophys. Acta* 940 (1), 158–164. doi:10.1016/0005-2736(88)90020-x

McNaught, A. D. (1996). Nomenclature of carbohydrates (IUPAC recommendations 1996). *Pure Appl. Chem.* 68 (10), 1919–2008. doi:10.1351/pac199668101919

Mihailescu, M., Vaswani, R. G., Jardon-Valadez, E., Castro-Roman, F., Freites, J. A., Worcester, D. L., et al. (2011). Acyl-chain methyl distributions of liquid-ordered and -disordered membranes. *Biophys. J.* 100 (6), 1455–1462. doi:10.1016/j.bpj.2011.01.035

Murzyn, K., and Pasenkiewicz-Gierula, M. (2015). Structural properties of the water/membrane interface of a bilayer built of the *E. coli* lipid A. *J. Phys. Chem. B* 119 (18), 5846–5856. doi:10.1021/jp5119629

Murzyn, K., Rog, T., Jezierski, G., Takaoka, Y., and Pasenkiewicz-Gierula, M. (2001). Effects of phospholipid unsaturation on the membrane/water interface: A molecular simulation study. *Biophys. J.* 81 (1), 170–183. doi:10.1016/S0006-3495(01)75689-5

Nakae, S., Shionyu, M., Ogawa, T., and Shirai, T. (2018). Structures of jacalin-related lectin PPL3 regulating pearl shell biomineralization. *Proteins* 86 (6), 644–653. doi:10.1002/prot.25491

Navarro-Retamal, C., Bremer, A., Ingolfsson, H. I., Alzate-Morales, J., Caballero, J., Thalhammer, A., et al. (2018). Folding and lipid composition determine membrane interaction of the disordered protein COR15A. *Biophys. J.* 115 (6), 968–980. doi:10.1016/j.bpj.2018.08.014

Nickels, J. D., and Katsaras, J. (2015). "Water and lipid bilayers," in *Membrane hydration*. Editor E. A. Disalvo (Switzerland: Springer), 45–67.

Nose, S. (1984). A unified formulation of the constant temperature molecular-dynamics methods. *J. Chem. Phys.* 81 (1), 511–519. doi:10.1063/1.447334

Ohta-Iino, S., Pasenkiewicz-Gierula, M., Takaoka, Y., Miyagawa, H., Kitamura, K., and Kusumi, A. (2001). Fast lipid disorientation at the onset of membrane fusion revealed by molecular dynamics simulations. *Biophys. J.* 81 (1), 217–224. doi:10.1016/S0006-3495(01)75693-7

Pabst, G., Kucerka, N., Nieh, M. P., Rheinstadter, M. C., and Katsaras, J. (2010). Applications of neutron and X-ray scattering to the study of biologically relevant model membranes. *Chem. Phys. Lipids* 163 (6), 460–479. doi:10.1016/j.chemphyslip.2010.03.010

Paracini, N., Schneck, E., Imberty, A., and Micciulla, S. (2022). Lipopolysaccharides at solid and liquid interfaces: Models for biophysical studies of the gram-negative bacterial outer membrane. *Adv. Colloid Interfac.* 301, 102603. doi:10.1016/j.cis.2022.102603

Parrinello, M., and Rahman, A. (1981). Polymorphic transitions in single crystals: A new molecular dynamics method. *J. Appl. Phys.* 52 (12), 7182–7190. doi:10.1063/1.328693

Pasenkiewicz-Gierula, M., Baczynski, K., Markiewicz, M., and Murzyn, K. (2016). Computer modelling studies of the bilayer/water interface. *Biochim. Biophys. Acta* 1858 (10), 2305–2321. doi:10.1016/j.bbamem.2016.01.024

Pasenkiewicz-Gierula, M., Takaoka, Y., Miyagawa, H., Kitamura, K., and Kusumi, A. (1997). Hydrogen bonding of water to phosphatidylcholine in the membrane as studied by a molecular dynamics simulation: Location, geometry, and lipid-lipid bridging via hydrogen-bonded water. *J. Phys. Chem. A* 101 (20), 3677–3691. doi:10.1021/jp962099v

Peric-Hassler, L., Hansen, H. S., Baron, R., and Hunenberger, P. H. (2010). Conformational properties of glucose-based disaccharides investigated using molecular dynamics simulations with local elevation umbrella sampling. *Carbohydr. Res.* 345 (12), 1781–1801. doi:10.1016/j.carres.2010.05.026

Pokorna, S., Jurkiewicz, P., Vazdar, M., Cwiklik, L., Jungwirth, P., Hof, M., et al. (2014). Does fluoride disrupt hydrogen bond network in cationic lipid bilayer? Time-dependent fluorescence shift of laurdan and molecular dynamics simulations. *J. Chem. Phys.* 141 (22), 22D516. doi:10.1063/1.4898798

Rand, R. P., and Fuller, N. L. (1994). Structural dimensions and their changes in a reentrant hexagonal-lamellar transition of phospholipids. *Biophys. J.* 66 (6), 2127–2138. doi:10.1016/S0006-3495(94)81008-2

Rand, R. P., and Parsegian, V. A. (1989). Hydration forces between phospholipid-bilayers. *Biochimica Biophysica Acta - Rev. Biomembr.* 988 (3), 351–376. doi:10.1016/0304-4157(89)90010-5

Rappolt, M., Hickel, A., Bringezu, F., and Lohner, K. (2003). Mechanism of the lamellar/inverse hexagonal phase transition examined by high resolution X-ray diffraction. *Biophys. J.* 84 (5), 3111–3122. doi:10.1016/S0006-3495(03)70036-8

Rog, T., Murzyn, K., Milhaud, J., Karttunen, M., and Pasenkiewicz-Gierula, M. (2009). Water isotope effect on the phosphatidylcholine bilayer properties: A molecular dynamics simulation study. *J. Phys. Chem. B* 113 (8), 2378–2387. doi:10.1021/jp8048235

Rog, T., Vattulainen, I., Bunker, A., and Karttunen, M. (2007). Glycolipid membranes through atomistic simulations: Effect of glucose and galactose head groups on lipid bilayer properties. *J. Phys. Chem. B* 111 (34), 10146–10154. doi:10.1021/jp0730895

Salditt, T., and Aeffner, S. (2016). X-ray structural investigations of fusion intermediates: Lipid model systems and beyond. *Semin. Cell Dev. Biol.* 60, 65–77. doi:10.1016/j.semcdb.2016.06.014

Sanderson, P. W., and Williams, W. P. (1992). Low-temperature phase behaviour of the major plant leaf lipid monogalactosyldiacylglycerol. *Biochim. Biophys. Acta* 1107 (1), 77–85. doi:10.1016/0005-2736(92)90331-f

Schmidt, J. M. (2013). A simple test on 2-vertex- and 2-edge-connectivity. *Inf. Process. Lett.* 113 (7), 241–244. doi:10.1016/j.ipl.2013.01.016

Selstam, E., Brentel, I., and Lindblom, G. (1990). "The phase-structure of galactolipids and their role in the formation of the prolamellar body," in *Current research in photosynthesis*. Editor M. Baltscheffsky (Dordrecht: Springer), 2749–2754.

Shannon, P., Markiel, A., Ozier, O., Baliga, N. S., Wang, J. T., Ramage, D., et al. (2003). Cytoscape: A software environment for integrated models of biomolecular interaction networks. *Genome Res.* 13 (11), 2498–2504. doi:10.1101/gr.1239303

Shipley, G. G., Green, J. P., and Nichols, B. W. (1973). The phase behavior of monogalactosyl, digalactosyl, and sulphoquinovosyl diglycerides. *Biochim. Biophys. Acta* 311 (4), 531–544. doi:10.1016/0005-2736(73)90128-4

Snyder, S., Kim, D., and McIntosh, T. J. (1999). Lipopolysaccharide bilayer structure: Effect of chemotype, core mutations, divalent cations, and temperature. *Biochemistry* 38 (33), 10758–10767. doi:10.1021/bi990867d

Srivastava, A., and Debnath, A. (2018). Hydration dynamics of a lipid membrane: Hydrogen bond networks and lipid-lipid associations. *J. Chem. Phys.* 148 (9), 094901. doi:10.1063/1.5011803

Srivastava, A., Malik, S., and Debnath, A. (2019). Heterogeneity in structure and dynamics of water near bilayers using TIP3P and TIP4P/2005 water models. *Chem. Phys.* 525, 110396. doi:10.1016/j.chemphys.2019.110396

Sundaralingam, M. (1972). Discussion paper: Molecular structures and conformations of the phospholipids and sphingomyelins. *Ann. N. Y. Acad. Sci.* 195 (20), 324–355. doi:10.1111/j.1749-6632.1972.tb54814.x

Szczelina, R., Baczynski, K., Markiewicz, M., and Pasenkiewicz-Gierula, M. (2020). Network of lipid interconnections at the interfaces of galactolipid and phospholipid bilayers. *J. Mol. Liq.* 298, 112002. doi:10.1016/j.molliq.2019.112002

Tian, C. A., and Chiu, C. C. (2018). Importance of hydrophilic groups on modulating the structural, mechanical, and interfacial properties of bilayers: A comparative molecular dynamics study of phosphatidylcholine and ion pair amphiphile membranes. *Int. J. Mol. Sci.* 19 (6), E1552. doi:10.3390/ijms19061552

van Meer, G., Voelker, D. R., and Feigenson, G. W. (2008). Membrane lipids: Where they are and how they behave. *Nat. Rev. Mol. Cell Biol.* 9 (2), 112–124. doi:10.1038/nrm2330

Volkov, V. V., Palmer, D. J., and Righini, R. (2007). Distinct water species confined at the interface of a phospholipid membrane. *Phys. Rev. Lett.* 99 (7), 078302. doi:10.1103/PhysRevLett.99.078302

Volkov, V. V., Palmer, D. J., and Righini, R. (2007). Heterogeneity of water at the phospholipid membrane interface. *J. Phys. Chem. B* 111 (6), 1377–1383. doi:10.1021/jp065886t

Webb, M. S., and Green, B. R. (1991). Biochemical and biophysical properties of thylakoid acyl lipids. *Biochimica Biophysica Acta - Bioenergetics* 1060 (2), 133–158. doi:10.1016/s0005-2728(09)91002-7

Wormald, M. R., Petrescu, A. J., Pao, Y. L., Glithero, A., Elliott, T., Dwek, R. A., et al. (2002). Conformational studies of oligosaccharides and glycopeptides: Complementarity of NMR, X-ray crystallography, and molecular modelling. *Chem. Rev.* 102 (2), 371–386. doi:10.1021/cr990368i

Wu, E. L., Engstrom, O., Jo, S., Stuhlsatz, D., Yeom, M. S., Klauda, J. B., et al. (2013). Molecular dynamics and NMR spectroscopy studies of *E. coli* lipopolysaccharide structure and dynamics. *Biophys. J.* 105 (6), 1444–1455. doi:10.1016/j.bpj.2013.08.002

Zhao, W., Moilanen, D. E., Fenn, E. E., and Fayer, M. D. (2008). Water at the surfaces of aligned phospholipid multibilayer model membranes probed with ultrafast vibrational spectroscopy. *J. Am. Chem. Soc.* 130 (42), 13927–13937. doi:10.1021/ja803252y

Ziolkowska, N. E., Shenoy, S. R., O'Keefe, B. R., McMahon, J. B., Palmer, K. E., Dwek, R. A., et al. (2007). Crystallographic, thermodynamic, and molecular modeling studies of the mode of binding of oligosaccharides to the potent antiviral protein griffithsin. *Proteins* 67 (3), 661–670. doi:10.1002/prot.21336

frontiers | Frontiers in Molecular Biosciences

TYPE Original Research
PUBLISHED 30 August 2022
DOI 10.3389/fmolb.2022.939834

OPEN ACCESS

EDITED BY
Elena G Govorunova,
University of Texas Health Science Center at Houston, United States

REVIEWED BY
Jin Liu,
Peking University, China
Jean-David Rochaix,
Université de Genève, Switzerland

*CORRESPONDENCE
Katrin Philippar,
katrin.philippar@uni-saarland.de

SPECIALTY SECTION
This article was submitted to Lipids, Membranes and Membranous Organelles,
a section of the journal
Frontiers in Molecular Biosciences

RECEIVED 09 May 2022
ACCEPTED 11 July 2022
PUBLISHED 30 August 2022

CITATION
Peter J, Huleux M, Spaniol B, Sommer F, Neunzig J, Schroda M, Li-Beisson Y and Philippar K (2022), Fatty acid export (FAX) proteins contribute to oil production in the green microalga Chlamydomonas reinhardtii.
Front. Mol. Biosci. 9:939834.
doi: 10.3389/fmolb.2022.939834

Fatty acid export (FAX) proteins contribute to oil production in the green microalga *Chlamydomonas reinhardtii*

Janick Peter[1], Marie Huleux[2], Benjamin Spaniol[3], Frederik Sommer[3], Jens Neunzig[1], Michael Schroda[3], Yonghua Li-Beisson[2] and Katrin Philippar[1]*

[1]Plant Biology, Center for Human- and Molecular Biology (ZHMB), Saarland University, Saarbrücken, Germany, [2]Aix Marseille Univ, CEA, CNRS, Institute of Bioscience and Biotechnology of Aix Marseille, BIAM, Saint Paul-Lez-Durance, France, [3]Molecular Biotechnology and Systems Biology, TU Kaiserslautern, Kaiserslautern, Germany

In algae and land plants, transport of fatty acids (FAs) from their site of synthesis in the plastid stroma to the endoplasmic reticulum (ER) for assembly into acyl lipids is crucial for cellular lipid homeostasis, including the biosynthesis of triacylglycerol (TAG) for energy storage. In the unicellular green alga *Chlamydomonas reinhardtii*, understanding and engineering of these processes is of particular interest for microalga-based biofuel and biomaterial production. Whereas in the model plant *Arabidopsis thaliana*, FAX (fatty acid export) proteins have been associated with a function in plastid FA-export and hence TAG synthesis in the ER, the knowledge on the function and subcellular localization of this protein family in Chlamydomonas is still scarce. Among the four FAX proteins encoded in the Chlamydomonas genome, we found Cr-FAX1 and Cr-FAX5 to be involved in TAG production by functioning in chloroplast and ER membranes, respectively. By *in situ* immunolocalization, we show that Cr-FAX1 inserts into the chloroplast envelope, while Cr-FAX5 is located in ER membranes. Severe reduction of Cr-FAX1 or Cr-FAX5 proteins by an artificial microRNA approach results in a strong decrease of the TAG content in the mutant strains. Further, overexpression of chloroplast Cr-FAX1, but not of ER-intrinsic Cr-FAX5, doubled the content of TAG in Chlamydomonas cells. We therefore propose that Cr-FAX1 in chloroplast envelopes and Cr-FAX5 in ER membranes represent a basic set of FAX proteins to ensure shuttling of FAs from chloroplasts to the ER and are crucial for oil production in Chlamydomonas.

KEYWORDS

chloroplast, endoplasmic reticulum, fatty acid transport, microalgae, oil production

Introduction

In all living organisms, fatty acids (FAs) are essential building blocks for polar, membrane-building structural lipids and energy-storage acyl lipids, mainly represented by neutral triacylglycerol (TAG) molecules that accumulate in lipid droplets. In photosynthetically active eukaryotes, ranging from algae to land plants, *de novo* synthesis of FAs takes place in the plastid stroma (Troncoso-Ponce et al., 2015; Li-Beisson et al., 2019). After synthesis, FAs are assembled into acyl lipids either in plastids *via* the so-called prokaryotic pathway or in the endoplasmic reticulum (ER) by the eukaryotic pathway. In the ER, all phospholipids for non-plastid, cellular lipid bilayer membranes, as well as precursors for complex extracellular lipophilic compounds in land plants are produced [for an overview on algal/plant lipid metabolism *see* (Li-Beisson et al. (2013), Li-Beisson et al. (2015), Lavell and Benning (2019))]. Further, ER membranes are the site for the biogenesis of lipid droplets (LDs). These are filled with TAG storage oils that have been assembled from glycerol and three acyl chains, which have been delivered and shuttled from the plastid (Bates, 2016; Xu and Shanklin, 2016; Li-Beisson et al., 2019; Li-Beisson et al., 2021). Thus, for a proper function of cellular lipid homeostasis in plant and algal cells, transport and distribution of lipophilic compounds are indispensable and mediated by membrane transport proteins (Li et al., 2016; Li-Beisson et al., 2017; Lavell and Benning, 2019) as well as *via* membrane contacts between organelles or vesicular traffic (Hurlock et al., 2014; Block and Jouhet, 2015; Michaud and Jouhet, 2019).

The green, unicellular alga *Chlamydomonas reinhardtii* in the past two decades has emerged as model organism for studying photosynthesis, flagella, carbon metabolism and more recently for dissecting molecular mechanisms of TAG synthesis and storage in LDs (Merchant et al., 2012; Scranton et al., 2015; Takeuchi and Benning, 2019). Thus, in the recent years, a focus was on understanding and engineering FA and TAG biosynthesis as well as LD biogenesis and disassembly in Chlamydomonas cells (Blatti et al., 2013; Kim et al., 2018; Gu et al., 2021; Li-Beisson et al., 2021). Since plant lipid transport is best understood in *Arabidopsis thaliana* (Li et al., 2016; Li-Beisson et al., 2017; LaBrant et al., 2018; Lavell and Benning, 2019), this model plant serves as blueprint for studies in Chlamydomonas, especially for subcellular distribution and transport of FAs from plastids to the ER. In the ER membrane, primary active ABC transporters that mediate uptake of FAs and/or acyl-CoA into the ER lumen in Arabidopsis (Kim et al., 2013) and in Chlamydomonas (Jang et al., 2020) have been described. Both proteins, which belong to the same ABC transporter subfamily, are crucial for the accumulation of TAGs in seed tissue (At-ABCA9) and Chlamydomonas cells (Cr-ABCA2). For the export of FAs from plastids, members of the FAX protein family have been pinpointed since the discovery of FAX1 in Arabidopsis (Li et al., 2015). At-FAX1 inserts with four membrane-intrinsic α-helices into the inner envelope (IE) membrane of chloroplasts and is able to mediate FA transport across lipid bilayer membranes. Further, our detailed study of At-FAX1 knockout and overexpressing lines in Arabidopsis revealed that the function of FAX1 is important for cellular lipid homeostasis, e.g. for ER-produced TAG oils and phospholipids, cuticular wax composition and lipophilic biopolymers of the outer pollen cell wall (Li et al., 2015). In addition, it was shown that seed-specific overexpression of At-FAX1 increases seed oil content in Arabidopsis and that the FAX1 ortholog in *Brassica napus* contributes to seed oil production, as well (Tian et al., 2018; Xiao et al., 2021). Thus, in land plants, the function of plastid IE-intrinsic members from the FAX-protein family is clearly associated with a role in export of FAs from plastids and hence affects the homeostasis of lipid compounds throughout plant development (Li et al., 2015; Tian et al., 2018; Tian et al., 2019; Li et al., 2020; Zhu et al., 2020; Cai et al., 2021; Huang et al., 2021; Xiao et al., 2021).

In unicellular algae, potential plastid envelope FAX-proteins have been analyzed in the red and green algal model systems *Cyanidioschyzon merolae* (Takemura et al., 2019) and *Chlamydomonas reinhardtii* (Li et al., 2019), respectively. The protein Cm-FAX1 in *C. merolae* most likely represents the ortholog to Arabidopsis At-FAX1 and was localized to plastid envelopes by indirect immuno-fluorescence microscopy on *C. merolae* cells overexpressing a FLAG-tagged Cm-FAX1 protein (Takemura et al., 2019). Further, Takemura and co-workers (2019) could show that a Cm-FAX1 null mutant in comparison to wild-type cells has higher free fatty acid (FFA) content. In a Cm-FAX1 overexpressor strain, however, the FFA level was reduced but the amount of TAG storage lipids increased by about 2.4-fold. In Chlamydomonas, two FAX-like proteins, named Cr-FAX1 and Cr-FAX2 were examined by Li et al. (2019). Although any data on subcellular localization of these proteins is missing, the authors conclude that both have similar functions to At-FAX1 and are involved in export of FAs from chloroplasts to the cytosol in Chlamydomonas cells. This hypothesis is purely based on some conserved sequence motifs between At-FAX1 and the two Cr-FAX proteins, and the finding that alleged overexpressing strains of Cr-FAX1 and Cr-FAX2 accumulate more TAG than wild type and affect FA as well as polar lipid homeostasis (Li et al., 2019). The data presented by Li et al. (2019) is somewhat disappointing since the overexpression of both FAX proteins is only followed in one single strain per protein and was analyzed only at the transcript level. The increase in transcript content in overexpression strains compared to wild type was small, i.e. around 1.5- and 1.3-fold for Cr-FAX1 and Cr-FAX2, respectively (Li et al., 2019). Although proteins of the Arabidopsis FAX5/6 and FAX7 subfamilies are predicted to be in ER and/or secretory pathway membranes (Li et al., 2015),

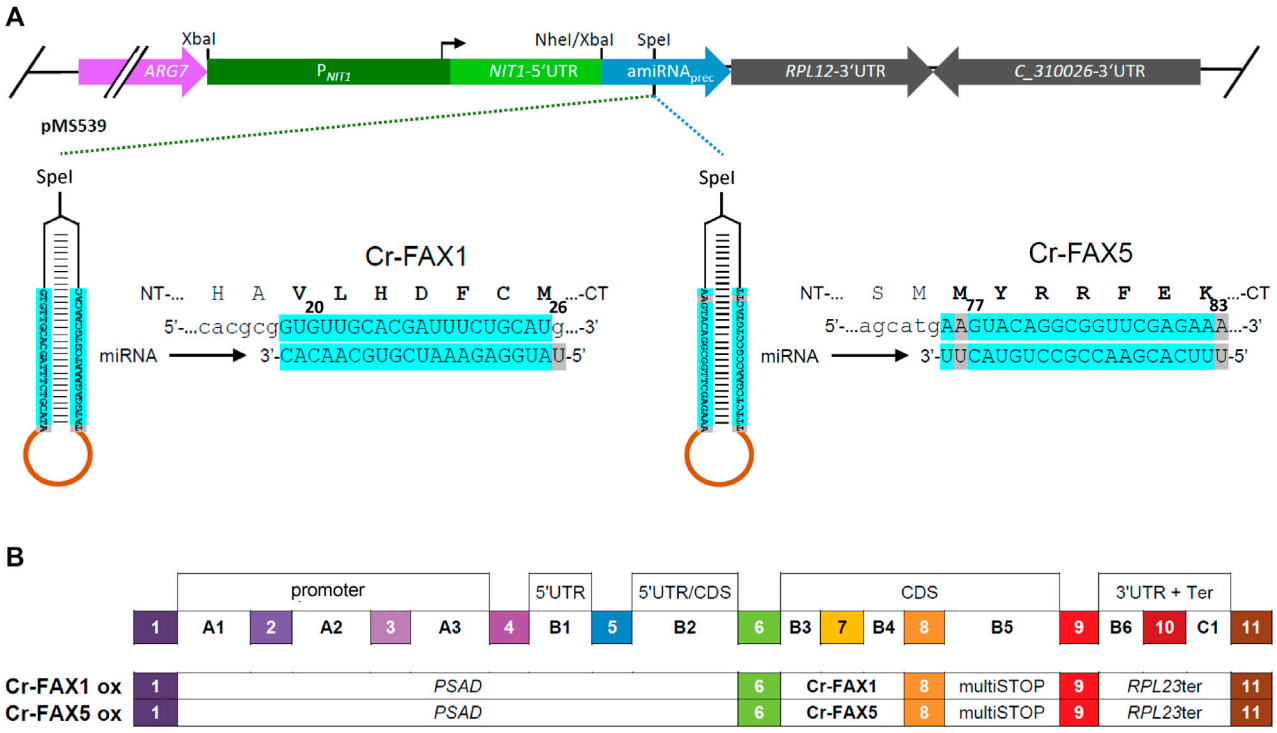

FIGURE 1
Knockdown and overexpression constructs for *Cr-FAX1* and *Cr-FAX5* genes. **(A)** Schematic drawing of artificial microRNA (amiRNA) constructs for knockdown of Cr-FAX1 and Cr-FAX5. The amiRNAs directed against Chlamydomonas *Cr-FAX1* (left) and *Cr-FAX5* genes (right) are *SpeI*-subcloned into the pMS539 plasmid vector (top), which harbors the inducible *NIT1* (nitrate reductase 1) promoter (for details see Schmollinger et al., 2010). The amiRNA generated by pMS539 targets regions in the second exons of *Cr-FAX1* (left) and *Cr-FAX5* (right), coding for amino acids 20–26 of mature Cr-FAX1 and 77–83 of Cr-FAX5, respectively. Base-pairing nucleotides of the amiRNA and *Cr-FAX1*, *Cr-FAX5* mRNAs are shaded in turquoise. **(B)** Schematic drawing of level 1 constructs according to the MoClo syntax (Patron et al., 2015; Crozet et al., 2018) for overexpression of *Cr-FAX1* and *Cr-FAX5* genes. The following level 0 modules were assembled in destination vector pICH47742 (Weber et al., 2011). PSAD, promoter of photosystem I reaction center subunit II (position A1-B2); respective *FAX* gene (position B3-B4); multiSTOP sequence (B5); *RPL23*ter: terminator of 50S ribosomal protein L23 (B6-C1).

so far no function of FAX5/6 and FAX7 proteins associated with FA/lipid transport and homeostasis has been described in the green lineage. As part of our long-term effort in understanding FA and lipid transport in green photosynthetic cells, here we have investigated in detail the subcellular localization and impact on lipid homeostasis of two distinct groups of FAX proteins - i.e. FAX1 and FAX5/6 - in the green microalga Chlamydomonas.

Materials and methods

Strains and culture conditions

Chlamydomonas reinhardtii strain cw15-325 (cw_d mt^+ *arg7 nit1*$^+$ *nit2*$^+$) was used for transformation with amiRNA constructs (containing the *ARG7* gene for selection). UVM4, which is derived from cw15-302 (cw_d mt^+ *arg7 nit1*$^-$ *nit2*$^-$), was used for immunolocalization as well as overexpression of Cr-FAX1 and Cr-FAX5 due to reduced transgene suppression (Neupert et al., 2009). Cultures were grown mixotrophically in Tris–acetate-phosphate (TAP) medium (Kropat et al., 2011) on a rotary shaker (140 rpm) at 20°C and continuous light (30 µmol photons m^{-2} s^{-1}). Growth was followed by determining the optical density of cultures at 750 nm (OD_{750}) and the cell number (Supplementary Figure S1). For growing cw15-325 cells prior to transformation, arginine (100 µg/ml) was added to the medium. For lipid analyses, cells were cultivated at 25°C with constant continuous light (80–100 µmol photons m^{-2} s^{-1}) in TAP liquid medium in conical glass flasks in incubators (Multitron, Infors HT) shaking at 120 rpm. Exponentially grown cells were counted with a Multisizer 4 (Beckman Coulter), and a fixed number of cells was harvested by centrifugation. Chlamydomonas strains were kept on TAP agar plates under constant light at 20–25°C in a culture room.

Generation of artificial microRNA constructs

The artificial microRNAs (amiRNAs) targeting Chlamydomonas *Cr-FAX1* and *Cr-FAX5* transcripts were designed with the WMD3 Web tool (Ossowski et al., 2008). The resulting oligonucleotides CrFAX1-amiFor, CrFAX1-amiRev, CrFAX5-amiFor, CrFAX5-amiRev (Supplementary Table S1) directed against the second exon of the respective *FAX* sequence (*see* Figure 1A), were annealed by boiling and slowly cooling-down in a thermocycler. The resulting DNA constructs were *Spe*I-subcloned into the pMS539 plasmid vector, which harbors the inducible *NIT1* (nitrate reductase 1) promoter (Schmollinger et al., 2010). Screening for correct constructs was done as described by (Molnar et al., 2009) and verified by sequencing. One microgram plasmid DNA was transformed into strain cw15-325 using the glass beads method (Kindle, 1990).

To evaluate the inducibility of the *NIT1* promoter for knockdown of Cr-FAX1 and Cr-FAX5, the respective Chlamydomonas strains were grown to mid-log phase (OD_{750} between 0.3 and 0.5) in TAP medium containing 7.5 mM NH_4Cl as nitrogen source. For induction of the *NIT1* promoter, the nitrogen source was switched from ammonium to nitrate. To this end, cells were pelleted by centrifugation for 3 min at 1,500 *g* and 4°C. The supernatant was discarded, and the cells were washed twice with TAP medium containing 7.5 mM KNO_3 as nitrogen source. Subsequently, growth continued in TAP-nitrate medium for up to 6 days.

Generation of FAX overexpression and mVenus constructs by modular cloning (MoClo)

Genomic DNA from Chlamydomonas was isolated as described in Spaniol et al. (2022). The genomic sequences for *Cr-FAX1* and *Cr-FAX5* were amplified by PCR and "domesticated" by removing endogenous, internal *Bbs*I and *Bsa*I restriction sites and introducing *Bbs*I restriction sites at the 5′ and 3′ ends by PCR-based mutagenesis (for oligonucleotides *see* Supplementary Table S1). The respective PCR products were cloned into the recipient plasmid pAGM1287 by adding *Bbs*I and T4 DNA ligase (Weber et al., 2011), resulting in level 0 constructs for *Cr-FAX1, Cr-FAX5*. According to the MoClo syntax (Patron et al., 2015; Crozet et al., 2018), the FAX genes were inserted at positions B3-B4. For level 1 constructs, the respective *FAX* gene, the *PSAD* promoter (position A1-B2), multiSTOP sequence (B5), *RPL23* terminator (B6-C1), and the destination vector pICH47742 (Weber et al., 2011) were directionally assembled with *Bsa*I and T4 DNA ligase (*see* Figure 1B). For mVenus fluorescent constructs in the chloroplast stroma and ER lumen, we assembled the following level 1 modules in pICH47742 (*see* Supplementary Figure S4B). Chloroplast targeted mVenus: *HSP70A-RBCS2* hybrid promoter (A1-B1); the chloroplast transit peptide of universal stress protein A (USPA; B2); mVenus(i2), harboring the second intron of RBCS, plus stop codon (B3-B5); and the *RPL23* terminator (B6-C1). ER-targeted mVenus: *HSP70A-RBCS2* hybrid promoter (A1-B1); the signal peptide of BiP2 (B2); mVenus(i2), harboring the second intron of RBCS (B3-B4); the 3XHA+KDEL (ER retention signal) sequence (B5); and the *RPL23* terminator (B6-C1).

Subsequently, the respective level 1 module was combined with a level 1 construct harboring the *aadA* gene conferring resistance to spectinomycin, a proper end-linker, and the destination vector pAGM4673 (Weber et al., 2011), digested with *BbsI* and ligated by T4 DNA ligase in order to obtain the final level 2 device for transformation. Transformations were carried out with the *Chlamydomonas reinhardtii* strain UVM4 with 1 µg plasmid DNA of the respective level 2 device using the glass beads method (Kindle, 1990). Selection of transformants was performed on TAP agar medium containing 100 µg/ml spectinomycin.

Isolation of proteins, membranes, and organelles

For the extraction of total cellular proteins, Chlamydomonas cells from 5–10 ml cultures were collected in mid-log growth phase (OD_{750} between 0.3 and 0.5, *see* Supplementary Figure S1) by centrifugation for 3 min at 1,500 g and 4°C. The cell pellet was resuspended in 60 µl DTT-carbonate buffer (0.1 M DTT, 0.1 M Na_2CO_3), to generate a homogenous solution prior to freezing at −20°C. After thawing, 55 µl SDS-sucrose buffer (5% [w/v] SDS, 30% [w/v] sucrose) was added and the sample was mixed thoroughly. Samples were then incubated at 99°C for 2 min, followed by 2 min on ice and insoluble material was removed by centrifugation at 16,000 *g* for 2 min. Next, the chlorophyll concentration of the supernatant, containing total cellular proteins, was determined. Chlorophyll was extracted with 80% acetone for 5 min on ice. After centrifugation at 16,000 *g* for 5 min, the absorption was measured at 645 and 663 nm. The chlorophyll concentration was calculated according to Porra and Scheer (1989): Chlorophyll [µg/µl] = [(A645 × 17.76) + (A663 × 7.34)].

For the isolation of total cellular membranes, cells were collected from 25 ml cultures grown to mid-log growth phase ($3–5*10^6$ cells/ml) by centrifugation for 5 min at 3,100 *g* (swing out buckets) and 4°C. The supernatant was discarded, and the cell pellet was resuspended in 1 ml lysis buffer (10 mM Tris-HCl, pH 8.0, 1 mM EDTA, 0.25XcOmplete protease inhibitor cocktail [Roche]). 200 µl were directly used as the whole cell protein fraction for immunoblot analysis. The remaining cells were broken up by four cycles of freezing and thawing (liquid nitrogen and room temperature, respectively) and cellular membranes were pelleted by centrifugation for 30 min at

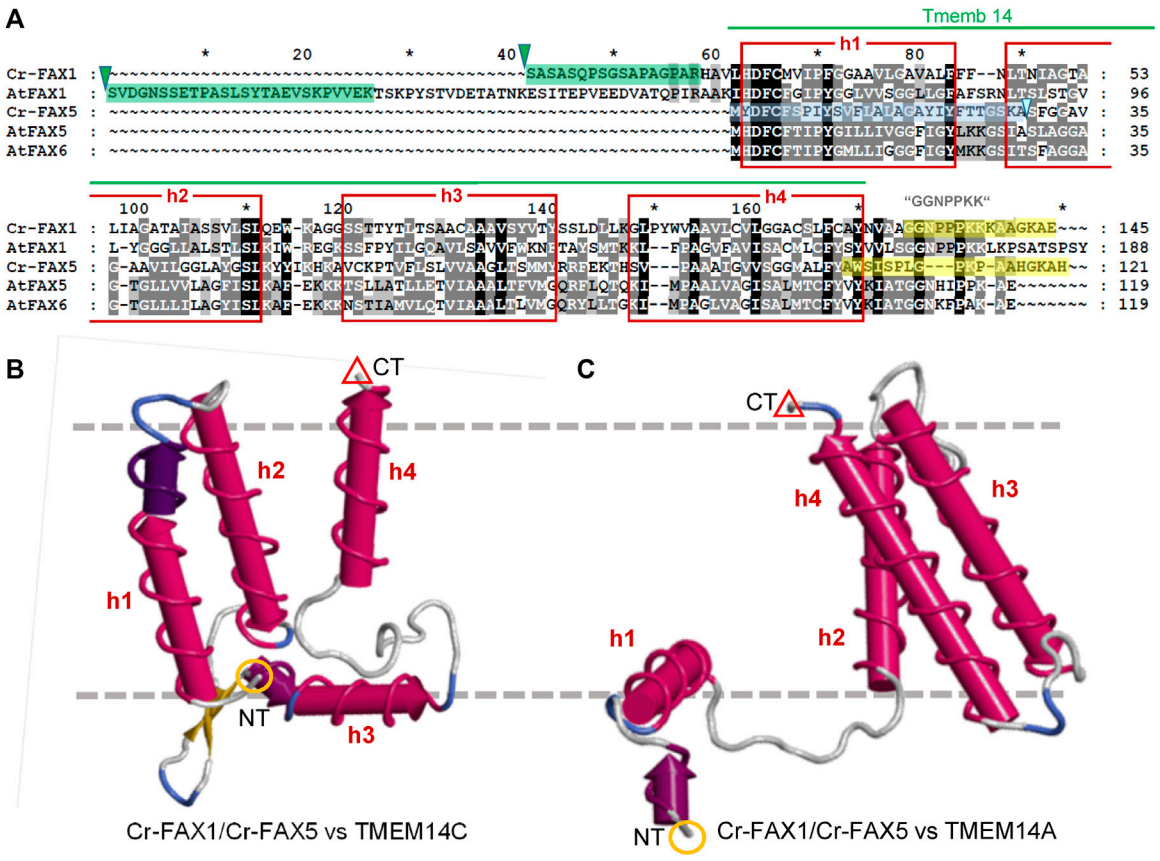

FIGURE 2
FAX1 and FAX5/6 proteins in Chlamydomonas and Arabidopsis. **(A)** Sequence alignment of mature FAX1 and FAX5/6 proteins in Chlamydomonas and Arabidopsis. The four membrane-embedded α-helices (red boxes) within the Tmemb_14 domain (pfam PF03647 motif, green line) are depicted according to the Aramemnon consensus prediction AramTmCon for At-FAX1 (Schwacke et al., 2003). Oligopeptides used to generate antisera against Cr-FAX1 and Cr-FAX5 are specified by yellow boxes. Processing sites for stromal peptidases according to TargetP2.0 (Almagro Armenteros et al., 2019) are indicated by green triangles, the presumed ER signal peptide for Cr-FAX5 is depicted by a blue box. The most N-terminal peptides of mature Cr-FAX1 and At-FAX1, identified after peptide sequencing are highlighted by green boxes. Among the FAX-protein family in Arabidopsis, Cr-FAX1 shows highest similarity to At-FAX1 (26% aa identity) and Cr-FAX5 is most likely related to At-FAX5 (32% identical aas). Names, gene codes (AGI, Phytozome), and protein IDs (UniProt) are as follows: Cr-FAX1 (Cre10.g421750, A8ICM7), At-FAX1 (At3g57280, Q93V66), Cr-FAX5 (Cre08.g366000, A8J403), At-FAX5 (At1g50740, Q9C6T7), At-FAX6 (At3g20510, Q9LJU6). Note that our Cr-FAX1 and Cr-FAX5 correspond to CrFAX1 and CrFAX2, described in (Li et al., 2019), respectively. **(B, C)** Structural modelling of Cr-FAX1 and Cr-FAX5 (Phyre2; Kelley et al., 2015) revealed high similarity to the structure of human TMEM14C and TMEM14A proteins (confidence 99.7–99.9%). Depicted are 3D models of **(B)** Cr-FAX5 versus TMEM14C (PDB entry c2losA) and **(C)** versus TMEM14A (PDB entry c2lopA; right) generated by *FirstGlance* in *Jmol* (firstglance.jmol.org). Note that models of Cr-FAX1 (not shown) are highly similar to those of Cr-FAX5. The four α-helices (h1–h4) of the Tmemb_14 domain of FAX/TMEM14 proteins are depicted as red cylinders. N- and C-terminal ends of the proteins are highlighted by orange circles (NT) and red triangles (CT). Boundaries of a lipid bilayer membrane are indicated by gray, dashed lines.

21,000 *g* and 4°C. The pellet, containing cellular membrane-intrinsic proteins was resuspended in 800 µl lysis buffer. The corresponding supernatant contained soluble cellular proteins and membrane vesicles of light density such as microsomes. The protein content of all fractions was determined by Bradford and BCA assays.

Chloroplast and microsomal membranes were isolated according to Jang et al. (2020). Therefore, cells were collected from 100 ml in mid-log growth phase (OD_{750} = 0.4–0.55, *see* Supplementary Figure S1) by centrifugation for 3 min at 1,500 *g* and 4°C. The cell pellet was resuspended in 40 ml homogenization buffer (250 mM sorbitol, 50 mM Tris-acetate pH 7.5, 1 mM EGTA-Tris pH 7.5, 2 mM DTT, 1XcOmplete protease inhibitor cocktail [Roche]). The suspension was kept at 4°C during homogenization by pulse sonication (UP50H [Hielscher, Germany]: cycle 0.4, intensity 20%). Subsequently, 20 ml of cell homogenate were subjected to serial centrifugation steps at 4°C, which precipitated non-broken cells and nuclei (500 *g*, 10 min), chloroplasts (3,000 *g*, 10 min), smaller organelles like mitochondria/peroxisomes (20,000 *g*, 30 min) and microsomes (100,000 *g*, 4 h, swing out rotor). The respective chloroplast and microsomal membrane pellets were each

resuspended in 500 µl homogenization buffer and the protein content was determined by a BCA assay.

Immunoblot analysis

For immunoblot analyses, proteins from Chlamydomonas cells, organelles and membranes were separated by SDS-PAGE and transferred to PVDF membranes. Primary antisera were used in 1:1,000 dilution in TTBS buffer (100 mM TRIS-HCl, pH 7.5, 150 mM NaCl, 0.2% Tween-20, 0.1% BSA). Secondary anti-rabbit IgG horseradish peroxidase (Santa Cruz Biotechnology) was diluted 1:10,000 in TTBS. Blots were stained in ECL solution (Pierce ECL Western Blotting Substrate, Thermo Scientific) according to the manufacturer's instructions and chemiluminescent signals were detected by the iBright1500 imaging system (Invitrogen). Cr-FAX1 and Cr-FAX5 antisera were raised in rabbit (Pineda Antibody Service, Berlin, Germany) against C-terminal peptide sequences of both proteins (*see* Figure 2A). For controls of chloroplast and microsomal fractions we used the following antisera, generated in rabbit: The antiserum against BiP luminal-binding protein (rabbit antibody, product No. AS09 481) was purchased from Agrisera (Sweden), α-Cr-ABCA2, directed against the ER-localized ABC transporter ABCA2 (Jang et al., 2020) was provided by Prof. Y. Lee, α-Lhcb4 for detection of thylakoid CP29 chlorophyll a/b binding protein of PSII from higher plants has been described previously (Duy et al., 2007).

For the detection of N-terminal peptides in mature Cr-FAX1 and At-FAX1 proteins, peptide sequencing of SDS gel slices of the same size as of the respective bands stained by antisera was carried out. To this end, a tryptic digest of PAGE separated proteins and mass spectrometric analysis was performed as described in Rütgers et al. (2017) on a TT6600 Instrument (AB Sciex). MS data analysis was performed with MaxQuant software v 1.6.0.1 using default settings including phospho-STY variable modifications and searching against proteins from *Arabidopsis thaliana* and *Chlamydomonas reinhardtii* derived from the UniProt database.

Immunofluorescence assays

UVM4 cells from 1 ml TAP medium culture grown to the mid-log phase (~5*10^6 cells/ml, *see* Supplementary Figure S1) were fixed on poly-L-lysin coated Poly-Prep slides (Sigma). Positioning of chloroplasts and nuclei was determined visually by screening through images with a confocal laser scanning microscope (Leica LSM780). Subsequently, slides were dipped for 2 min in cold methanol (−20°C), followed by rinsing five times with phosphate-buffered saline (PBS: 27 mM NaCl, 2.7 mM KCl, 10 mM Na_2HPO_4, 1.8 mM KH_2PO_4, pH 7.4). Blocking of unspecific signals was achieved by incubation with 1% BSA in PBS for 30 min, again followed by rinsing five times with PBS solution. Primary antisera against Cr-FAX1 (1:1,000), Cr-FAX5 (1:1,000) or hemagglutinin (HA; 1:500; Agrisera, Sweden) were applied in PBS + 1% BSA for 3 h, followed by rinsing five times with PBS solution. Subsequently, all steps were performed in darkness and fixed cells were incubated with the secondary antibody anti-rabbit IgG-TRITC (IgG-tetramethylrhodamine-isothiocyanate; Sigma), diluted 1:250 in PBS + 1% BSA for 1 h. Fixed cells were washed five times with PBS solution before being overlayed with Prolong Gold antifade reagent (Invitrogen). Pseudo transmission images (PTI) as well as TRITC fluorescence signals (excitation at 561 nm, emission from 565 to 583 nm) were collected with an LSM780.

As controls for chloroplast stroma and ER lumen, signals from Chlamydomonas cells expressing mVenus fluorescent constructs were recorded. For this, the respective strains were grown to mid-log phase in TAP medium and immobilized by adding 2.5% glutaraldehyde. By centrifugation at 1,500 *g*, cells were concentrated and placed on a glass slide. Signals for mVenus fluorescence were collected from 520 to 564 nm with a confocal laser scanning microscope (Leica LSM780) after excitation at 512 nm. The laser line at 458 nm was used for excitation of chlorophyll signals, which were collected from 626 to 735 nm.

Lipid extraction and analyses

Total lipids were extracted from Chlamydomonas cells using a protocol based on isopropanol and methyl-tert-butyl ether (MTBE) extraction as detailed in Legeret et al. (2016). Briefly, cells were harvested in glass tubes by centrifugation at 3,200 *g*, 5 min at 4°C. Hot isopropanol (1 ml) containing 0.01% (w/v) butylated hydroxytoluene (BHT; pre-heated to 85°C) were added to the cell pellet, vortexed and heated up for 10 min at 85°C. Once cooled down, MTBE and water were added to reach a final ratio of isopropanol/MTBE/water of 1:3:1 (v/v/v). The mixture was vortexed and then phase separated by centrifugation at 4°C for 2 min at 3,200 *g*. The organic upper phase was transferred to a clean glass tube using a Pasteur pipette. An additional volume of MTBE was added to the cell pellet to extract remaining lipids, and again the upper phase collected after a brief centrifugation. The combined organic phases were then evaporated under a gentle stream of N_2 and re-dissolved in a mixture of chloroform/methanol (2:1, v/v) and kept at −20°C until further analysis.

TAGs and polar lipids were quantified using a densitometry method after being separated from each other using Thin Layer Chromatography (TLC) techniques. An ATS5 autosampler (Camag Switzerland) was used to deposit lipid extracts to a silica TLC plate made of silica gel 60 F254 (Merck KGaA, Germany). Lipid classes were then separated by developing the plate in an ADC2 automatic developing chamber (Camag) using a hexane/diethyl ether/acetic acid (17/3/0.2, v/v/v) solvent mixture for TAG analysis or acetone/toluene/water (91/30/8, v/v/v) solvent mixture for polar lipid analysis. TLC plates were

TABLE 1 FAX proteins in *Chlamydomonas reinhardtii*.

name	Gene	Protein-ID	Length [aa]	MW [kDa]	Pre-loc	At ortholog [id/sim aa]
Cr-FAX1 *	Cre10.g421750	A8ICM7	199 (**145**)	19.9 (**14.3**)	**C**	At-FAX1 [26/37%]
Cr-FAX3	Cre08.g383300	A0A2K3DI83	208 (171)	19.7 (15.7)	C	At-FAX3 [24/38%]
Cr-FAX5 *	Cre08.g366000	A8J403	**121** (92)	**12.7** (9.5)	**ER**/SP	At-FAX5 [32/51%]
Cr-FAX7	Cre09.g387838	A0A2K3DDV7	109	11.2	-	At-FAX7 [28/47%]

The Chlamydomonas genome harbors four genes encoding for FAX-like proteins. Listed are names, genes (Phytozome; Goodstein et al., 2012), and protein-IDs (UniProtKB), length in amino acids (aa), molecular weight in kDa and the predicted subcellular localization (TargetP 2.0; Almagro Armenteros et al., 2019). In brackets are values for the respective predicted mature proteins; bold letters indicate proteins and verified features of this study. The similarity to the presumed Arabidopsis ortholog (*see* also Supplementary Figure S2B) is given in % identical (id) and similar (sim) aa. *: Note that Cr-FAX1/Cre10.g421750 and Cr-FAX5/Cre08.g366000 correspond to CrFAX1 and CrFAX2, described in Li et al. (2019), respectively. C, chloroplast; ER, endoplasmic reticulum; SP; secretory pathway; -, no location can be predicted.

thoroughly dried under the hood, before being dipped for 6 s in a solution containing $CuSO_4$ reagent (20 g $CuSO_4$, 200 ml methanol, 8 ml H_2SO_4, 8 ml H_3PO_4), heated at 141°C for 30 min on a TLC plate heater and finally scanned using a TLC Scanner 3 with WinCATs software (Camag). TAG or polar lipids were then quantified by comparing to a curve generated with corresponding lipid standard (Sigma-Aldrich, Saint-Louis, United States; Larodan Fine Chemicals AB, Malmö, Sweden). Lipid standards used were triheptadecanoin (C17:0 TAG, Sigma-Aldrich, Saint-Louis, United States), monogalactosyl-distearoylglyceride (MGDG; Larodan Fine Chemicals AB, Malmö, Sweden), digalactosyl-distearoylglyceride (DGDG; Larodan Fine Chemicals AB), 1,2-dipalmitoyl-*sn*-glycerol-3-phospho-(1′-rac-glycerol) (PG; Avanti Polar Lipids, AL, United States) and 1,2-dipalmitoyl-*sn*-glycerol-3-phospho-ethanolamine (PE; Avanti Polar Lipids).

For fatty acid composition analysis, a fraction of the extracted lipids or whole cells were converted to fatty acid methyl esters (FAMEs) using an acid-based transmethylation. Briefly, to cell pellet or total lipid extracts, 1 ml of 5% H_2SO_4 in methanol was added in a glass tube with a Teflon-lined screw cap. In addition, we added 0.01% BHT (final concentration) and 250 µl of toluene to improve solubility when TAG content is high. The internal standard used was triheptadecanoin (C17:0 TAG). The mixture was heated up at 85°C for 1.5 h. Once cooled down, hexane and 1 ml of 0.9% NaCl solution was added to extract FAMEs and allow phase separation. After centrifugation, the upper organic phase was transferred to a new tube and dried under a stream of N_2, then analyzed by a GC-MS detailed in Legeret et al. (2016).

All lipid data were analyzed by student t-test (double sided *p*-value: $^{***}p < 0.001$; $^{**}p < 0.01$; $^{*}p < 0.05$).

Results

Chlamydomonas contains four FAX proteins with distinct structural features

When we examined publicly available databases, we identified four FAX-like proteins in *Chlamydomonas reinhardtii* (Table 1). According to TargetP 2.0 predictions (Almagro Armenteros et al., 2019), the proteins encoded by Cre10.g421750 and Cre08.g383300 are in chloroplasts and possess cleavable, N-terminal transit peptides of 54 and 37 amino acids (aa), respectively. In contrast, the protein corresponding to Cre08.g366000 is expected to hold an N-terminal signal peptide of 29 aa for the ER, and no prediction for subcellular targeting of the gene product from Cre09.g387838 was possible (Table 1). All four Cr-FAX proteins are annotated to belong to the FAX/TMEM14 protein family (PANTHER "transmembrane protein 14" subfamily, PTHR12668) and contain the FAX-like Tmemb_14 domain (Pfam entry PF03647) with four conserved α-helical domains (Figure 2 and Supplementary Figure S2A). In comparison with sequences and motifs of the plant FAX protein family, we found that the chloroplast predicted Cre10.g421750 and Cre08.g383300 are most similar to FAX1- and FAX3-subfamilies, respectively (Supplementary Figure S2). Thus, in the following we refer to Cre10.g421750 as Cr-FAX1 and to Cre08.g383300 as Cr-FAX3 (Table 1). The protein encoded by Cre08.g366000 we named Cr-FAX5, since it most likely represents the ortholog to At-FAX5, and Cre09.g387838/Cr-FAX7 corresponds to At-FAX7 (Figure 2 and Supplementary Figure S2). Note that Cr-FAX1 is identical to the protein named CrFAX1 by Li et al. (2019). For our Cr-FAX5, however, Li and coworkers chose the name CrFAX2, although no similarity to the seed-plant and plastid-specific FAX2 proteins [*see* Figure 2A; Supplementary Figure S2B and Tian et al. (2019), Li et al. (2020)] can be found.

The mature Cr-FAX1 protein is predicted to have 14.3 kDa and within the Tmemb_14 domain contains the typical peptide stretches identified for the plant FAX1 subfamily (Figure 2A). Besides the confirmed cleavage site for a chloroplast stromal peptidase, in particular the C-terminal "GGNPPKK" motif and the highly conserved sequence in the first α-helix classify Cr-FAX1 to be a FAX1-like protein. Structural modelling revealed that like for At-FAX1 [*see* Li et al. (2015)], the structure of Cr-FAX1 with high similarity fits to that documented for the human TMEM14C and TMEM14A proteins (Figures 2B,C; Klammt et al., 2012). Thus, most likely the third α-helix of Cr-FAX1

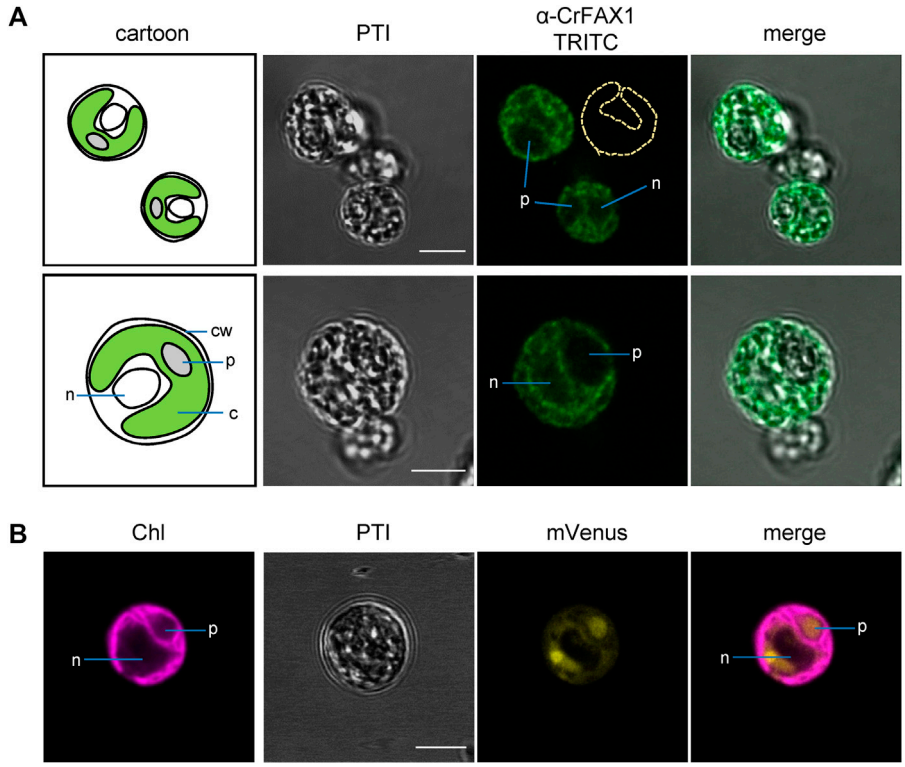

FIGURE 3
Cr-FAX1 can be found in the chloroplast envelope of Chlamydomonas. **(A)** *In situ* immunofluorescence signals of α-CrFAX1 in Chlamydomonas cells. Intact, fixed wild-type UVM4 *C. reinhardtii* cells were treated with α-CrFAX1 antiserum and signals of the secondary antibody were detected by coupled fluorescence of TRITC (tetramethylrhodamine-isothiocyanate). Shown are pseudo transmission images (PTI), pictures of TRITC-fluorescence (green) and an overlay of both. A cartoon (left) illustrates positioning and organelles of the respective Chlamydomonas cells that were recorded prior to antiserum treatment. Location of the chloroplast envelope and its lobes is indicated by a yellow dashed line (α-CrFAX1/TRITC upper panel). TRITC fluorescence was excited at 561 nm and recorded between 565 and 583 nm by a Leica LSM780 confocal microscope. For a background control of unspecific TRITC fluorescence in comparison to chlorophyll, see Supplementary Figure S4A. c, chloroplast; cw, cell wall; n, nucleus; p, pyrenoid. **(B)** Fluorescence signals of chloroplast controls. Intact, fixed *C. reinhardtii* cells of an UVM4 strain transformed with an mVenus-fluorescence construct, which is targeted to the chloroplast stroma, were examined by fluorescence microscopy. Shown are pseudo transmission images (PTI) as well as chlorophyll (purple) and mVenus (yellow) fluorescence and an overlay of both. (mVenus: excitation at 514 nm, emission at 520–564 nm; chlorophyll: excitation at 458 nm, emission at 626–735 nm; Leica LSM780 confocal microscope). Note that the soluble mVenus construct in **(B)** shows signals in the chloroplast stroma and the pyrenoid, while chlorophyll fluorescence **(B)** and α-CrFAX1 signals in **(A)** only appear at thylakoid and envelope membranes, respectively. All scale bars are 5 µm.

has an amphiphilic character and orients perpendicular to the lipid bilayer membrane. Analogous to At-FAX1, also the first helix of Cr-FAX1 shows amphiphilic character due to conserved hydrophilic residues at the N-terminal end and thus might be somewhat tilted vertically inside the membrane. Further, this first α-helix of the Tmemb_14 domain of Cr-FAX1 is not only highly similar to At-FAX1, but also to Cr-FAX5 and At-FAX5/At-FAX6, another conserved feature of plant FAX1- and also of FAX5/6-subfamilies. The FAX5/6 subfamily is conserved throughout plant species, but not always represented by two gene copies like for the presumed paralogs At-FAX5, At-FAX6 in Arabidopsis (Könnel et al., 2019). Cr-FAX5 is most similar to At-FAX5 (Table 1) and in the green microalga Chlamydomonas represents the only FAX5/6-like protein that could be identified. In consequence, we classify Cr-FAX5 to be the Chlamydomonas member of the plant FAX5/6 group. The molecular mass of Cr-FAX5 is calculated to be 12.7 kDa and an N-terminal ER signal-peptide that includes the first α-helix of the Tmemb_14 domain is predicted (Table 1 and Figure 2). Again, the topology of Cr-FAX5 can be modeled to that of hm-TMEM14C and TMEM14A (Figures 2B,C). We therefore conclude that Cr-FAX1 and Cr-FAX5 have a very similar topology inside the lipid bilayer membrane: *1*) When modeled according to hm-TMEM14C the third α-helix of Cr-FAX1 and Cr-FAX5 represents a "classical," type II amphiphilic helix (Gkeka and Sarkisov, 2010), which plunges into the lipid bilayer parallel to the membrane surface (Figure 2B). Helix 1 of Cr-FAX1 and Cr-FAX5 in this model instead represent type III amphiphilic helices where hydrophilic residues are clustered only at the N-terminal end and thereby the membrane-spanning helix is tilted vertically

inside the membrane [compare Könnel et al. (2019)]. 2) In comparison to hm-TMEM14A, however, the first α-helix of Cr-FAX1/FAX5 would be perpendicular to the lipid bilayer membrane, whereas helix 3 and 4 would be tilted vertically (Figure 2C). Because both structural models appear with highest confidence (99.7–99.9% by Phyre^2; Kelley et al., 2015), we cannot assign the final membrane topology for FAX1 and FAX5/6 proteins, however, in both models helices 1 and 3 display an amphiphilic character.

In addition to Cr-FAX1 and Cr-FAX5 that have been described simplistically earlier [*see* Li et al. (2019)], we could identify two more FAX proteins in Chlamydomonas, i.e. Cr-FAX3 and Cr-FAX7 (Table 1 and Supplementary Figure S2). Cr-FAX3 is most similar to At-FAX3 and, in addition to a cleavable, N-terminal chloroplast transit peptide, has a poly-glycine region N-terminally of the Tmemb_14 domain, which is typical for all plant FAX3 proteins (Supplementary Figure S2A). The mature Cr-FAX3 has a predicted mass of 15.7 kDa. The protein encoded by Cre09.g387838 has about 11.2 kDa and is related to At-FAX7 (Table 1 and Supplementary Figure S2) and therefore was named Cr-FAX7. Like for At-FAX7, no targeting peptide for subcellular localization could be predicted for Cr-FAX7 (Table 1).

Since Cr-FAX1 and Cr-FAX5 have very similar structural features and appear to represent a basic set of chloroplast (Cr-FAX1) and ER (Cr-FAX5) predicted FAX proteins, which is conserved throughout the plant kingdom [compare also Könnel et al. (2019)], we chose to further characterize these two proteins in Chlamydomonas.

Cr-FAX1 is in chloroplast membranes and Cr-FAX5 in ER membranes of Chlamydomonas cells

To experimentally verify the subcellular localization of Cr-FAX1 and Cr-FAX5 proteins in Chlamydomonas cells, we generated antisera against C-terminal peptides of both proteins (Figure 2A). Subsequently, we used our antisera, specific for Cr-FAX1 and Cr-FAX5, for immunohistochemical staining. After incubation with a fluorescent secondary antibody, we thereby could follow *in situ* localization in wild-type Chlamydomonas cells. For Cr-FAX1, we could detect specific fluorescent signals in the chloroplast envelope (Figure 3). Compared to respective controls in the literature, Cr-FAX1 has a rather non-homogeneous distribution in the chloroplast envelope, similar to the protein import translocon protein Tic20 [*see* Mackinder et al. (2017)]. Cr-FAX5 signals, however, clearly associated with non-chloroplast membranes connected to the nucleus (Figure 4). In comparison to fluorescent signals of an ER targeted mVenus control (Figure 4B) and to the ER lumen protein BiP (Mackinder et al., 2017), we deduce that these membranes belong to the ER.

Testing of our antisera by immunoblot analysis on proteins from a crude membrane preparation of wild-type Chlamydomonas cells confirms the predicted molecular mass of mature Cr-FAX1 (about 14 kDa) and of Cr-FAX5 (around 11–12 kDa; Supplementary Figure S3A). Moreover, peptide sequencing of a respective SDS gel slice at 14 kDa, exactly validated the predicted processing site of a chloroplast stromal peptidase (compare Figure 2A). Thus, we can conclude that Cr-FAX1 has a cleavable, N-terminal transit peptide of 54 aa and that the mature, processed Cr-FAX1 protein of 14.3 kDa is 145 amino acids long. Because signals of Cr-FAX5 antisera appeared at approximately 11–12 kDa (Supplementary Figure S3A), we assume that the predicted N-terminal, α-helical ER signal-sequence is actually a signal anchor sequence that is not cleaved, as observed for type II integral membrane proteins in the ER (Liaci and Forster, 2021). Indeed, with 19 aa, the first hydrophobic α-helix of Cr-FAX5 is a bit too long to act as cleavable signal peptide. Furthermore, the required small, hydrophobic residues at position -1 and -3 relative to the predicted protease cleavage site are not exactly positioned in Cr-FAX5 (compare with Figure 2A). We thus conclude that the full Cr-FAX5 protein is 121 amino acids long and has a molecular mass around 12 kDa (*see* Table 1). As expected, the signal of α-Cr-FAX1 was highly enriched in fractionated membrane proteins, which in Chlamydomonas cells primarily consist of chloroplast integral membrane proteins as documented by the control Lhcb4 (Supplementary Figure S3A). Remarkably, signals for Cr-FAX5 appeared in the supernatant and not in the pellet of the crude membrane preparation, indicating that this protein most likely localizes to non-chloroplast, light membrane fractions. To further follow Cr-FAX1 and Cr-FAX5 localization, we separated Chlamydomonas chloroplasts and microsomes from other organellar membranes by differential centrifugation, which in particular is described for purification of microsomal membranes. After immunoblot analysis, we here again observed that Cr-FAX1 is in chloroplast membranes. Cr-FAX5 in contrast to Cr-FAX1 and well in line with the *in situ* immunolocalization, clearly associated with the microsomal fraction and co-localized with signals of antisera against the ER-membrane integral Cr-ABCA2 (Jang et al., 2020) and BiP (binding immunoglobulin protein), a marker for the ER lumen (Supplementary Figure S3B).

In summary, we could show by two direct immunological approaches on purified membrane proteins and *in situ* on intact Chlamydomonas wild-type cells, that Cr-FAX1 integrates into the chloroplast envelope and that Cr-FAX5 is an integral membrane protein of the ER. Thus, the mature Cr-FAX1 inserts with its four hydrophobic α-helical domains into a chloroplast envelope membrane, which due to the presence of a classical N-terminal chloroplast transit peptide and in comparison to Arabidopsis and pea FAX1 (Li et al., 2015), most likely is the chloroplast IE. Cr-FAX5 appears to be a type II integral membrane protein of the ER, which contains a signal anchor sequence in the first hydrophobic α-helix.

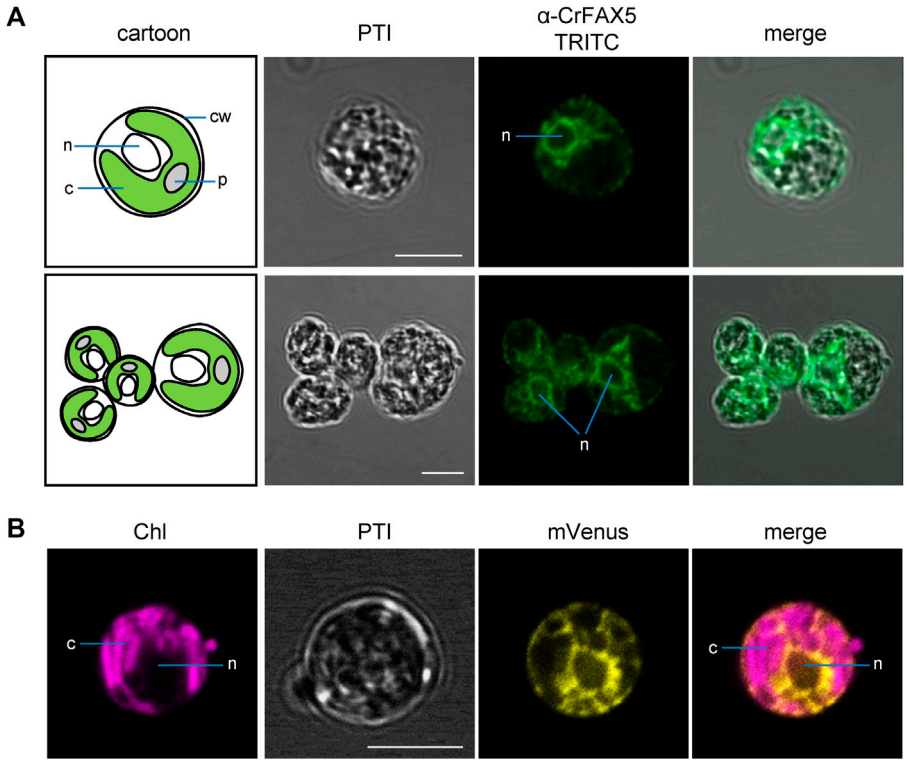

FIGURE 4
Cr-FAX5 can be found in ER membranes of Chlamydomonas. **(A)** *In situ* immunofluorescence signals of α-CrFAX5 in Chlamydomonas cells. Intact, fixed wild-type UVM4 *C. reinhardtii* cells were treated with α-CrFAX5 antiserum and signals of the secondary antibody were detected by coupled fluorescence of TRITC (tetramethylrhodamine-isothiocyanate). Shown are pseudo transmission images (PTI), pictures of TRITC-fluorescence (green) and an overlay of both. A cartoon (left) illustrates positioning and organelles of the respective Chlamydomonas cells that were recorded prior to antiserum treatment. TRITC fluorescence was excited at 561 nm and recorded between 565 and 583 nm by a Leica LSM780 confocal microscope. For a background control of unspecific TRITC fluorescence in comparison to chlorophyll, see Supplementary Figure S4A. c, chloroplast; cw, cell wall; n, nucleus; p, pyrenoid. **(B)** Fluorescence signals of an ER lumen control. Intact, fixed *C. reinhardtii* cells of an UVM4 strain transformed with an mVenus-fluorescence construct, which is targeted to and retained in the ER lumen, were examined by fluorescence microscopy. Shown are pseudo transmission images (PTI) as well as chlorophyll (purple) and mVenus (yellow) fluorescence and an overlay of both (mVenus: excitation at 514 nm, emission at 520–564 nm; chlorophyll: excitation at 458 nm, emission at 626–735 nm; Leica LSM780 confocal microscope). Note that the signals of mVenus in the ER lumen **(B)** and of α-CrFAX5 **(A)** are very similar surrounding the nucleus and do neither overlap with chloroplasts or chlorophyll fluorescence. All scale bars are 5 μm.

The oil content can be manipulated by varying Cr-FAX1 or Cr-FAX5 protein levels

To dissect the function of the two FAX proteins in lipid homeostasis, we generated mutant lines using an artificial microRNA (amiRNA) approach (Figure 1A). Two independent lines for each gene were validated as true and constitutive knockdown of Cr-FAX1 or Cr-FAX5, respectively as shown by immunoblot (Figure 5A). In addition, these immunoblots verified the specificity of our antisera α-CrFAX1 and α-CrFAX5 (compare Supplementary Figure S3) as well as the apparent molecular mass of the mature Cr-FAX1 and Cr-FAX5 proteins (*see* above and Table 1). Although under control of the inducible *NIT1* (nitrate reductase 1) promoter (Schmollinger et al., 2010), the strains kd-C#22, kd-C#24 for Cr-FAX1 and kd-E#22, kd-E#28 for Cr-FAX5 (Figure 5A and Supplementary Figure S5) constitutively showed a strong reduction of FAX proteins. This constitutive activity of the *NIT1* promoter in some transformants most likely is due to position effects imposed by the chromatin structure at the ectopic integration site of the transgene in the genome (Schroda, 2019). The strains C#12 and E#4, however, without *NIT1* induction did not exhibit reduced Cr-FAX1 and Cr-FAX5 protein levels, respectively (compare Supplementary Figure S5). Therefore, we used these two lines as controls with wild type-like Cr-FAX1 and Cr-FAX5 protein content under non-inducing growth conditions. Lipid analysis of exponentially grown cells showed that all four Cr-FAX knockdown strains made around 60% less TAG than their corresponding control lines (Figure 5B). Among all membrane lipids, only DGDG and DGTS (diacylglyceryl-trimethyl-

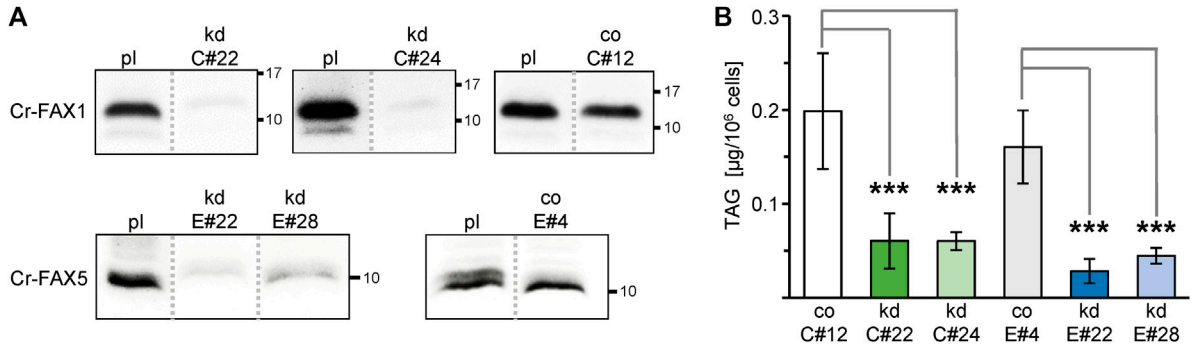

FIGURE 5
Knockdown of Cr-FAX1 and Cr-FAX5 affects oil content in Chlamydomonas. **(A)** Knockdown of Cr-FAX1 and Cr-FAX5 in cw15-325 Chlamydomonas cells. Immunoblot analysis of Cr-FAX1 and Cr-FAX5 in protein extracts from Chlamydomonas cells that were transformed with amiRNA knockdown constructs for Cr-FAX1 (kd-C, upper panels) and for Cr-FAX5 (kd-E, lower panels) under control of the inducible *NIT1* promoter (see Figure 1A). Proteins were extracted from cells of the independently derived Cr-FAX1 strains kd-C#22, kd-C#24, co-C#12 and Cr-FAX5 strains kd-E#28, kd-E#22, co-E#4 as well as the respective untransformed parental strain cw15-325 (pl). Equal amounts of proteins (isolated from the same quantity of cells corresponding to 2 µg chlorophyll) were separated by SDS-PAGE and subjected to immunoblot analysis using antisera directed against Cr-FAX1 (upper panels) and Cr-FAX5 (lower panels). Numbers indicate molecular mass of proteins in kDa. Note that all protein samples were extracted from non-induced Chlamydomonas cells, i.e., knockdowns result from leaky expression of the *NIT1* promoter. While for the strains kd-C#22, kd-C#24, and kd-E#22, kd-E#28, we observed a strong reduction of Cr-FAX1 and Cr-FAX5 proteins, respectively, the strains co-C#12, co-E#4 showed no knockdown effect under these conditions and thus were used as control (co) lines. All boxed immunoblot signals were generated on one identical blot with equal amounts of sample loaded. Signals of other strains, which are not subject of this study, have been removed as indicated by gray, dotted lines (compare Supplementary Figure S5). **(B)** Knockdown (kd) of chloroplast Cr-FAX1 and ER-localized Cr-FAX5 decreases TAG oil content in Chlamydomonas cells. Two independently generated *C. reinhardtii* strains each for knockdown of Cr-FAX1: lines kd-C#22 (green) and kd-C#24 (light green), and Cr-FAX5: lines kd-E#22 (blue) and kd-E#28 (light blue) as well as the respective control lines with wild-type levels for Cr-FAX1 (co-C#12; white) and Cr-FAX5 (co-E#4; gray) were grown in TAP medium and harvested in the exponential growth phase for determination of neutral lipids via thin layer chromatography (TLC). For protein levels in all lines see **(A)**. TAG neutral lipids [µg/10^6 cells] were quantified densitometrically after separation by TLC from five individual liquid cultures of each strain (n = 5 ± SD). *p*-values for significantly different TAG content when compared to the respective control strains (co-C#12 for Cr-FAX1kd, co-E#4 for Cr-FAX5kd) are indicated (double-sided student t-test): *** $p < 0.001$.

homoserine) showed significant reduction by 15 and 45%, respectively, in the Cr-FAX5 knockdown lines (Supplementary Figure S6A). Knockdown of Cr-FAX1, however, did not result in any variations in content of polar lipid classes. Further, the total lipid content and the distribution of different FA species in all lipids analyzed did not change in any of the Cr-FAX1, Cr-FAX5 knockdown strains when compared to the respective controls (Supplementary Figures 6B,C).

To further elucidate the impact of Cr-FAX proteins on lipid homeostasis in Chlamydomonas, we generated overexpression lines for each gene *Cr-FAX1* and *Cr-FAX5* (Figure 1B) under control of the constitutive and strong promoter for photosystem I reaction center subunit II (*PSAD*; Fischer and Rochaix, 2001). Overexpression in two independent strains for each Cr-FAX1 (ox-C#8, ox-C#12) and Cr-FAX5 (ox-E#1, ox-E#8) was confirmed by immunoblotting (Figure 6A and Supplementary Figure S7). Lipid analysis in these lines revealed that overexpression of Cr-FAX1 in Chlamydomonas almost doubled the TAG content when compared to the parental strain UVM4 (Figure 6B). Overexpression of Cr-FAX5, however, did not bring any difference in TAG levels, but showed a mild reduction in MGDG and DGDG polar lipids (Supplementary Figure S8A). Similar to the knockdown lines, the total lipid content in all overexpression strains did not substantially change in comparison to the UVM4 parental line (Supplementary Figure S8B). However, some modifications could be observed in the distribution of FA molecule species (Supplementary Figure S8C): most prominent was a reduction of C16:1(7) and the C18:1(9) FAs in lipids from all overexpression strains for Cr-FAX1 or Cr-FAX5, respectively.

In summary, knockdown of both Cr-FAX1 and Cr-FAX5 led to a strong decrease in TAG levels in Chlamydomonas, whereas overexpression only of the chloroplast Cr-FAX1 almost doubled the TAG content. Effects on polar lipids and FA species in acyl lipids, however, were only marginal. Since all mutant strains grew normally under standard cultivation conditions (Supplementary Figure S9), we conclude that changes in TAG content are a direct effect of changing Cr-FAX protein levels.

Discussion

In this study, we provide a general overview on FAX proteins in the green microalga *Chlamydomonas reinhardtii* in comparison to the model plant *Arabidopsis thaliana*. With Cr-

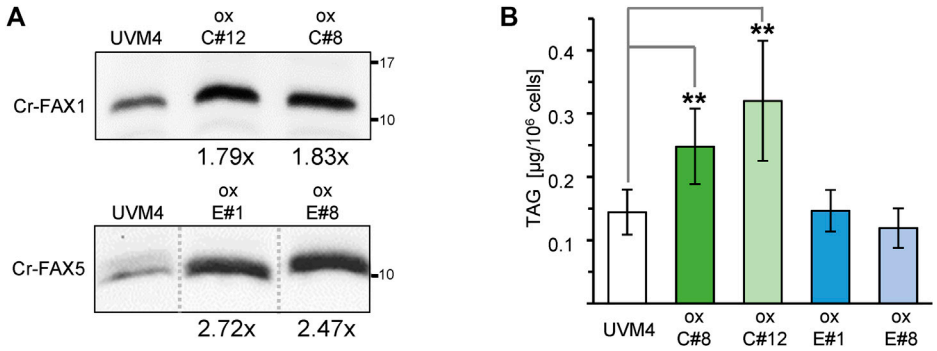

FIGURE 6
Overexpression of Cr-FAX1 affects oil content in Chlamydomonas. **(A)** Overexpression of Cr-FAX1, Cr-FAX5 in UVM4 *C. reinhardtii* cells. Immunoblot analysis of Cr-FAX1 (top) and Cr-FAX5 (bottom) in protein extracts from Chlamydomonas cells that were transformed with overexpression constructs for Cr-FAX1 (ox-C) and Cr-FAX5 (ox-E) under control of the constitutive *PSAD* promoter (see Figure 1B). Proteins were extracted from cells of independently derived Cr-FAX1ox strains C#12, C#8 (top) and Cr-FAX5ox strains E#1, E#8 (bottom) as well as the respective untransformed, parental strain UVM4. Equal amounts of proteins (isolated from the same quantity of cells corresponding to 2 µg chlorophyll) were separated by SDS-PAGE and subjected to immunoblot analysis using antisera directed against Cr-FAX1 or Cr-FAX5. Numbers indicate molecular mass of proteins in kDa. The increase in protein amount compared to UVM4 could be estimated to be around 1.8-fold for both Cr-FAX1ox C#8 (1.83 ± 0.13), C#12 (1.79 ± 0.16) and at 2.7-fold, 2.5-fold for Cr-FAX5ox E#1 (2.72 ± 0.38) and E#8 (2.47 ± 0.07), respectively (n = 3–4 independent immunoblots ± SD). Note that all boxed immunoblot signals were generated on one identical blot (see Supplementary Table S7). Signals of other mutant lines, which are not subject of this study, have been removed as indicated by gray, dotted lines. **(B)** Overexpression of chloroplast Cr-FAX1 increases TAG oil content in Chlamydomonas cells. Two independently generated *C. reinhardtii* strains (see **(A)**) each for overexpression of Cr-FAX1: lines ox-C#8 (green) and ox-C#12 (light green), and Cr-FAX5: lines ox-E#1 (blue) and ox-E#8 (light blue) as well as the respective wild-type parental strain UVM4 (white) were grown in TAP medium and harvested in the exponential growth phase for determination of neutral lipids via TLC. TAG neutral lipids [µg/10^6 cells] were quantified densitometrically after separation by TLC from five individual liquid cultures of each strain (n = 5 ± SD). *p*-values for significantly different TAG contents when compared to UVM4 are indicated (double-sided student t-test): ** $p < 0.01$.

FAX1/Cr-FAX5 and, most likely, also with Cr-FAX3/Cr-FAX7, Chlamydomonas appears to harbor two basic sets of FAX proteins, in which one FAX is targeted to membranes of chloroplasts (FAX1 and FAX3) and the other to the ER/secretory pathway (FAX5 and FAX7). Members of FAX2 and FAX4 subfamilies, which can be found in land plants, appear to be absent in the Chlamydomonas genome. Due to similar secondary structure and conserved amino acid sequence motifs of Cr-FAX1 and Cr-FAX5, an analogous function of both membrane proteins is likely. Since Cr-FAX1 is predicted to be localized to the chloroplast envelope and Cr-FAX5 to ER/secretory pathway membranes, we chose to verify their subcellular localization and to investigate their function. In contrast to a previous report, where the protein equivalent to Cr-FAX5 was assumed to be in chloroplasts (Li et al., 2019), here by *in situ* immunolocalization we show unequivocally that Cr-FAX5 in Chlamydomonas cells is targeted to ER membranes. Although an N-terminal ER signal sequence is weakly predicted for Cr-FAX5, the protein of around 12 kDa (121 amino acids) most likely is not processed and represents a type II integral membrane protein of the ER (Liaci and Forster, 2021). Further, we provide experimental evidence that Cr-FAX1 inserts into the chloroplast envelope. Due to determination of the processing site for a chloroplast stromal peptidase by peptide sequencing, we conclude that the mature Cr-FAX1 protein contains 145 amino acids with a molecular mass of about 14.3 kDa. Whereas in the unicellular red alga *C. merolae*, chloroplast envelope localization of the FAX1 ortholog Cm-FAX1 was demonstrated on overexpression strains with FLAG-tagged Cm-FAX1 (Takemura et al., 2019), our studies rely on endogenous protein levels in non-modified UVM4 cells, detected by specific antisera for Cr-FAX1 and Cr-FAX5. In comparison to the IE-membrane intrinsic At-FAX1 and Ps-FAX1 (Li et al., 2015), Cr-FAX1 with its four α-helical domains most likely integrates into the IE membrane of Chlamydomonas chloroplasts as well. In comparison to proteolytic pattern of Ps-FAX1 in purified IE membrane vesicles from pea chloroplasts (JP and KP, unpublished results), Cr-FAX1 presumably orients with the N-terminus to the stroma and the C-terminus exposed to the inter membrane space (Figure 7). Because in Chlamydomonas as well as in Arabidopsis [compare Könnel et al. (2019)], secondary structure and the predicted membrane topology of mature FAX1 and FAX5 proteins are very similar, we suppose that Cr-FAX1 and Cr-FAX5 function in the same metabolic pathway in chloroplast envelope and ER membranes, respectively.

To test this assumption, we generated amiRNA knockdown strains for Cr-FAX1 and Cr-FAX5 in Chlamydomonas, resulting in a drastic reduction of FAX protein levels. In land plants, the function of plastid-intrinsic FAX-proteins is associated with a role in export of FAs from plastids and hence an effect on the homeostasis of lipid compounds throughout plant development (Li et al., 2015; Tian et al., 2018; Tian et al., 2019; Li et al., 2020;

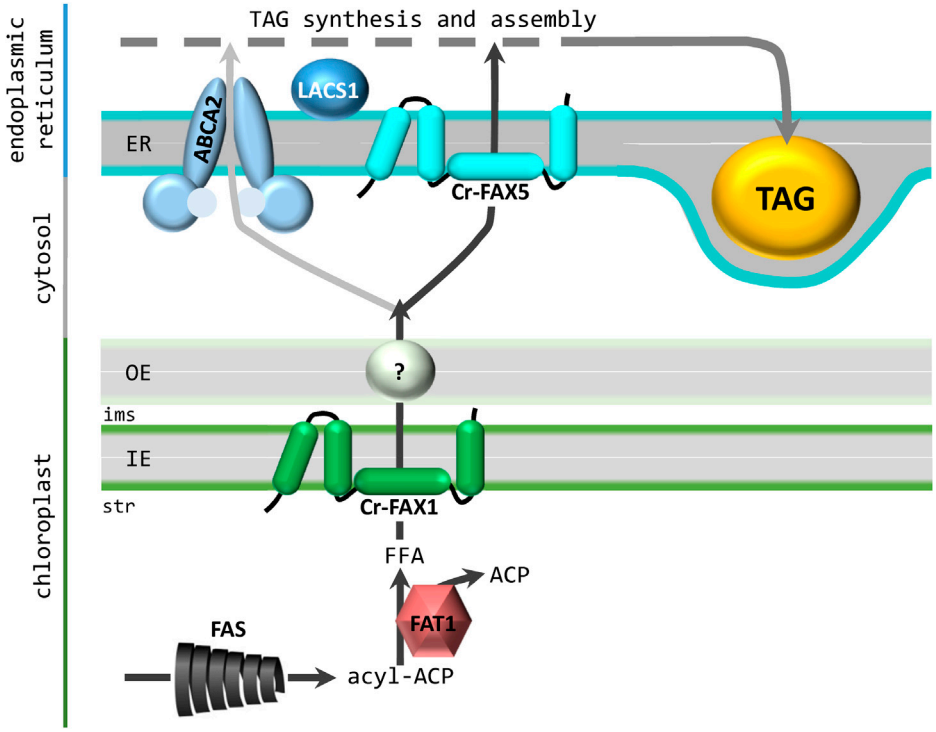

FIGURE 7
Contribution of Cr-FAX1 and Cr-FAX5 for oil synthesis in Chlamydomonas. According to our working hypothesis, Cr-FAX1 with its 4 α-helical domains (green) integrates in an asymmetric fashion into the inner envelope (IE) membrane of chloroplasts. Most likely the N-terminus is in the stroma (str) and the C-terminus in the intermembrane space (ims). In comparison to proteolytic pattern of Ps-FAX1 in purified IE membrane vesicles from pea chloroplasts (JP and KP, unpublished results), Cr-FAX1 presumably orients with the N-terminus to the stroma and the C-terminus exposed to the ims. Upon proteolysis of this C-terminus of Ps-FAX1, intermediate bands can be detected by an antiserum directed against an N-terminal peptide stretch (JP and KP, unpublished results). Since the C-terminus of the structural model shown in Figure 2C is almost completely protected by the lipid bilayer, the model of Figure 2B, which is adapted here, is more likely to lead to these intermediate band pattern. Cr-FAX5 (turquoise) in a similar fashion sits in the membrane of the endoplasmic reticulum (ER). De novo fatty acid synthesis (FAS) occurs in the chloroplast stroma and the acyl-ACP thioesterase 1 (FAT1) generates free fatty acids (FFA) for export mediated by FAX1. The transport mode for FAs across the outer envelope (OE) membrane still is unclear. Import of FFAs and/or acyl-CoA into the ER occurs via the ABC transporter ABCA2 and with the help of FAX5. If both proteins act together or represent different FA import routes remains to be elucidated. However, function of ABCA2 and FAX5, most likely contributes acyl chains for triacylglycerol (TAG) synthesis and assembly in the ER. As described in the text, we assume that FAT1, FAX1, FAX5 and LACS1 (long chain acyl CoA synthetase 1) function in the same transport pathway from chloroplast to the ER for fueling FAs into TAG oil synthesis.

Zhu et al., 2020; Cai et al., 2021; Huang et al., 2021; Xiao et al., 2021). The *in planta* task of ER-localized FAX5/6, to our knowledge, has not been elucidated yet. In consequence, we here studied the impact of reduced levels of Cr-FAX1 and Cr-FAX5 proteins on lipid homeostasis in Chlamydomonas. Remarkably, knockdown lines for both Cr-FAX1 and Cr-FAX5 exhibited a strong and reproducible decrease in ER-made TAG, with levels down to 30% of controls in both Cr-FAX1 knockdowns, and to 18 and 28% in the two Cr-FAX5 knockdowns. The total lipid content and distribution of FA-molecule species in acyl lipids did not change and polar lipids were only slightly affected in Cr-FAX5 knockdowns, indicating that potential membrane lipid remodeling (Young and Shachar-Hill, 2021) to compensate for the reduction in TAG does not occur. However, the pronounced reduction of the ER-produced DGTS to 46 and 62.5% in both Cr-FAX5 knockdown lines points to an ER-specific function of Cr-FAX5 in lipid synthesis. Thus, in Chlamydomonas we can provide a proof of principle for the implication of chloroplast FAX1 proteins in TAG production and show that a FAX5 protein in the ER membrane is involved in the same physiological process, most likely the transfer of FAs from chloroplasts into the ER for assembly of acyl lipids (Figure 7).

In comparison to the Chlamydomonas ER membrane-intrinsic ABC-transporter CrABCA2, which most likely imports FAs and/or acyl-CoA into the ER and has been described to be crucial for TAG accumulation under nitrogen deprivation (Jang et al., 2020), the contribution of Cr-FAX1 and Cr-FAX5 to TAG assembly appears to be stronger. Knockdowns of CrABCA2 only reduced TAG levels to 70–80% of the corresponding wild type, although values are difficult to compare because of different Chlamydomonas strains,

promoters, and growth conditions. Knockdowns for Cr-FAX1 have not been described in the literature, however, a knockout strain of the *C. merolae* ortholog Cm-FAX1 did not affect red algal TAG levels (Takemura et al., 2019). In Arabidopsis, the loss of At-FAX1 function leads to a decrease in TAG content by only 4.3–7.2% in leaf and flower tissue, respectively. Thus, the effect of reduced chloroplast Cr-FAX1 protein levels on TAG production in Chlamydomonas appears to be more stringent and direct than in *C. merolae* and Arabidopsis. In Arabidopsis, redundancy of plastid IE- localized FAX proteins – i.e. FAX1, FAX2, FAX3, FAX4 – might compensate for the loss of FAX1 in single knockouts, while in Chlamydomonas only the chloroplast predicted Cr-FAX3 could functionally replace Cr-FAX1.

To further track the function of FAX proteins in lipid homeostasis and to contribute knowledge for potential biofuel production in microalgae, we also generated overexpression strains for Cr-FAX1 and Cr-FAX5. While the amiRNA generated knockdown of Cr-FAX1 and Cr-FAX5 was quite efficient, overexpression under control of the constitutive *PSAD* promoter in comparison was rather modest with about 1.8-fold and 2.5–2.7-fold higher protein levels for Cr-FAX1 and Cr-FAX5, respectively. However, this mild increase in Cr-FAX1 protein levels resulted in a doubling of the oil content: line Cr-FAX1ox C#8 produced 1.7-fold, and line Cr-FAX1ox C#12 produced 2.2-fold more TAG when compared to their parental strain. In contrast, increase of Cr-FAX5 proteins did not affect TAG levels. Similar to knockdown lines, changes in total lipid content could not be recorded and the polar lipids MGDG and DGDG were only marginally reduced in Cr-FAX5 overexpression lines. Most prominent for the distribution of FA species in total lipids was a reduction of C16:1(7) and C18:1(9) FAs in lipids of all overexpression strains for Cr-FAX1 or Cr-FAX5. Both FA species are desaturated within the chloroplast, and their reduction in relative proportion in FAX overexpressing lines suggests that an enhanced flow of FAs between subcellular organelles can affect FA desaturation levels. Our results for Cr-FAX1 overexpression are comparable to the very strong overexpression of Cm-FAX1, which leads to a 2.4-fold increase in total TAG in *C. merolae* cells (Takemura et al., 2019). The reported 1.3-fold increase of TAG in single lines supposedly overexpressing Cr-FAX1 and Cr-FAX5 in Chlamydomonas (Li et al., 2019) are difficult to relate, because the only very marginal rise of transcripts by around 1.5- and 1.3-fold for CrFAX1 and CrFAX2/alias Cr-FAX5, respectively, casts doubts on the overexpression at the protein level. Also, the strong changes in polar lipids, observed by Li and coworkers (2019) in their strains cannot be reproduced by our study. In Arabidopsis, very strong overexpression of At-FAX1 results in a quite modest increase of TAG content when compared to wild type tissue, i.e. 3.2% in leaf and 6.6% in flower tissue (Li et al., 2015). Thus, the impact of moderately increased protein levels of chloroplast IE-intrinsic FAX1 in Chlamydomonas is significant, and the protein definitely represents a target for biotechnological oil production in unicellular green and red microalgae like *Chlamydomonas reinhardtii* and *Cyanidioshyzon merolae*.

Interestingly, in contrast to overexpression of Cr-FAX1, overexpression of Cr-FAX5 in our study did not affect the TAG content in Chlamydomonas cells. In strains with increased levels of the ER intrinsic FA/acyl-CoA importer CrABCA2, however, the TAG yield could be mildly improved by 1.2–1.6-fold under standard conditions (Jang et al., 2020). It is thus tempting to speculate that a bottleneck for increasing Chlamydomonas oil content might rather be in FA export from chloroplasts *via* FAX1 proteins than in FA/acyl-CoA import into the ER, mediated by FAX5. Only very recently, *Cr-FAX1* and *Cr-FAX5* were described to be co-expressed with chloroplast-intrinsic acyl-ACP thioesterase 1 (*FAT1*), and the long-chain acyl CoA synthetase *LACS1*, indicating that these genes function in the same pathway for enhanced FA transport from chloroplast to ER for TAG production (Choi et al., 2022). Well in line with a chloroplast FA-delivery bottleneck for TAG assembly in the ER, overexpression of *Cr-FAT1*, which generates free fatty acids for export into the chloroplast stroma by Choi and coworkers (2022) could increase the TAG content by 1.5-fold.

In summary, we conclude that Cr-FAX1 in the chloroplast IE and Cr-FAX5 in the ER membrane function together in shuttling FA acyl chains from the site of synthesis in the chloroplast stroma to the ER lumen for TAG lipid assembly (Figure 7).

Data availability statement

The original contributions presented in the study are included in the article/Supplementary Material, further inquiries can be directed to the corresponding author.

Author contributions

JP, MS, YL-B, and KP conceived and designed experiments. JP, MH, BS, FS, and JN performed experiments. KP wrote the manuscript.

Funding

This work was funded by the DFG (Deutsche Forschungsgemeinschaft) grants PH73/7-1 and PH73/6-1 to KP, and TRR175 (project C02) to MS. We also acknowledge the European Union Regional Developing Fund (ERDF), the Région Provence Alpes Côte d'Azur, the French Ministry of Research and the CEA for funding the HelioBiotec platform at CEA, and thanks for CEA internal funding LD-power.

Acknowledgments

We gratefully acknowledge excellent technical assistance by Angelika Anna, and we thank Maja Zeller for help selecting Chlamydomonas mutant strains. We also thanks Bertrand Legeret for maintaining the lipid analysis platform HelioBiotec at the CEA Cadarache and Youngsook Lee for providing CrABCA2 antiserum.

Conflict of interest

The authors declare that the research was conducted in the absence of any commercial or financial relationships that could be construed as a potential conflict of interest.

Publisher's note

All claims expressed in this article are solely those of the authors and do not necessarily represent those of their affiliated organizations, or those of the publisher, the editors and the reviewers. Any product that may be evaluated in this article, or claim that may be made by its manufacturer, is not guaranteed or endorsed by the publisher.

Supplementary material

The Supplementary Material for this article can be found online at: https://www.frontiersin.org/articles/10.3389/fmolb.2022.939834/full#supplementary-material

References

Almagro Armenteros, J. J., Salvatore, M., Emanuelsson, O., Winther, O., von Heijne, G., Elofsson, A., et al. (2019). Detecting sequence signals in targeting peptides using deep learning. *Life Sci. Alliance* 2, e201900429. doi:10.26508/lsa.201900429

Bates, P. D. (2016). Understanding the control of acyl flux through the lipid metabolic network of plant oil biosynthesis. *Biochim. Biophys. Acta* 1861, 1214–1225. doi:10.1016/j.bbalip.2016.03.021

Blatti, J. L., Michaud, J., and Burkart, M. D. (2013). Engineering fatty acid biosynthesis in microalgae for sustainable biodiesel. *Curr. Opin. Chem. Biol.* 17, 496–505. doi:10.1016/j.cbpa.2013.04.007

Block, M. A., and Jouhet, J. (2015). Lipid trafficking at endoplasmic reticulum-chloroplast membrane contact sites. *Curr. Opin. Cell Biol.* 35, 21–29. doi:10.1016/j.ceb.2015.03.004

Cai, G., Wang, G., Kim, S. C., Li, J., Zhou, Y., Wang, X., et al. (2021). Increased expression of fatty acid and ABC transporters enhances seed oil production in camelina. *Biotechnol. Biofuels* 14, 49. doi:10.1186/s13068-021-01899-w

Choi, B. Y., Shim, D., Kong, F., Auroy, P., Lee, Y., Li-Beisson, Y., et al. (2022). The Chlamydomonas transcription factor MYB1 mediates lipid accumulation under nitrogen depletion. *New Phytol.* 235, 595–610. doi:10.1111/nph.18141

Crozet, P., Navarro, F. J., Willmund, F., Mehrshahi, P., Bakowski, K., Lauersen, K. J., et al. (2018). Birth of a photosynthetic chassis: a MoClo toolkit enabling synthetic biology in the microalga *Chlamydomonas reinhardtii*. *ACS Synth. Biol.* 7, 2074–2086. doi:10.1021/acssynbio.8b00251

Duy, D., Wanner, G., Meda, A. R., von Wiren, N., Soll, J., Philippar, K., et al. (2007). PIC1, an ancient permease in Arabidopsis chloroplasts, mediates iron transport. *Plant Cell* 19, 986–1006. doi:10.1105/tpc.106.047407

Fischer, N., and Rochaix, J. D. (2001). The flanking regions of PsaD drive efficient gene expression in the nucleus of the green alga *Chlamydomonas reinhardtii*. *Mol. Genet. Genomics* 265, 888–894. doi:10.1007/s004380100485

Gkeka, P., and Sarkisov, L. (2010). Interactions of phospholipid bilayers with several classes of amphiphilic alpha-helical peptides: insights from coarse-grained molecular dynamics simulations. *J. Phys. Chem. B* 114, 826–839. doi:10.1021/jp908320b

Goodstein, D. M., Shu, S., Howson, R., Neupane, R., Hayes, R. D., Fazo, J., et al. (2012). Phytozome: a comparative platform for green plant genomics. *Nucleic Acids Res.* 40, D1178–D1186. doi:10.1093/nar/gkr944

Gu, X., Cao, L., Wu, X., Li, Y., Hu, Q., Han, D., et al. (2021). A lipid bodies-associated galactosyl hydrolase is involved in triacylglycerol biosynthesis and galactolipid turnover in the unicellular green alga *Chlamydomonas reinhardtii*. *Plants (Basel)* 10, 675. doi:10.3390/plants10040675

Huang, K. L., Tian, J., Wang, H., Fu, Y. F., Li, Y., Zheng, Y., et al. (2021). Fatty acid export protein BnFAX6 functions in lipid synthesis and axillary bud growth in Brassica napus. *Plant Physiol.* 186, 2064–2077. doi:10.1093/plphys/kiab229

Hurlock, A. K., Roston, R. L., Wang, K., and Benning, C. (2014). Lipid trafficking in plant cells. *Traffic* 15, 915–932. doi:10.1111/tra.12187

Jang, S., Kong, F., Lee, J., Choi, B. Y., Wang, P., Gao, P., et al. (2020). CrABCA2 facilitates triacylglycerol accumulation in *Chlamydomonas reinhardtii* under nitrogen starvation. *Mol. Cells* 43, 48–57. doi:10.14348/molcells.2019.0262

Kelley, L. A., Mezulis, S., Yates, C. M., Wass, M. N., and Sternberg, M. J. (2015). The Phyre2 web portal for protein modeling, prediction and analysis. *Nat. Protoc.* 10, 845–858. doi:10.1038/nprot.2015.053

Kim, S., Yamaoka, Y., Ono, H., Kim, H., Shim, D., Maeshima, M., et al. (2013). AtABCA9 transporter supplies fatty acids for lipid synthesis to the endoplasmic reticulum. *Proc. Natl. Acad. Sci. U. S. A.* 110, 773–778. doi:10.1073/pnas.1214159110

Kim, Y., Terng, E. L., Riekhof, W. R., Cahoon, E. B., and Cerutti, H. (2018). Endoplasmic reticulum acyltransferase with prokaryotic substrate preference contributes to triacylglycerol assembly in *Chlamydomonas*. *Proc. Natl. Acad. Sci. U. S. A.* 115, 1652–1657. doi:10.1073/pnas.1715922115

Kindle, K. L. (1990). High-frequency nuclear transformation of *Chlamydomonas reinhardtii*. *Proc. Natl. Acad. Sci. U. S. A.* 87, 1228–1232. doi:10.1073/pnas.87.3.1228

Klammt, C., Maslennikov, I., Bayrhuber, M., Eichmann, C., Vajpai, N., Chiu, E. J., et al. (2012). Facile backbone structure determination of human membrane proteins by NMR spectroscopy. *Nat. Methods* 9, 834–839. doi:10.1038/nmeth.2033

Könnel, A., Bugaeva, W., Guegel, I. L., and Philippar, K. (2019). BANFF: bending of bilayer membranes by amphiphilic alpha-helices is necessary for form and function of organelles[1]. *Biochem. Cell Biol.* 97, 243–256. doi:10.1139/bcb-2018-0150

Kropat, J., Hong-Hermesdorf, A., Casero, D., Ent, P., Castruita, M., Pellegrini, M., et al. (2011). A revised mineral nutrient supplement increases biomass and growth rate in *Chlamydomonas reinhardtii*. *Plant J.* 66, 770–780. doi:10.1111/j.1365-313X.2011.04537.x

LaBrant, E., Barnes, A. C., and Roston, R. L. (2018). Lipid transport required to make lipids of photosynthetic membranes. *Photosynth. Res.* 138, 345–360. doi:10.1007/s11120-018-0545-5

Lavell, A. A., and Benning, C. (2019). Cellular organization and regulation of plant glycerolipid metabolism. *Plant Cell Physiol.* 60, 1176–1183. doi:10.1093/pcp/pcz016

Legeret, B., Schulz-Raffelt, M., Nguyen, H. M., Auroy, P., Beisson, F., Peltier, G., et al. (2016). Lipidomic and transcriptomic analyses of *Chlamydomonas reinhardtii* under heat stress unveil a direct route for the conversion of membrane lipids into storage lipids. *Plant Cell Environ.* 39, 834–847. doi:10.1111/pce.12656

Li, N., Gügel, I. L., Giavalisco, P., Zeisler, V., Schreiber, L., Soll, J., et al. (2015). FAX1, a novel membrane protein mediating plastid fatty acid export. *PLoS Biol.* 13, e1002053. doi:10.1371/journal.pbio.1002053

Li, N., Xu, C., Li-Beisson, Y., and Philippar, K. (2016). Fatty acid and lipid transport in plant cells. *Trends Plant Sci.* 21, 145–158. doi:10.1016/j.tplants.2015.10.011

Li, N., Zhang, Y., Meng, H., Li, S., Wang, S., Xiao, Z., et al. (2019). Characterization of Fatty Acid Exporters involved in fatty acid transport for oil accumulation in the green alga *Chlamydomonas reinhardtii*. *Biotechnol. Biofuels* 12, 14. doi:10.1186/s13068-018-1332-4

Li, N., Meng, H., Li, S., Zhang, Z., Zhao, X., Wang, S., et al. (2020). Two plastid fatty acid exporters contribute to seed oil accumulation in Arabidopsis. *Plant Physiol.* 182, 1910–1919. doi:10.1104/pp.19.01344

Liaci, A. M., and Forster, F. (2021). Take me home, protein roads: Structural insights into signal peptide interactions during ER translocation. *Int. J. Mol. Sci.* 22, 11871. doi:10.3390/ijms222111871

Li-Beisson, Y., Shorrosh, B., Beisson, F., Andersson, M. X., Arondel, V., Bates, P. D., et al. (2013). "Acyl-lipid metabolism," in *The Arabidopsis book* (American Society of Plant Biologists), 11, e0161.

Li-Beisson, Y., Beisson, F., and Riekhof, W. (2015). Metabolism of acyl-lipids in *Chlamydomonas reinhardtii*. *Plant J.* 82, 504–522. doi:10.1111/tpj.12787

Li-Beisson, Y., Neunzig, J., Lee, Y., and Philippar, K. (2017). Plant membrane-protein mediated intracellular traffic of fatty acids and acyl lipids. *Curr. Opin. Plant Biol.* 40, 138–146. doi:10.1016/j.pbi.2017.09.006

Li-Beisson, Y., Thelen, J. J., Fedosejevs, E., and Harwood, J. L. (2019). The lipid biochemistry of eukaryotic algae. *Prog. Lipid Res.* 74, 31–68. doi:10.1016/j.plipres.2019.01.003

Li-Beisson, Y., Kong, F., Wang, P., Lee, Y., and Kang, B. H. (2021). The disassembly of lipid droplets in *Chlamydomonas*. *New Phytol.* 231, 1359–1364. doi:10.1111/nph.17505

Mackinder, L. C. M., Chen, C., Leib, R. D., Patena, W., Blum, S. R., Rodman, M., et al. (2017). A spatial interactome reveals the protein organization of the algal CO2-concentrating mechanism. *Cell* 171, 133–147.e14. doi:10.1016/j.cell.2017.08.044

Merchant, S. S., Kropat, J., Liu, B., Shaw, J., and Warakanont, J. (2012). TAG, you're it! Chlamydomonas as a reference organism for understanding algal triacylglycerol accumulation. *Curr. Opin. Biotechnol.* 23, 352–363. doi:10.1016/j.copbio.2011.12.001

Michaud, M., and Jouhet, J. (2019). Lipid trafficking at membrane contact sites during plant development and stress response. *Front. Plant Sci.* 10, 2. doi:10.3389/fpls.2019.00002

Molnar, A., Bassett, A., Thuenemann, E., Schwach, F., Karkare, S., Ossowski, S., et al. (2009). Highly specific gene silencing by artificial microRNAs in the unicellular alga *Chlamydomonas reinhardtii*. *Plant J.* 58, 165–174. doi:10.1111/j.1365-313X.2008.03767.x

Neupert, J., Karcher, D., and Bock, R. (2009). Generation of Chlamydomonas strains that efficiently express nuclear transgenes. *Plant J.* 57, 1140–1150. doi:10.1111/j.1365-313X.2008.03746.x

Ossowski, S., Schwab, R., and Weigel, D. (2008). Gene silencing in plants using artificial microRNAs and other small RNAs. *Plant J.* 53, 674–690. doi:10.1111/j.1365-313X.2007.03328.x

Patron, N. J., Orzaez, D., Marillonnet, S., Warzecha, H., Matthewman, C., Youles, M., et al. (2015). Standards for plant synthetic biology: a common syntax for exchange of DNA parts. *New Phytol.* 208, 13–19. doi:10.1111/nph.13532

Porra, R. J., and Scheer, H. (1989). Towards a more accurate future for chlorophyll a and b determinations: the inaccuracies of daniel arnon's assay. *Photosynth. Res.* 140, 215–219. doi:10.1007/s11120-018-0579-8

Rütgers, M., Muranaka, L. S., Mühlhaus, T., Sommer, F., Thoms, S., Schurig, J., et al. (2017). Substrates of the chloroplast small heat shock proteins 22E/F point to thermolability as a regulative switch for heat acclimation in *Chlamydomonas reinhardtii*. *Plant Mol. Biol.* 95, 579–591. doi:10.1007/s11103-017-0672-y

Schmollinger, S., Strenkert, D., and Schroda, M. (2010). An inducible artificial microRNA system for Chlamydomonas reinhardtii confirms a key role for heat shock factor 1 in regulating thermotolerance. *Curr. Genet.* 56, 383–389. doi:10.1007/s00294-010-0304-4

Schroda, M. (2019). Good news for nuclear transgene expression in *Chlamydomonas*. *Cells* 8, 1534. doi:10.3390/cells8121534

Schwacke, R., Schneider, A., van der Graaff, E., Fischer, K., Catoni, E., Desimone, M., et al. (2003). ARAMEMNON, a novel database for Arabidopsis integral membrane proteins. *Plant Physiol.* 131, 16–26. doi:10.1104/pp.011577

Scranton, M. A., Ostrand, J. T., Fields, F. J., and Mayfield, S. P. (2015). Chlamydomonas as a model for biofuels and bio-products production. *Plant J.* 82, 523–531. doi:10.1111/tpj.12780

Spaniol, B., Lang, J., Venn, B., Schake, L., Sommer, F., Mustas, M., et al. (2022). Complexome profiling on the Chlamydomonas lpa2 mutant reveals insights into PSII biogenesis and new PSII associated proteins. *J. Exp. Bot.* 73, 245–262. doi:10.1093/jxb/erab390

Takemura, T., Imamura, S., and Tanaka, K. (2019). Identification of a chloroplast fatty acid exporter protein, CmFAX1, and triacylglycerol accumulation by its overexpression in the unicellular red alga Cyanidioschyzon merolae. *Algal Res.* 38, 101396. doi:10.1016/j.algal.2018.101396

Takeuchi, T., and Benning, C. (2019). Nitrogen-dependent coordination of cell cycle, quiescence and TAG accumulation in *Chlamydomonas*. *Biotechnol. Biofuels* 12, 292. doi:10.1186/s13068-019-1635-0

Tian, Y., Lv, X., Xie, G., Zhang, J., Xu, Y., Chen, F., et al. (2018). Seed-specific overexpression of AtFAX1 increases seed oil content in Arabidopsis. *Biochem. Biophys. Res. Commun.* 500, 370–375. doi:10.1016/j.bbrc.2018.04.081

Tian, Y., Lv, X., Xie, G., Wang, L., Dai, T., Qin, X., et al. (2019). FAX2 mediates fatty acid export from plastids in developing Arabidopsis seeds. *Plant Cell Physiol.* 60, 2231–2242. doi:10.1093/pcp/pcz117

Troncoso-Ponce, M. A., Nikovics, K., Marchive, C., Lepiniec, L., and Baud, S. (2015). New insights on the organization and regulation of the fatty acid biosynthetic network in the model higher plant *Arabidopsis thaliana*. *Biochimie* 120, 3–8. doi:10.1016/j.biochi.2015.05.013

Weber, E., Engler, C., Gruetzner, R., Werner, S., and Marillonnet, S. (2011). A modular cloning system for standardized assembly of multigene constructs. *Plos One* 6, e16765. doi:10.1371/journal.pone.0016765

Xiao, Z., Tang, F., Zhang, L., Li, S., Wang, S., Huo, Q., et al. (2021). The Brassica napus fatty acid exporter FAX1-1 contributes to biological yield, seed oil content, and oil quality. *Biotechnol. Biofuels* 14, 190. doi:10.1186/s13068-021-02035-4

Xu, C., and Shanklin, J. (2016). Triacylglycerol metabolism, function, and accumulation in plant vegetative tissues. *Annu. Rev. Plant Biol.* 67, 179–206. doi:10.1146/annurev-arplant-043015-111641

Young, D. Y., and Shachar-Hill, Y. (2021). Large fluxes of fatty acids from membranes to triacylglycerol and back during N-deprivation and recovery in *Chlamydomonas*. *Plant Physiol.* 185, 796–814. doi:10.1093/plphys/kiaa071

Zhu, L., He, S., Liu, Y., Shi, J., and Xu, J. (2020). Arabidopsis FAX1 mediated fatty acid export is required for the transcriptional regulation of anther development and pollen wall formation. *Plant Mol. Biol.* 104, 187–201. doi:10.1007/s11103-020-01036-5

frontiers | Frontiers in Molecular Biosciences

TYPE Mini Review
PUBLISHED 14 November 2022
DOI 10.3389/fmolb.2022.1035574

OPEN ACCESS

EDITED BY
Isabel María López-Lara,
UNAM Campus Morelos, National Autonomous University of Mexico, Mexico

REVIEWED BY
Elizabeth Fozo,
The University of Tennessee, Knoxville, United States
Xuechen Li,
The University of Hong Kong, Hong Kong SAR, China

*CORRESPONDENCE
Truc T. Tran,
tttran4@houstonmethodist.org

SPECIALTY SECTION
This article was submitted to Lipids, Membranes and Membranous Organelles, a section of the journal Frontiers in Molecular Biosciences

RECEIVED 02 September 2022
ACCEPTED 26 October 2022
PUBLISHED 14 November 2022

CITATION
Nguyen AH, Hood KS, Mileykovskaya E, Miller WR and Tran TT (2022), Bacterial cell membranes and their role in daptomycin resistance: A review. *Front. Mol. Biosci.* 9:1035574. doi: 10.3389/fmolb.2022.1035574

Bacterial cell membranes and their role in daptomycin resistance: A review

April H. Nguyen[1,2], Kara S. Hood[1,2], Eugenia Mileykovskaya[3], William R. Miller[1,2] and Truc T. Tran[1,2]*

[1]Center for Infectious Diseases Research, Houston Methodist Research Institute, Houston, TX, United States, [2]Division of Infectious Diseases, Department of Medicine, Houston Methodist Hospital, Houston, TX, United States, [3]Department of Biochemistry and Molecular Biology, McGovern Medical School, University of Texas Health Science Center, Houston, TX, United States

Lipids play a major role in bacterial cells. Foremost, lipids are the primary constituents of the cell membrane bilayer, providing structure and separating the cell from the surrounding environment. This makes the lipid bilayer a prime target for antimicrobial peptides and membrane-acting antibiotics such as daptomycin. In response, bacteria have evolved mechanisms by which the membrane can be adapted to resist attack by these antimicrobial compounds. In this review, we focus on the membrane phospholipid changes associated with daptomycin resistance in enterococci, *Staphylococcus aureus*, and the Viridans group streptococci.

KEYWORDS

daptomycin, resistance, phospholipids, enterococci, *Staphylococcus aureus*, streptococci

Introduction

The cell membrane is a vital component of the bacterial cell, serving as a part of the protective barrier against the surrounding environment and as a scaffold for metabolic and regulatory proteins. Bacterial membranes are primarily composed of a bilayer of phospholipids with varying headgroups, acyl chain lengths, and acyl saturation which can influence membrane properties such as fluidity or charge. The major lipids in Gram-positive bacteria, particularly the firmicutes, are anionic phospholipids (APLs) [e.g., phosphatidylglycerol (PG), cardiolipin (CL)] and their derivatives (lysyl-PG, alanyl-PG), zwitterionic phospholipids, as well as other lipid classes like glycolipids and diacylglycerols (Sohlenkamp and Geiger, 2016). While the traditional "fluid mosaic model" describes a uniform bilayer whereby lipids and proteins are free to diffuse throughout the space, there is increasing evidence of the existence of distinct domains within the membrane (Matsumoto et al., 2006). These phospholipid domains have been described across several clinically important species of Gram-positive organisms, including "functional membrane microdomains" in *S. aureus* (García-Fernández et al., 2017), APL microdomains in *Enterococcus faecalis* (Tran et al., 2013a), or the ExPortal of *Streptococcus* spp. (Vega and Caparon, 2013). Importantly, alterations in these domains

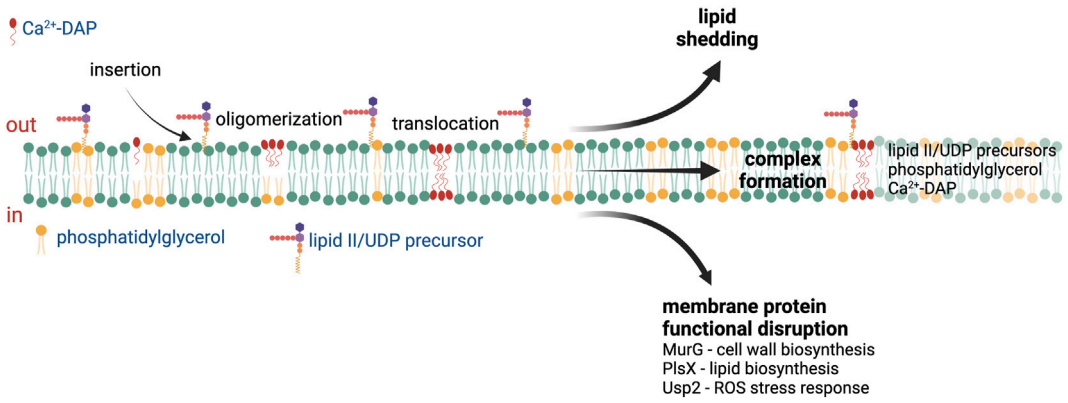

FIGURE 1
Proposed mechanisms of action of daptomycin. After insertion into the cell membrane, the Ca^{2+}-daptomycin complex oligomerize in the outer leaflet of the cell membrane. Ca^{2+}-daptomycin oligomers are translocated to the inner leaflet of the cell membrane which result in lipid shedding, tripartite formation with phosphatidylglycerol and lipid II/UDP precursors, or membrane protein functional disruption. See text for details. ROS—reactive oxygen species, UDP—undecaprenyl. Figure produced with BioRender.

have been associated with specific roles in the bacterial response to antibiotics and antimicrobial peptides active at the cell envelope.

The relative accessibility and essential functions of the bacterial membrane components make them effective targets for antimicrobials. The rise of multidrug resistant organisms such as methicillin-resistant *Staphylococcus aureus* (MRSA) and vancomycin-resistant enterococci (VRE) (Munita et al., 2015; Khan et al., 2018) spurred interest in antibiotics with alternative mechanisms of action that could bypass resistance to available agents. Daptomycin (DAP) has emerged as a treatment option that retained *in vitro* activity against resistant Gram-positive organisms and has seen increasing use against invasive infections due to MRSA and particularly VRE (Jorgensen et al., 2003; Mortin et al., 2007). Resistance to DAP is being reported with increasing frequency in clinical isolates, approaching 15%–28% in centers with heavy use of DAP (Kamboj et al., 2011; Munita et al., 2015; DiPippo et al., 2017; Wang et al., 2018). This review will address the role of the cell membrane in DAP resistance (DAP-R), with a focus on the alteration and adaptation of membrane phospholipids in Gram-positive bacteria of clinical importance.

Mechanism of action of daptomycin

DAP is a lipopeptide antibiotic originally isolated from *Streptomyces roseosporus* in the 1980s (Eisenstein et al., 2010). DAP possesses a cyclic peptide core linked to a fatty acyl chain and requires calcium to adopt an amphipathic conformation that facilitates oligomerization and insertion into the bacterial membrane. In addition, complex formation with calcium masks the lipopeptides's negative charge and increases its affinity for the membrane lipid PG, the major constituent of Gram-positive membranes (typically comprising 50%–65% of the total APL content in *S. aureus* and *E. faecalis* (Müller et al., 2016; DeMars et al., 2020; Kotsogianni et al., 2021; Woodall et al., 2021). Recent structural analysis of Ca^{2+}-DAP in lipid bilayers containing PG shows that DAP forms tetramers within the outer leaflet (Beriashvili et al., 2020). These tetramers can reversibly flip between the outer and inner leaflets and associate with one another to form a complex that spans the entire membrane (Zhang et al., 2014), resulting in membrane leakage and depolarization in cells after prolonged incubation with Ca^{2+}-DAP (Silverman et al., 2003).

Multiple DAP mechanisms of action have been proposed based on the different reported cellular responses to DAP exposure (Figure 1), including membrane permeabilization, inhibition of cell wall synthesis, and physical alteration of membrane fluidity or curvature (Mengin-Lecreulx et al., 1990; Silverman et al., 2003; Pogliano et al., 2012; Müller et al., 2016). A recent study published by Grein et al. demonstrated that in *S. aureus* Ca2^{+}-DAP oligomers form a tripartite complex with PG and lipid II (or other undecaprenyl cell envelope precursors, UDP), which are primarily located at the cell septum (Figure 1). The DAP-PG-lipid II complex not only sequesters lipid II substrate, but also disrupts the localization and assembly of the peptidoglycan synthesis machinery (Grein et al., 2020). In *Bacillus subtilis*, the insertion of DAP complexes in the membrane and subsequent alteration in membrane fluidity leads to mislocalization of crucial membrane proteins (Müller et al., 2016). After prolonged incubation, the DAP-UDP-PG complexes spread throughout the membrane, compromising envelope integrity and leading to cell death (Grein et al., 2020). The ability of DAP to

TABLE 1 Genes associated with membrane changes and daptomycin resistance.

Organism	Relevant gene	Predicted function	Phospholipids and fatty acids impacted	Surface charge and fluidity/ rigidity	Proposed mechanism of resistance	References
Enterococcus faecalis	*liaF*	three-component regulatory system	• alterations in PG	• alterations in surface charge	APL microdomain redistribution	Arias et al. (2011); Miller et al. (2019)
	cls	cardiolipin synthase	• alteration in diglycodiacylglycerol			
	gdpD	glycerophosphodiester phosphodiesterase	• alteration in L-PGalteration in CL			
	dak	fatty acid kinase				
Enterococcus faecium	*cls*	cardiolipin synthase	• alterations in PG	• alterations in surface charge	Increased net surface charge	Tran et al. (2013b); Diaz et al. (2014); Prater et al. (2019)
	cfa	cyclopropan-fatty-acyl-phospholipid synthase	• alterations in L-PG	• alterations in membrane rigidity/ fluidity	APL microdomain redistribution	
	dlt	D-alanylation of techoic acid	• alteration in digalactosyldiacylglycerols			
	mprF	multiple peptide resistance factor	• alterations in unsaturated and cyclic fatty acids			
	yvcRS	ABC transporter				
	oatA	O-acetyltransferase				
	divIVA	cell division and chromosome segregation				
Staphylococcus aureus	*vraSR*	two-component stress response system	• alterations in PG	• alterations in surface charge	Increased net surface charge	Peschel et al. (2001); Mishra et al. (2011a); Mehta et al. (2012); Peleg et al. (2012); Mishra and Bayer (2013); Hines et al. (2017); Jiang et al. (2019)
	yycFG	two-component cell wall biosynthesis	• alterations in L-PG	• alterations in membrane rigidity/ fluidity	Decrease/loss of target phospholipids	
	pgsA	CDP-diacylglycerol-glycerol-3-phosphate-3-phosphatidyltransferase	• alternations in CL			
	cls	cardiolipin synthase	• no changes in fatty acids			
	mprF	multiple peptide resistance factor				
Viridans groupstreptococci	*cdsA*	phosphatidate cytidylyltransferase	• alterations in PG	• alterations in surface charge	Decrease/loss of target phospholipids	Akins et al. (2015); Adams et al. (2017); Mishra et al. (2017); Kebriaei et al. (2019); Tran et al. (2019)
			• alterations in PA	• alterations in membrane rigidity/ fluidity		
	pgsA	CDP-diacylglycerol-glycerol-3-phosphate-3-phosphatidyltransferase	• alternations in CL			

APL, anionic phospholipid; CL, cardiolipin; L-PG, lysyl-phosphatidylglyerol; PA, phosphatidic acid; PG, phosphatidylglycerol

disrupt cell wall biosynthesis is also supported by multiple *in vitro* and *ex vivo* studies where synergy or re-sensitization of DAP was observed upon combination with cell-wall acting antibiotics such as β-lactams (Dhand et al., 2011; Sakoulas et al., 2013; Sakoulas et al., 2014; Smith et al., 2015a; Smith et al., 2015b; Werth et al., 2015; Yim et al., 2017; Kebriaei et al., 2019; Johnson et al., 2021). Additionally, DAP has been shown to induce production of reactive oxygen species in *S. aureus* via binding to the universal stress response protein Usp2, a membrane protein which has been postulated to mediate the response to oxidative stress (Po et al., 2021). Thus, the binding and action of DAP is tied to the specific properties of the target bacterial membrane.

Alterations of membrane lipids associated with changes in daptomycin susceptibility

A recurring theme in the emergence of DAP resistance across species is the presence of mutations leading to changes in both proteins of the lipid metabolic pathways and two-component sensors (TCS) involved in regulating cell envelope homeostasis (Tran et al., 2015). These changes can lead to alterations in the synthesis and modification of membrane lipid species and acyl-groups, thus impacting the composition and properties of the membrane (Table 1). In addition to *de novo* synthesis, bacteria can utilize exogenous fatty acids from their environment,

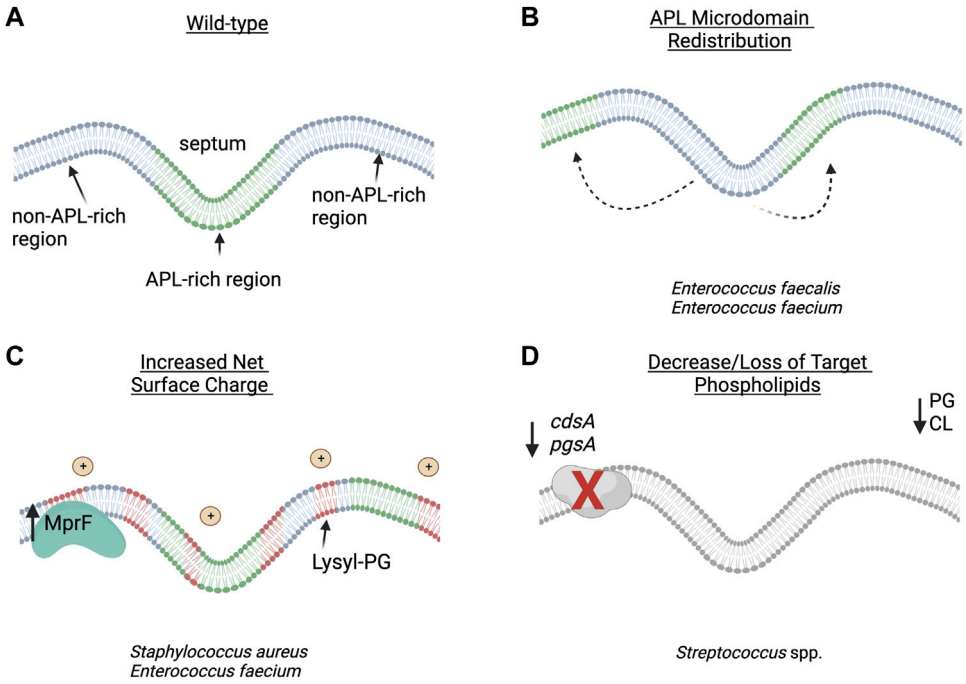

FIGURE 2
Proposed strategies of daptomycin resistance in Gram-positive pathogens: **(A)** wild-type bacterial cell membrane with anionic phospholipid (APL) microdomains clustered at the division septum. **(B)** In *Enterococcus faecalis*, redistribution of APL diverts daptomycin (DAP) away from the critical division septum. **(C)** In *Staphylococcus aureus* and *E. faecium*, changes in membrane phospholipid content and net surface charge lead to decreased daptomycin binding and oligomerization to the cell membrane. **(D)** In Viridans group streptococci, the decrease or loss of target phospholipid, PG and CL, are associated with overall decreased binding to the cell membrane or hyperaccumulation of daptomycin in a small subset of the bacterial population. APL–anionic phospholipid; CL–cardiolipin; PG–phosphatidylglycerol. Figure produced with BioRender.

including from human hosts, and importantly these exogenous acyl-chain profiles may be substantially different from those achievable by *de novo* synthesis in bacteria (Parsons et al., 2014a; Parsons et al., 2014b; Saito et al., 2014). These findings are also seen in model membranes where phospholipid head group and fatty acid residues in phospholipids can influence the membrane properties and alter the sensitivity to DAP (Beriashvili et al., 2018). The specific mechanisms by which these alterations impact the membrane are the subject of ongoing investigation, but shifts in membrane lipid content, fatty acid saturation, and alteration of membrane surface charge are common features of resistant isolates (Table 1).

Enterococcus faecalis and *Enterococcus faecium*

E. faecalis and *E. faecium* are important opportunistic human pathogens that cause a variety of infections ranging from skin and soft tissue infections to bacteremia and endocarditis (Krawczyk et al., 2021). DAP has emerged as a front-line agent against complicated VRE infections; however, emergence of DAP-R has threatened its utility in clinical practice. Characterization of both lab-evolved and clinical DAP-R strains has shed light on the genetic and phenotypic changes associated with DAP-R in enterococci (Arias et al., 2011; Palmer et al., 2011; Tran et al., 2013b; Miller et al., 2013; Diaz et al., 2014; Wang et al., 2018; Miller et al., 2019). In *E. faecalis*, there is an observable re-distribution of APL microdomains, while in *E. faecium* a DAP repulsion phenotype similar to *S. aureus* is seen (Ernst et al., 2009; Tran et al., 2013a; Diaz et al., 2014; Khan et al., 2019) (Figure 2).

Enterococci predominantly contain the APL PG in their cell membranes, in addition to CL, cationic PG derivatives such as lysyl-PG, and various glycolipids and diacylglycerols. In DAP-R enterococcal isolates, several general patterns in membrane lipid changes begin to emerge. Two studies using the clinical strain pair *E. faecalis* S613 (DAP-S) and R712 (DAP-R) grown to stationary phase found that the DAP-R isolate had a significant reduction in the amount of membrane PG as compared to its DAP-S parent, and an increase in glycerolphospho-diglycodiacylglycerol (GP-DGDAG) (Mishra et al., 2012; Hines et al., 2017). Further, an analysis of the laboratory strain *E. faecalis* OG1RF and two derivative strains

rendered DAP-R via *in vitro* passage showed decreases in PG and lysyl-PG in the resistant isolates during mid-logarithmic phase growth (Rashid et al., 2017). In paired isolates of *E. faecium*, the DAP-R isolate showed a significant decrease in PG (14% vs. 33%) and increases in GP-DGDAG (23% vs. 12%) as compared to the susceptible parent strain (Mishra et al., 2012). Taken together, these data appear to indicate that a relative loss of PG, the primary phospholipid involved in DAP binding, may contribute to the resistant phenotype. Interestingly, a different analysis of membrane lipids of the DAP-R *E. faecalis* strain performed by 2D-TLC during exponential growth showed a significant increase in PG, a reduction in CL, and no differences in lysyl-PG as compared to S613, while levels of GP-DGDAG were not reported (Khan et al., 2019). Thus, lipid alterations other than a decrease in membrane PG are likely to also contribute to DAP-R. A recent study showed that the absence of CL in *E. faecalis* OG1RF, achieved by deletion of both CL synthases, increased sensitivity to DAP and other cell damaging agents such as SDS, while the absence of lysyl-PG, resulting from deletion of *mprF2*, did not change sensitivity to DAP but rendered the mutant more resistant to SDS (Woodall et al., 2021). The triple mutant, which lacked CL and lysyl-PG, restored membrane tolerance to DAP and SDS to the level of parental strain OG1RF. These results further demonstrate the complexity of membrane lipid adaptation to DAP and other cell membrane damaging compounds.

The importance of cell surface charge in the DAP-R phenotype can be inferred from direct measurement and the pattern of mutations in resistant isolates. Both the clinical DAP-R strains *E. faecalis* and *E. faecium* displayed increased positive surface charge relative to their DAP-S counterparts (Arias et al., 2011; Mishra et al., 2012). Mutations impacting the *dlt* operon and *mprF* have been associated with DAP-R in *E. faecium* (Diaz et al., 2014). Further, *in vitro* adaptation of *E. faecium* to DAP led to the identification of additional genes associated with increases in cell surface charge, including *yvcRS*, *oatA*, and *divIVA* (Prater et al., 2019). Despite these observations, levels of lysyl-PG do not show a predictive trend in net surface charge in DAP-R strains (Mishra et al., 2012).

Alteration of membrane fluidity has also been observed in association with changes in DAP susceptibility. Differences in the length, saturation, and cyclization of fatty acyl chains of individual lipid species influence fluidity by altering lipid packing, and DAP has been reported to preferentially locate to regions of increased fluidity (Müller et al., 2016). Thus, changes in fluidity may alter DAP insertion and oligomerization in the membrane. Decreases in membrane fluidity (i.e., more rigid membranes) are associated with DAP-R resistance in enterococci. In *E. faecium*, this phenotype was associated with a decrease in the total proportion of unsaturated fatty acids and an increase in cyclic fatty acids which may be associated with mutations in *cfa* (cyclopropane fatty acid synthase) (Tran et al., 2013b; Diaz et al., 2014). Increased membrane rigidity has also been described in *E. faecalis* in association with changes in genes involved in the lipid metabolic pathway, including *cls, gdpD* (glycerophosphodiester phosphodiesterase), and *dak* (encoding a homologue of Fak, the staphylococcal fatty acid kinase) (Miller et al., 2019).

Further evidence supporting the potential importance of acyl-chain composition comes from a series of experiments examining the influence of exogenous fatty acids on the enterococcal membrane. Using laboratory isolates of *E. faecalis*, Harp and colleagues demonstrated that supplementation of growth media with oleic and linoleic acid induced tolerance to membrane stress, including protecting against DAP mediated killing (Saito et al., 2014; Harp et al., 2016). Subsequent studies profiling the changes in *E. faecalis* membranes associated with supplementation of a range of both saturated and unsaturated fatty acids found that exogenous fatty acids were rapidly incorporated into the acyl-chains of phospholipids. Unlike oleic acid, supplementation with saturated fatty acids and the native enterococcal monounsaturated fatty acid *cis*-vaccenic acid did not confer a survival advantage in the presence of DAP (Saito et al., 2017) while other combinations of "protective" fatty acids could induce DAP tolerance (Brewer et al., 2020). Thus, it is likely that variations in acyl-chains, as well as overall lipid species, play a role in protecting the membrane against daptomycin induced stress.

Staphylococcus aureus

S. aureus is an important pathogen that causes a wide range of infections including cellulitis, bacteremia, and infective endocarditis (Tong et al., 2015). Vancomycin has been the mainstay of therapy for infections due to methicillin-resistant MRSA, however DAP has seen increasing use as salvage therapy for recalcitrant MRSA infections (Lee et al., 2018). While DAP retains activity against the vast majority of MRSA isolates, the overlap of genetic pathways leading to vancomycin-intermediate *S. aureus* (VISA) and heterogenous VISA isolates and decreased susceptibility to DAP has contributed to the emergence of DAP-R on therapy (Patel et al., 2006; Julian et al., 2007; Kelley et al., 2011).

Similar to enterococci, resistance to DAP has been linked to mutations in genes encoding TCS (*vraSR, yycFG*) and lipid biosynthetic enzymes (*pgsA, cls*, and *mprF*), with subsequent alteration of membrane composition and surface charge associated with reduced binding of DAP (Table 1) (Friedman et al., 2006; Muthaiyan et al., 2008; Mehta et al., 2012; Peleg et al., 2012; Bayer et al., 2013). It has been noted that DAP-R associated mutations in *yycG* (also known as WalK, a histidine kinase sensor involved in cell wall biosynthesis) could play a role in modulating fatty acid biosynthesis and potentially membrane fluidity as shown by the role of the YycFG homologue in *S. pneumoniae*

(Mohedano et al., 2005). Interestingly, *S. aureus* has also been shown to exhibit "lipid shedding," where DAP exposure triggered active release of membrane phospholipids that were able to inactivate DAP and protect from bacterial killing (Pader et al., 2016). This phenomenon has since been shown in other organisms, including in *E. faecalis* and *Streptococcus* spp. (Ledger et al., 2022).

Although a variety of lipids exist in staphylococcal membranes, the major phospholipids include PG, CL, and lysyl-PG, with PG and lysyl-PG being the most abundant (DeMars et al., 2020). Like enterococci, membranes from DAP-R *S. aureus* tend to have decreased amounts of PG, with increases in lysyl-PG which are closely correlated with mutations in *mprF*. Mutations in *mprF* are thought to lead to a gain-of-function, with increased production and/or flipping of lysyl-PG into the outer leaflet of the membrane (Ernst et al., 2009; Slavetinsky et al., 2022). In a DAP-S/DAP-R clinical strain pair, Jones et al. showed increased levels of lysyl-PG with decreased levels of PG in the resistant isolate (Jones et al., 2008). Other independent studies which analyzed MRSA strain pairs containing mutations in *mprF*, *yycG* and/or *cls2* showed similar increased levels of lysyl-PG in the DAP-R strains (Peleg et al., 2012; Mishra and Bayer, 2013). Conversely, a DAP-R MRSA strain containing mutations in *pgsA* (encoding PG synthase), *mprF*, and *yycG* amongst others showed reduced levels of PG, but also reduced levels of lysyl-PG and CL (Hines et al., 2017). This may be explained by the hypothesis that, in addition to electrostatic repulsion, MprF-mediated resistance may also reduce the available pool of PG for DAP to target, which has been supported through biochemical work using large unilamellar vesicles (Kilelee et al., 2010). Mutations in *dltABCD* (involved in D-alanylation of teichoic acids) have also been associated with DAP-R in *S. aureus* (Bayer et al., 2013; Bayer et al., 2016). Gain-of-function mutations in this operon are proposed to increase overall cell surface charge through alanylation of lipoteichoic acids and wall teichoic acids (Table 1; Figure 2), and deletion of *dlt* results in increased susceptibility to cationic antimicrobial peptides (Peschel et al., 1999).

Mutations in *cls2*, one of the two staphylococcal CL synthases, have been implicated in DAP-R. Alterations of the enzyme resulted in increased biosynthetic activity, increased levels of CL, decreased levels of PG, and no changes in lysyl-PG levels. CL-rich membranes have shown to have increased thickness by neutron reflectometry, which was associated with decrease in penetration and aggregation of DAP. This impaired ability of DAP insertion and translocation, which was postulated as the as mechanism underlying DAP-R in these strains (Jiang et al., 2019). Increases in CL and decreased levels of PG has also been linked to DAP-tolerance in serum-adapted strains of *S. aureus* (Ledger et al., 2022).

In addition, changes in membrane fluidity also correlate with decreased DAP bactericidal activity. In contrast to enterococci, clinical isolates of *S. aureus* have in general shown increases in membrane fluidity associated with DAP-R (Jones et al., 2008; Mishra et al., 2011a; Mishra and Bayer, 2013). While no significant differences in fatty acid content in saturation levels, length, or branching, the fluidity changes may be explained by membrane carotenoid content of *S. aureus*. In many clinical isolates, there was a statistically significant decrease in the membrane carotenoid staphyloxanthin accompanied by a decrease in membrane fluidity. Staphyloxanthin is expressed by the majority of *S. aureus* isolated from infections and has previously been implicated in protecting the bacteria from DAP and antimicrobial peptide mediated killing, although prior studies in laboratory strains associated resistance with increased staphyloxanthin content and more rigid membranes (Mishra et al., 2011b). Interestingly, a more rigid membrane phenotype has also been observed in isolates arising from *in vitro* adaptation experiments or exposure to other cell envelope active compounds (such as the lipoglycopeptide dalbavancin) for which there was also cross resistance to DAP (Mishra et al., 2009; Zhang et al., 2022). These changes were related to differences in the ratio of long and short-chain fatty acids; however, differences in strain background mutations and growth media prevent a direct comparison. It is not clear if the observed shifts in fluidity are mechanistically important in disrupting the binding or translocation of DAP in the membrane, or merely a consequence of the alterations of membrane composition.

Streptococcus spp.

Viridans group streptococci (VGS) include a variety of species (i.e., *S. mitis, S. oralis, S. anginosus,* among others) that can cause severe infections including infective endocarditis, and resistance to commonly used antibiotics such as β-lactams is increasing (Doern et al., 1996; Marron et al., 2001; Prabhu et al., 2004). Unfortunately, high-level DAP-R [minimum inhibitory concentration (MIC) ≥ 256 μg/ml] can rapidly emerge in VGS upon DAP exposure (García-De-La-Mària et al., 2013; Akins et al., 2015).

While wild-type DAP-S cells contain PG and CL as the predominant phospholipids in the membrane, DAP-R VGS strains show no detectable PG or CL. Instead, cell membranes of resistant derivatives contain increased levels of the phospholipid precursor phosphatidic acid (PA) and decreased levels of phosphatidylcholine (not found in *E. faecalis* or *S. aureus*) (Adams et al., 2017; Mishra et al., 2017; Tran et al., 2019). This correlates with the identification of loss-of-function mutations in *cdsA*, a gene that encodes the phosphatidate cytidyltransferase enzyme (which generates the substrate CDP-diacylglycerol from PA for downstream phospholipid synthesis). The disappearance of CL and PG in various VGS strains harboring mutations in *cdsA* and/or *pgsA* was confirmed by lack of fluorescence in binding studies with 10-N-nonyl

acridine orange NAO (Mishra et al., 2017), a fluorescent dye which binds APLs (Mileykovskaya and Dowhan, 2000).

Despite the lack of PG and CL in the membrane, several patterns of DAP binding have been observed in DAP-R streptococci (Figure 2). In *S. oralis* strains that developed DAP-R in association with mutations in *pgsA*, binding of DAP to the cell membrane appears to be uniform, but with significantly less binding overall (Tran et al., 2019). Conversely, strains that developed DAP-R via mutations in *cdsA* demonstrated hyperaccumulation of DAP in a small population of the cells (Mishra et al., 2017). The authors of this study hypothesized that a minority of bacterial cells may sequester DAP and allow the larger population to survive the antibiotic exposure, although the viability of cells as determined by propidium iodide uptake did not correlate with DAP hyperaccumulation. The discordance between a lack of PG and overall binding of DAP in VGS strains remains unexplained. While lack of PG and CL are consistent with many DAP-R VGS strains which have been adapted by serial passage or in an *ex vivo* simulated endocarditis vegetation model (SEV), there are other strains that showed no significant changes in lipid content (Kebriaei et al., 2019).

Overall, alterations in cell membrane fluidity have not been a consistent or predictable phenotype of DAP-R in VGS. Initial studies showed an increase in membrane fluidity was associated with resistance in *S. mitis/oralis* strains that were obtained from serial passage (Mishra et al., 2017; Mishra et al., 2020). These findings were later confirmed by Kebriaei et al. in an SEV model using the same strain. However, these changes may be isolate specific, as adaptation of a different strain background identified no differences in fluidity in the DAP-R derivative, and displayed a similar membrane lipid content relative to its DAP-S parent (Kebriaei et al., 2019). In a separate study, Tran et al. found no changes in fluidity between parental strains and evolved DAP-R derivatives of *S. mitis* or *S. oralis* strains despite the complete disappearance of PG and CL (Tran et al., 2019).

Similarly, alterations in cell surface charge have varied across DAP-R VGS. In *S. mitis* and *S. oralis* strains which developed DAP-R via mutations in *pgsA* or *cdsA*, Tran et al. found no changes in surface charge between parental strains and evolved DAP-R derivatives (Tran et al., 2019). In a serial passage experiment, DAP-R in *S. mitis/oralis* SF100 was associated with a decrease in net surface positive charge while maintaining the similar overall DAP binding profiles between the DAP-R and DAP-S strain (Mishra et al., 2020). However, in the SEV model Kebriaei et al. found no difference in surface charge in the DAP-R SF100 strain (Kebriaei et al., 2019). Furthermore, DAP-R in *S. anginosus* has been linked to changes in capsular polysaccharide and other cell surface modification genes that may affect surface charge. Substitutions in genes encoding *cls, yycG* and the *dlt* operon were identified in the DAP-R strain (Rahman et al., 2016) however, the exact contribution of surface charge to DAP-R in VGS remains unclear.

In summary, changes in lipid content associated with DAP-R in *S. mitis/oralis* seem to be dependent on strain and the type of mutation present despite a similar phenotype of high-level DAP-R (MIC ≥256 μg/ml). The precise mechanism of DAP-R in VGS or how this group of bacteria maintains cell envelope function and integrity despite the absence of PG and CL remains unclear. Further evaluation is warranted to determine the impact of membrane changes on DAP-R in VGS.

Conclusion

The bacterial cell membrane is a dynamic structure that has evolved to adapt to changing environmental conditions. Understanding how bacteria alter their membrane in the face of external stress is critical to preserve the usefulness of membrane active antibiotics such as DAP. While the precise role of membrane lipid changes in the mechanism of resistance to DAP has yet to be completely explored, a deeper understanding of this process can be leveraged to overcome the limitations of current therapeutics.

Author contributions

AN, KH, EM, WM, and TT conceptualized the manuscript. AN and KH prepared the manuscript. EM, WM, and TT revised and edited the manuscript. All authors contributed to the article and approved the final version.

Funding

KH is supported by a training fellowship from the Gulf Coast Consortia, on the Texas Medical Center Training Program in Antimicrobial Resistant (TPAMR) (NIH Grant No. T32AI141349). WM is supported by National Institute of Allergy and Infectious Disease of the National Institutes of Health (Award Number K08AI135093).

Conflict of interest

WM has received grants and/or honoraria from Entasis Therapeutics and UpToDate.

The remaining authors declare that the research was conducted in the absence of any commercial or financial relationships that could be construed as a potential conflict of interest.

Publisher's note

References

Adams, H. M., Joyce, L. R., Guan, Z., Akins, R. L., and Palmer, K. L. (2017). *Streptococcus mitis* and *S. oralis* lack a requirement for CdsA, the enzyme required for synthesis of major membrane phospholipids in bacteria. *Antimicrob. Agents Chemother.* 61 (5), e02552-16. doi:10.1128/AAC.02552-16

Akins, R. L., Katz, B. D., Monahan, C., and Alexander, D. (2015). Characterization of high-level daptomycin resistance in viridans group streptococci developed upon *in vitro* exposure to daptomycin. *Antimicrob. Agents Chemother.* 59 (4), 2102–2112. doi:10.1128/AAC.04219-14

Arias, C. A., Panesso, D., Mcgrath, D. M., Qin, X., Mojica, M. F., Miller, C., et al. (2011). Genetic basis for *in vivo* daptomycin resistance in enterococci. *N. Engl. J. Med.* 365, 892–900. doi:10.1056/NEJMoa1011138

Bayer, A. S., Mishra, N. N., Cheung, A. L., Rubio, A., and Yang, S. J. (2016). Dysregulation of *mprF* and *dltABCD* expression among daptomycin-non-susceptible MRSA clinical isolates. *J. Antimicrob. Chemother.* 71 (8), 2100–2104. doi:10.1093/jac/dkw142

Bayer, A. S., Schneider, T., and Sahl, H. G. (2013). Mechanisms of daptomycin resistance in *Staphylococcus aureus*: Role of the cell membrane and cell wall. *Ann. N. Y. Acad. Sci.* 1277 (1), 139–158. doi:10.1111/J.1749-6632.2012.06819.X

Beriashvili, D., Spencer, N. R., Dieckmann, T., Overduin, M., and Palmer, M. (2020). Characterization of multimeric daptomycin bound to lipid nanodiscs formed by calcium-tolerant styrene-maleic acid copolymer. *Biochim. Biophys. Acta. Biomembr.* 1862 (6), 183234. doi:10.1016/J.BBAMEM.2020.183234

Beriashvili, D., Taylor, R., Kralt, B., Abu Mazen, N., Taylor, S. D., and Palmer, M. (2018). Mechanistic studies on the effect of membrane lipid acyl chain composition on daptomycin pore formation. *Chem. Phys. Lipids* 216, 73–79. doi:10.1016/j.chemphyslip.2018.09.015

Brewer, W., Harrison, J., Saito, H. E., and Fozoa, E. M. (2020). Induction of daptomycin tolerance in *Enterococcus faecalis* by fatty acid combinations. *Appl. Environ. Microbiol.* 86 (20), e01178–20. doi:10.1128/AEM.01178-20

DeMars, Z., Singh, V. K., and Bose, J. L. (2020). Exogenous fatty acids remodel staphylococcus aureus lipid composition through fatty acid kinase. *J. Bacteriol.* 202 (14), e00128-20. doi:10.1128/JB.00128-20

Dhand, A., Bayer, A. S., Pogliano, J., Yang, S. J., Bolaris, M., Nizet, V., et al. (2011). Use of antistaphylococcal beta-lactams to increase daptomycin activity in eradicating persistent bacteremia due to methicillin-resistant *Staphylococcus aureus*: Role of enhanced daptomycin binding. *Clin. Infect. Dis.* 53 (2), 158–163. doi:10.1093/cid/cir340

Diaz, L., Tran, T. T., Munita, J. M., Miller, W. R., Rincon, S., Carvajal, L. P., et al. (2014). Whole-genome analyses of Enterococcus faecium isolates with diverse daptomycin MICs. *Antimicrob. Agents Chemother.* 58 (8), 4527–4534. doi:10.1128/AAC.02686-14

DiPippo, A. J., Tverdek, F. P., Tarrand, J. J., Munita, J. M., Tran, T. T., Arias, C. A., et al. (2017). Daptomycin non-susceptible Enterococcus faecium in leukemia patients: Role of prior daptomycin exposure. *J. Infect.* 74 (3), 243–247. doi:10.1016/j.jinf.2016.11.004

Doern, G. V., Ferraro, M. J., Brueggemann, A. B., and Ruoff, K. L. (1996). Emergence of high rates of antimicrobial resistance among Viridans group streptococci in the United States. *Antimicrob. Agents Chemother.* 40 (4), 891–894. doi:10.1128/AAC.40.4.891

Eisenstein, B. I., Oleson, F. B., and Baltz, R. H. (2010). Daptomycin: From the mountain to the clinic, with essential help from francis tally, MD. *Clin. Infect. Dis.* 50 (1), S10–S15. doi:10.1086/647938

Ernst, C. M., Staubitz, P., Mishra, N. N., Yang, S. J., Hornig, G., Kalbacher, H., et al. (2009). The bacterial defensin resistance protein MprF consists of separable domains for lipid lysinylation and antimicrobial peptide repulsion. *PLoS Pathog.* 5 (11), e1000660. doi:10.1371/journal.ppat.1000660

Friedman, L., Alder, J. D., and Silverman, J. A. (2006). Genetic changes that correlate with reduced susceptibility to daptomycin in *Staphylococcus aureus*. *Antimicrob. Agents Chemother.* 50 (6), 2137–2145. doi:10.1128/AAC.00039-06

García-De-La-Mària, C., Pericas, J. M., Del Río, A., Castaneda, X., Vila-Farres, X., Armero, Y., et al. (2013). Early *in vitro* and *in vivo* development of high-level daptomycin resistance is common in mitis group streptococci after exposure to daptomycin. *Antimicrob. Agents Chemother.* 57 (5), 2319–2325. doi:10.1128/AAC.01921-12

García-Fernández, E., Koch, G., Wagner, R. M., Fekete, A., Stengel, S. T., Schneider, J., et al. (2017). Membrane microdomain disassembly inhibits MRSA antibiotic resistance. *Cell* 171 (6), 1354–1367. doi:10.1016/j.cell.2017.10.012

Grein, F., Müller, A., Scherer, K. M., Liu, X., Ludwig, K. C., Klöckner, A., et al. (2020). Ca2+-Daptomycin targets cell wall biosynthesis by forming a tripartite complex with undecaprenyl-coupled intermediates and membrane lipids. *Nat. Commun.* 11 (1), 1455. doi:10.1038/s41467-020-15257-1

Harp, J. R., Saito, H. E., Bourdon, A. K., Reyes, J., Arias, C. A., Campagna, S. R., et al. (2016). Exogenous fatty acids protect *Enterococcus faecalis* from daptomycin induced membrane stress independent of the response regulator LiaR. *Appl. Environ. Microbiol.* 82, 4410–4420. doi:10.1128/AEM.00933-16

Hines, K. M., Waalkes, A., Penewit, K., Holmes, E. A., Salipante, S. J., Werth, B. J., et al. (2017). Characterization of the mechanisms of daptomycin resistance among Gram- positive bacterial pathogens by multidimensional lipidomics. *mSphere* 2 (6), e00492-17. doi:10.1128/mSphere.00492-17

Jiang, J. H., Bhuiyan, M. S., Shen, H. H., Cameron, D. R., Rupasinghe, T. W. T., Wu, C. M., et al. (2019). Antibiotic resistance and host immune evasion in *Staphylococcus aureus* mediated by a metabolic adaptation. *Proc. Natl. Acad. Sci. U. S. A.* 116 (9), 3722–3727. doi:10.1073/pnas.1812066116

Johnson, T. M., Molina, K. C., Miller, M. A., Kiser, T. H., Huang, M., and Mueller, S. W. (2021). Combination ceftaroline and daptomycin salvage therapy for complicated methicillin-resistant *Staphylococcus aureus* bacteraemia compared with standard of care. *Int. J. Antimicrob. Agents* 57 (4), 106310. doi:10.1016/j.ijantimicag.2021.106310

Jones, T., Yeaman, M. R., Sakoulas, G., Yang, S. J., Proctor, R. A., Sahl, H. G., et al. (2008). Failures in clinical treatment of *Staphylococcus aureus* infection with daptomycin are associated with alterations in surface charge, membrane phospholipid asymmetry, and drug binding. *Antimicrob. Agents Chemother.* 52 (1), 269–278. doi:10.1128/AAC.00719-07

Jorgensen, J. H., Crawford, S. A., Kelly, C. C., and Patterson, J. E. (2003). *In vitro* activity of daptomycin against vancomycin-resistant enterococci of various Van types and comparison of susceptibility testing methods. *Antimicrob. Agents Chemother.* 47 (12), 3760–3763. doi:10.1128/AAC.47.12.3760-3763.2003

Julian, K., Kosowska-Shick, K., Whitener, C., Roos, M., Labischinski, H., Rubio, A., et al. (2007). Characterization of a daptomycin-nonsusceptible vancomycin-intermediate *Staphylococcus aureus* strain in a patient with endocarditis. *Antimicrob. Agents Chemother.* 51 (9), 3445–3448. doi:10.1128/AAC.00559-07

Kamboj, M., Cohen, N., Gilhuley, K., Babady, N. E., Seo, S. K., and Sepkowitz, K. A. (2011). Emergence of daptomycin-resistant VRE: Experience of a single institution. *Infect. Control Hosp. Epidemiol.* 32 (4), 391–394. doi:10.1086/659152

Kebriaei, R., Rice, S. A., Stamper, K. C., Seepersaud, R., Garcia-de-la-Maria, C., Mishra, N. N., et al. (2019). Daptomycin dose-ranging evaluation with single-dose versus multidose ceftriaxone combinations against streptococcus mitis/oralis in an *ex vivo* simulated endocarditis vegetation model. *Antimicrob. Agents Chemother.* 63 (6), e00386-19. doi:10.1128/AAC.00386-19

Kelley, P. G., Gao, W., Ward, P. B., and Howden, B. P. (2011). Daptomycin non-susceptibility in vancomycin-intermediate *Staphylococcus aureus* (VISA) and heterogeneous-VISA (hVISA): Implications for therapy after vancomycin treatment failure. *J. Antimicrob. Chemother.* 66 (5), 1057–1060. doi:10.1093/JAC/DKR066

Khan, A., Davlieva, M., Panesso, D., Rincon, S., Miller, W. R., Diaz, L., et al. (2019). Antimicrobial sensing coupled with cell membrane remodeling mediates antibiotic resistance and virulence in *Enterococcus faecalis*. *Proc. Natl. Acad. Sci. U. S. A.* 116 (52), 26925–26932. doi:10.1073/pnas.1916037116

Khan, A., Miller, W. R., and Arias, C. A. (2018). Mechanisms of antimicrobial resistance among hospital-associated pathogens. *Expert Rev. anti. Infect. Ther.* 16 (4), 269–287. doi:10.1080/14787210.2018.1456919

Kilelee, E., Pokorny, A., Yeaman, M. R., and Bayer, A. S. (2010). Lysyl-phosphatidylglycerol attenuates membrane perturbation rather than surface association of the cationic antimicrobial peptide 6W-RP-1 in a model membrane system: Implications for daptomycin resistance. *Antimicrob. Agents Chemother.* 54 (10), 4476–4479. doi:10.1128/AAC.00191-10

Kotsogianni, I., Wood, T. M., Alexander, F. M., Cochrane, S. A., and Martin, N. I. (2021). Binding studies reveal phospholipid specificity and its role in the calcium-dependent mechanism of action of daptomycin. *ACS Infect. Dis.* 7 (9), 2612–2619. doi:10.1021/acsinfecdis.1c00316

Krawczyk, B., Wityk, P., Gałęcka, M., and Michalik, M. (2021). The many faces of Enterococcus spp.—commensal, probiotic and opportunistic pathogen. *Microorganisms* 9 (9), 1900. doi:10.3390/MICROORGANISMS9091900

Ledger, E. V. K., Mesnage, S., and Edwards, A. M. (2022). Human serum triggers antibiotic tolerance in *Staphylococcus aureus*. *Nat. Commun.* 13 (1), 2041–2119. doi:10.1038/s41467-022-29717-3

Ledger, E., Mesnage, S., and Edwards, A. M. (2022). Human serum triggers antibiotic tolerance in *Staphylococcus aureus*. *Nat. Commun.* 13 (1), 2401. doi:10.1038/s41467-022-29717-3

Lee, A. S., de Lencastre, H., Garau, J., Kluytmans, J., Malhotra-Kumar, S., Peschel, A., et al. (2018). Methicillin-resistant *Staphylococcus aureus*. *Nat. Rev.* 4, 18033. doi:10.1038/NRDP.2018.33

Marron, A., Carratalà, J., Alcaide, F., Fernández-Sevilla, A., Gudiol, F., and Fernandez-SevillA, A. (2001). High rates of resistance to cephalosporins among viridans-group streptococci causing bacteraemia in neutropenic cancer patients. *J. Antimicrob. Chemother.* 47 (1), 87–91. doi:10.1093/jac/47.1.87

Matsumoto, K., Kusaka, J., Nishibori, A., and Hara, H. (2006). Lipid domains in bacterial membranes. *Mol. Microbiol.* 61 (5), 1110–1117. doi:10.1111/j.1365-2958.2006.05317.x

Mehta, S., Cuirolo, A. X., Plata, K. B., Riosa, S., Silverman, J. A., Rubio, A., et al. (2012). VraSR two-component regulatory system contributes to mprF-mediated decreased susceptibility to daptomycin in *in vivo*-selected clinical strains of methicillin-resistant *Staphylococcus aureus*. *Antimicrob. Agents Chemother.* 56 (1), 92–102. doi:10.1128/AAC.00432-10

Mengin-Lecreulx, D., Allen, N. E., Hobbs, J. N., and van Heijenoort, J. (1990). Inhibition of peptidoglycan biosynthesis in Bacillus megaterium by daptomycin. *FEMS Microbiol. Lett.* 57 (3), 245–248. doi:10.1016/0378-1097(90)90074-Z

Mileykovskaya, E., and Dowhan, W. (2000). Visualization of phospholipid domains in *Escherichia coli* by using the cardiolipin-specific fluorescent dye 10-N-nonyl acridine orange. *J. Bacteriol.* 182 (4), 1172–1175. doi:10.1128/JB.182.4.1172-1175.2000

Miller, C., Kong, J., Tran, T. T., Arias, C. A., Saxer, G., and Shamoo, Y. (2013). Adaptation of *Enterococcus faecalis* to daptomycin reveals an ordered progression to resistance. *Antimicrob. Agents Chemother.* 57 (11), 5373–5383. doi:10.1128/AAC.01473-13

Miller, W. R., Tran, T. T., Diaz, L., Rios, R., Khan, A., Reyes, J., et al. (2019). LiaR-independent pathways to daptomycin resistance in *Enterococcus faecalis* reveal a multilayer defense against cell envelope antibiotics. *Mol. Microbiol.* 111 (3), 811–824. doi:10.1111/MMI.14193

Mishra, N. N., and Bayer, A. S. (2013). Correlation of cell membrane lipid profiles with daptomycin resistance in methicillin-resistant staphylococcus aureus. *Antimicrob. Agents Chemother.* 57 (2), 1082–1085. doi:10.1128/AAC.02182-12

Mishra, N. N., Bayer, A. S., Tran, T. T., Shamoo, Y., Mileykovskaya, E., Dowhan, W., et al. (2012). Daptomycin resistance in enterococci is associated with distinct alterations of cell membrane phospholipid content. *PLoS One* 7 (8), e43958. doi:10.1371/JOURNAL.PONE.0043958

Mishra, N. N., Liu, G. Y., Yeaman, M. R., Nast, C. C., Proctor, R. A., McKinnell, J., et al. (2011). Carotenoid-related alteration of cell membrane fluidity impacts *Staphylococcus aureus* susceptibility to host defense peptides. *Antimicrob. Agents Chemother.* 55 (2), 526–531. doi:10.1128/AAC.00680-10

Mishra, N. N., McKinnell, J., Yeaman, M. R., Rubio, A., Nast, C. C., Chen, L., et al. (2011). *In vitro* cross-resistance to daptomycin and host defense cationic antimicrobial peptides in clinical methicillin-resistant *Staphylococcus aureus* isolates. *Antimicrob. Agents Chemother.* 55 (9), 4012–4018. doi:10.1128/AAC.00223-11

Mishra, N. N., Tran, T. T., Arias, C. A., Seepersaud, R., Sullam, P. M., and Bayer, A. S. (2020). Strain-specific adaptations of Streptococcus mitis-oralis to serial *in vitro* passage in daptomycin (DAP): Genotypic and phenotypic characteristics. *Antibiotics* 9 (8), 520. doi:10.3390/ANTIBIOTICS9080520

Mishra, N. N., Tran, T. T., Seepersaud, R., Garcia-de-la-Maria, C., Faull, K., Yoon, A., et al. (2017). Perturbations of phosphatidate cytidylyltransferase (CdsA) mediate daptomycin resistance in Streptococcus mitis/oralis by a novel mechanism. *Antimicrob. Agents Chemother.* 61 (4), e02435-16. doi:10.1128/AAC.02435-16

Mishra, N. N., Yang, S. J., Sawa, A., Rubio, A., Nast, C. C., Yeaman, M. R., et al. (2009). Analysis of cell membrane characteristics of in vitro-selected daptomycin-resistant strains of methicillin-resistant *Staphylococcus aureus*. *Antimicrob. Agents Chemother.* 53 (6), 2312–2318. doi:10.1128/AAC.01682-08

Mohedano, M. L., Overweg, K., De La Fuente, A., Reuter, M., Altabe, S., Mulholland, F., et al. (2005). Evidence that the essential response regulator YycF in Streptococcus pneumoniae modulates expression of fatty acid biosynthesis genes and alters membrane composition. *J. Bacteriol.* 187 (7), 2357–2367. doi:10.1128/JB.187.7.2357-2367.2005

Mortin, L. I., Li, T., Van Praagh, A. D. G., Zhang, S., Zhang, X. X., and Alder, J. D. (2007). Rapid bactericidal activity of daptomycin against methicillin-resistant and methicillin-susceptible *Staphylococcus aureus* peritonitis in mice as measured with bioluminescent bacteria. *Antimicrob. Agents Chemother.* 51 (5), 1787–1794. doi:10.1128/AAC.00738-06

Müller, A., Wenzel, M., Strahl, H., Grein, F., Saaki, T. N. V., Kohl, B., et al. (2016). Daptomycin inhibits cell envelope synthesis by interfering with fluid membrane microdomains. *Proc. Natl. Acad. Sci. U. S. A.* 113 (45), E7077–E7086. doi:10.1073/PNAS.1611173113

Munita, J. M., Bayer, A. S., and Arias, C. A. (2015). Evolving resistance among gram-positive pathogens. *Clin. Infect. Dis.* doi:10.1093/cid/civ523

Muthaiyan, A., Silverman, J. A., Jayaswal, R. K., and Wilkinson, B. J. (2008). Transcriptional profiling reveals that daptomycin induces the *Staphylococcus aureus* cell wall stress stimulon and genes responsive to membrane depolarization. *Antimicrob. Agents Chemother.* 52 (3), 980–990. doi:10.1128/AAC.01121-07

Pader, V., Hakim, S., Painter, K. L., Wigneshweraraj, S., Clarke, T. B., and Edwards, A. M. (2016). *Staphylococcus aureus* inactivates daptomycin by releasing membrane phospholipids. *Nat. Microbiol.* 2, 16194. doi:10.1038/NMICROBIOL.2016.194

Palmer, K. L., Daniel, A., Hardy, C., Silverman, J., and Gilmore, M. S. (2011). Genetic basis for daptomycin resistance in enterococci. *Antimicrob. Agents Chemother.* 55 (7), 3345–3356. doi:10.1128/AAC.00207-11

Parsons, J. B., Broussard, T. C., Bose, J. L., Rosch, J. W., Jackson, P., Subramanian, C., et al. (2014). Identification of a two-component fatty acid kinase responsible for host fatty acid incorporation by *Staphylococcus aureus*. *Proc. Natl. Acad. Sci. U. S. A.* 111 (29), 10532–10537. doi:10.1073/PNAS.1408797111

Parsons, J. B., Frank, M. W., Jackson, P., Subramanian, C., and Rock, C. O. (2014). Incorporation of extracellular fatty acids by a fatty acid kinase-dependent pathway in *Staphylococcus aureus*. *Mol. Microbiol.* 92 (2), 234–245. doi:10.1111/MMI.12556

Patel, J. B., Jevitt, L. A., Hageman, J., McDonald, L. C., and Tenover, F. C. (2006). An association between reduced susceptibility to daptomycin and reduced susceptibility to vancomycin in *Staphylococcus aureus*. *Clin. Infect. Dis.* 42 (11), 1652–1653. doi:10.1086/504084

Peleg, A. Y., Miyakis, S., Ward, D. V., Earl, A. M., Rubio, A., Cameron, D. R., et al. (2012). Whole genome characterization of the mechanisms of daptomycin resistance in clinical and laboratory derived isolates of *Staphylococcus aureus*. *PLoS One* 7 (1), e28316. doi:10.1371/journal.pone.0028316

Peschel, A., Jack, R. W., Otto, M., Collins, L. V., Staubitz, P., Nicholson, G., et al. (2001). *Staphylococcus aureus* resistance to human defensins and evasion of neutrophil killing via the novel virulence factor MprF is based on modification of membrane lipids with l-lysine. *J. Exp. Med.* 193 (9), 1067–1076. doi:10.1084/jem.193.9.1067

Peschel, A., Otto, M., Jack, R. W., Kalbacher, H., Jung, G., and Götz, F. (1999). Inactivation of the dlt operon in *Staphylococcus aureus* confers sensitivity to defensins, protegrins, and other antimicrobial peptides. *J. Biol. Chem.* 274 (13), 8405–8410. doi:10.1074/jbc.274.13.8405

Po, K. H. L., Chow, H. Y., Cheng, Q., Chan, B. K., Deng, X., Wang, S., et al. (2021). Daptomycin exerts bactericidal effect through induction of excessive ROS production and blocking the function of stress response protein Usp2. *Nat. Sci.* 1 (2), e10023. doi:10.1002/ntls.10023

Pogliano, J., Pogliano, N., and Silverman, J. A. (2012). Daptomycin-mediated reorganization of membrane architecture causes mislocalization of essential cell division proteins. *J. Bacteriol.* 194 (17), 4494–4504. doi:10.1128/JB.00011-12

Prabhu, R. M., Piper, K. E., Baddour, L. M., Steckelberg, J. M., Wilson, W. R., and Patel, R. (2004). Antimicrobial susceptibility patterns among viridans group streptococcal isolates from infective endocarditis patients from 1971 to 1986 and 1994 to 2002. *Antimicrob. Agents Chemother.* 48 (11), 4463–4465. doi:10.1128/AAC.48.11.4463-4465.2004

Prater, A. G., Mehta, H. H., Kosgei, A. J., Miller, W. R., Tran, T. T., Arias, C. A., et al. (2019). Environment shapes the accessible daptomycin resistance mechanisms in *Enterococcus faecium*. *Antimicrob. Agents Chemother.* 63 (10), e00790-19. doi:10.1128/AAC.00790-19

Rahman, M., Nguyen, S. V., McCullor, K. A., King, C. J., Jorgensen, J. H., and Michael McShan, W. (2016). Comparative genome analysis of the daptomycin-resistant Streptococcus anginosus strain J4206 associated with breakthrough bacteremia. *Genome Biol. Evol.* 8 (11), 3446–3459. doi:10.1093/GBE/EVW241

Rashid, R., Cazenave-Gassiot, A., Gao, I. H., Nair, Z. J., Kumar, J. K., Gao, L., et al. (2017). Comprehensive analysis of phospholipids and glycolipids in the opportunistic pathogen *Enterococcus faecalis*. *PLoS One* 12 (4), e0175886. doi:10.1371/journal.pone.0175886

Saito, H. E., Harp, J. R., and Fozo, E. M. (2017). *Enterococcus faecalis* responds to individual exogenous fatty acids independently of their degree of saturation or chain length. *Appl. Environ. Microbiol.* 84 (1), e01633-17. doi:10.1128/AEM.01633-17

Saito, H. E., Harp, J. R., and Fozo, E. M. (2014). Incorporation of exogenous fatty acids protects *Enterococcus faecalis* from membrane-damaging agents. *Appl. Environ. Microbiol.* 80 (20), 6527–6538. doi:10.1128/AEM.02044-14

Sakoulas, G., Nonejuie, P., Nizet, V., Pogliano, J., Crum-Cianflone, N., and Haddad, F. (2013). Treatment of high-level gentamicin-resistant *Enterococcus faecalis* endocarditis with daptomycin plus ceftaroline. *Antimicrob. Agents Chemother.* 57 (8), 4042–4045. doi:10.1128/AAC.02481-12

Sakoulas, G., Rose, W., Nonejuie, P., Olson, J., Pogliano, J., Humphries, R., et al. (2014). Ceftaroline restores daptomycin activity against daptomycin-nonsusceptible vancomycin-resistant *Enterococcus faecium*. *Antimicrob. Agents Chemother.* 58 (3), 1494–1500. doi:10.1128/AAC.02274-13

Silverman, J. A., Perlmutter, N. G., and Shapiro, H. M. (2003). Correlation of daptomycin bactericidal activity and membrane depolarization in *Staphylococcus aureus*. *Antimicrob. Agents Chemother.* 47 (8), 2538–2544. doi:10.1128/AAC.47.8.2538-2544.2003

Slavetinsky, C. J., Hauser, J. N., Gekeler, C., Slavetinsky, J., Geyer, A., Kraus, A., et al. (2022). Sensitizing *Staphylococcus aureus* to antibacterial agents by decoding and blocking the lipid flippase MprF. *Elife* 11, e66376. doi:10.7554/ELIFE.66376

Smith, J. R., Barber, K. E., Raut, A., Aboutaleb, M., Sakoulas, G., and Rybak, M. J. (2015). β-Lactam combinations with daptomycin provide synergy against vancomycin-resistant *Enterococcus faecalis* and *Enterococcus faecium*. *J. Antimicrob. Chemother.* 70 (6), 1738–1743. doi:10.1093/jac/dkv007

Smith, J. R., Barber, K. E., Raut, A., and Rybak, M. J. (2015). β-Lactams enhance daptomycin activity against vancomycin-resistant *Enterococcus faecalis* and *Enterococcus faecium* in *in vitro* pharmacokinetic/pharmacodynamic models. *Antimicrob. Agents Chemother.* 59 (5), 2842–2848. doi:10.1128/AAC.00053-15

Sohlenkamp, C., and Geiger, O. (2016). Bacterial membrane lipids: Diversity in structures and pathways. *FEMS Microbiol. Rev.* 40 (1), 133–159. doi:10.1093/femsre/fuv008

Tong, S. Y. C., Davis, J. S., Eichenberger, E., Holland, T. L., and Fowler, V. G. (2015). *Staphylococcus aureus* infections: Epidemiology, pathophysiology, clinical manifestations, and management. *Clin. Microbiol. Rev.* 28 (3), 603–661. doi:10.1128/CMR.00134-14

Tran, T. T., Mishra, N. N., Seepersaud, R., Diaz, L., Rios, R., Dinh, A. Q., et al. (2019). Mutations in *cdsA* and *pgsA* Correlate with Daptomycin Resistance in *Streptococcus mitis* and *S. oralis*. *Antimicrob. Agents Chemother.* 63 (2018), e01531-18–e01536. doi:10.1128/AAC.01531-18

Tran, T. T., Munita, J. M., and Arias, C. A. (2015). Mechanisms of drug resistance: Daptomycin resistance. *Ann. N. Y. Acad. Sci.* 1354 (1), 32–53. doi:10.1111/NYAS.12948

Tran, T. T., Panesso, D., Gao, H., Roh, J. H., Munita, J. M., Reyes, J., et al. (2013b). Whole-genome analysis of a daptomycin-susceptible enterococcus faecium strain and its daptomycin-resistant variant arising during therapy. *Antimicrob. Agents Chemother.* 57 (1), 261–268. doi:10.1128/AAC.01454-12

Tran, T. T., Panesso, D., Mishra, N. N., Mileykovskaya, E., Guan, Z., Munita, J. M., et al. (2013a). Daptomycin-resistant *Enterococcus faecalis* diverts the antibiotic molecule from the division septum and remodels cell membrane phospholipids. *mBio* 4 (4e00281-13), e00281–13. doi:10.1128/mBio.00281-13

Vega, L. A., and Caparon, M. G. (2013). Cationic antimicrobial peptides disrupt the Streptococcus pyogenes ExPortal. *Mol. Microbiol.* 85 (6), 1119–1132. doi:10.1111/j.1365-2958.2012.08163.x

Wang, G., Yu, F., Lin, H., Murugesan, K., Huang, W., Hoss, A. G., et al. (2018). Evolution and mutations predisposing to daptomycin resistance in vancomycin-resistant Enterococcus faecium ST736 strains. *PLoS One* 13 (12), e0209785. doi:10.1371/JOURNAL.PONE.0209785

Werth, B. J., Barber, K. E., Tran, K. N. T., Nonejuie, P., Sakoulas, G., Pogliano, J., et al. (2015). Ceftobiprole and ampicillin increase daptomycin susceptibility of daptomycin-susceptible and -resistant VRE. *J. Antimicrob. Chemother.* 70 (2), 489–493. doi:10.1093/jac/dku386

Woodall, B. M., Harp, J. R., Brewer, W. T., Tague, E. D., Campagna, S. R., and Fozo, E. M. (2021). *Enterococcus faecalis* readily adapts membrane phospholipid composition to environmental and genetic perturbation. *Front. Microbiol.* 12. doi:10.3389/fmicb.2021.616045

Yim, J., Smith, J. R., Singh, N. B., Rice, S., Stamper, K., Garcia de la Maria, C., et al. (2017). Evaluation of daptomycin combinations with cephalosporins or gentamicin against Streptococcus mitis group strains in an *in vitro* model of simulated endocardial vegetations (SEVs). *J. Antimicrob. Chemother.* 72 (8), 2290–2296. doi:10.1093/jac/dkx130

Zhang, R., Polenakovik, H., Barreras Beltran, I. A., Waalkes, A., Salipante, S. J., Xu, L., et al. (2022). Emergence of dalbavancin, vancomycin, and daptomycin nonsusceptible *Staphylococcus aureus* in a patient treated with dalbavancin: Case report and isolate characterization. *Clin. Infect. Dis.* 1, ciac341. doi:10.1093/CID/CIAC341

Zhang, T. H., Muraih, J. K., Tishbi, N., Herskowitz, J., Victor, R. L., Silverman, J., et al. (2014). Cardiolipin prevents membrane translocation and permeabilization by daptomycin. *J. Biol. Chem.* 289 (17), 11584–11591. doi:10.1074/jbc.M114.554444

frontiers | Frontiers in Molecular Biosciences

TYPE Review
PUBLISHED 06 January 2023
DOI 10.3389/fmolb.2022.1058381

OPEN ACCESS

EDITED BY
Isabel María López-Lara,
UNAM Campus Morelos, National Autonomous University of Mexico, Mexico

REVIEWED BY
Daniel Balleza,
Instituto Tecnológico de Veracruz, Mexico
Daniela Medeot,
National University of Río Cuarto, Argentina

*CORRESPONDENCE
Anandi Tamby,
Anandi.tamby@nioz.nl

SPECIALTY SECTION
This article was submitted to Lipids, Membranes and Membranous Organelles, a section of the journal Frontiers in Molecular Biosciences

RECEIVED 30 September 2022
ACCEPTED 29 November 2022
PUBLISHED 06 January 2023

CITATION
Tamby A, Sinninghe Damsté JS and Villanueva L (2023), Microbial membrane lipid adaptations to high hydrostatic pressure in the marine environment.
Front. Mol. Biosci. 9:1058381.
doi: 10.3389/fmolb.2022.1058381

Microbial membrane lipid adaptations to high hydrostatic pressure in the marine environment

Anandi Tamby[1]*, Jaap S. Sinninghe Damsté[1,2] and Laura Villanueva[1,2]

[1]Department of Marine Microbiology and Biogeochemistry (MMB), NIOZ Royal Netherlands Institute for Sea Research, Den Burg, Netherlands, [2]Department of Earth Sciences, Faculty of Geosciences, Utrecht University, Utrecht, Netherlands

The deep-sea is characterized by extreme conditions, such as high hydrostatic pressure (HHP) and near-freezing temperature. Piezophiles, microorganisms adapted to high pressure, have developed key strategies to maintain the integrity of their lipid membrane at these conditions. The abundance of specific membrane lipids, such as those containing unsaturated and branched-chain fatty acids, rises with increasing HHP. Nevertheless, this strategy is not universal among piezophiles, highlighting the need to further understand the effects of HHP on microbial lipid membranes. Challenges in the study of lipid membrane adaptations by piezophiles also involve methodological developments, cross-adaptation studies, and insight into slow-growing piezophiles. Moreover, the effects of HHP on piezophiles are often difficult to disentangle from effects caused by low temperature that are often characteristic of the deep sea. Here, we review the knowledge of membrane lipid adaptation strategies of piezophiles, and put it into the perspective of marine systems, highlighting the future challenges of research studying the effects of HHP on the microbial lipid composition.

KEYWORDS

piezophile, high hydrostatic pressure, extremophile, membrane, membrane adaptation, microbial adaptation, phospholipid

1 Introduction

The deep-sea is defined by a water depth of >1,000 m and encompasses most of Earth's biosphere. At these depths, the average sea temperature is 2°C and the hydrostatic pressure is >10 MPa (100 bars) increasing by 1 MPa (10 bars) every 100 m (Jannasch and Taylor, 1984). High hydrostatic pressure (HHP) in deep-sea environments usually coincides with low bottom-water temperatures except for areas in the vicinity of hydrothermal vents and warm seas, such as the Mediterranean, and the Black Sea, which average bottom temperature are 12°C and 8°C, respectively (Lacombe et al., 1985; Vargas-Yáñez et al., 2017).

Microorganisms adapted to HHP are usually known as piezophiles, referring to their preference for high pressure (Kato, 2011). Regarding the adaptability to HHP, microorganisms can be piezolerant, if they can withstand HHP but have similar or faster growth rates at atmospheric pressure, while obligate piezophiles can only grow under HHP (Kato, 2011). Piezophiles are usually found at the bottom of the water column thus these microorganisms are both piezophiles and psychrophiles (adapted to low temperatures). The fact that these two factors coincide makes it challenging to discern the effects of HHP and low temperature on microorganisms. A strategy to pinpoint the microbial effects of HHP solely is to focus on microorganisms isolated from warmer deep-sea bottom waters or from locations close to hydrothermal vents outside of areas with extremely high temperatures. Nevertheless, to our knowledge research to pull these two effects apart are scarce (Bartlett, 1999; Nogi, 2008; Wang et al., 2009).

HHP impacts protein folding, metabolic rate, and membrane stability, leading to cell disruption. Thus, piezotolerant and piezophiles have developed various adaptive strategies to cope with HHP, such as accumulation of protein-stabilizing solutes, gene expression modulation (such as induction of genes encoding for heat shock protein), and changes in the composition of the cell membrane (Simonato et al., 2006; Oger and Jebbar, 2011).

An essential microbial cell feature that has been observed to change under HHP is the composition of the cell membrane, which represents the cell barrier against environmental stimuli. The cell membrane is a dynamic compartment composed of membrane lipids and proteins. HHP has been seen to affect membrane proteins, for example, by increasing membrane diffusion by the activation of porins (proteins forming membrane channels) (Bartlett, 1999), or by increasing the abundance of respiratory terminal oxidase able to maintain their integrity under HHP (Tamegai et al., 2011). Changes in the membrane lipid composition to keep the membrane fluid are known as homeoviscous adaptation, while the modification of the proportion of lipids in a crystalline state is referred as homeophasic adaptation (Bartlett, 2002; Fang and Bazylinski, 2008). Membrane fluidity (i.e., a parameter describing the freedom of movement of lipids and proteins within the membrane) can be adapted by modifying the degree of lipid packing, which directly affects the water permeability across the membrane. In addition, other biophysical characteristics of the cell membrane have been seen to be relevant to modulate the integrity of the membrane such as thickness, phase properties, and viscosity (Chwastek et al., 2020).

Here, we review the knowledge of membrane lipid adaptation strategies of piezotolerant and piezophile microbes encountered in the water column of marine systems. Most studies have been conducted in this setting since the deep-sea represents by far the most widespread environment where microorganisms thrive under HHP. Several structural features of the membranes have been examined, such as the composition of polar headgroups and degree of unsaturation and methylation of fatty acyl chains, and the presence of hopanoids and sterols. We conclude this review by outlining the future challenges to determine membrane lipid adaptations to HHP.

2 Microbial membrane lipids and their response to HHP

Bacteria and eukaryotes have similar adaptive strategies, as they share characteristics in the structure of their lipid membranes with their lipids composed of fatty acyl chains connected through ester bonds to glycerol-3-phosphate at positions *sn*-1 and *sn*-2, and polar head groups (Figure 1A). Both bacterial/eukaryotic and archaeal membrane lipids have mainly glycerophospholipids (GPLs) composed by a glycerol moiety, a phosphate group, and a variable head group. GPLs are polar lipids - they have an amphiphilic nature, meaning they have both a hydrophilic (with a strong affinity to water, soluble in water) and a hydrophobic (lacking affinity for water) part.

Archaeal membrane lipids differ substantially from those of bacteria and eukaryotes as they are composed of two linear isoprenoidal alkyl chains made up of a phytanyl chain (containing 20 carbon atoms, or C20) bound through ether-bonds to the *sn*-2 and *sn*-3 position of glycerol-1-phosphate (G1P) (Figure 1A). Thus, they are referred to as glycerol diether or archaeol. In addition, archaea can also form monolayers of tetraethers or so-called glycerol dibiphytanyl glycerol tetraethers (GDGTs) (Figure 1A). The isoprenoid cores can be modified by unsaturation, hydroxylation, or presence of cyclopentane or cyclohexane rings (only in the case of crenarchaeol synthesized by Thaumarchaeota) (Schouten et al., 2013).

These fundamental chemical differences between bacterial/eukaryotic and archaeal membranes lead to specific adaptation when encountering membrane-disrupting parameters such as HHP, depressurization, or extreme temperature (Siliakus et al., 2017). To adapt to HHP and extreme temperature, bacteria and eukaryotes modulate the degrees of unsaturation and branching of their acyl chain (Figure 1B) and adapt the type and proportion of polar headgroups, while archaea modulate their ratio of diether lipid to GDGT (Figure 1C).

3 Adaptations in the composition of bacterial/eukaryotic membrane lipids to HHP

3.1 Acyl chain composition

Most research on membrane lipid adaptation has focused on modulation of the fatty acyl chains of the bacterial/eukaryotic lipids in response to physical parameters. For example, saturated

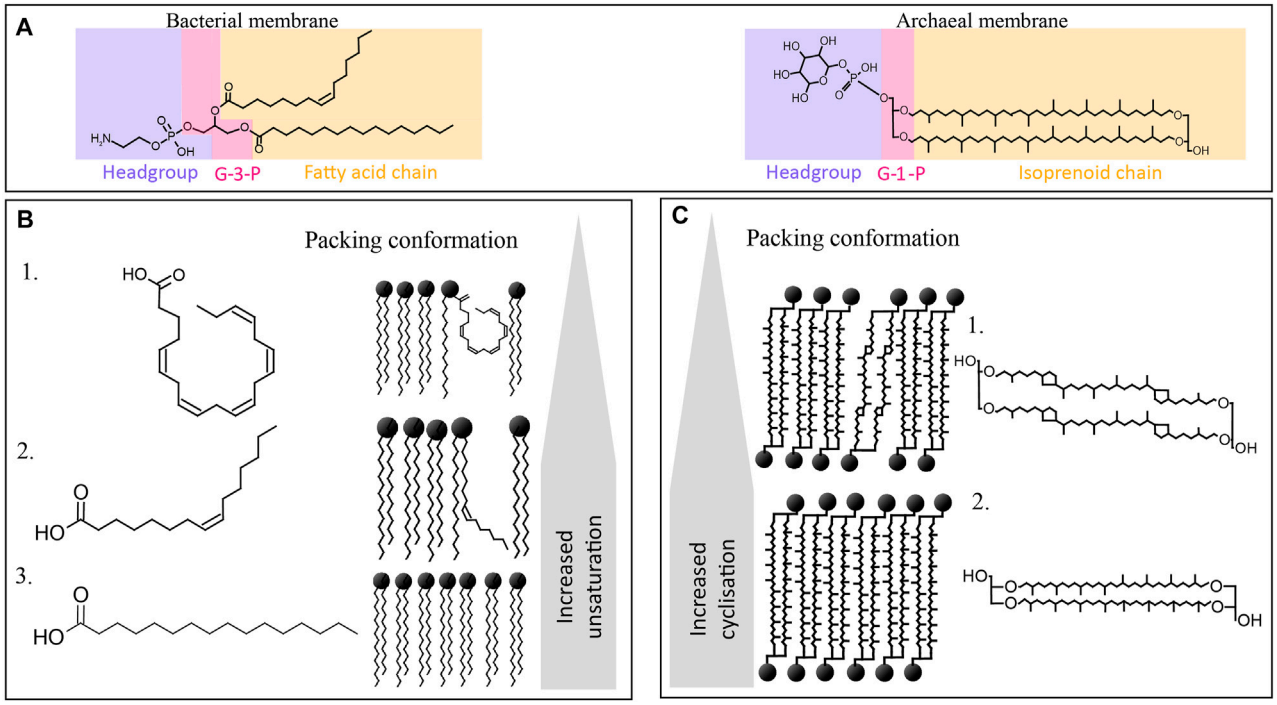

FIGURE 1
Overview of the chemical structures of bacterial and archaeal membrane lipids, including **(A)** different stereochemistry in the backbone being glycerol-3-phosphate (G3P) in bacteria and G1P in archaea (labeled in pink), and a different type of side chain (in yellow), i.e., fatty acids esterified to the G3P in bacteria, and isoprenoid alkyl chains linked through ether bonds to the G1P moiety in archaea. Polar headgroup is labeled in blue. **(B)** Different fatty acid side chains of phospholipid fatty acids (PLFA) commonly encountered in the bacterial membranes of piezophiles, with (B1) being C20:5, (B2) being (Z)-hexadec-9-enoic acid or palmitoleic acid, and (B3) being hexadecenoic acid or palmitic acid (C16), and their influence in the packing conformation and fluidity of the membrane. **(C)** Archaeal tetraether membrane lipids, being (C1) GDGT-4 with four cyclopentane moieties, and (C2) GDGT with no cyclopentane moieties (i.e., GDGT-0), and their impact on the conformation and fluidity of the membrane.

fatty acyl chains allow the lipids to be packed in a tighter and denser configuration than lipids with unsaturated chains, resulting in a more rigid membrane structure (Small, 1984); (Figure 1B). Monounsaturated phospholipid fatty acyl chains lead to a slight curled configuration, thus loosening the membrane, leading to an increase in fluidity (Figure 1B). In addition to unsaturation, hydroxylation (i.e., the presence of hydroxy groups), methylation, and length of the fatty acyl chain can also impact the fluidity of the membrane by impacting the melting temperature (Ernst et al., 2016).

In general, piezophiles are known to increase the level of fatty acyl chain unsaturation as an adaptive response to HHP. For instance, the model organism *Photobacterium profundum* SS9, a piezo- and psychrophile, has been reported to increase the unsaturation in its fatty acyl chain upon HHP as well as the bacterium *Alteromonas 4033-B* (Table 1; Kamimura et al., 1993; Allen et al., 1999). The presence of multiple unsaturations of the fatty acyl chain, or so-called polyunsaturated fatty acids (PUFAs), is also a common strategy among piezophiles. PUFAs that are most frequently associated with adaptation to HHP are C20:5 and C22:6 (Bartlett, 1999; Kawamoto et al., 2011; Usui et al., 2012; Moi et al., 2018). For example, two strains of *Psychromonas* (2D2 and 16C1) were isolated from the intestines of a deep-sea fish, *Coryphaenoides yaquinae*, which lives at 6,000 m depth. Under HHP, both strains significantly increased the content of C20:5 and C22:6, confirming that this lipid plays an important role in microbial adaptation under HHP (Table 1; Yano et al., 1998). Another example is *Shewanella piezotolerans* WP3, which increases the relative abundance of C20:5 upon HHP [Table 1; (Wang et al., 2009; Kawamoto et al., 2011)]. Surprisingly, however, the phylogenetically related piezophile *Shewanella violacea* DSS12 adopts an opposite strategy; it decreases the relative abundance of C20:5 upon HHP (Kawamoto et al., 2011).

Although these studies confirm that the microbial membrane can adapt to HHP by changing the relative abundance of the PUFA C20:5, other studies have shown that the presence of this PUFA is not essential to withstand HHP since, e.g., some bacterial strains such as the piezotolerant *Pseudomonas* sp. BT1, do not contain C20:5 in its membrane (Kaneko et al., 2000). Moreover, the lack of production of C20:5 by mutation of specific biosynthetic genes in the piezotolerant strains *S.*

TABLE 1 Summary of piezophiles and piezotolerant microorganism.

Organism	Strain number	Optimal growth pressure and temperature	Relative abundance of main FA under optimal conditions	Main change observed under HHP incubations	Reference
Photobacterium profundum	SS9	15°C—28 MPa	C16:1 (30%)	Increase of C20:5	Bartlett et al. (2014)
			C16:0 (22%)		
			C14:0 (10%)		
			C18:1 (7%)		
			C20:5 (7%)		
			Iso C16:0 (6%)		
			C14:1 (4%)		
Alteromonas sp	RS103	25°C—25 MPa	*Iso* C15:0 (30%)	Increase of unsaturated fatty acid	Kamimura et al. (1993)
			Iso C17:1 (20%)		
			Iso C17:0 (12%)		
			C16:1 (10%)		
			C18:1 (8%)		
			C16:0 (8%)		
Psychromonas	2D2	5°C—40 MPa	C16:1 (50%)	Increase content of C22:6	Yano et al. (1998)
			C22:6 (20%)		
			C14:0 (11%)		
			C16:1 (10%)		
Psychromonas	16C1	5°C—20 MPa	C16:1 (58%)	Increase content of C22:6	Yano et al. (1998)
			C16:0 (13%)		
			C14:0 (10%)		
			C22:6 (10%)		
			C14:1 (6%)		
Shewanella piezotolerans	WP3	15°C–20°C—20 MPa	C16:1 (23%)	Increase of branched fatty acid Increase of C20:5	(Xiao et al., 2007; Wang et al., 2009)
			C15:0 (12%)		
			Iso C13:0 (9%)		
			C18:1 (8%)		
			C20:5 (6%)		
Shewanella violaceae	DSS12	8°C—30 MPa	C16: 1 (19%)	Decrease of C20:5	Nogi et al. (1998b)
			C16: 0 (16%)		
			C20:5 (15%)		
			Iso C15:0 (14%)		
			C15:0 (7%)		
			C14:0 (6%)		
Pseudomonas sp	BT1	30°C—10 MPa	C18:1 (47%)	Increase of phosphatidylethanolamine (PE)	Kaneko et al. (2000)
			C16:1 (30%)		

(Continued on following page)

TABLE 1 (*Continued*) Summary of piezophiles and piezotolerant microorganism.

Organism	Strain number	Optimal growth pressure and temperature	Relative abundance of main FA under optimal conditions	Main change observed under HHP incubations	Reference
			C16:0 (18%)		
			C18:0 (4%)		
Psychromonas hadalis	K41G	6°C—60 MPa	C16:1 (37%)	*Only cultured in optimal conditions*	Nogi et al. (2007)
			C16:0 (31%)		
			C22:6 (8%)		
Shewanella benthica	ATCC 43992	10°C—70 MPa	C16:1 (37%)	*Only cultured in optimal conditions*	Nogi et al. (1998b)
			C14:0 (17%)		
			C16:0 (15%)		
			Iso C13:0 (11%)		
			C20:5 (8%)		
Moritella japonica	JCM 10249	15°C—50 MPa	C16:1 (50%)	*Only cultured in optimal conditions*	Nogi et al. (1998a)
			C16:0 (21%)		
			C18:0 (18%)		
			C22:6 (6%)		
Colwellia piezophila	Y223G	10°C—60 MPa	C16:1 (50%)	*Only cultured in optimal conditions*	Nogi et al. (2004)
			C16:0 (30%)		
			C14:0 (10%)		
Moritella yayanosii	DB21MT-5	70°C—10 MPa	C16:1 (48%)	*Only cultured in optimal conditions*	Nogi and Kato (1999)
			C14:0 (15%)		
			C16:0 (13%)		
			C22:6 (9%)		
			C14:1 (6%)		
Sporosarcina sp	DSK25	35°C—0.1 MPa	*Iso* C15:0 (25%)	Increase of *anteiso*-C15:0 FA	Wang et al. (2014)
			Anteiso C15:0 (24%)		
			C16:1 (15%)		
			Anteiso C17:0 (10%)		
			Anteiso C17:0 (10%)		
			C16:0 (6%)		
			Anteiso C17:1 (4%)		
Clostridium paradoxum	DSM 7308	60°C—22 MPa	*Iso* C15:0 (65%)	Increased of branched fatty acid	Scoma et al. (2019)
			Anteiso C15:0 (7%)		
			C16:0 (6%)		
			C14:0 (6%)		
			Iso C13:0 (4%)		

(Continued on following page)

TABLE 1 (*Continued*) **Summary of piezophiles and piezotolerant microorganism.**

Organism	Strain number	Optimal growth pressure and temperature	Relative abundance of main FA under optimal conditions	Main change observed under HHP incubations	Reference
Psychromonas kaikoae	JCM 11054	10°C—50 MPa	C16:1 (56%)	*Only cultured in optimal conditions*	Nogi et al. (2007)
			C16:0 (13%)		
			C14:1 (10%)		
			C14:0 (7%)		
Archaea					
Thermococcus barophilus	MP	85°C—40 MPa	-	Increased relative abundance of diethers	Cario et al. (2015)
Methanococcus jannaschii	-	85°C—25 MPa	GDGT-0 (35%)	Increase of macrocyclic archaeol	Kaneshiro and Clark (1995)
			Macrocyclic archeol (65%)	Decrease of GDGT-0	

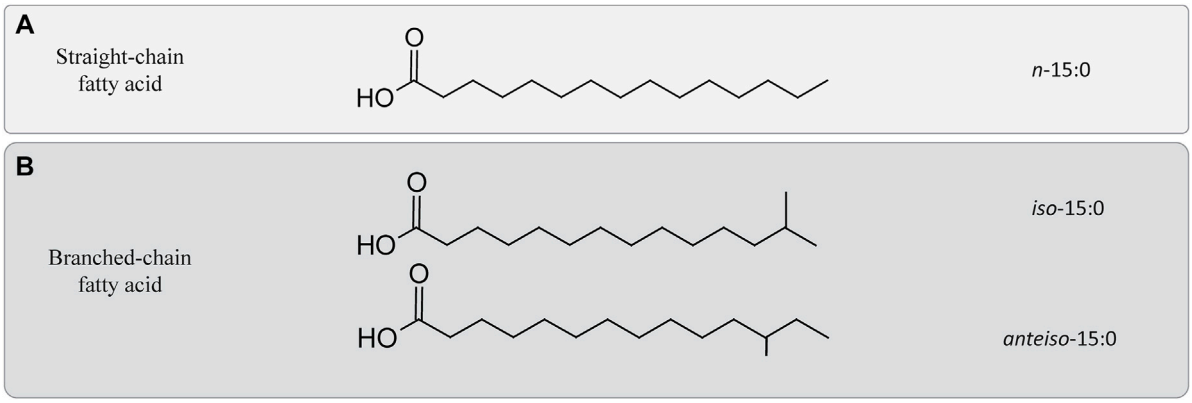

FIGURE 2
Differences between straight and branched-chain fatty acids. **(A)** Example of a straight-chain fatty acid containing 15 carbons. **(B)** Two branched-chain fatty acids chain containing 15 carbons. *Iso*-15:0 refers to configuration of the acyl chain containing a methyl group attached on the penultimate, while *anteiso*-15:0 refers to a similar configuration in which the methyl group would be attached to the antepenultimate carbon of the acyl chain.

piezotolerans WP3 and *S. violacea* did not impair their cell viability but only reduced their growth rate under HHP conditions suggesting the synthesis of PUFA is not a requirement to withstand HHP (Wang et al., 2009; Usui et al., 2012). Both strains compensated for the absence of C20:5 by increasing the relative abundance of monounsaturated fatty acids (MUFAs), supporting the fact that both PUFAs and MUFAs are involved in the membrane adaptation to HHP (Table 1). This is further supported by other studies, showing that mutant strains of *P. profundum* with a deficit in C20:5 could withstand both low temperature and high pressure, while mutants with reduced C18:1 were unable to grow under those conditions (Allen et al., 1999). The membrane of piezophilic and piezotolerant microorganisms harbors also other types of PUFAs, such as the C22:6 (Table 1), which typically occurs in the piezophilic and piezotolerant strains of the genera *Moritella* and *Colwellia* (DeLong and Yayanos, 1986; Oger and Cario, 2014), as well as *Psychromonas hadalis, Psychromonas* strain 2D2, and strain 16C1 (Table 1; Yano et al., 1998; Nogi et al., 2007).

Another acyl change modification of the bacterial/eukaryotic fatty acids that has been related to the homeoviscous adaptation under HHP is related to an increase in the degree of branching of the esterified fatty acids (Mostofian et al., 2019). In piezophile and piezotolerant strains, the most commonly occurring branched-chain fatty acids are *iso* and *anteiso* fatty acids (Figure 2). *Iso* and *anteiso* fatty acids are usually found in Gram-positive and sulfate-reducing bacteria (Kaneda, 1991), but they have also been reported in the membrane of some piezophiles (Fang and Kato, 2007). For example, *Shewanella benthica* and *P. profundum* both synthesize *iso* fatty acids

under HHP (Allen et al., 1999; Fang and Kato, 2007). Consequently, changes in their relative abundance have been previously interpreted as a strategy to deal with HHP (Bartlett, 1999). As an example, the gram-positive *Clostridium paradoxum* increased its relative abundance of *iso* and *anteiso* fatty acids at increasing hydrostatic pressure at a given growth temperature (Table 1; Li et al., 1993; Scoma et al., 2019). This strategy in *C. paradoxum* coincided with an increase of the proportion of shorter carbon chain fatty acids in the membrane with increasing hydrostatic pressure to increase the fluidity of the membrane (Scoma et al., 2019). Nevertheless, other piezotolerant bacteria, e.g., *Colwellia piezophila, Moritella yayanosii,* and *Psychromonas kaikoae,* do not produce branched-chain fatty acids (Table 1), revealing that branched-chain fatty acids solely are not required to achieve piezophily for some microbial groups (Kaneda, 1991).

3.2 Polar head groups

Polar head groups attached to the glycerol backbone, both in eukaryotic/bacterial lipids, confer specific structural characteristics, such as anchorage of proteins or curvature to the membrane (Castell, 2019). Head group polarity is also a key factor to regulate membrane packing. Zwitterionic lipids, which contain an equal amount of negative and positive charges, are expected to be packed more tightly than lipids with a net positive or negative charge. Thus, polar headgroup have an important effect on the packing and in the curvature of the membrane, and can play an important role for homeoviscous adaptation.

The membrane polar head groups can be diverse, but the most common ones are serine, ethanolamine, glycerol, choline, and myo-inositol, which are found in the phospholipids in all three domains of life (Sohlenkamp and Geiger, 2015). Most of the studies that have evaluated changes in the cell membrane upon environmental stimuli, including HHP, have focused on changes in the core lipid, while little is known of how the polar head groups change in these conditions. Nonetheless, a study by Kaneko et al. (2000) reported an increase in the relative abundance of intact polar lipids (IPLs) with the phosphatidylethanolamine (PE) head group with increasing pressure in a piezotolerant strain of *Pseudomonas* sp. isolated from the deep sea and grown at elevated temperature and HHP (Canganella et al., 2000). Another study also reported an increase in the relative abundance of IPLs with phosphatidylcholine (PC) head group for the deep-sea bacterium *Photobacterium profundum* grown at HHP and low temperature (Allen et al., 1999). In contrast, a recent study reported a decrease of the relative abundance of PC IPLs at HHP in two strains of the family Marinifilaceae of the phylum Bacteroidetes (Yadav et al., 2020). Yadav et al. (2020) also observed opposing changes in the polar head group distribution upon HHP for different analyzed strains of the same genus, with PE IPLs either increasing or decreasing at HHP, concomitantly with an increase or decrease of the ornithine lipid (OL). (Yadav et al., 2020). Therefore, it is likely that polar head group modifications upon HHP are not a universal feature. In general, all the studies on the membrane adaptation upon HHP suggest that the membrane lipid response is a combination of changes on both the polar head group and the core lipids (fatty acids) as a whole, and that the nature and the direction of this change is highly dependent on the taxonomy of the strains under study.

4 Hopanoids and sterols

Apart from membrane lipids, other lipid-based components are part of the membrane and act as regulators modifying the permeability of the membrane by increasing its rigidity and decreasing its permeability, being these hopanoids and sterols.

Hopanoids are a diverse group of pentacyclic triterpenoids mainly produced by bacteria. Their functionalized derivatives are referred as bacteriohopanepolyols (BHPs). The structure of hopanoids resemble the one of sterols (tetracyclic triterpenoids) found mostly in eukaryotic membranes. Previous studies have been shown that hopanoids have a similar location and function than sterols (Joung et al., 2008). Both sterols and hopanoids are derived from the same precursor, squalene, which is one of the products of the isoprenoid biosynthetic pathways (Kannenberg and Poralla, 1999; Micera et al., 2020). Sterols have also been observed in a few bacterial species of aerobic methanotrophs, myxobacteria and planctomycetes and members of the Bacteroidetes. Nevertheless, these have a very low structural complexity in comparison with those of eukaryotes.

The effect of HHP on the composition and/or abundance of sterols or hopanoids in cell membranes is poorly constrained. Two piezotolerant Marinifiliceae from the Black Sea possess BHPs biosynthetic genes, however the conditions inducing the productions of those hopanoids have not yet been identified (Yadav et al., 2020). A study by Abe, (2021), evaluated the effect of HHP on the growth of the yeast *Saccharomyces cerevisiae* by using functional genomics and transcriptomics analyses, concluding that mutations causing a decrease in the abundance of the sterol ergosterol in their membrane, made the cells more sensitive to HHP and to low temperature (Abe, 2021). More studies on the changes in membrane lipids in sterol and hopanoid-producers need to be conducted to further clarify if an increase of these membrane regulators upon HHP is a universal feature or not.

5 Adaptation to HHP in archaeal membrane lipids

Archaeal membrane lipids are based on ether-bonded isoprenoid chains with modifications, such as methylations,

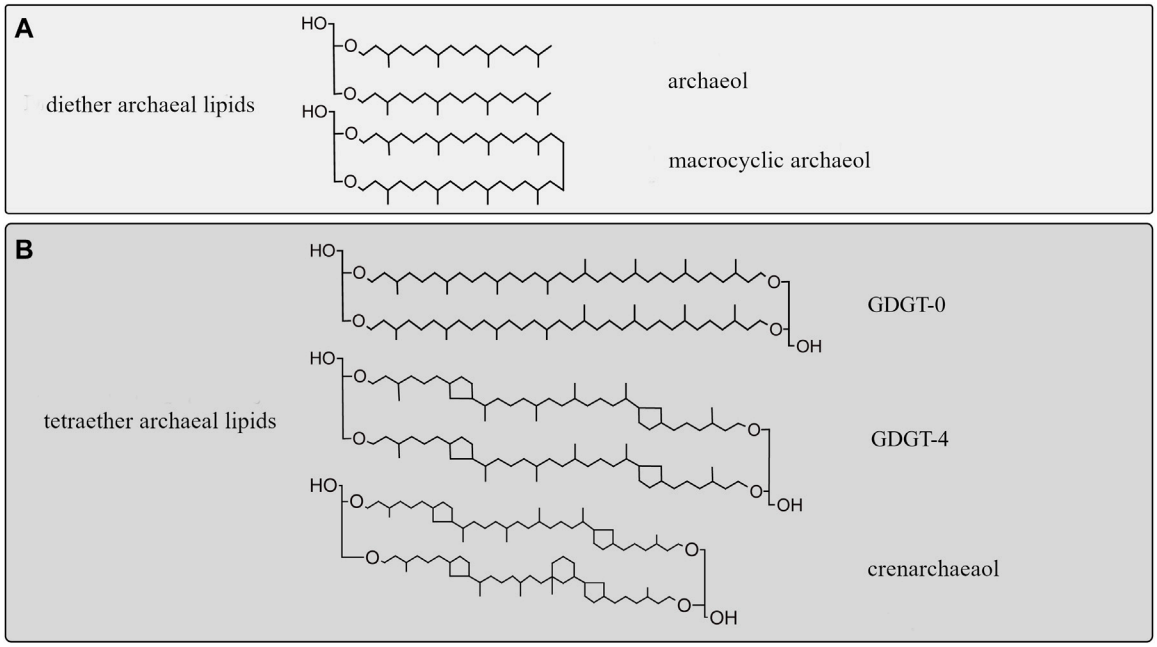

FIGURE 3
Diversity of isoprenoid chains in archaeal membrane lipids. **(A)** Archaeol (diether) membrane lipids encountered in piezophiles. **(B)** Diversity of archaeal tetraether lipids with and without moieties. Top: GDGT-0, with no cyclopentane moieties. Middle: GDGT-4 containing four cyclopentane rings, bottom: crenarchaeol, containing four cyclopentane rings and a cyclohexane ring (Damsté et al., 2002; Holzheimer et al., 2021).

hydroxy groups covalent bonds, and ring moieties, the abundance of which has been related to membrane fluidity adaptation to compensate for environmental changes (Figure 3; Siliakus et al., 2017; Jebbar et al., 2015).

Membrane adaptation under HHP has only been studied in two archaeal species; in *Methanococcus jannaschii*, a thermophilic methanogen, and in *Thermococcus barophilus*, a hyperthermophile piezophile [Table 1; Kaneshiro and Clark, 1995; Cario et al., 2015)]. In both species, the ratio of diether to GDGT membrane lipids increased when they were grown at higher than optimal pressure (Cario et al., 2015). This change would theoretically result in a bulkier membrane with higher lateral mobility and lower bending rigidity (Shinoda et al., 2005). In *M. jannaschii*, this transition to diether lipid results in a strong increase of macrocyclic archaeol at the expense of GDGT-0 and archaeol (Figure 3A). The increase of macrocyclic molecules in the membrane results in a tightly packed membrane, and prevents potential leakage of solute, proton or water (Jebbar et al., 2015). Although the studies on *M. jannaschii* and *T. barophilus* point to similar adaptive strategies, the lack of additional study on piezophile or piezotolerant archaea does not allow to identify specific adaptive response to HHP in archaea.

6 Methodological challenges of studying the effect of HHP on the membranes of marine microbes

To gain more insight into the potential contained in piezophiles, isolation and cultivation of piezophilic microorganisms under laboratory conditions is essential. Nevertheless, the maintenance of HHP during sampling and further cultivation is rather challenging and advancements in this regard have been only possible as a result of developments in specific equipments (Bartlett, 2002; Garel et al., 2019). These constraints have severely biased the types of piezophiles available in culture from which their physiology has been investigated, with a preference for oxygen-consuming (aerobic) microbes or piezophilic (hyper)thermophiles collected from hydrothermal vents. In this regard, most of the studied piezophiles are bacteria, while little is known about piezophilic archaea due to their slower growth rate and because they either consume or generate gasses out of their metabolism.

Methods to extract and analyze microbial membranes in general, and membrane lipids in particular, have been widely optimized (Carrasco-Pancorbo et al., 2009; Aldana et al., 2020). Nevertheless, the main problem is to assure that microbial

membranes do not change upon decompression of the cultures or enrichments prior to analysis. Previous studies have assessed the effect of decompression on microbial growth, cell mobility and morphology, but the effect on membrane composition has yet to be examined (Cario et al., 2022a). Similar caveats have been faced when studying changes in microbial gene expression upon HHP, and a solution to it has been to fix samples while they are under HHP (Feike et al., 2012). To the best of our knowledge, no studies have been performed with fixed samples under HHP for the purpose of lipid analysis, and there is no knowledge regarding how membranes, or membrane lipids specifically, would be affected by the use of fixatives that would arrest cell activity. Still, these kinds of studies would be essential to discard changes in the microbial membrane during decompression which would be independent on those caused by HHP.

Among future challenges are the live observation of changes in the permeability or integrity of the cell membrane upon changes in hydrostatic pressure by using live-cell imaging methods. In this regard, previous studies have adjusted microscope setups to be able to perform high-resolution quantitative imaging of live cells under HHP (Bourges et al., 2020). In addition, the development of microfluidic chip now allows to observe phenotype change of microbes under HHP in real-time, without depressurization (Cario et al., 2022b). Another way to determine potential changes in the membrane lipids upon HHP, might be to determine the microbial genomic potential to synthesize unsaturated and branched-chain fatty acids, which have been seen to increase as a response to HHP. Lipid biosynthetic pathways and their protein-coding genes are, in some cases, quite constrained and it is possible to detect, determine the diversity, and or the expression of specific genes as a proxy of the diversity of microorganisms producing a given lipid, or the up and downregulation of the gene expression leading to it (Pearson et al., 2007; Villanueva et al., 2014). This approach has proven to be very useful when applied to environmental settings to better constrain the distribution and/or abundance of producers of specific membrane lipids (Kim et al., 2016; Besseling et al., 2018).

7 Conclusions and future challenges

In conclusion, piezophiles and piezotolerant prokaryotes have multiple mechanisms to maintain the integrity of their cell membrane when challenged to grow under HHP, such as an increased degree of unsaturation or branching of fatty acids. However, the extent of those mechanisms is not fully constrained as most studies have focused solely on modifications in the acyl chain, and the impact of HHP on polar head groups, the presence of hopanoids and/or sterols, and membrane proteins remains largely unknown. Unveiling those aspects of membrane adaptations would allow to have a comprehensive picture of microbial adaptation, and possibly explain the substantial differences in fatty acid distribution found even between species of the same genus. Similarly, the limited research on the impact of the chemical composition of archaeal membrane on its physical properties does not allow at present to draw broad conclusion on archaeal adaptation, although the two piezophiles archaea studied seem to have similar adaptive strategies. This scarcity can be explained by the difficulty of studying piezophiles and piezotolerant microbes in the lab. Developments of accessible and low-maintenance high pressure incubators would allow to culture and identify more piezophiles and piezotolerant strains, and potentially highlight specific adaptations to HHP.

Another challenge for high pressure incubators and samplers is the decompression process: the transition to atmospheric pressure is likely to impact the membrane composition—the extent of this impact being still unknown. Alternatively, molecular omics methods present a way to circumvent the culturing difficulty and allow to predict the potential of a microbial community. Such studies require well-characterized lipid biosynthetic pathways. Future challenges would include a combined omics study, combining lipidomics, metagenomics and proteomics, to fully assess the specific membrane lipid adaptations of environmental microbial communities.

Author contributions

LV and AT contributed equally to the conception and design of the review. AT combined the bibliography, analyzed the main trends, and wrote the first draft. LV wrote sections of the manuscript. JD provided supervision and edition of the manuscript.

Funding

All authors received funding from the Soehngen Institute for Anaerobic Microbiology (SIAM) through a Gravitation Grant (024.002.002) from the Dutch Ministry of Education, Culture, and Science (OCW).

Conflict of interest

The authors declare that the research was conducted in the absence of any commercial or financial relationships that could be construed as a potential conflict of interest.

Publisher's note

References

Abe, F. (2021). Molecular responses to high hydrostatic pressure in eukaryotes: Genetic insights from studies on saccharomyces cerevisiae. *Biology* 10 (12), 1305–1315. doi:10.3390/biology10121305

Aldana, J., Romero-Otero, A., and Cala, M. P. (2020). Exploring the lipidome : Current lipid extraction techniques for mass spectrometry analysis. *Metabolites* 10 (6), 231–236. doi:10.3390/metabo10060231

Allen, E. E., Facciotti, D., and Bartlett, D. H. (1999). Monounsaturated but not polyunsaturated fatty acids are required for growth of the deep-sea bacterium *Photobacterium profundum* SS9 at high pressure and low temperature. *Appl. Environ. Microbiol.* 65 (4), 1710–1720. doi:10.1128/aem.65.4.1710-1720.1999

Bartlett, D. H. (1999). Microbial adaptations to the psychrosphere/piezosphere. *J. Mol. Microbiol. Biotechnol.* 1 (1), 93–100.

Bartlett, D. H. (2002). Pressure effects on *in vivo* microbial processes. *Biochimica Biophysica Acta - Protein Struct. Mol. Enzym.* 1595 (1–2), 367–381. doi:10.1016/S0167-4838(01)00357-0

Bartlett, D. H., Ferguson, G., and Valle, G. (2014). Adaptations of the psychrotolerant piezophile *Photobacterium profundum* Strain SS9. *High-Pressure Microbiol.* 319–337. doi:10.1128/9781555815646.ch18

Besseling, M. A., Hopmans, E. C., Boschman, R. C., Sinninghe Damste, J. S., and Villanueva, L. (2018). Benthic archaea as potential sources of tetraether membrane lipids in sediments across an oxygen minimum zone. *Biogeosciences* 15, 4047–4064. doi:10.5194/bg-15-4047-2018

Bourges, A. C., Lazarev, A., Declerck, N., Rogers, K. L., and Royer, C. A. (2020). Quantitative high-resolution imaging of live microbial cells at high hydrostatic pressure. *Biophysjcs* 118 (11), 2670–2679. doi:10.1016/j.bpj.2020.04.017

Buckles, L. K., Villanueva, L., Weijers, J. W. H., Verschuren, D., and Damste, J. S. S. (2013). Linking isoprenoidal GDGT membrane lipid distributions with gene abundances of ammonia-oxidizing *Thaumarchaeota* and uncultured crenarchaeotal groups in the water column of a tropical lake (Lake Challa , East Africa). *Environ. Microbiol.* 15 (9), 2445–2462. doi:10.1111/1462-2920.12118

Canganella, F., GambAcortA, A., Kato, C., and HoriKoshi, K. (2000). Effects of hydrostatic pressure and temperature on physiological traits of *Thermococcus guaymasensis* and *Thermococcus aggregans* growing on starch. *Microbiol. Res.* 154 (4), 297–306. doi:10.1016/S0944-5013(00)80003-8

Cario, A., Grossi, V., Schaeffer, P., and Oger, P. M. (2015). Membrane homeoviscous adaptation in the piezo-hyperthermophilic archaeon *Thermococcus barophilus*. *Front. Microbiol.* 6 (OCT), 1–12. doi:10.3389/fmicb.2015.01152

Cario, A., Larzilliere, M., Nguyen, O., Alain, K., and Marre, S. (2022a). High-pressure microfluidics for ultra-fast microbial phenotyping. *Front. Microbiol.* 13, 866681. doi:10.3389/fmicb.2022.866681

Cario, A., Oliver, G. H., and Rogers, K. L. (2022b). Characterizing the piezosphere : The effects of decompression on microbial growth dynamics. *Front. Microbiol.* 13 (MAY), 1–15. doi:10.3389/fmicb.2020.01023

Carrasco-Pancorbo, A., Navas-Iglesias, N., and Cuadros-Rodríguez, L. (2009). From lipid analysis towards lipidomics, a new challenge for the analytical chemistry of the 21st century. *Part I Morder lipid analysis' TrAC Trends Anal. Chem.* 28 (3), 263–278. doi:10.1016/j.trac.2008.12.005

Castell, M. S. (2019). *Apolar lipids, the membrane adaptation toolbox of extremophiles*. Lyon, France: Institut des Sciences Appliquées de Lyon. [PhD thesis] [Lyon (FR)].

Chwastek, G., Surma, M. A., Rizk, S., Grosser, D., Lavrynenko, O., Rucinska, M., et al. (2020). Principles of membrane adaptation revealed through environmentally induced bacterial lipidome remodeling. *Cell Rep.* 32, 108165. doi:10.1016/j.celrep.2020.108165

Damsté, J. S. S., Schouten, S., Hopmans, E. C., van Duin, A. C. T., and Geenevasen, J. A. J. (2002). Crenarchaeol : The characteristic core glycerol dibiphytanyl glycerol tetraether membrane lipid of cosmopolitan pelagic crenarchaeota. *J. Lipid Res.* 43, 1641–1651. doi:10.1194/jlr.M200148-JLR200

DeLong, E. F., and Yayanos, A. A. (1986). Biochemical function and ecological significance of novel bacterial lipids in deep-sea procaryotes. *Appl. Environ. Microbiol.* 51 (4), 730–737. doi:10.1128/aem.51.4.730-737.1986

Ernst, R., Ejsing, C. S., and Antonny, B. (2016). Homeoviscous adaptation and the regulation of membrane lipids. *J. Mol. Biol.* 428 (24), 4776–4791. doi:10.1016/j.jmb.2016.08.013

Fang, J., and Bazylinski, D. A. (2008). Deep-sea piezosphere and piezophiles: Geomicrobiology and biogeochemistry. *Trends Microbiol.* 18 (9), 413–422. doi:10.1016/j.tim.2010.06.006

Fang, J., and Kato, C. (2007). *FAS or PKS, lipid biosynthesis and stable carbon isotope fractionation in deep-sea piezophilic bacteria*. Badajoz: Science and Technology.

Feike, J., Jurgens, K., Hollibaugh, J. T., Kruger, S., Jost, G., and Labrenz, M. (2012). Measuring unbiased metatranscriptomics in suboxic waters of the central Baltic Sea using a new *in situ* fixation system. *ISME J.* 6, 461–470. doi:10.1038/ismej.2011.94

Garel, M., Bonin, P., Martini, S., Guasco, S., Roumagnac, M., Bhairy, N., et al. (2019). Pressure-retaining sampler and high-pressure systems to study deep-sea microbes under *in situ* conditions. *Front. Microbiol.* 10 (APR), 1–13. doi:10.3389/fmicb.2019.00453

Holzheimer, M., Sinninghe Damste, J. S., Schouten, S., Havenith, R. W. A., Cunha, A. V., and Minnaard, A. J. (2021). Total synthesis of the alleged structure of crenarchaeol enables structure revision. *J. Ger. Chem. Soc.* 60 (32), 17504–17513. doi:10.1002/anie.202105384

Jannasch, H. W., and Taylor, C. D. (1984). Deep-sea microbiology. *Annu. Rev. Microbiol.* 38, 487–514. doi:10.1146/annurev.mi.38.100184.002415

Jebbar, M., Franzetti, B., Girard, E., and Oger, P. (2015). Microbial diversity and adaptation to high hydrostatic pressure in deep-sea hydrothermal vents prokaryotes. *Extremophiles* 19, 721–740. doi:10.1007/s00792-015-0760-3

Joung, T. H., Lee, J. H., Nho, I. S., Lee, C. M., Lee, P. M., Aoki, T., et al. (2008). A study on the pressure vessel design, structural analysis and pressure test of a 6000 m depth-rated unmanned underwater vehicle. *Ships Offshore Struct.* 3 (3), 205–214. doi:10.1080/17445300802204371

Kamimura, K., Fuse, H., Takimura, O., and Yamaoka, Y. (1993). Effects of growth pressure and temperature on fatty acid composition of a barotolerant deep-sea bacterium. *Appl. Environ. Microbiol.* 59 (3), 924–926. doi:10.1128/aem.59.3.924-926.1993

Kaneda, T. (1991). Iso- and anteiso-fatty acids in bacteria: Biosynthesis, function, and taxonomic significance. *Microbiol. Rev.* 55 (2), 288–302. doi:10.1128/mr.55.2.288-302.1991

Kaneko, H., Takami, H., Inoue, A., and HoriKoshi, K. (2000). Effects of hydrostatic pressure and temperature on growth and lipid composition of the inner membrane of barotolerant *Pseudomonas* sp. BT1 isolated from the deep-sea. *Biosci. Biotechnol. Biochem.* 64, 72–79. doi:10.1271/bbb.64.72

Kaneshiro, S. M., and Clark, D. S. (1995). Pressure effects on the composition and thermal behavior of lipids from the deep-sea thermophile *Methanococcus jannaschii*. *J. Bacteriol.* 177 (13), 3668–3672. doi:10.1128/jb.177.13.3668-3672.1995

Kannenberg, E. L., and Poralla, K. (1999). Hopanoid biosynthesis and function in bacteria. *Naturwissenschaften* 86 (4), 168–176. doi:10.1007/s001140050592

Kato, C. (2011). *Distribution of piezophiles*, 644–655. doi:10.1007/978-4-431-53898-1*Extrem. Handb.*

Kawamoto, J., Sato, T., Nakasone, K., Kato, C., Mihara, H., Esaki, N., et al. (2011). Favourable effects of eicosapentaenoic acid on the late step of the cell division in a piezophilic bacterium, *Shewanella violacea* DSS12, at high-hydrostatic pressures. *Environ. Microbiol.* 13, 2293–2298. doi:10.1111/j.1462-2920.2011.02487.x

Kim, J-H., Villanueva, L., Zell, C., and Sinninghe Damsté, J. S. (2016). *Biological source and provenance of deep-water derived isoprenoid tetraether lipids along the Portuguese continental margin*, 172, 177–204. doi:10.1016/j.gca.2015.09.010

Lacombe, H., Tchernia, P., and Gamberoni, L. (1985). Variable bottom water in the Western Mediterranean basin. *Prog. Oceanogr.* 14 (C), 319–338. doi:10.1016/0079-6611(85)90015-1

Li, Y., Mandelc, L., and Wiegel, J. (1993). Isolation and characterization of a moderately thermophilic anaerobic alkaliphile, *Clostridium paradoxum* sp. nov. *Int. J. Syst. Bacteriol.* 43 (3), 450–460. doi:10.1099/00207713-43-3-450

Micera, M., Botto, A., Geddo, F., Antoniotti, S., Bertea, C. M., Levi, R., et al. (2020). Squalene: More than a step toward sterols. *Antioxidants* 9 (8), 1–14. doi:10.3390/antiox9080688

Moi, I. M., Leow, A. T. C., Ali, M. S. M., Rahman, R. N. Z. R. A., Salleh, A. B., and Sabri, S. (2018). Polyunsaturated fatty acids in marine bacteria and strategies to enhance their production. *Appl. Microbiol. Biotechnol.* 102 (14), 5811–5826. doi:10.1007/s00253-018-9063-9

Mostofian, B., Zhuang, T., Cheng, X., and Nickels, J. D. (2019). Branched-chain fatty acid content modulates structure, fluidity, and phase in model microbial cell membranes. *J. Phys. Chem.* 123 (27), 5814–5821. doi:10.1021/acs.jpcb.9b04326

Nogi, Y. (2008). Bacteria in the deep sea: Psychropiezophiles. *Psychrophiles Biodivers. Biotechnol.* 73, 73–82. doi:10.1007/978-3-540-74335-4_5

Nogi, Y., Hosoya, S., Kato, C., and Horikoshi, K. (2004). *Colwellia piezophila* sp. nov., a novel piezophilic species from deep-sea sediments of the Japan Trench. *Int. J. Syst. Evol. Microbiol.* 54 (5), 1627–1631. doi:10.1099/ijs.0.03049-0

Nogi, Y., Hosoya, S., Kato, C., and Horikoshi, K. (2007). *Psychromonas hadalis* sp. nov., a novel piezophilic bacterium isolated from the bottom of the Japan Trench. *Int. J. Syst. Evol. Microbiol.* 57 (6), 1360–1364. doi:10.1099/ijs.0.64933-0

Nogi, Y., Kato, C., and Horikoshi, K. (1998a). *Moritella japonica* sp. nov., a novel barophilic bacterium isolated from a Japan Trench sediment. *J. General Appl. Microbiol.* 44, 289–295. doi:10.2323/jgam.44.289

Nogi, Y., Kato, C., and Horikoshi, K. (1998b). Taxonomic studies of deep-sea barophilic *Shewanella* strains and description of *Shewanella violacea* sp. nov. *Archives Microbiol.* 170 (5), 331–338. doi:10.1007/s002030050650

Nogi, Y., and Kato, C. (1999). Taxonomic studies of extremely barophilic bacteria isolated from the Mariana Trench and description of *Moritella yayanosii* sp. nov., a new barophilic bacterial isolate. *Extremophiles* 3 (1), 71–77. doi:10.1007/s007920050101

Oger, P., and Cario, A. (2014). The high pressure life of piezophiles. *Biol. Aujourd'hui* 208 (3), 193–206. doi:10.1051/jbio/2014023

Oger, P., and Jebbar, M. (2011). The many ways of coping with pressure. *Res. Microbiol.* 161 (10), 799–809. doi:10.1016/j.resmic.2010.09.017

Pearson, A., Flood Page, S. R., Jorgensen, T. L., Fischer, W. W., and Higgins, M. B. (2007). Novel hopanoid cyclases from the environment. *Environ. Microbiol.* 9, 2175–2188. doi:10.1111/j.1462-2920.2007.01331.x

Schouten, S., Hopmans, E. C., and Damsté, J. S. S. (2013). The organic geochemistry of glycerol dialkyl glycerol tetraether lipids: A review. *Org. Geochem.* 54, 19–61. doi:10.1016/j.orggeochem.2012.09.006

Scoma, A., Garrido-Amador, P., Nielsen, S. D., Roy, H., and Kjeldsen, K. U. (2019). The polyextremophilic bacterium *Clostridium paradoxum* attains piezophilic traits by modulating its energy metabolism and cell membrane composition. *Appl. Environ. Microbiol.* 85 (15), e00802-e00819. doi:10.1128/AEM.00802-19

Shinoda, W., Shinoda, K., Baba, T., and Mikami, M. (2005). Molecular dynamics study of bipolar tetraether lipid membranes. *Biophysical J.* 89 (5), 3195–3202. doi:10.1529/biophysj.105.060962

Siliakus, M. F., van der Oost, J., and Kengen, S. W. M. (2017). Adaptations of archaeal and bacterial membranes to variations in temperature, pH and pressure. *Extremophiles* 21 (4), 651–670. doi:10.1007/s00792-017-0939-x

Simonato, F., Campanaro, S., Lauro, F. M., Vezzi, A., D'Angelo, M., Vitulo, N., et al. (2006). Piezophilic adaptation: A genomic point of view. *J. Biotechnol.* 126 (1), 11–25. doi:10.1016/j.jbiotec.2006.03.038

Small, D. M. (1984). Lateral chain packing in lipids and membranes. *J. Lipid Res.* 25 (13), 1490–1500. doi:10.1016/s0022-2275(20)34422-9

Sohlenkamp, C., and Geiger, O. (2015). Bacterial membrane lipids: Diversity in structures and pathways. *FEMS Microbiol. Rev.* 40 (1), 133–159. doi:10.1093/femsre/fuv008

Tamegai, H., Ota, Y., Haga, M., Fujimori, H., Kato, C., Nogi, Y., et al. (2011). Piezotolerance of the respiratory terminal oxidase activity of the piezophilic *Shewanella violacea* DSS12 as compared with non-piezophilic *Shewanella* species. *Biosci. Biotechnol. Biochem.* 75 (5), 919–924. doi:10.1271/bbb.100882

Usui, K., Hiraki, T., Kawamoto, J., Kurihara, T., Nogi, Y., Kato, C., et al. (2012). Eicosapentaenoic acid plays a role in stabilizing dynamic membrane structure in the deep-sea piezophile *Shewanella violacea*: A study employing high-pressure time-resolved fluorescence anisotropy measurement. *Biochimica Biophysica Acta - Biomembr.* 1818 (3), 574–583. doi:10.1016/j.bbamem.2011.10.010

Vargas-Yáñez, M., Garcia-Martinez, M., Moya, F., Balbin, R., Lopez-Jurado, J., Serra, M., et al. (2017). Updating temperature and salinity mean values and trends in the Western Mediterranean: The RADMED project. *Prog. Oceanogr.* 157 (AUG), 27–46. doi:10.1016/j.pocean.2017.09.004

Villanueva, L., del Campo, J., and Geyer, R. (2010). Intact phospholipid and quinone biomarkers to assess microbial diversity and redox state in microbial mats. *Microb. Ecol.* 60 (1), 226–238. doi:10.1007/s00248-010-9645-2

Villanueva, L., Rijpstra, W. I. C., Schouten, S., and Damste, J. S. S. (2014). Genetic biomarkers of the sterol-biosynthetic pathway in microalgae. *Environ. Microbiol. Rep.* 6 (1), 35–44. doi:10.1111/1758-2229.12106

Wang, F., Xiao, X., Ou, H. Y., and Gai, Y. (2009). Role and regulation of fatty acid biosynthesis in the response of *Shewanella piezotolerans* WP3 to different temperatures and pressures. *J. Bacteriol.* 191 (8), 2574–2584. doi:10.1128/JB.00498-08

Wang, J., Li, J., Dasgupta, S., Zhang, L., Golovko, M. Y., Golovko, S. A., et al. (2014). Alterations in membrane phospholipid fatty acids of gram-positive piezotolerant bacterium *Sporosarcina* sp. DSK25 in response to growth pressure. *Lipids* 49 (4), 347–356. doi:10.1007/s11745-014-3878-7

Xiao, X., Wang, P., Zeng, X., Bartlett, D. H., and Wang, F. (2007). *Shewanella psychrophila* sp. nov. and *Shewanella piezotolerans* sp. nov., isolated from west Pacific deep-sea sediment. *Int. J. Syst. Evol. Microbiol.* 57 (1), 60–65. doi:10.1099/ijs.0.64500-0

Yadav, S., Villanueva, L., Bale, N., Koenen, M., Hopmans, E. C., and Damste, J. S. S. (2020). Physiological, chemotaxonomic and genomic characterization of two novel piezotolerant bacteria of the family *Marinifilaceae* isolated from sulfidic waters of the Black Sea. *Syst. Appl. Microbiol.* 43 (5), 1–10. doi:10.1016/j.syapm.2020.126122

Yano, Y., NakAyAmA, A., Ishihara, K., and Saito, H. (1998). Adaptive changes in membrane lipids of barophilic bacteria in response to changes in growth pressure. *Appl. Environ. Microbiol.* 64 (2), 479–485. doi:10.1128/aem.64.2.479-485.1998

frontiers | Frontiers in Molecular Biosciences

TYPE Original Research
PUBLISHED 23 February 2023
DOI 10.3389/fmolb.2023.1141081

OPEN ACCESS

EDITED BY
Elena G. Govorunova,
University of Texas Health Science Center at Houston, United States

REVIEWED BY
Giray Enkavi,
University of Helsinki, Finland
Ekaitz Errasti Murugarren,
University of Barcelona, Spain
Kei Higuchi,
Tokyo University of Pharmacy and Life Sciences, Japan

*CORRESPONDENCE
Ina L. Urbatsch,
ina.urbatsch@ttuhsc.edu

SPECIALTY SECTION
This article was submitted to Lipids, Membranes and Membranous Organelles, a section of the journal Frontiers in Molecular Biosciences

RECEIVED 09 January 2023
ACCEPTED 06 February 2023
PUBLISHED 23 February 2023

CITATION
Tran NNB, Bui ATA, Jaramillo-Martinez V, Weber J, Zhang Q and Urbatsch IL (2023), Lipid environment determines the drug-stimulated ATPase activity of P-glycoprotein.
Front. Mol. Biosci. 10:1141081.
doi: 10.3389/fmolb.2023.1141081

Lipid environment determines the drug-stimulated ATPase activity of P-glycoprotein

Nghi N. B. Tran[1,2], A. T. A. Bui[1,2], Valeria Jaramillo-Martinez[1,2], Joachim Weber[2,3], Qinghai Zhang[4] and Ina L. Urbatsch[1,2]*

[1]Department of Cell Biology and Biochemistry, Texas Tech University Health Sciences Center, Lubbock, TX, United States, [2]Center for Membrane Protein Research, Texas Tech University Health Sciences Center, Lubbock, TX, United States, [3]Department of Chemistry and Biochemistry, Texas Tech University, Lubbock, TX, United States, [4]Department of Integrative Structural and Computational Biology, The Scripps Research Institute, La Jolla, CA, United States

P-glycoprotein (Pgp) is a multidrug transporter that uses the energy from ATP binding and hydrolysis to export from cells a wide variety of hydrophobic compounds including anticancer drugs, and mediates the bioavailability and pharmacokinetics of many drugs. Lipids and cholesterol have been shown to modulate the substrate-stimulated ATPase activity of purified Pgp in detergent solution and the substrate transport activity after reconstitution into proteoliposomes. While lipid extracts from *E. coli*, liver or brain tissues generally support well Pgp's functionality, their ill-defined composition and high UV absorbance make them less suitable for optical biophysical assays. On the other hand, studies with defined synthetic lipids, usually the bilayer-forming phosphatidylcholine with or without cholesterol, are often plagued by low ATPase activity and low binding affinity of Pgp for drugs. Drawing from the lipid composition of mammalian plasma membranes, we here investigate how different head groups modulate the verapamil-stimulated ATPase activity of purified Pgp in detergent-lipid micelles and compare them with components of *E. coli* lipids. Our general approach was to assay modulation of verapamil-stimulation of ATPase activity by artificial lipid mixtures starting with the bilayer-forming palmitoyloyl-phosphatidylcholine (POPC) and -phosphatidylethanolamine (POPE). We show that POPC/POPE supplemented with sphingomyelin (SM), cardiolipin, or phosphatidic acid enhanced the verapamil-stimulated activity (V_{max}) and decreased the concentration required for half-maximal activity (EC_{50}). Cholesterol (Chol) and more so its soluble hemisuccinate derivative cholesteryl hemisuccinate substantially decreased EC_{50}, perhaps by supporting the functional integrity of the drug binding sites. High concentrations of CHS (>15%) resulted in a significantly increased basal activity which could be due to binding of CHS to the drug binding site as transport substrate or as activator, maybe acting cooperatively with verapamil. Lastly, Pgp reconstituted into liposomes or nanodiscs displayed higher basal activity and sustained high levels of verapamil stimulated activity. The findings establish a stable source of artificial lipid mixtures containing either SM and cholesterol or CHS that restore Pgp functionality with activities and affinities similar to those in the natural plasma membrane environment and will pave the way for future functional and biophysical studies.

KEYWORDS

P-glycoprotein, multidrug ABC transporter, verapamil-stimulated ATPase activity, membrane lipid composition, artificial plasma membrane mimic, mixed detergent/lipid micelles, liposomes, nanodiscs

Introduction

P-glycoprotein, also known as MDR1 or ABCB1, is a plasma membrane protein that can pump a wide range of hydrophobic, structurally diverse substances out of cells (Chufan et al., 2015). The Pgp substrates include many chemotherapeutic drugs used for the treatment of cancer, HIV/AIDS, neurodegenerative and cardiovascular diseases (Al-Khazaali et al., 2014; Waghray and Zhang, 2018; Jia et al., 2020). Pgp participates in the transepithelial transport of drugs and metabolites which makes it an important determinant in the absorption, distribution, metabolism and excretion (ADME) that affect the pharmacokinetics and drug-drug interactions of therapeutics across many diseases (Giacomini et al., 2010; Yee et al., 2018). Pgp is also richly expressed at several blood-organ barriers including the brain and placenta where it protects those sanctuaries from harmful xenobiotics, environmental pollutants, and waste products of cellular metabolism (Storelli et al., 2021). Additionally, Pgp is a key player in multidrug resistance (MDR) of cancers (Robey et al., 2018). Therefore, it is critical to comprehend the mechanism by which Pgp recognizes and extrudes medicines in the context of the tissue microenvironment.

Pgp is an ATP-binding cassette (ABC) transporter that consists of two nucleotide binding domains (NBDs) that energize transport by binding and hydrolyzing ATP, and two transmembrane domains (TMDs) that harbor the drug binding site(s) within the lipid bilayer. A large hydrophobic binding surface in the center of the transmembrane domains was shown in Pgp structures determined by X-ray crystallography and cryo-electron microscopy (cryo-EM). Pgp structures have been solved with multiple bound substrates, such as QZ-59 cyclopeptides, vincristine, taxol, and as well as with inhibitors elacridar, tariquidar, zosuquidar (Aller et al., 2009; Szewczyk et al., 2015; Alam et al., 2018; Alam et al., 2019; Nosol et al., 2020). Because Pgp substrates are generally hydrophobic, they are likely extruded from within the membrane rather than from the aqueous phase. Indeed, Pgp is thought to act as "hydrophobic vacuum cleaner" (Gottesman and Ling, 2006) that intercepts hydrophobic compounds from the inner leaflet of the membrane bilayer before they reach the cytoplasm and pumps them back out of cells. As a membrane transporter and because of the intricate interactions of the hydrophobic substrate with the bilayer, the surrounding lipid environment is an important regulator of Pgp activity (Sharom, 2014; Stieger et al., 2021).

Phospholipids modulate Pgp function

Early studies of Pgp in native plasma membranes fractions from mammalian cells showed robust stimulation of the ATPase activity by transport substrates like verapamil and vinblastine (al-Shawi and Senior, 1993). Purification of Pgp in detergents often led to reduced ATPase activity but could be restored with the supplementation of lipids (e.g., tissue extracts from *E. coli*, sheep or bovine brain, bovine liver, for available lipid composition see Table 1). However, the basal activity (in the absence of added drug) and the drug-stimulated activities varied considerably depending on the detergent used for solubilization and the lipid source (Ambudkar et al., 1992; Sharom et al., 1993; Urbatsch and Senior, 1995). Similar studies with extracts of defined phospholipids or synthetic lipids including phosphatidylcholine (PC), -ethanolamine (PE), -serine (PS) and -inositol (PI); showed that they all supported basal ATPase activity of purified Pgp and protected its thermal inactivation (Doige et al., 1993; Yang et al., 2017). This may be due to specific phospholipid binding to the outer surface of Pgp, which may affect the protein stability and activity (Marcoux et al., 2013).

It has been suggested in the literature that phospholipids themselves are substrates for Pgp (Rothnie et al., 2001). Sharom et al. detected the flippase activity of Pgp using the NBD fluorescence-labeled PC, PE and PS derivatives, reviewed in (Sharom, 2014). Albeit this flippase activity is much lower than the dedicated PC-lipid flippase activity of its close relative MDR2 (ABCB4) both of which are prominent in the liver canalicular membrane duct, where they work together with cholesterol transporter ABCG5/G8 and the bile salt export pump ABCB11 to excrete hydrophobic drugs, lipids and cholesterol dissolved in bile acids (Neumann et al., 2017).

Cholesterol modulates bilayer properties and Pgp function

Cholesterol is one of the key components in animal cell membranes. It influences membrane properties such as membrane packing, elasticity and fluidity, affects lateral and transmembrane diffusion and overall stabilizes the structure of phospholipid bilayers. Over the years, a connection between Pgp activity and cholesterol has evolved. Pgp ATPase activity has been reported to be affected by the presence of lipid and cholesterol (Sharom, 2008). Besides its effect on Pgp transport activity, cholesterol may alter the availability of hydrophobic drugs in the membrane (Rothnie et al., 2001; Modok et al., 2004; Belli et al., 2009). Interestingly, ordered POPE and cholesterol molecules have been found in cryo-EM structures tightly associated with human Pgp in nanodiscs composed of brain lipid extract supplemented with cholesterol (Alam et al., 2019). On the contrary, phospholipids and cholesterol have not been revealed in the internal cavity of existing high-resolution Pgp structures. Hence the evidence for Pgp as a lipid or cholesterol transporter is still lacking. More likely, the membrane lipids modulate the conformational changes associated with drug binding and transport.

We previously have reconstituted Pgp into *E. coli* lipid nanodiscs that displayed high verapamil-stimulated ATPase activity. These nanometer-scale discoidal structures contain a phospholipid bilayer encased by membrane scaffold proteins (MSPs), which are soluble and stable in aqueous solutions (Zoghbi et al., 2017). Although nanodiscs differ from native membranes in physical properties such as curvature, and in the complexity of their lipid composition, they are

TABLE 1 Lipid composition of native mammalian membranes.

	E. coli polar lipid extract	Bovine liver polar lipid extract	Porcine brain polar lipid extract	Mammalian total cell lipid[a]	Human liver microsomes	Rat liver plasma membrane[b]	Plasma membrane mimic
Phosphatidylcholine (PC)		42	13	45 to 55 [b]	42	36 to 41	~40
Phosphatidylethanolamine (PE)	67	26	22	15 to 25	31	23 to 26	~24
Phosphatidylserine (PS)		10	19	2 to 10	5	9 to 10	~9
Phosphatidylinositol (PI)			4	10 to 15	13	4 to 8	[c]
Phosphatidylglycerol (PG)	23						
Sphingomyelin (SM)				5 to 10	4	16 to 25	~22
Cardiolipin	10			2 to 5			
PA, BMP			1	1 to 2		0.5	
Residual		17 [d]	31 [d]			1 to 2	
Cholesterol		5		10 to 20	7		
Cholesterol:phospholipid						ratio 1:1[e]	ratio 1:1
References	Avanti Polar Lipids	Avanti Polar Lipids	Avanti Polar Lipids	Vance and Steenbergen (2005)	Kapitulnik et al. (1987)	Zambrano et al. (1975); van Meer et al. (2008)	This study

[a]Cultured cell extracts from a typical mammalian cell (Vance and Steenbergen, 2005); examples from HEK, CHO, MDCK, and other cell lines can be found in (Symons et al., 2021).
[b]Original references are from rat plasma membranes; these are considered similar to human plasma membranes (Ingólfsson et al., 2014; Domicevica et al., 2018; Symons et al., 2021).
[d]Residuals are not specified on the Avanti Polar Lipids website.
[e]Values are given in % (w/w); cholesterol is often reported as a weight ration relative to total phospholipid content. A ratio of 1:1 amounts to 50% total cholesterol (w/w).
[c]Was not include due to inhibitory effect, see text.

excellent lipid–bilayer platforms for many biophysical applications including optical measurements that require reduced light scattering (Ritchie et al., 2009). With access from both sides, nanodisc allows the protein to interact with the substrate from different directions. However, tissue extracts of lipids, including *E. coli* lipids, carry very high fluorescence in the tryptophan excitation/emission (290/345 nm) range and are not suitable for biophysical studies using the intrinsic fluorescence of Pgp's eleven native tryptophans.

Phospholipid and cholesterol composition of membranes

The composition of lipid components in different organelles and tissues varies greatly; thus, it is traditionally difficult to assess the endogenous activity of Pgp. In a typical mammalian cell, the total membrane lipid composition consist of roughly 45%–55% PC, 15%–25% PE, 5%–10% PS, 10%–15% PI, 5%–10% sphingomyelin (SM), and 10%–20% cholesterol (Table 1) (Vance and Steenbergen, 2005; van Meer et al., 2008). Human liver microsomes, which contain a mixture of endoplasmic reticulum, Golgi and plasma membranes, generally have a higher content of about 31% PE and lower relative contents of SM and cholesterol. In contrast, plasma membranes are enriched in total SM (>15%) and cholesterol (ratio is approximately 1:1 cholesterol: phospholipid, w/w) accounting for its greater rigidness (Symons et al., 2021). Furthermore, within the plasma membrane SM (up to 26%) and cholesterol are accumulating in detergent-insoluble microcompartments known as lipid rafts, in which Pgp tends to gather (Ismair et al., 2009; Hullin-Matsuda et al., 2014). In both microsomes and plasma membranes, PC is the most abundant phospholipid (36%–42%), followed by PE and SM with lower PS and PI contents (Table 1).

In this study, we measure the effects of individual lipids and lipid mixtures on the basal and verapamil-stimulated ATPase function of Pgp. We use both natural lipids and defined synthetic lipids to identify those that promote Pgp activity. We further probe increasing concentrations of supplemental cholesterol and its more soluble hemisuccinate derivative CHS and demonstrate favorable interaction of CHS on the Pgp ATPase function. By these measurements, we establish a stable source of artificial lipid mixtures containing POPC, POPE, and cholesterol/CHS that can support Pgp ATPase activity, and optimize the reconstitution of Pgp into lipid nanodiscs with high yields and high activity. Our study reassures that the phospholipid and cholesterol composition play a crucial role in the basal and drug-stimulated ATPase activity affecting both the apparent binding affinity for verapamil and the V_{max}.

Methods and materials

Materials

Protein kinase A, lactate dehydrogenase, and phosphoenol-pyruvate were purchased from Roche CustomBiotech

(Indianapolis, IN). Adenosine-5′-triphosphate disodium salt (ATP) ultrapure 98% was obtained from Alfa Aesar (Tewksbury, MA). Verapamil was acquired from Sigma Aldrich (Saint Louis, MO). n-dodecyl-β-D-maltopyranoside (DDM) was bought from Inalco S. p.A (Milano, Italy). Nicotinamide adenine dinucleotide (NADH) was purchased from Sigma-Aldrich (Burlington, MA).

E. coli polar lipids (polar extract) and synthetic lipids were acquired from Avanti (Alabaster, AL); these include 1-palmitoyl-2-oleoyl-sn-glycero-3-phosphocholine or 16:0-18:1 PC (POPC), 1-Palmitoyl-2-oleoyl-sn-glycero-3-phosphatidylethanolamine (POPE), 1-palmitoyl-2-oleoyl-sn-glycero-3-phospho-L-serine (POPS), 1-palmitoyl-2-oleoyl-sn-glycero-3-phosphatidylinositol (POPI), 1-Palmitoyl-2-oleoyl-sn-glycero-3-phosphatidylglycerol (POPG), DPPA, 1,2-dipalmitoyl-sn-glycero-3-phosphate or 16:0 PA, 1,2-dimyristoyl-sn-glycero-3-phosphocholine (DMPC). Sphingomyelin (SM) was >99% pure from porcine brain with major acyl chains of 18:0 (50%) and 21:1 (21%), and cardiolipin (CL) was from >99% bovine heart with major acyl chains of 18:2 (90%). All synthetic lipids, SM and CL had very low tryptophan fluorescence (ex/em 295/350 nm) if purchased as powder. Cholesterol (Chol) and cholesteryl hemisuccinate (CHS) were purchased from Anatrace (Maumee, OH).

General chemicals were at the highest grade from Thermo Fisher Scientific (Waltham, Massachusetts).

Tryptophan-free membrane scaffold protein mutagenesis

The membrane scaffold protein MSP1E3D1 plasmid was a gift from Stephen Sligar (Addgene plasmid # 20066; http://n2t.net/addgene:20066; RRID:Addgene_20066) obtained from Addgene (Denisov et al., 2009). The three native tryptophans (Trps) were substituted by PCR mutagenesis (W41R/W77Q/W143Q) to create a Trp-less MSP1E3D1 named WL-MSP. Wild-type and WL-MSP were expressed in BL21Gold (DE3) *E. coli* cells in Terrific broth with 70 μg/ml kanamycin after induction with 1 mM IPTG for 2–4 h at 37°C as described (Ritchie et al., 2009). The N-terminal hepta histidine-tag was used for purification by established protocols (Ritchie et al., 2009) with the following modifications: Because Triton-X100 has a very high absorption around 280 nm, 1% DDM was substituted for Triton during cell breakage. WL-MSP bound to Ni-NTA resin was first washed with buffer M (40 mM TrisCl pH = 8, 300 mM NaCl) containing 50 mM sodium cholate (10 column volumes (cv)), followed by 50 mM sodium cholate buffer M containing 20 mM imidazole (10 cv). Then cholate was washed off with buffer M containing 0.1% DDM (10 cv), followed by a stringent wash in detergent-free buffer (10 cv) containing 50 mM imidazole to remove tightly bound contaminants. The WL-MSP protein was eluted in detergent-free buffer M with 400 mM imidazole, dialyzed against buffer M and frozen in aliquots. Protein concentration was determined by its absorption at 280 nm using a molar extinction coefficient ε of 11,520 $M^{-1}cm^{-1}$ with 1 absorption unit containing 2.84 mg/ml protein.

Lipid mixtures of varied composition

Lipids from Avanti Polar Lipids were obtained as lyophilized powder. Calculated amounts of lipid powder were weighed into a glass vial and pumped under vacuum at ≤20 microns for 16–20 h at room temperature to remove trace amounts of solvent. Lipid mixtures were suspended into 50 mM TrisCl buffer pH, 7.4 at a final concentration of 20 mg/ml by rotating for at least 8–10 h at room temperature, followed by several freeze cycles at −80°C followed by thawing at room temperature. Lipid powder and suspension were kept under inert nitrogen gas at all times and stored frozen at −80°C. For nanodisc reconstitutions, lipid mixtures were dissolved in DDM at a ratio of 4:1 DDM to lipid (w/w) unless otherwise indicated. For lipid mixtures containing CHS, the indicated amount of phospholipids and CHS powder were weighted prior to dissolving in TrisCl buffer.

Protein purification and quantification

Mouse mdr1a Pgp (codon-optimized abcb1a, GenBank JF834158) was expressed in *Pichia pastoris*, and grown in fermentor cultures as previously described (Bai et al., 2011). Tobacco, Etch Virus protease (TEV)-cleavable Twin-Strep and His_6 –tags were engineered to the C-terminus to facilitate purification by tandem affinity chromatography on Ni-NTA and Strep-Tactin resins as described (Swartz et al., 2020), with the following modifications. Microsomal membrane preparations were solubilized at a concentration of 2–3 mg/ml keeping a constant ratio of detergent to protein of 4:1 (w/w). All purification buffers contained 50 mM Tris pH 8, 10% glycerol, and 500 mM NaCl (Buffer A). Detergent concentrations were reduced to 0.05% DDM during chromatography. Pgp was eluted from the Strep-Tactin superflow resin (Qiagen, Valencia, CA) in the presence of 1 mM DTT, 1 mM TCEP by competition with 4 mM desthiobiotin.

The concentrations of purified Pgp preparations were initially determined from the absorbance at A280 nm using a calculated molar extinction coefficient ε including the purification tags of 126,630 $M^{-1}cm^{-1}$. Protein concentrations were verified by the bicinchoninic acid (BCA) protein assay using BSA as a standard. Finally, increasing protein amounts of a Pgp standard and newly purified Pgps were resolved side-by-side on SDS-PAGE gels, stained with Coomassie Brilliant Blue, and the Pgp bands quantified using ImageJ (http://rsbweb.nih.gov) to compare mutant Pgp levels between purifications, and after reconstitutions. From 100 g of cells, we routinely purified 6–7 mg of highly pure Pgp at the concentration of 0.8–1 mg/mL. Pgp was frozen in aliquots of 100–200 μl at −80°C.

ATPase activity measurements

To determine the ATPase activity, purified Pgp (~100 μL) in detergent was activated by incubation with 10 mM DTT and an equal volume of 20 mg/ml of lipids added, giving a final concentration of 1% (w/v) lipids for 15 min at 4°C. Then the protein concentration was adjusted with TrisCl buffer to 0.075 μg/μl 0.5–1.0 μg (~10 μl) samples were added to 200 μl of ATP cocktail in 96-well plates. The rate of ATP hydrolysis was measured at 37°C in an enzyme linked continuous optical assay utilizing an ATP regeneration system (Urbatsch et al., 1995;

Urbatsch et al., 2000), in the absence and presence of increasing concentrations of verapamil. Purified Pgp mixed with *E. coli* polar lipids typically displayed a specific ATPase activity at 30 μM Verapamil of 3.8–4.0 μmol/min/mg.

Verapamil stocks (50 mM) and 2x-serial dilutions were made in water, 2 μl of the serial dilutions were added to 200 μl of ATP cocktail. ATP activity was monitored for 20 min to 2 h during which the slopes were constant. Statistical analyses were done as described (Swartz et al., 2013; Swartz et al., 2014). EC_{50} values were calculated from fits according to $f = V_b+((V_{max}-V_b)*X^b/(Ks^b + X^b))$, where Vb is the basal activity (in the absence of verapamil), V_{max} is the maximum activity, X is the concentration of verapamil, b is the Hill coefficient of the upward curve, Ks is the concentration for half-maximal stimulation or EC_{50}. For each data fit, R^2 was greater than 0.97 and each of the parameters was statistically significant ($p < 0.05$). Lines in the graphs represent fits to the data points (open and closed symbols) using the following equation $f = V_b+((V_{max}-V_b)*X^b/(K_s^b + X^b))+(V_{max}-(V_{max}-V\infty)*X^m/(K_i^m + X^m))$, where Vb is the basal activity (in the absence of verapamil), V_{max} is the maximum activity, X is the concentration of verapamil, b is the Hill coefficient of the upward curve, Ks is the concentration for half-maximal stimulation or EC_{50}, V∞ is the activity at infinite verapamil concentrations, m is the Hill coefficient of the downward curve, and Ki is the concentration for half-maximal inhibition or IC_{50}. All statistical analyses were performed with Sigmaplot 11.

Protein reconstitution and quantification

For liposome reconstitutions, purified Pgp in detergent was activated with 10 mM DTT and lipid mixture at a ratio of 1: 250 Pgp:lipids (mol/mol). The sample was then diluted with 50 mM TrisCl buffer to give a final glycerol concentration of 4%.

For nanodisc reconstitution, purified Pgp in detergent was activated with 10 mM DTT before adding membrane scaffold protein (MSP) and lipid mixture at a ratio of 1:5:250 Pgp:MSP: lipids (mol/mol/mol). The sample then diluted using 50 mM TrisCl, buffer to give a final glycerol concentration of 4%. For both liposome and nanodisc reconstitutions, for every 1 mg of purified protein, 2 mg of Bio-Beads were added in two additions to remove the detergent. First addition consisted of 1/3 of the total Bio-Beads then placed on a rocker for 2 h at 4°C before adding the second batch of Bio-Beads with continuous rocking for 16–18 h at 4°C. Bio-Beads were removed by filtration through a chromatography column (BioRad) and washed with twice the initial volume of 50 mM TrisCl, 150 mM NaCl, 2% glycerol (buffer M). The filtrate was centrifuged for 15 min at 12,000 g and 4°C to pellet precipitated protein. The supernatant contained a mixture of Pgp-discs and "empty" lipid-nanodiscs that had not entrapped Pgp. This mixture can be directly used for ATPase activity measurement of Pgp since empty nanodiscs show zero activity. Pgp liposomes were directly used for ATPase assays and were not further purified.

Freshly prepared proteoliposomes were snap-frozen at 80°C in small aliquots and assayed within 2 days. Aliquots were thawed at room temperature, and then 2.5–5 μl were diluted into 200 ul of ATPase cocktail, and the ATP hydrolysis monitored at 37°C as above. To test the orientation of the NBDs in the proteoliposomes, aliquots were incubated overnight at 4°C on a rotator without or with TEV protease that cleaves the C-terminal Strep-tag of only those Pgp molecules with the NBDs accessible facing outside of sealed proteoliposomes. Loss of the Strep-tag was detected on Western blots with the anti-Strep tag antibody (Qiagen) and the SuperSignal™ West Pico enhanced chemiluminescent (ECL) substrate; luminescence signals were quantitated with the ImageQuant software.

For separation of Pgp-discs and empty nanodiscs, we took advantage of the Twin-Strep tag on Pgp to bind the protein to Strep-Tactin resin and wash off empty nanodiscs in detergent-free buffers. For this, 1 mg Pgp reconstituted as detailed above was incubated with 1 ml of Strep-tactin resin in 1.5 ml total volume by rotating in a sealed chromatography column for 5 h at 4°C. The flow-through was collected in the same column, and unbound empty nanodiscs were washed off with 10 column volume of size exclusion chromatography (SEC) buffer (20 mM HEPES pH 7.4, 150 mM NaCl, 4% glycerol). The Pgp-discs were eluted off the resin by cleavage of the tag. For this TEV protease was added to the resin at a Pgp:TEV ratio of 4:1 (w/w) in a total of one cv by rotating in the same column for 16–18 h at 4°C to allow for optimal cleavage. The flow through was collected and the Strep-tactin resin was washed with 2 cv of SEC buffer to collect all cleaved sample and combined with the column elution.

Isolated Pgp-discs were analyzed for purity and Pgp concentration on Coomassie-stained SDS-gels and cross-referenced with ATPase activity. The Pgp protein bands were quantified by comparison with a purified Pgp standard using ImageJ. We routinely obtained Pgp concentration of 0.04–0.05 μg/μl; total protein recovery was variable between experiments and was about 25% ± 6% of the starting Pgp using POPC/POPE/Chol/CHS lipid mixtures. For ATPase assays, about 20 μL Pgp-disc samples were mixed with 200 μl ATP cocktail containing 30 μM verapamil and incubated for 50 min to 2 h at 37°C, and ATPase activity calculated as above. ATPase measurements of samples "Before" and "After" separation on Strep-Tactin resin were assayed in triplicates, and the total ATPase activity calculated per input Pgp.

In all cases, data are expressed as means of at least two independent reconstitutions ± range. Graphs were plotted using SigmaPlot 11.0 from Systat Software, Inc., San Jose California United States, www.systatsoftware.com. Statistical analyses were performed using GraphPad Prism 9 Software (San Diego, California United States). Statistical differences between groups were analyzed by two-tailed unpaired Student's t-test, or by one-way analysis of variance (ANOVA) followed by Dunnett's, Bonferroni's, or Tukey's test, for single and multiple comparisons; a $p < 0.05$ was considered significant. For these statistical tests, the normality was confirmed using the GraphPad Prism 9 software.

Results

Parameters analyzed to evaluate Pgp function

The overarching goal of this study was to compare Pgp functionality in different lipid environments. For this purpose, we measured V_{max} and, in order to assess the affinity for transport substrates, EC_{50} for verapamil-induced ATPase activity. In some cases with a high basal activity (i.e., in absence of verapamil), the

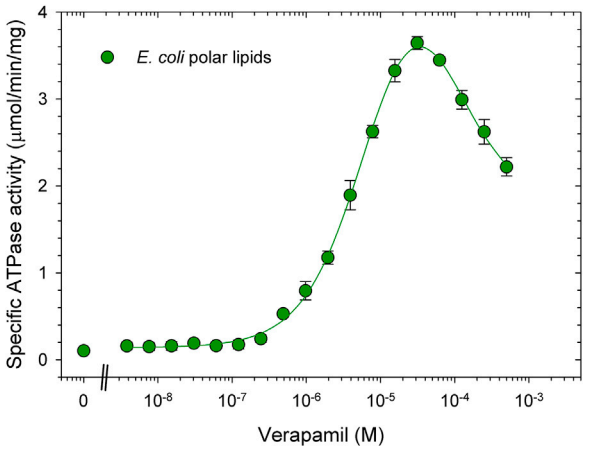

FIGURE 1
Verapamil-induced stimulation of ATPase activity in DDM-*E. coli* lipid mixed micelles. Purified Pgp in detergent solution was activated with 1% *E. coli* polar lipids and 10 mM DTT as described in experimental procedures. ATPase activity was measured in the presence of increasing concentrations of verapamil as indicated. Data points represent the mean ± SEM (n = 3). Kinetic parameters obtained from a fit (solid line) to the data points is listed in Table 2, for details see Methods.

additional activation by verapamil was too small to reliably determine EC_{50}. In those cases, it was easier to determine the verapamil concentration necessary for maximal ATPase activity.

Pgp ATPase activity in *E. coli* lipid

The ATPase activity of Pgp was previously measured using *E. coli* polar lipid extract (Avanti Polar Lipids) (Bai et al., 2011; Shukla et al., 2017). Typically with *E. coli* lipids, purified Pgp in DDM was activated by simply mixing the protein in detergent solution (usually 0.1% DDM) with lipids, together with 10 mM DTT to fully reduce inhibitory disulfide bonds (Urbatsch et al., 2001). The highest activation of ATPase by verapamil in this detergent/lipid mixture was reported at around 30 µM, with a V_{max} of 3.8 µmol/min/mg and an EC_{50} of around 3 µM. (Figure 1, see also (Urbatsch et al., 2000; Bai et al., 2011). Basal ATPase activity in the absence of verapamil was low at around 0.15 µmol/min/mg. In dose-response curves for verapamil activation of ATPase activity we have consistently observed a Hill coefficient of greater than 1.2 suggesting two binding sites that interact with positive cooperativity. Moreover, a negative slope of the curve at high concentrations of verapamil suggests (an) secondary inhibitory site(s) with a lower affinity for verapamil.

Pgp ATPase activity in defined phospholipids

The first specific aim of this study was to create an artificial lipid mixture that can better mimic the mammalian plasma membrane composition but still promote Pgp ATPase activity in the same way that *E. coli* lipids can. While there is a large variety of phospholipids, the major species of fatty acids in phospholipids of the mammalian cell membranes are 16:0-18:1 (Kalvodova et al., 2009). As to the phospholipid head group, two major phospholipids found in plasma membranes are PC and PE (Table 1). Thus, the synthetic phospholipids POPC and POPE were chosen as basis to analyze the effect of individual phospholipids on Pgp ATPase activity. Purified Pgp treated with POPC alone yielded low activity. With the addition of POPE to POPC at a weight ratio of 1 to 1, half the maximum activity was reached compared to *E. coli* lipids (Figure 2; Table 2). Supplementing POPC/POPE with 10% cardiolipin increased V_{max} more than 2.5-fold but higher concentrations (17%) reversed this effect. The addition of 22% sphingomyelin also increased V_{max} significantly.

Importantly, addition of cardiolipin as well as SM and the acidic lipid POPS to POPC/POPE all significantly decreased the EC_{50} to around 3 µM, a value similar to *E. coli* lipids. The largest decrease in EC_{50} was observed when POPC/POPE was supplemented with the negatively charged free acid DPPA. POPS alone had little effect on V_{max}, but when combined with the polar head group lipid POPI, the activity was reduced. Pgp activity was also reduced by the acidic lipid POPG. Taken together, the data demonstrate that the lipid head group plays a key role in the interaction of Pgp with verapamil, affecting V_{max} and its apparent affinity for drugs, as manifested in the effects on EC_{50} for verapamil.

Cholesterol and CHS strongly affect Pgp ATPase activity

Cholesterol is a key component of mammalian lipid bilayers, accounting for up to 50% of the plasma membrane lipid mass (see Table 1). Biochemical studies using cholesterol, on the other hand, can be cumbersome due to its very hydrophobic nature. The hemisuccinate ester of cholesterol, CHS, is more water-soluble and therefore more suitable for many biochemical applications. CHS has been shown to be able to mimic cholesterol function (Kulig et al., 2014). Here, we examined the effects of both cholesterol and CHS on the ATPase function of Pgp.

We found that supplementing POPC/POPE lipid with 15% cholesterol had little effect on the verapamil-stimulation of the Pgp ATPase activity and on the EC_{50}. Addition of 30% or 50% cholesterol to POPC/POPE decreased V_{max} moderately and gradually reduced EC_{50} (Figure 3A; Table 3). A plasma membrane mimic composition was created using POPC:POPE: POPS:SM at a ratio of 42:25:10:23 (w/w) with 50% cholesterol. The mixture was able to produce an activity similar to *E. coli* lipids while decreasing the EC_{50} by more than 20-fold (Figure 3B; Table 3). Interestingly, in both cases where 50% cholesterol was used the basal activity (in the absence of verapamil) increased.

If POPC/POPE with 15% cholesterol was additionally supplemented with as little as 1% CHS, a left-shift in the verapamil dose-response curve was observed. The decrease in EC_{50} was even more pronounced upon increasing the CHS concentration to 5% or 10%, reflecting a 20-fold increase in apparent affinity for verapamil (Figure 4A; Table 4). Interestingly, the effect of 10% CHS could even be observed in absence of cholesterol.

Increasing the CHS concentrations to 15% or 20%, in the absence or presence of up to 20% cholesterol, dramatically increased the basal activity to values much higher than those seen with cholesterol, no longer allowing the determination of EC_{50} values with certainty (Figure 4B; Table 4). Maximum activity was observed between 0.1 and 1 µM verapamil, concentrations roughly 100-fold lower than in absence of

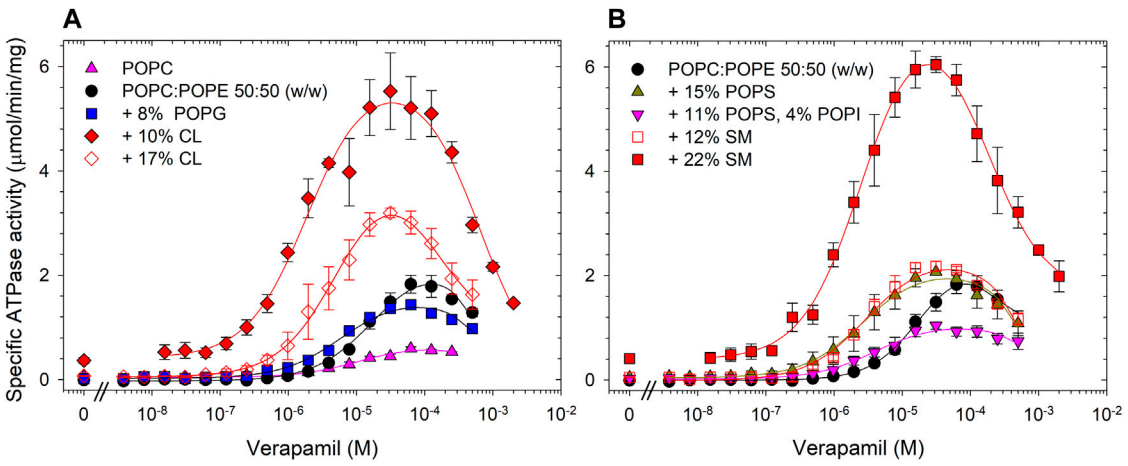

FIGURE 2
Effects of phospholipid head groups on the verapamil-stimulation of ATPase. **(A)** Lipid components of *E. coli* polar lipids, and **(B)** phospholipids found in mammalian plasma membranes. Purified Pgp was activated with 10 mM DTT and 1% POPC:POPE (50:50, w/w) lipid supplemented with indicated phospholipids as described in Experimental Procedures. Data points represent the mean ± SEM (n = 3). Kinetic parameters obtained from fits (solid lines) to the data points are listed in Table 2.

TABLE 2 POPC:POPE (50:50, w/w) was supplemented with indicated phospholipids and the verapamil stimulation of ATPase activity was assayed (n = 3).

POPC:POPE supplemented with	V_{max} (µmol/min/mg)	EC_{50} (µM)	Hill coefficient	Basal activity (µmol/min/mg)
POPC only	1.30 ± 0.3	6.5 ± 1.3	1.1 ± 0.2	0.05
POPC:POPE	1.83 ± 0.2	11 ± 1	1.5 ± 0.1	0.10
10% Cardiolipin	5.07 ± 0.3	1.5 ± 0.3	1.2 ± 0.1	0.38
17% Cardiolipin	3.20 ± 0.1	2.8 ± 0.4	1.4 ± 0.2	0.07
12% SM	2.18 ± 0.1	2.7 ± 0.1	1.5 ± 0.1	0.04
22% SM	5.65 ± 0.2	1.8 ± 0.2	1.2 ± 0.1	0.45
15% POPS	1.80 ± 0.1	2.4 ± 0.3	1.3 ± 0.2	0.05
11% POPS, 4% POPI	0.82 ± 0.3	2.7 ± 0.4	1.3 ± 0.2	<0.01
8% POPG	1.25 ± 0.1	4.8 ± 0.5	1.3 ± 0.2	0.05
2% DPPA	3.64 ± 0.2	0.81 ± 0.1	1.3 ± 0.2	0.83
6% DPPA	3.00 ± 0.4	0.73 ± 0.04	1.3 ± 0.1	0.16
E. coli polar lipids	3.65 ± 0.07	3.9 ± 0.3	1.2 ± 0.1	0.14

CHS. Taken together, these results show that CHS, either alone or in combination with cholesterol, substantially increases the apparent affinity of Pgp for verapamil. Interestingly, CHS also improves the thermostability of Pgp significantly (Supplementary Figure S1), as has been demonstrated for cholesterol (Rothnie et al., 2001; Bucher et al., 2007; Sharom, 2008).

Increasing the bilayer POPC content

Since POPE does not naturally form bilayers, we explored increasing the concentration of POPC to better promote membrane formation and repeated the experiments by supplementing with either cholesterol alone or cholesterol plus CHS (see Supplementary Figure S2, Supplementary Table S1). Trends with POPC:POPE at a ratio of 80:20 (w/w) were similar as with POPC:POPE at a ratio of 50:50 (w/w). However, the higher POPC:POPE ratio of 80:20 (w/w) resulted in lower V_{max} and higher EC_{50} values as compared to the 50:50 ratio (w/w); the latter was chosen for all subsequent experiments.

Reconstitution of Pgp-discs

The second aim of this study was to reconstitute Pgp into lipid nanodiscs with high recovery. Since the invention of nanodisc technology, protocols for reconstitution of Pgp have been reported with variations in the nanodisc size (MSP1D1 or MSP1E3D1), the lipid source, and the ratio of the components during assembly (Ritchie et al., 2009; Zoghbi et al., 2017; Alam et al.,

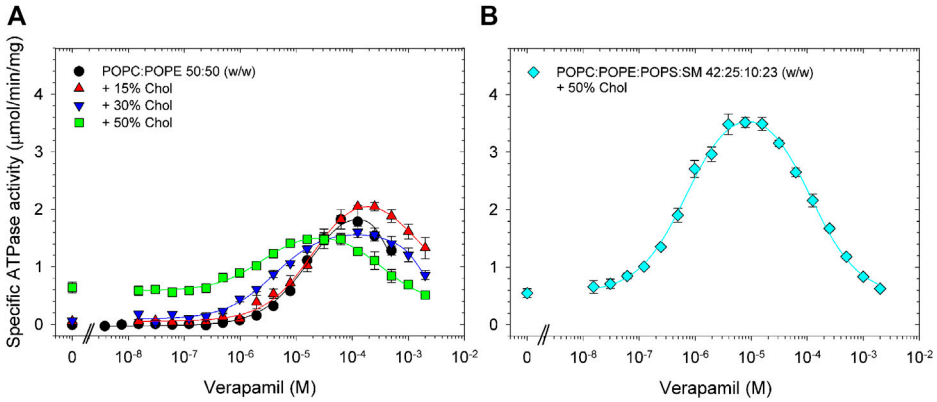

FIGURE 3
Effects of cholesterol on the verapamil-stimulation of ATPase. Purified Pgp was activated with 10 mM DTT and **(A)** POPC:POPE (50:50, w/w) lipid supplemented with 15% (w/w), 30% or 50% cholesterol. **(B)** A POPC:POPE:POPS:SM mixture (42:25:10:23, w/w) plus 50% cholesterol was used. ATPase activity was assayed as described in Experimental Procedures. Data points represent the mean ± SEM (n = 3).

TABLE 3 POPC:POPE (50:50, w/w) was supplemented with indicated concentration of cholesterol and the verapamil stimulation of ATPase activity was assayed (n = 3).

POPC:POPE supplemented with	V_{max} (µmol/min/mg)	EC_{50} (µM)	Hill coefficient	Basal activity (µmol/min/mg)	Verapamil concentration for maximum activity (µM)
None	1.9 ± 0.1	13 ± 1	1.5 ± 0.1	<0.1	60
15% Chol	2.0 ± 0.1	14 ± 1	1.1 ± 0.1	0.1	125
30% Chol	1.5 ± 0.1	3.8 ± 0.1	1.1 ± 0.1	0.1	125
50% Chol	1.2 ± 0.2	1.9 ± 0.2	1.2 ± 0.2	0.6	30
POPC:POPE:POPS:SM+ 50% Chol	3.5 ± 0.1	0.52 ± 0.06	1.2 ± 0.1	0.7	10

2019; Clouser et al., 2021). Typically, to facilitate the insertion of a protein into lipid bilayers, a lipid mixture is dissolved in detergent, mixed with the protein of interest and MSP, and then the detergent is removed using Bio-Beads to initiate reconstitution. After detergent removal, Pgp-discs can be isolated from "empty" nanodiscs devoid of Pgp by affinity chromatography taking advantage of engineered purification tags on Pgp. To track recovery of Pgp-discs we recorded the verapamil-stimulated ATPase activity and quantitate the Pgp protein bands on SDS-gels before and after purification on Strep-tactin resin.

Dissolving the lipid

First, we tested different DDM:lipid ratios from 1:1 to 8:1 (w/w) to dissolve the POPC/POPE 50:50 (w/w) mix with 15% cholesterol and 5% CHS. After detergent removal using Bio-Beads, we tracked Pgp recovery using its ATPase function. A range of DDM/lipid ratios from 1:1 to 6:1 (w/w) were effective in completely dissolving the lipid and resulted in good recovery of ATPase activity with a maximum observed at the ratio of 4:1 DDM:lipid (w/w). Increasing the DDM/lipid ratio to 7:1 or more reduced the recovered ATPase activity (Supplementary Figure S3).

Amount of bio-beads

Second, we tested the amount of Bio-Beads needed for maximum recovery. While Bio-Beads are effective in removing detergent, excess amounts of Bio-Beads may rapidly deplete the detergent causing the protein to precipitate before it is inserted into the lipid disc (Rothnie et al., 2001). On the other hand, not using sufficient amounts of Bio-Beads can leave traces of detergent in the solution which may bind to the drug binding sites and alter the ATPase activity (Shukla et al., 2017; Zoghbi et al., 2017). Therefore, finding the optimal amount of Bio-Beads is crucial to protein recovery and Pgp function. We tested four different ratios of Bio-Beads of 1, 2, 3, and 4 mg per 1 mg of purified Pgp. 2 mg of Bio-Beads per 1 mg Pgp produced high ATPase activity while increasing the ratio of Bio-Beads to Pgp diminished the yield of Pgp-discs. Of note, as the concentration of Bio-Beads was increased, larger protein pellets, indicative of protein precipitation, were observed concomitant with a decrease in recovered ATPase activity (Supplementary Figure S4A). Recovery of ATPase activity at 2 mg Bio-Beads per mg Pgp was around 24% ± 6% and agreed well with the recovery of the Pgp protein band of Pgp-discs resolved on Coomassie Blue-stained SDS-gels which ranged from 20% to 25% (Supplementary Figure S4B).

10.3389/fmolb.2023.1141081

TABLE 4 POPC:POPE (50:50, w/w) was supplemented with the indicated concentrations of cholesterol and CHS and the verapamil stimulation of ATPase activity was assayed (n = 3).

POPC:POPE supplemented with	V_{max} (μmol/min/mg)	EC_{50} (μM)	Hill coefficient	Basal activity (μmol/min/mg)	Verapamil concentration for maximum activity (μM)
None	1.9 ± 0.1	13 ± 1	1.5 ± 0.1	<0.1	60
10% CHS	1.9 ± 0.2	0.49 ± 0.09	1.6 ± 0.2	0.2	4
20% CHS	3.0 ± 0.2	ND[a]	ND[a]	2.5	0.1
15% Chol, 1% CHS	1.8 ± 0.1	3.7 ± 0.3	1.5 ± 0.2	0.1	30
15% Chol, 5% CHS	1.9 ± 0.1	0.76 ± 0.06	1.3 ± 0.1	0.1	8
15% Chol, 10% CHS	2.4 ± 0.1	0.63 ± 0.09	1.5 ± 0.2	0.3	4
15% Chol, 15% CHS	2.8 ± 0.1	ND[a]	ND[a]	1.8	1
15% Chol, 20% CHS	2.4 ± 0.1	ND[a]	ND[a]	2.0	0.1
20% Chol, 20% CHS	2.5 ± 0.1	ND[a]	ND[a]	1.7	0.5

[a]For samples containing 15% CHS, or more the basal activity (in the absence of verapamil) was high and an EC_{50} or Hill coefficient could not be determined (ND).

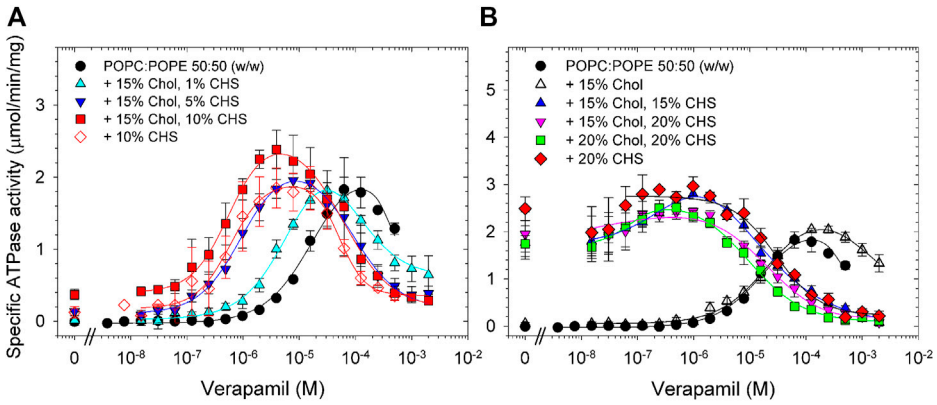

FIGURE 4
Effects on cholesterol and CHS on the verapamil-stimulation of ATPase. Purified Pgp was activated with 10 mM DTT and POPC:POPE (50:50, w/w) supplemented with the indicated concentrations of cholesterol and CHS. **(A)** 1%–10% CHS; **(B)** 15% or 20% CHS. ATPase activity was assayed as described in Experimental Procedures. Data points represent the mean ± SEM (n = 3).

Ratio of MSP to phospholipids

To assemble Pgp-discs, two membrane scaffold proteins (MSPs) are needed to enclose one Pgp molecule in a lipid nanodisc. Using excess MSP will increase the number of "empty" nanodiscs devoid of Pgp, while excess lipids can create Pgp proteoliposomes instead of or in addition to nanodiscs. Therefore, finding the optimal ratio of MSP to phospholipid is important. We tested a range of MSP: phospholipid ratios from 1:30 to 1:70 (mol/mol) using POPC/POPE supplemented with 15% cholesterol and 10% CHS. After Bio-Beads treatment and purification on Strep-tactin resin, the highest ATPase activity was recovered at a ratio of 1:40-1:50 of MSP to lipid (mol/mol) (Supplementary Figure S5). At an MSP:lipid ratio of 1:60 or less, recovery declined.

Reconstitution of Pgp in proteoliposomes and nanodiscs

Using the optimized conditions described above, we reconstituted Pgp-discs in POPC/POPE supplemented with 15% cholesterol and 0%, 10%, or 20% CHS to observe the effect of CHS on reconstitution. Purified protein was mixed with a detergent-lipid mixture and then the detergent was removed using Bio-Beads to initiate reconstitution. One sample received an addition of MSP to generate nanodiscs while the other sample without MSP will form proteoliposomes. Pgp-discs were isolated by affinity chromatography. Recovery of Pgp-discs was tracked by measuring verapamil-stimulated ATPase activity after purification on Strep-tactin resin.

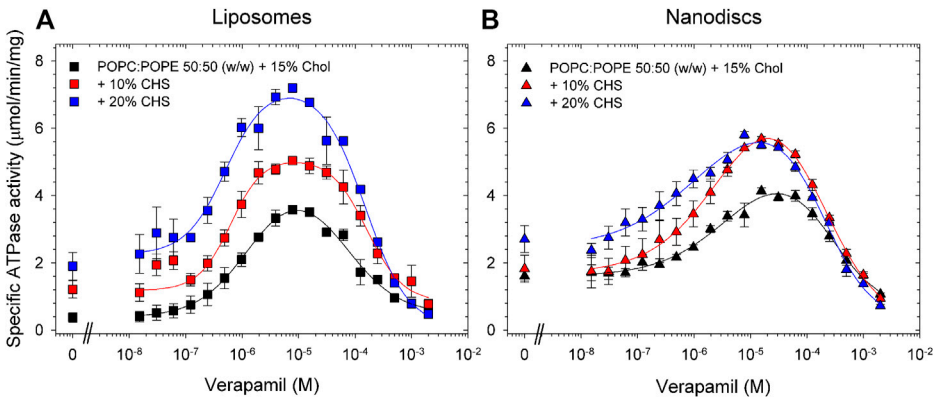

FIGURE 5
Effects of CHS on the verapamil-stimulation of ATPase in proteoliposomes and nanodiscs. Purified Pgp was reconstituted into **(A)** liposomes and **(B)** lipid nanodiscs containing POPC/POPE supplemented with 15% cholesterol and 0%, 10%, and 20% CHS. ATPase activity was measured as described in Experimental Procedures. Data points represent the mean ± SEM (n = 3). In liposomes, more than 86% of Pgp's NBDs were oriented inside-out and accessible to ATP hydrolysis as inferred from accessible to cleavage of the C-terminal Strep-tag, see Fig. S7.

TABLE 5 Pgp was reconstituted into liposomes prepared from POPC/POPE with the indicated concentrations of CHS and the verapamil stimulation of ATPase activity was assayed (n = 3).

POPC:POPE liposomes supplemented with	V_{max} (µmol/min/mg)	EC_{50} (µM)	Hill coefficient	Basal activity (µmol/min/mg)	Verapamil concentration for maximum activity (µM)
15% Chol	3.6 ± 0.1	0.89 ± 0.07	1.1 ± 0.1	0.4	8
15% Chol, 10% CHS	5.0 ± 0.1	0.69 ± 0.12	1.4 ± 0.4	1.2	8
15% Chol, 20% CHS	7.2 ± 0.1	0.48 ± 0.09	1.3 ± 0.3	1.9	8

TABLE 6 Pgp was reconstituted into lipid nanodiscs prepared from POPC/POPE with the indicated concentrations of CHS and the verapamil stimulation of ATPase activity was assayed (n = 3).

POPC:POPE nanodiscs supplemented with	V_{max} (µmol/min/mg)	EC_{50} (µM)	Hill coefficient	Basal activity (µmol/min/mg)	Verapamil concentration for maximum activity (µM)
15% Chol	4.1 ± 0.1	1.83 ± 0.37	1.0 ± 0.2	1.6	16
15% Chol, 10% CHS	5.7 ± 0.1	1.14 ± 0.19	1.0 ± 0.2	1.8	16
15% Chol, 20% CHS	5.8 ± 0.1	0.68 ± 0.31	0.7 ± 0.2	2.7	8

Compared to the results obtained with lipid-activated Pgp (Figure 4; Table 4), the reconstituted protein (Figure 5; Tables 5, 6) demonstrated overall superior function. In absence of CHS, reconstituted Pgp showed an increased ATPase activity by a factor of about 2 and a roughly 10-fold decrease in EC_{50} for verapamil activation, both in proteoliposomes and in nanodiscs. Addition of 10% or 20% CHS resulted in an increase of ATPase activity and a gradual decrease of EC_{50} in all cases, although the effect on EC_{50} was smaller for the reconstituted samples due to their already reduced EC_{50} in absence of CHS. Recovery was similar without or with CHS (Supplementary Figure S6). Compared to lipid-activated Pgp, the reconstituted samples had a higher basal activity, especially in nanodiscs.

Finally, we reconstituted Pgp in proteoliposomes and nanodiscs containing the phospholipid composition mimicking plasma membranes (POPC:POPE:POPS:SM at a ratio of 42:25:10:23 (w/w) with 50% cholesterol). In contrast to the samples reconstituted in POPC/POPE/cholesterol (Figure 5; Tables 5, 6), reconstitution of Pgp in plasma membrane mimic lipids, either as proteoliposomes or as nanodiscs, did not improve functionality compared to the lipid-activated protein. While the V_{max} of verapamil-stimulated ATPase activity was slightly to moderately increased, the apparent affinity

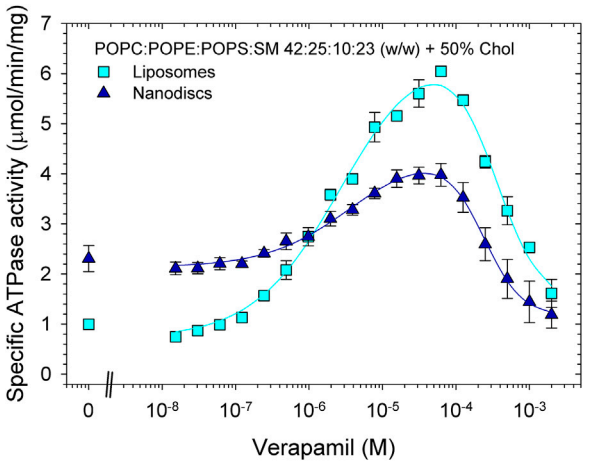

FIGURE 6
Effects of reconstitution on the verapamil-stimulation of ATPase in lipids mimicking plasma membranes. Purified Pgp was reconstituted into liposomes and lipid nanodiscs. ATPase activity was measured as described in Experimental Procedures. Data points represent the mean ± SEM (n = 3). In liposomes, more than 84% of Pgp's NBDs were accessible, see Fig. S7.

for verapamil decreased by a factor of 4 (Figure 6; Table 7). Again, Pgp in nanodiscs showed a high basal activity.

Discussion

In this study, we created an artificial lipid mixture that comes closer to the mammalian plasma membrane composition but still promotes Pgp ATPase activity in the same way that *E. coli* lipids can. Our study will facilitate future investigations of the mechanism of Pgp such as using tryptophan fluorescence, in order to overcome the high background signal from natural lipid extracts (such as *E. coli* lipids). Two major components of mammalian plasma membranes are PC and PE, while *E. coli* polar lipids contain a large amount of PE, but no PC. Using a mixture of synthetic POPC and POPE in a ratio of 50:50, Pgp fell short of reaching the verapamil-stimulated ATPase activity and apparent verapamil affinity observed with *E. coli* polar lipids. However, with supplements such as cardiolipin, SM, or DPPA, the POPC/POPE mixture was able to restore Pgp functionality to the same level observed with *E. coli* polar lipids or even higher. It should be emphasized that the activities and affinities reached here are similar to those found in the natural environment of Pgp, the plasma membrane (al-Shawi and Senior, 1993; Shukla et al., 2017).

The main effect of these lipid supplements was to reduce the EC_{50} for verapamil, while verapamil-stimulated ATPase activity (V_{max}) was only moderately affected, if at all. Of these three components, only SM is found in mammalian plasma membranes in significant amounts. It is not clear how these components support Pgp functionality or if they do it by the same mechanism. Cardiolipin and DPPA are negatively charged, but SM is not; furthermore, the negatively charged phospholipids POPS and POPG did not improve Pgp performance. Both DPPA and the SM preparation used in this study contain exclusively or nearly exclusively saturated fatty acids, which tend to reduce the membrane fluidity. On the other hand, the cardiolipin preparation used here carries mostly doubly-unsaturated fatty acids, which are expected to increase membrane fluidity.

Cholesterol is a major component of mammalian plasma membranes. However, adding cholesterol to the POPC/POPE mixture, even in amounts as high as 50%, did not improve Pgp functionality to a pronounced extent. While the apparent ligand binding affinity was somewhat increased, the ATPase activity dropped. In contrast, a mammalian plasma membrane mimic, containing POPC:POPE:POPS: SM at a ratio of 42:25:10:23 (w/w) with 50% cholesterol gave a verapamil-stimulated ATPase activity similar to *E. coli* lipids while increasing the apparent affinity for verapamil significantly. Taken the results described above into account, this increase in Pgp functionality is most likely due to the presence of SM, not POPS.

Another compound we identified as supportive of Pgp performance was CHS. Adding 10% CHS to a POPC/POPE mix supplemented with 15% cholesterol improved the V_{max} of verapamil-stimulated ATPase activity only slightly but increased the apparent affinity for verapamil by a factor of 20. High concentrations of CHS resulted in a significantly increased basal activity which could be due to binding of CHS to the drug binding site as transport substrate or as activator, maybe acting cooperatively with verapamil to increase the verapamil affinity. Alternatively, cholesterol has been shown by cryo-EM to bind to grooves on the surface of the TMDs of Pgp (Alam et al., 2019). CHS might do the same and stabilize Pgp in a conformation that is hydrolysis-active and has a high affinity for verapamil. The notion of direct interactions of CHS with Pgp, whether in the drug binding site or on the surface of the transmembrane region, is supported by the finding that CHS increases the thermostability of DDM-solubilized Pgp.

Following the systematic investigation of lipid effect on Pgp activity, we optimized conditions for reconstitution of Pgp in nanodiscs, especially with regard to recovery, and to see if the artificial lipid mixtures identified above also worked well in nanodiscs. The optimal DDM:lipid ratio for solubilizing the lipids ratio was determined to be 4: 1 and the best ratio of Bio-Beads to Pgp was found to be 2 mg Bio-Beads per 1 mg Pgp. The MSP:lipid ratio was optimal at 1:40–1:50. Using these conditions, we reconstituted Pgp into proteoliposomes and nanodiscs using POPC/POPE with 15% cholesterol and 0%, 10% or 20% CHS. Especially when prepared in presence of CHS, the resulting

TABLE 7 Pgp was reconstituted intp proteoliposomes and lipid nanodiscs prepared from plasma membrane mimicking lipids, and the verapamil stimulation of ATPase activity was assayed (n = 3).

Sample preparation	V_{max} (µmol/min/mg)	EC_{50} (µM)	Hill coefficient	Basal activity (µmol/min/mg)	Verapamil concentration for maximum activity (µM)
Lipid-activated	3.5 ± 0.1	0.52 ± 0.06	1.2 ± 0.1	0.7	10
Proteoliposomes	6.0 ± 0.1	2.2 ± 0.3	1.1 ± 0.1	1.0	60
Nanodiscs	4.0 ± 0.2	2.1 ± 0.4	0.7 ± 0.1	2.3	30

proteoliposomes and nanodiscs both strongly supported Pgp functionality. Both verapamil-stimulated ATPase activity and apparent verapamil affinity were actually superior to results observed in preparations where detergent-solubilized Pgp was just mixed with lipids, without undergoing the reconstitution procedure.

When using the plasma membrane mimic lipid mixture (POPC: POPE:POPS:SM at a ratio of 42:25:10:23 (w/w) with 50% cholesterol for the reconstitution, we obtained again proteoliposomes and nanodiscs with active Pgp. However, the verapamil-stimulated ATPase activity in nanodiscs was only about half of the activity observed in proteoliposomes. While the lipid composition of the proteoliposomes likely reflects the composition of the lipid mix user for the reconstruction, this might not be the case for the nanodiscs. It could be shown that nanodiscs prepared from binary mixtures of POPC and POPG or POPS in different ratios have a lipid composition reflecting the original mixture (Hoi et al., 2016). However, these phospholipids are very similar, just differing in the head group. Experimental data on nanodiscs prepared from more mixtures of structurally more diverse lipids are lacking (Li et al., 2019). Another possible problem is a heterogeneous distribution of lipids in nanodiscs due to the presence of MSP. A molecular dynamics study found an even distribution of cholesterol in the nanodiscs, while the negatively charged CHS preferred to bind to positively charged amino acid residues in MSP (Augustyn et al., 2019). Even if some CHS binds to MSP, the results of the present study show that there must be still CHS molecules available to bind to Pgp and improve its functionality.

In conclusion, we could identify improved lipid mixtures that are able to sustain high levels of activity and verapamil binding affinities very similar to Pgp in plasma membranes. This will pave the way for future functional and biophysical studies of Pgp in a lipid environment that supports enzyme activity and mirrors the drug binding properties in its native membrane environment.

Data availability statement

The original contributions presented in the study are included in the article/Supplementary Material, further inquiries can be directed to the corresponding author.

Author contributions

NT and IU designed experiments, performed experiments, and analyzed data, NT wrote the first draft of the manuscript, AB perform experiments and analyzed data, VJ-M analyzed data and edited the manuscript, JW analyzed data, edited the results and discussion, QZ provided insightful comments, some data of protein stability, and edited the manuscript.

Funding

This work was supported by the National Institute of General Medical Sciences R01 GM141216 (IU) and GM118594 (QZ), and the South Plains Foundation (IU).

Acknowledgments

We thank Matthew Guerra, Rozenn Kenny Moundounga, and Devin Mangold for technical assistance with membrane preparations. We thank Arne Moeller and his group for insightful comments.

Conflict of interest

The authors declare that the research was conducted in the absence of any commercial or financial relationships that could be construed as a potential conflict of interest.

Publisher's note

Supplementary material

The Supplementary Material for this article can be found online at: https://www.frontiersin.org/articles/10.3389/fmolb.2023.1141081/full#supplementary-material

References

Al-Khazaali, A., Arora, R., al-Shawi, M. K., and Senior, A. E. (2014). P-Glycoprotein: A focus on characterizing variability in cardiovascular pharmacotherapeuticsCharacterization of the adenosine triphosphatase activity of Chinese hamster P-glycoprotein. *Am. J. TherJ Biol. Chem.* 21268 (16), 24197–94206. doi:10.1016/s0021-9258(18)53597-3

Alam, A., Kowal, J., Broude, E., Roninson, I., and Locher, K. P. (2019). Structural insight into substrate and inhibitor discrimination by human P-glycoprotein. *Science* 363 (6428), 753–756. doi:10.1126/science.aav7102

Alam, A., Kung, R., Kowal, J., McLeod, R. A., Tremp, N., Broude, E. V., et al. (2018). Structure of a zosuquidar and UIC2-bound human-mouse chimeric ABCB1. *Proc. Natl. Acad. Sci. U. S. A.* 115 (9), E1973–E1982. doi:10.1073/pnas.1717044115

Aller, S. G., Yu, J., Ward, A., Weng, Y., Chittaboina, S., Zhuo, R., et al. (2009). Structure of P-glycoprotein reveals a molecular basis for poly-specific drug binding. *Science* 323 (5922), 1718–1722. doi:10.1126/science.1168750

Ambudkar, S. V., Lelong, I. H., Zhang, J., Cardarelli, C. O., Gottesman, M. M., and Pastan, I. (1992). Partial purification and reconstitution of the human multidrug-resistance pump: Characterization of the drug-stimulatable ATP hydrolysis. *Proc. Natl. Acad. Sci. U. S. A.* 89 (18), 8472–8476. doi:10.1073/pnas.89.18.8472

Augustyn, B., Stepien, P., Poojari, C., Mobarak, E., Polit, A., Wisniewska-Becker, A., et al. (2019). Cholesteryl hemisuccinate is not a good replacement for cholesterol in lipid nanodiscs. *J. Phys. Chem. B* 123 (46), 9839–9845. doi:10.1021/acs.jpcb.9b07853

Bai, J., Swartz, D. J., ProtasevichII, Brouillette, C. G., Harrell, P. M., Hildebrandt, E., et al. (2011). A gene optimization strategy that enhances production of fully functional P-glycoprotein in Pichia pastoris. *PLoS One* 6 (8), e22577. doi:10.1371/journal.pone.0022577

Belli, S., Elsener, P. M., Wunderli-Allenspach, H., and Krämer, S. D. (2009). Cholesterol-mediated activation of P-glycoprotein: Distinct effects on basal and

drug-induced ATPase activities. *J. Pharm. Sci.* 98 (5), 1905–1918. doi:10.1002/jps.21558

Bucher, K., Belli, S., Wunderli-Allenspach, H., and Krämer, S. D. (2007). P-Glycoprotein in proteoliposomes with low residual detergent: The effects of cholesterol. *Pharm. Res.* 24 (11), 1993–2004. doi:10.1007/s11095-007-9326-0

Chufan, E. E., Sim, H. M., and Ambudkar, S. V. (2015). Molecular basis of the polyspecificity of P-glycoprotein (ABCB1): Recent biochemical and structural studies. *Adv. Cancer Res.* 125, 71–96. doi:10.1016/bs.acr.2014.10.003

Clouser, A. F., Alam, Y. H., and Atkins, W. M. (2021). Cholesterol asymmetrically modulates the conformational ensemble of the nucleotide-binding domains of P-glycoprotein in lipid nanodiscs. *Biochemistry* 60 (1), 85–94. doi:10.1021/acs.biochem.0c00824

Denisov, I. G., Frank, D. J., and Sligar, S. G. (2009). Cooperative properties of cytochromes P450. *Pharmacol. Ther.* 124 (2), 151–167. doi:10.1016/j.pharmthera.2009.05.011

Doige, C. A., Yu, X., and Sharom, F. J. (1993). The effects of lipids and detergents on ATPase-active P-glycoprotein. *Biochim. Biophys. Acta* 1146 (1), 65–72. doi:10.1016/0005-2736(93)90339-2

Domicevica, L., Koldsø, H., and Biggin, P. C. (2018). Multiscale molecular dynamics simulations of lipid interactions with P-glycoprotein in a complex membrane. *J. Mol. Graph Model* 80, 147–156. doi:10.1016/j.jmgm.2017.12.022

Giacomini, K. M., Huang, S. M., Tweedie, D. J., Benet, L. Z., Brouwer, K. L., Chu, X., et al. (2010). Membrane transporters in drug development. *Nat. Rev. Drug Discov.* 9 (3), 215–236. doi:10.1038/nrd3028

Gottesman, M. M., and Ling, V. (2006). The molecular basis of multidrug resistance in cancer: The early years of P-glycoprotein research. *FEBS Lett.* 580 (4), 998–1009. doi:10.1016/j.febslet.2005.12.060

Hoi, K. K., Robinson, C. V., and Marty, M. T. (2016). Unraveling the composition and behavior of heterogeneous lipid nanodiscs by mass spectrometry. *Anal. Chem.* 88 (12), 6199–6204. doi:10.1021/acs.analchem.6b00851

Hullin-Matsuda, F., Taguchi, T., Greimel, P., and Kobayashi, T. (2014). Lipid compartmentalization in the endosome system. *Semin. Cell Dev. Biol.* 31, 48–56. doi:10.1016/j.semcdb.2014.04.010

Ingólfsson, H. I., Melo, M. N., van Eerden, F. J., Arnarez, C., Lopez, C. A., Wassenaar, T. A., et al. (2014). Lipid organization of the plasma membrane. *J. Am. Chem. Soc.* 136 (41), 14554–14559. doi:10.1021/ja507832e

Ismair, M. G., Häusler, S., Stuermer, C. A., Guyot, C., Meier, P. J., Roth, J., et al. (2009). ABC-transporters are localized in caveolin-1-positive and reggie-1-negative and reggie-2-negative microdomains of the canalicular membrane in rat hepatocytes. *Hepatology* 49 (5), 1673–1682. doi:10.1002/hep.22807

Jia, Y., Wang, N., Zhang, Y., Xue, D., Lou, H., and Liu, X. (2020). Alteration in the function and expression of SLC and ABC transporters in the neurovascular unit in alzheimer's disease and the clinical significance. *Aging Dis.* 11 (2), 390–404. doi:10.14336/ad.2019.0519

Kalvodova, L., Sampaio, J. L., Cordo, S., Ejsing, C. S., Shevchenko, A., and Simons, K. (2009). The lipidomes of vesicular stomatitis virus, semliki forest virus, and the host plasma membrane analyzed by quantitative shotgun mass spectrometry. *J. Virol.* 83 (16), 7996–8003. doi:10.1128/jvi.00635-09

Kapitulnik, J., Weil, E., Rabinowitz, R., and Krausz, M. M. (1987). Fetal and adult human liver differ markedly in the fluidity and lipid composition of their microsomal membranes. *Hepatology* 7 (1), 55–60. doi:10.1002/hep.1840070113

Kulig, W., Tynkkynen, J., Javanainen, M., Manna, M., Rog, T., Vattulainen, I., et al. (2014). How well does cholesteryl hemisuccinate mimic cholesterol in saturated phospholipid bilayers? *J. Mol. Model* 20 (2), 2121. doi:10.1007/s00894-014-2121-z

Li, M. J., Atkins, W. M., and McClary, W. D. (2019). Preparation of lipid nanodiscs with lipid mixtures. *Curr. Protoc. Protein Sci.* 98 (1), e100. doi:10.1002/cpps.100

Marcoux, J., Wang, S. C., Politis, A., Reading, E., Ma, J., Biggin, P. C., et al. (2013). Mass spectrometry reveals synergistic effects of nucleotides, lipids, and drugs binding to a multidrug resistance efflux pump. *Proc. Natl. Acad. Sci.* 110 (24), 9704–9709. doi:10.1073/pnas.1303888110

Modok, S., Heyward, C., and Callaghan, R. (2004). P-glycoprotein retains function when reconstituted into a sphingolipid- and cholesterol-rich environment. *J. Lipid Res.* 45 (10), 1910–1918. doi:10.1194/jlr.M400220-JLR200

Neumann, J., Rose-Sperling, D., and Hellmich, U. A. (2017). Diverse relations between ABC transporters and lipids: An overview. *Biochim. Biophys. Acta Biomembr.* 1859 (4), 605–618. doi:10.1016/j.bbamem.2016.09.023

Nosol, K., Romane, K., Irobalieva, R. N., Alam, A., Kowal, J., Fujita, N., et al. (2020). Cryo-EM structures reveal distinct mechanisms of inhibition of the human multidrug transporter ABCB1. *Proc. Natl. Acad. Sci. U. S. A.* 117 (42), 26245–26253. doi:10.1073/pnas.2010264117

Ritchie, T. K., Grinkova, Y. V., Bayburt, T. H., Denisov, I. G., Zolnerciks, J. K., Atkins, W. M., et al. (2009). Chapter 11 - reconstitution of membrane proteins in phospholipid bilayer nanodiscs. *Methods Enzymol.* 464, 211–231. doi:10.1016/S0076-6879(09)64011-8

Robey, R. W., Pluchino, K. M., Hall, M. D., Fojo, A. T., Bates, S. E., and Gottesman, M. M. (2018). Revisiting the role of ABC transporters in multidrug-resistant cancer. *Nat. Rev. Cancer* 18 (7), 452–464. doi:10.1038/s41568-018-0005-8

Rothnie, A., Theron, D., Soceneantu, L., Martin, C., Traikia, M., Berridge, G., et al. (2001). The importance of cholesterol in maintenance of P-glycoprotein activity and its membrane perturbing influence. *Eur. Biophys. J.* 30 (6), 430–442. doi:10.1007/s002490100156

Sharom, F. J. (2014). Complex interplay between the P-glycoprotein multidrug efflux pump and the membrane: Its role in modulating protein function. *Front. Oncol.* 4, 41. doi:10.3389/fonc.2014.00041

Sharom, F. J., Yu, X., and Doige, C. A. (1993). Functional reconstitution of drug transport and ATPase activity in proteoliposomes containing partially purified P-glycoprotein. *J. Biol. Chem.* 268 (32), 24197–24202. doi:10.1016/s0021-9258(20)80510-9

Sharom, P. D. W. E. a. F. J., and Sharom, F. J. (2008). Interaction of the P-glycoprotein multidrug efflux pump with cholesterol: Effects on ATPase activity, drug binding and transport. *Biochemistry* 47 (51), 13686–13698. doi:10.1021/bi801409r

Shukla, S., Abel, B., Chufan, E. E., and Ambudkar, S. V. (2017). Effects of a detergent micelle environment on P-glycoprotein (ABCB1)-ligand interactions. *J. Biol. Chem.* 292 (17), 7066–7076. doi:10.1074/jbc.M116.771634

Stieger, B., Steiger, J., and Locher, K. P. (2021). Membrane lipids and transporter function. *Biochim. Biophys. Acta Mol. Basis Dis.* 1867 (5), 166079. doi:10.1016/j.bbadis.2021.166079

Storelli, F., Anoshchenko, O., and Unadkat, J. D. (2021). Successful prediction of human steady-state unbound brain-to-plasma concentration ratio of P-gp substrates using the proteomics-informed relative expression factor approach. *Clin. Pharmacol. Ther.* 110 (2), 432–442. doi:10.1002/cpt.2227

Swartz, D. J., Mok, L., Botta, S. K., Singh, A., Altenberg, G. A., and Urbatsch, I. L. (2014). Directed evolution of P-glycoprotein cysteines reveals site-specific, non-conservative substitutions that preserve multidrug resistance. *Biosci. Rep.* 34 (3), e00116. doi:10.1042/BSR20140062

Swartz, D. J., Singh, A., Sok, N., Thomas, J. N., Weber, J., and Urbatsch, I. L. (2020). Replacing the eleven native tryptophans by directed evolution produces an active P-glycoprotein with site-specific, non-conservative substitutions. *Sci. Rep.* 10 (1), 3224. doi:10.1038/s41598-020-59802-w

Swartz, D. J., Weber, J., and Urbatsch, I. L. (2013). P-glycoprotein is fully active after multiple tryptophan substitutions. *Biochimica Biophysica Acta (BBA)-Biomembranes* 1828 (3), 1159–1168. doi:10.1016/j.bbamem.2012.12.005

Symons, J. L., Cho, K. J., Chang, J. T., Du, G., Waxham, M. N., Hancock, J. F., et al. (2021). Lipidomic atlas of mammalian cell membranes reveals hierarchical variation induced by culture conditions, subcellular membranes, and cell lineages. *Soft Matter* 17 (2), 288–297. doi:10.1039/d0sm00404a

Szewczyk, P., Tao, H., McGrath, A. P., Villaluz, M., Rees, S. D., Lee, S. C., et al. (2015). Snapshots of ligand entry, malleable binding and induced helical movement in P-glycoprotein. *Acta Crystallogr. Sect. D. Biol. Crystallogr.* 71 (3), 732–741. doi:10.1107/S1399004715000978

Urbatsch, I. L., Gimi, K., Wilke-Mounts, S., Lerner-Marmarosh, N., Rousseau, M.-E., Gros, P., et al. (2001). Cysteines 431 and 1074 are responsible for inhibitory disulfide cross-linking between the two nucleotide-binding sites in human P-glycoprotein. *J. Biol. Chem.* 276 (29), 26980–26987. doi:10.1074/jbc.M010829200

Urbatsch, I. L., Gimi, K., Wilke-Mounts, S., and Senior, A. E. (2000). Conserved walker A Ser residues in the catalytic sites of P-glycoprotein are critical for catalysis and involved primarily at the transition state step. *J. Biol. Chem.* 275 (32), 25031–25038. doi:10.1074/jbc.M003962200

Urbatsch, I. L., Sankaran, B., Weber, J., and Senior, A. E. (1995). P-glycoprotein is stably inhibited by vanadate-induced trapping of nucleotide at a single catalytic site. *J. Biol. Chem.* 270 (33), 19383–19390. doi:10.1074/jbc.270.33.19383

Urbatsch, I. L., and Senior, A. E. (1995). Effects of lipids on ATPase activity of purified Chinese hamster P-glycoprotein. *Arch. Biochem. Biophys.* 316 (1), 135–140. doi:10.1006/abbi.1995.1020

van Meer, G., Voelker, D. R., and Feigenson, G. W. (2008). Membrane lipids: Where they are and how they behave. *Nat. Rev. Mol. Cell Biol.* 9 (2), 112–124. doi:10.1038/nrm2330

Vance, J. E., and Steenbergen, R. (2005). Metabolism and functions of phosphatidylserine. *Prog. Lipid Res.* 44 (4), 207–234. doi:10.1016/j.plipres.2005.05.001

Waghray, D., and Zhang, Q. (2018). Inhibit or evade multidrug resistance P-glycoprotein in cancer treatment. *J. Med. Chem.* 61 (12), 5108–5121. doi:10.1021/acs.jmedchem.7b01457

Yang, Z., Zhou, Q., Mok, L., Singh, A., Swartz, D. J., Urbatsch, I. L., et al. (2017). Interactions and cooperativity between P-glycoprotein structural domains determined by thermal unfolding provides insights into its solution structure and function. *Biochim. Biophys. Acta Biomembr.* 1859 (1), 48–60. doi:10.1016/j.bbamem.2016.10.009

Yee, S. W., Brackman, D. J., Ennis, E. A., Sugiyama, Y., Kamdem, L. K., Blanchard, R., et al. (2018). Influence of transporter polymorphisms on drug disposition and response: A perspective from the international transporter consortium. *Clin. Pharmacol. Ther.* 104 (5), 803–817. doi:10.1002/cpt.1098

Zambrano, F., Fleischer, S., and Fleischer, B. (1975). Lipid composition of the golgi apparatus of rat kidney and liver in comparison with other subcellular organelles. *Biochimica Biophysica Acta (BBA) - Lipids Lipid Metabolism* 380 (3), 357–369. doi:10.1016/0005-2760(75)90104-6

Zoghbi, M. E., Mok, L., Swartz, D. J., Singh, A., Fendley, G. A., Urbatsch, I. L., et al. (2017). Substrate-induced conformational changes in the nucleotide-binding domains of lipid bilayer-associated P-glycoprotein during ATP hydrolysis. *J. Biol. Chem.* 292 (50), 20412–20424. doi:10.1074/jbc.M117.814186

Nomenclature

Abbreviations

Pgp P-glycoprotein

ABC ATP Binding Cassette

TMD transmembrane domain

NBD nucleotide binding domain

WL-MSP tryptophan-free membrane scaffold protein

DDM n-dodecyl-β-D-maltopyranoside

CHS cholesteryl hemisuccinate

POPC 1-palmitoyl-2-oleoyl-sn-glycero-3-phosphocholine or 16:0-18:1 PC

POPE 1-palmitoyl-2-oleoyl-sn-glycero-3-phosphatidylglycerol

POPS 1-palmitoyl-2-oleoyl-sn-glycero-3-phospho-L-serine

POPI 1-palmitoyl-2-oleoyl-sn-glycero-3-phosphatidylinositol

POPG 1-palmitoyl-2-oleoyl-sn-glycero-3-phosphatidylethanolamine

SM sphingomyelin

DPPA 1,2-dipalmitoyl-sn-glycero-3-phosphate or 16:0 PA

CL cardiolipin

TEV tobacco etch virus protease

Frontiers in
Molecular Biosciences

Explores biological processes in living organisms on a molecular scale

Focuses on the molecular mechanisms underpinning and regulating biological processes in organisms across all branches of life.

Discover the latest Research Topics

See more →

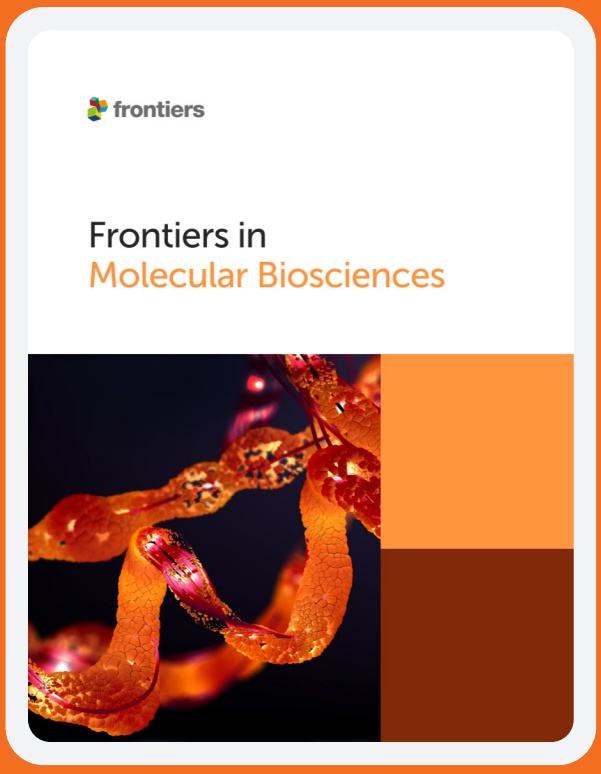

Frontiers

Avenue du Tribunal-Fédéral 34
1005 Lausanne, Switzerland
frontiersin.org

Contact us

+41 (0)21 510 17 00
frontiersin.org/about/contact